

---

# Study of optical properties and galaxy populations of galaxy clusters

Filiberto Giorgio Braglia

---



München 2008



---

# Study of optical properties and galaxy populations of galaxy clusters

Filiberto Giorgio Braglia

---

Dissertation  
an der Fakultät für Physik  
der Ludwig-Maximilians-Universität  
München

vorgelegt von  
Filiberto Giorgio Braglia  
aus Milano, Italien

München, den 17 Oktober 2008

Erstgutachter: Prof. Dr. Hans Boehringer  
Zweitgutachter: Prof. Dr. Ortwin Gerhard  
Tag der mündlichen Prüfung: 17 Oktober 2008

# Contents

<b>Zusammenfassung</b>	<b>3</b>
<b>Summary</b>	<b>7</b>
<b>1 General framework</b>	<b>9</b>
1.1 Galaxy clusters: an overview . . . . .	9
1.1.1 Optical classification of galaxy clusters . . . . .	11
1.1.2 X-ray emission of galaxy clusters . . . . .	12
1.1.3 Clusters and the large-scale structure . . . . .	16
1.2 X-ray surveys of clusters . . . . .	16
1.2.1 The REFLEX-DXL Sample . . . . .	18
1.3 Galaxy morphology, star-formation activity and interactions in clusters	19
1.3.1 The interactions of cluster galaxies . . . . .	21
1.4 The luminosity function of galaxies in clusters . . . . .	23
1.5 Determination of cluster masses . . . . .	24
1.5.1 Mass-to-light ratios . . . . .	25
1.6 The thesis: aims and methods . . . . .	26
1.6.1 Previous studies on the analyzed clusters . . . . .	29
<b>2 Transformation of galaxy colours along cluster-feeding filaments</b>	<b>41</b>
2.1 Introduction . . . . .	42
2.2 Data description and reduction . . . . .	43
2.3 Analysis . . . . .	44
2.3.1 Evidence of large-scale structure . . . . .	44
2.3.2 Star formation along the large-scale structure . . . . .	47
2.4 Discussion and conclusions . . . . .	51
<b>3 Evolution of the star formation activity across massive galaxy clusters</b>	<b>57</b>
3.1 Introduction . . . . .	57
3.2 Data description and reduction procedures . . . . .	59
3.2.1 Spectroscopic data . . . . .	59
3.2.2 Photometric data . . . . .	63

## Contents

---

3.2.3	UV data . . . . .	67
3.2.4	X-ray data . . . . .	68
3.3	Photometric catalogues . . . . .	68
3.3.1	RXCJ0014.3-3022 . . . . .	72
3.3.2	RXCJ2308.3-0211 . . . . .	73
3.4	Spectroscopic catalogues . . . . .	73
3.4.1	Cluster membership . . . . .	73
3.4.2	RXCJ0014.3-3023 . . . . .	74
3.4.3	RXCJ2308.3-0211 . . . . .	76
3.5	Results . . . . .	77
3.5.1	Cluster morphology . . . . .	77
3.5.2	Spectral index analysis . . . . .	83
3.6	Discussion . . . . .	92
3.7	Conclusions . . . . .	95
<b>4</b>	<b>Connecting dynamical state and galaxy populations in massive clusters</b>	<b>105</b>
4.1	Introduction . . . . .	105
4.2	The data and cluster member catalogues . . . . .	107
4.2.1	Statistical weighting of spectroscopic cluster members . . . . .	108
4.3	Dynamics . . . . .	111
4.3.1	RXCJ0014.3-3022 . . . . .	113
4.3.2	RXCJ2308.3-0211 . . . . .	115
4.4	Optical luminosity function . . . . .	118
4.4.1	Total cluster luminosity . . . . .	119
4.4.2	Luminosity function parameters for RXCJ0014.3-3022 . . . . .	121
4.4.3	Luminosity function parameters for RXCJ2308.3-0211 . . . . .	128
4.5	Discussion . . . . .	133
4.6	Conclusions . . . . .	138
<b>5</b>	<b>Concluding remarks</b>	<b>149</b>
	<b>References</b>	<b>153</b>
<b>A</b>	<b>Useful techniques</b>	<b>155</b>
A.1	Surface density maps . . . . .	155
A.2	Calculation of spectral indices . . . . .	157
<b>B</b>	<b>Spectroscopic members catalogue of RXCJ0014.3-3022 (A 2744)</b>	<b>159</b>
<b>C</b>	<b>Spectroscopic members catalogue of RXCJ2308.3-0211 (A 2537)</b>	<b>169</b>

# Zusammenfassung

Galaxienhaufen markieren die dichtesten Regionen der großräumigen Struktur des Universums. Sie besitzen typische Massen im Bereich von  $10^{13} - 10^{15} M_{\odot}$  und Ausdehnungen in der Größenordnung eines Megaparsecs. Der größte Massenanteil von Galaxienhaufen besteht aus Dunkler Materie. Der Anteil gewöhnlicher Materie liegt bei weniger als  $\sim 20\%$  der Gesamthaufenmasse, von dieser wiederum befindet sich nur ein Bruchteil (etwa  $3\%$  der Gesamtmasse) in Form von Sternen. Der Großteil der gewöhnlichen Materie in Galaxienhaufen liegt als vollständig ionisiertes Plasma des Innerhaufengases (*Intra Cluster Medium*, ICM) vor.

Das aktuelle Paradigma für die Entstehung und Entwicklung kosmischer Strukturen sagt voraus, dass Galaxienhaufen durch den Kollaps von Materieüberdichten entstehen. Während dieses Prozesses erreichen die Haufengalaxien hohe Virialisationsgeschwindigkeiten von der Größenordnung  $\sim 10^3 \text{ km s}^{-1}$ . Auch das Innerhaufengas erreicht ein Gleichgewicht mit den Galaxien und wird dabei auf Temperaturen im Bereich von  $10^7 - 10^8 \text{ K}$  aufgeheizt, die groß genug sind, um Röntgenphotonen mit Energien von  $1 - 10 \text{ keV}$  auszusenden. Im optischen Bereich erscheinen Galaxienhaufen als lokalisierte Überdichten von hunderten bis tausenden Galaxien. Im Abbild der Röntgenstrahlung dagegen sind Galaxienhaufen wohldefinierte Objekte mit Luminositäten im Bereich von  $10^{43} - 10^{45} \text{ erg s}^{-1}$ .

Galaxienhaufen dienen als astrophysikalische Labore, da sie Stichproben tausender gleichartiger Galaxien in einer einheitlichen kosmischen Umgebung beinhalten. Haufengalaxien entwickeln sich nicht unabhängig voneinander, sondern wechselwirken miteinander, sowie mit dem Innerhaufengas und dem bindenden Gravitationspotenzial. Galaxienhaufen stellen somit eine einzigartige Möglichkeit dar, die Entwicklung und Wechselwirkung von Galaxien und die Einflüsse der Haufenumgebung auf ihre Eigenschaften zu untersuchen.

In der vorliegenden Doktorarbeit untersuche ich die Eigenschaften massereicher Galaxienhaufen und ihrer Galaxienpopulationen mit Hilfe von Daten verschiedener Wellenlängenbereiche vom optischen bis zum Röntgenregime. Das Hauptziel dieser Arbeit ist die ganzheitliche Beschreibung der Galaxienpopulation in Haufen und das Verständnis, wie die Galaxieneigenschaften mit der Umgebung und der globalen Haufendynamik korrelieren. Die untersuchten Objekte sind Teil der REFLEX-DXL (*Distant X-ray Luminous*) Stichprobe massereicher, entfernter ( $z \sim 0.3$ ) und extrem röntgenheller ( $L_X \sim 10^{45} \text{ erg s}^{-1}$ ) Haufen aus der REFLEX Himmelsdurchmusterung.

Diese zählen somit zu den leuchtkräftigsten und massereichsten bekannten Galaxienhaufen im Universum und beinhalten eine große Bandbreite morphologischer und dynamischer Entwicklungsstadien.

Kapitel 2 beschreibt eine Pilotstudie des Objekts RXCJ0014.3-3022, ein DXL Haufen in einem dramatischen Stadium eines Verschmelzungsprozesses. Die kombinierte Analyse der Röntgen- und optischen Morphologie, der großräumigen Dynamik und von Galaxienfarben ermöglichte es zwei großskalige filamentartige Strukturen zu identifizieren, die die Haupteinfallachsen von Materie in den Haufen darstellen. Diese Filamente erstrecken sich bis außerhalb des Virialradius des Haufens und können überdies durch die Analysen der Dynamik und der Röntgenemission bestätigt werden. Entlang dieser Filamente wurde im Bereich des Virialradius eine abrupte Änderung der Galaxienfarbe detektiert, die einen Anstieg der Sternentstehungsaktivität der Galaxien durch Eintritt in den Haufen aus der niederdichten Umgebung suggeriert. Außerdem wurde eine Population sehr leuchtkräftiger kompakter blauer Galaxien in diesen Filamenten gefunden, deren Existenz auch als Folge des Übergangs von der Feldumgebung in den Haufen interpretiert werden kann.

Kapitel 3 und 4 beinhalten detaillierte Untersuchungen zweier DXL Galaxienhaufen, den schon beschriebenen Haufen im Verschmelzungsstadium RXCJ0014.3-3022 und den Haufen RXCJ2308.3-0211 mit einem kühlen Zentralbereich (cool core cluster). Diese beiden Haufen befinden sich in entgegengesetzten dynamischen Stadien und stellen somit ideale Labore für das Verständnis des Zusammenhangs der Galaxieneigenschaften mit der globalen Haufenumgebung zur Verfügung. Durch die Kombination der optischen und Röntgenmorphologie konnten spezifische Regionen besonderer Aktivität identifiziert werden. In diesen Bereichen konnte durch die Verbindung einer Spektralanalyse mit optischen und UV Farben die Sternentstehungsrate von Haufengalaxien und deren Zeitentwicklung nachgezeichnet werden. Galaxien in den Außenbereichen stellten sich im Durchschnitt als jünger heraus als die Population in den Zentralbereichen, eine Beobachtung, die als Alterssequenz interpretiert werden kann: Galaxien fallen von außen in den Haufen ein, wobei die Sternentstehungsaktivität Schritt für Schritt durch die Haufenumgebung unterdrückt wird, bis sie im Zentralbereich schließlich vollständig erlischt. Überdies ist der Galaxienhaufen im Verschmelzungsstadium global gesehen jünger als der relaxierte Haufen mit kühlem Zentralbereich, was sich aus der erhöhten Anzahl von Galaxien mit den Emissionseigenschaften aktiver Sternentstehung ableiten ließ. Dies kann als Folge des Verschmelzungsprozesses interpretiert werden, durch dessen Effekt plötzliche Episoden von Sternentstehungsaktivität in den Galaxien verursacht werden können (Kapitel 3). Die komplementäre Untersuchung der Haufendynamik lieferte eine unabhängige Bestimmung der Haufenmassen, welche mit den Röntgenresultaten verglichen werden können. Gleichzeitig ermöglichte die Analyse der Leuchtkraftfunktion (LF) der Haufengalaxien in den identifizierten Regionen einen weiteren Nachweis für eine veränderte Galaxienpopulation. Die LF nähert sich in den Außenbereichen derjenigen



der Feldumgebung an, was wiederum eine Transformation der Galaxienpopulation während des Akkretionsprozesses in den Haufen nahelegt. Insbesondere wurden ausgeprägte Änderungen der Form der LF in den Übergansregionen beobachtet, welche zusätzlich scheinbar eine Umgebungsabhängigkeit aufweisen. Dieses kann wiederum als Effekt des Einfalls interpretiert werden: während die Galaxien in den Haufen eintreten verursacht die Wechselwirkung mit anderen Haufengalaxien und mit dem Innerhaufengas eine Veränderung der gesamten Galaxienpopulation (Kapitel 4).

Ein Teil dieser Ergebnisse (Kapitel 2) wurde schon in referierten Fachzeitschriften publiziert, während weitere Resultate (Kapitel 3 und 4) bald zur Veröffentlichung eingereicht werden.



# Summary

Clusters of galaxies mark the densest regions in the large-scale web of the Universe. They have typical masses ranging from  $10^{13} - 10^{15} M_{\odot}$  and dimensions of the order of the Mpc. The largest fraction of the mass of a galaxy cluster is made by dark matter. Less than  $\sim 20\%$  of the total cluster mass is composed by ordinary matter, with only a small fraction of it (about  $3\%$  of the total mass) actually condensed in stars. The largest part of the ordinary matter content of a cluster is a completely ionised plasma called *Intra Cluster Medium* (ICM).

The current paradigm for formation and evolution of structures in the Universe predicts that clusters of galaxies form by collapse of matter overdensities. During this process, cluster galaxies reach high virialization velocities of order  $\sim 10^3 \text{ km s}^{-1}$ . The ICM also reaches equilibrium with the galaxies and is heated to temperatures of order  $10^7 - 10^8 \text{ K}$ , enough to emit X-ray photons with energies of order  $1 - 10 \text{ keV}$ . In optical, galaxy clusters appear as localised overdensities of hundreds to thousands of galaxies. In X-rays, clusters appear instead as defined entities with luminosities ranging from  $10^{43} - 10^{45} \text{ ergs s}^{-1}$ .

As astrophysical laboratories, clusters provide samples of thousands of coeval galaxies within a well defined environment. Cluster galaxies do not evolve independently, interacting with each other, with the ICM and with the cluster potential. Clusters thus provide a unique opportunity to study the evolution and interaction of galaxies and the effect of environment on their properties.

In this thesis I investigate the properties of massive galaxy clusters and of their galaxy populations using multi-wavelength data from the optical to the X-rays. The aim is to provide a description as complete as possible of the galaxy population in clusters and to understand how the galaxy properties correlate with their environment and with the global cluster dynamics. The studied clusters are part of the REFLEX-DXL (*Distant X-ray Luminous*), a sample of massive, distant ( $z \sim 0.3$ ) and extremely X-ray luminous ( $L_X \sim 10^{45} \text{ ergs}^{-1}$ ) clusters drawn from the REFLEX survey. They are among the most luminous and massive clusters known in the Universe and encompass a wide range of morphological and dynamical stages.

Chapter 2 introduces a pilot study of RXCJ0014.3-3022, a DXL cluster in a dramatic stage of merging. From the combined analysis of X-ray and optical morphology, large-scale dynamics and galaxy colours it was possible to identify two large-scale filamentary structures driving the infall of matter in the cluster. These filaments extend

## Summary

---

beyond the cluster virial radius and are confirmed by dynamics and X-ray emission. Along the filaments a sudden change in the colours of galaxies was detected just beyond the virial radius, suggesting an increase in the star formation activity as galaxies enter the cluster from the low-density field. A population of very luminous and compact blue galaxies was also found in the filaments, their presence being again interpreted as an effect of the transition from the field to the cluster environment.

Chapters 3 and 4 show more detailed studies of two DXL cluster, the already introduced merging cluster RXCJ0014.3-3022 and the cool core cluster RXCJ2308.3-0211. These two clusters are in opposite dynamical stages, and provide two ideal laboratories to understand how galaxy properties depend on the global cluster environment. Combination of optical and X-ray morphology enabled to identify specific regions of interest in the studied clusters. In these regions, spectral index analysis, coupled with optical and UV colours, allowed to track the star formation activity and history of cluster galaxies. Galaxies are found to be on average younger in the outskirts than in the cluster cores, this being interpreted as an age sequence: galaxies infall on the cluster from the field and are progressively quenched until they cease their star formation activity in the cluster core. Moreover, the merging cluster is found to be globally younger than the relaxed cool core, having more galaxies with active emission from star formation activity. This is interpreted as due to the merger, whose effect on the galaxy population is able to trigger sudden episodes star formation activity (Chapter 3). The complementary study of the cluster dynamical state provided an independent determination of cluster masses to be compared with the X-ray determination. At the same time, the evaluation of the luminosity function (LF) of cluster members in the interesting regions previously defined allowed to detect definite changes in the galaxy population. The LF is found to become more similar to the field in the cluster outskirts, suggesting a transformation of the galaxy population during accretion on the cluster. In particular, in the transition regions the shape of the LF dramatically changes to shapes that appear to be dependent on environment. This is again interpreted as an effect of infall: as galaxies enter the clusters, their interaction with cluster galaxies and the ICM produce changes in the overall galaxy population (Chapter 4).

Part of these results (Chapter 2) has already been published on refereed journals, while others (Chapter 3 and 4) will be soon submitted.

# 1

## General framework

Massive galaxy clusters are ideal laboratories for astrophysical and cosmological studies. By providing large samples of coeval galaxies with a well-defined environment, they allow the study of the galaxy evolution, star formation history, mass-to-light ratio and the dependence of these properties on the environment. On the other hand, galaxy clusters trace the mass distribution in the cosmic web, giving valuable information about the large scale structure and the cosmology: in particular, as the cluster mass function probes the amplitude of the matter density fluctuations over scales of about  $5\text{-}10\ h^{-1}\ \text{Mpc}$ , they are valuable tools for the measure of the cosmological parameters, namely  $\Omega_0$  (the mean matter density in the Universe), the power spectrum and  $\sigma_8$  (the matter density variance at the cluster scale).

### 1.1 Galaxy clusters: an overview

Cluster of galaxies mark the densest regions of mass concentration in the large-scale web of the Universe. They have typical masses ranging from  $10^{13} - 10^{15} M_\odot$  and dimensions of the order of the Mpc. Their dimensions are usually described in terms of  $R_{500}$  or  $R_{200}$ , i.e. the radial distance from the cluster centre where the local matter density is, respectively, 500 or 200 times higher than the mean cosmic density. In the cluster cores, densities are usually hundreds of times higher.

The largest fraction of the mass of a galaxy cluster is made by undetectable dark matter, which defines and shapes the potential well binding together the galaxies and the X-ray luminous gas in the system. Less than  $\sim 20\%$  of the total cluster mass is composed by ordinary matter (what is usually called *baryonic* content), and only a

## 1 General framework

---

small fraction of it (about 3% of the total mass) actually condenses into stars and galaxies. The largest part of the baryonic component of a cluster lies in the form of a completely ionised plasma called *Intra Cluster Medium* (ICM hereafter).

The current paradigm for formation and evolution of structures in the Universe predicts that clusters of galaxies form by collapse of overdensities of dark matter, which forms the potential well in which galaxies lie and evolve. Massive clusters are then assembled across cosmic time by merging of smaller systems. During this process, galaxies feeling the gravitational potential of the dark matter halo gain energy and reach high virialization velocities, up to and in excess of  $\sim 10^3 \text{ km s}^{-1}$  in the cluster core. Similarly, the ICM is shocked and heated by the energy released by mergers and by adiabatic compression until it reaches virialization within the dark matter halo and with galaxies. This brings the gas to energies of order 1–10 keV ( $10^7 - 10^8$  K), enough to almost completely ionise it and cause it to emit X-ray radiation.

Clusters of galaxies have thus a well defined appearance both in optical and X-rays. In optical, they appear as definite, localised overdensities of galaxies, with hundreds to thousands of galaxies tightly concentrated on the plane of the sky. Conversely, in X-rays clusters appear as single, extended entities, shining brightly in the X-ray sky with luminosities ranging from  $10^{43} - 10^{45} \text{ ergs s}^{-1}$ . In both cases, the cluster cores usually stand out as the densest regions in the surrounding field.

Given their characteristics in this framework, clusters of galaxies are thus both powerful probes for cosmology and ideal laboratories for astrophysical studies. As clusters sample the highest mass peaks in the distribution of cosmic matter and probe the amplitudes of mass fluctuations on their scale, their spatial distribution and its evolution in time provide strong bounds to the cosmological parameters. For the same reasons, their matter content can be considered as representative of the global matter content in the Universe, providing an independent way of constraining the relative abundance of dark matter and baryonic matter. Moreover, under fair assumptions they provide a direct way to measure the large-scale geometry of the Universe.

As astrophysical laboratories, clusters provide samples of thousands of coeval galaxies within a well defined and limited environment. Cluster galaxies do not evolve independently, instead they interact with each other, with the ICM and with the cluster itself through its gravitational well. Consequently, clusters provide a unique opportunity to study the evolution and mutual interaction of galaxies and how the local environment affects their properties. The study of star formation activity and history in individual cluster galaxies and of the properties of the global cluster galaxy population can provide strong insights on the physical processes that shape both galaxies and clusters.

Throughout this chapter, the main characteristics of galaxy clusters, their population and the physics ruling these systems will be presented.

### 1.1.1 Optical classification of galaxy clusters

The fact that galaxies are not uniformly distributed on the sky is acknowledged since the works of Messier in XVIII century. First Charles Messier and then William and John Herschel noticed that many of their “nebulae” were aggregated in the regions of the Virgo and Coma Berenices constellations. Humboldt in the XIX century noted how about a third of the known nebulae were localised in a small region of the sky around Virgo. Now, the Virgo and Coma clusters are known to be only the closest galaxy clusters making the backbone of the cosmic large-scale structure. Optical observation of galaxy clusters reveals them as large overdensities of galaxies, with the local density in the core being several times higher than in the surrounding field. Several studies have been undertaken since the second half of the last century to detect and classify galaxy clusters.

Abell ((1958); (1965)) produced a first catalogue of several thousands of galaxy clusters detected through visual inspection of optical plates from the Palomar All-Sky Survey. This catalogue has been expanded in time to include clusters from the southern hemisphere (ACO catalogue, Abell et al. (1989)). Abell also introduced a first classification based on the cluster *richness*, i.e. the approximate number of galaxies composing the cluster. This was estimated as the background-corrected number of galaxies within a projected radius of  $R_A = 1.5h^{-1}Mpc$  (the so-called Abell radius) and with magnitude in the interval  $m_3$  and  $m_3 + 2$ , where  $m_3$  is the observed magnitude of the third most luminous galaxy in the cluster region. According to this classification, Abell Class 0 is the least populated class with less than 50 galaxies, while Class 5 is the richest with more than 300 galaxies. Abell clusters are typically in the local Universe ( $z \lesssim 0.2$ ), with some very bright members up to  $z \sim 0.4$ .

Zwicky proposed ((1961-1968)) a classification based on the cluster apparent shape on the plates. Depending on the number of galaxies in apparent contact, clusters are thus classified as compact, partly compact or open.

Bautz & Morgan ((1970)) proposed another classification, based on the dominance of the *Brightest Cluster Galaxy* (BCG hereafter). Type I clusters have a single dominant, very bright galaxy, Type II clusters have a typical elliptical as central galaxy, Type III clusters have multiple BCGs or no detectable BCG. Intermediate types, i.e. I–II and II–III, also can be defined.

Another interesting classification was suggested by Rood & Sastry ((1971)), where clusters are classified on a tuning fork diagram not much different from the original galaxy classification diagram of Hubble. This classification again relies on the optical shape of the cluster, defining CD (Core Dominant) clusters, B (Binary) clusters and then L (Line) and F (Flat) cluster on a side and C (compact) and I (Irregular) on the other side of the fork.

Additional methods for optical detection and classification of clusters have been developed in recent times. Matched filter techniques (see Postman et al. (1996);

## 1 General framework

---

Olsen et al. (1999); Schuecker & Böhringer (1998); Lobo et al. (2000)) apply maximum likelihood methods to match the distribution of galaxies in the sky and in flux with a given density profile and luminosity function. The red sequence technique (see Gladders & Yee (2000); (2001)) has been used to detect galaxy clusters in two-band imaging surveys. It was proved to be efficient in detecting clusters independently from their masses and to provide a reliable redshift estimate, although its efficiency depends on the actual presence of a red sequence in the colour-magnitude diagram of the observed fields, thus in principle preventing the detection of very young clusters (where a red sequence could still be in formation). More recently, a refinement of the red sequence technique, the MaxBCG algorithm, was introduced by Koester et al. ((2007a); (2007b)). This method is based on the detection of overdensities of red galaxies and the presence of a BCG in the cluster cores. They applied this method to the SDSS data, obtaining a catalogue of almost 14000 optically-selected galaxy clusters. Comparison with X-ray selected samples and with mock samples has shown that this approach is almost complete ( $\sim 85 - 90\%$ ) out to  $z \sim 0.3$  and for clusters with masses in excess of  $10^{14} h^{-1} M_{\odot}$ .

These and other different optical classifications try to link in some way the cluster with its mass, assuming that the more rich a cluster is, the largest is its mass. Indeed, the mass of a cluster is in principle the most desirable parameter by which to classify clusters, thus defining complete catalogues and samples containing clusters beyond a certain mass threshold. However, if redshift data are not available in large numbers, a direct link between mass and richness is difficult to establish.

A primary problem with optical classification of clusters is the fact that clusters are not isolated, but instead lie in front of a populated background field which is usually not homogeneous, presenting structure on all scales. Consequently, an unambiguous definition of richness is rather difficult to achieve. Moreover, projection effects (i.e. galaxy groups or filamentary structures aligned on the line of sight) can mimic the appearance of a rich cluster, thus providing spurious detections (see e.g. van Haarlem (1997)). Indeed, about 10% of Abell clusters have been found not to be real structures, being instead produced by such effects.

### 1.1.2 X-ray emission of galaxy clusters

Cluster of galaxies were detected clearly as bright X-ray sources since the first high-energy experiments successfully detected X-ray sources in the sky. Already the first observations revealed that the emission is mainly due to an optically thin, ionised plasma with mean density of order  $10^{-4} - 10^{-2} \text{cm}^{-3}$ . The ICM was then found from UV emission to be mainly composed by hydrogen and helium in relative proportions similar to the cosmic abundances ( $\sim 75\%$  H,  $\sim 24\%$  He), with heavier elements later confirmed by their X-ray emission lines (Felten et al. (1966); Catura et al. (1972); Mitchell et al. (1976); also see Mushotzky (2004)).



## 1.1 Galaxy clusters: an overview

---

The general modelling and description of the ICM (Cavaliere et al. (1971)) predicts that, given its high temperature and low density, it is almost completely ionised and that electrons and nuclei are in a state of collisional equilibrium. Under this assumption, the plasma will primarily emit via thermal bremsstrahlung. This provides many different opportunities to obtain important information from the X-ray spectroscopy and imaging of cluster emission. First of all, bremsstrahlung emissivity is proportional to both ion density  $n_i$  and electron density  $n_e$ :

$$\epsilon_{bs} = \frac{2^5 \pi e^6}{3 m_e c^3} \left( \frac{2\pi}{3 m_e k} \right)^{1/2} Z^2 n_e n_i g_{ff} T_g^{-1/2} e^{-h\nu/kT_g} \quad (1.1)$$

(where  $T_g$  is the gas temperature,  $Z$  is the ion charge and  $g_{ff} \sim 1/2$  is the Gaunt factor, a dimensionless quantity depending on the scatter mean distance between electrons and ions). Thus, bremsstrahlung emission is basically proportional to the squared density of the ICM. This means that galaxy clusters clearly stand out as X-ray sources in the sky. For comparison, optical detection of clusters relies on identification of overdensities of galaxies, thus basically cluster optical emission from clusters is proportional to the mass density. Moreover, the exponential cutoff of  $\epsilon_{bs}$  means that the spectrum shape is very sensitive to the temperature, thus allowing its determination. This description is largely valid and confirmed for temperatures higher than  $kT \geq 3$  keV; for lower temperatures, contribution from metal emission lines must also be accounted for.

Assuming that the ICM is virialized and in hydrostatic equilibrium in the cluster, the potential and thus the cluster mass can be derived. This assumption can generally be considered true, at least in the central region of the cluster. Indeed, the typical sound crossing time for the thin, hot ICM is of order of  $10^8 - 10^9$  yr, short compared to the typical cluster ages of several Gyr. Under assumption of hydrostatic equilibrium:

$$\frac{1}{\rho_g} \frac{dP}{dr} = -G \frac{M}{r^2} \quad (1.2)$$

the cluster mass can be derived assuming an ideal gas to relate gas pressure  $P$  to temperature  $T_g$ , density  $\rho_g$  and mean molecular mass  $\mu$ :

$$M = -\frac{kTr}{\mu m_p G} \left( \frac{\partial \ln \rho_g}{\partial \ln r} + \frac{\partial \ln T_g}{\partial \ln r} \right) \quad (1.3)$$

### 1.1.2.1 Cluster scaling relations

Modelling the density, temperature and entropy profile of the ICM provides additional tools to obtain information about the mass distribution and processes at work in observed clusters. King ((1962)) already showed that the radial density profile of the

## 1 General framework

---

inner regions of a self-gravitating isothermal gas sphere can be well approximated with what is now called King profile:

$$\rho(R) = \rho(0) \left[ 1 + \left( \frac{r}{r_c} \right)^2 \right]^{3/2} \quad (1.4)$$

where  $r_c$  is known as *core radius*. This profile is used to describe the radial density profile of galaxies in a cluster. Cavaliere & Fusco-Femiano ((1976)) showed that a similar profile can be used to describe the radial density profile for the gas. Under assumption of virialization between gas and galaxies (thus using a constant temperature and an isotropic velocity dispersion for cluster galaxies), from the King profile is possible to derive the  $\beta$ -model:

$$\rho(R) = \rho(0) \left[ 1 + \left( \frac{r}{r_c} \right)^2 \right]^{3\beta/2} \quad (1.5)$$

where  $\beta = \frac{\mu m_p \sigma^2}{kT}$  is the galaxy-to-gas velocity dispersion, i.e. the ratio of galaxy kinetic energy and gas thermal energy. Typical values for  $r_c$  and  $\beta$  are  $0.12R_{200}$  and  $2/3$ , respectively. Although this model is not completely realistic (it relies on the complete relaxation of the cluster, which could not be always fulfilled), it provides generally a good fit to the observations and has the advantage that integrals can be analytically solved.

Dark matter density profiles have been derived using N-body simulations (see Navarro, Frenk & White (1996) and (1996); Ghigna & Moore (1998)). Also the dark matter is found to exhibit precise scaling relations, whose trend is well described by the Navarro, Frenk & White (NFW) profile:

$$\rho(R) = \frac{\rho_c \delta_c}{(R/R_s)(1 + R/R_s)^2} \quad (1.6)$$

$$\delta_c = \frac{200}{3} \frac{c^3}{[\ln(1+c) - c/(1+c)]} \quad (1.7)$$

where  $\rho_c = \frac{3H^2}{8\pi G}$  is the critical cosmic density and  $c$  is the concentration parameter of the dark matter halo, defined as the ratio between  $R_{200}$  and the scale radius  $R_s$ . The Ghigna & Moore profile is similar, although with a steeper slope in the core (the exponent in the denominator being 3 instead of 2). Both profiles show a steep central cusp, in contrast with the King and  $\beta$  models.

Clusters also show a strong similarity in the temperature profiles beyond the core region (De Grandi & Molendi (2001); Vikhlinin et al. (2005); Pratt et al. (2007)). Still, the temperature profile is apparently connected with the cluster dynamical state. Relaxed clusters show indeed a drop in temperature below  $\sim 0.1R_{200}$ , this

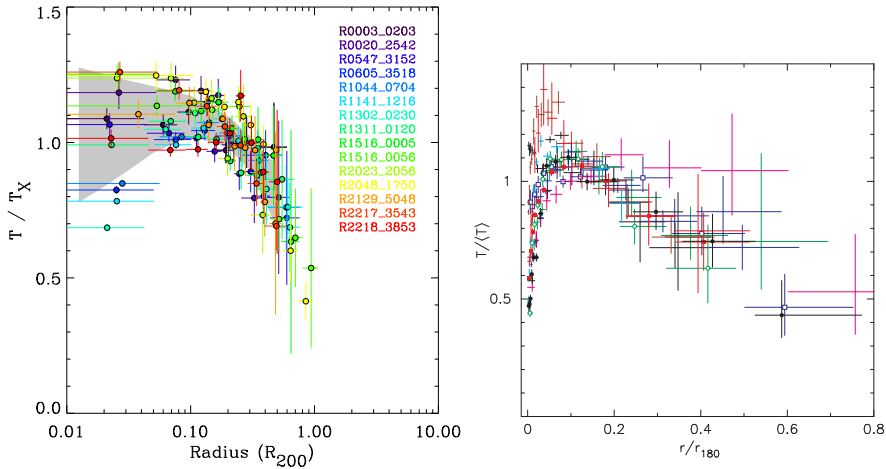


**Figure 1.1:** Scaled temperature profiles for two independent cluster samples. Left: XMM-Newton temperature profiles from Pratt et al. 2007. Right: *Chandra* temperature profiles from Vikhlinin et al. 2005.

being typically due to a *cool core* (see e.g. De Grandi & Molendi (2001); also see below). This self-similarity has been confirmed by several studies (Allen et al. (2001); Piffaretti et al. (2005); Zhang et al. (2006); Pratt et al. (2007)), also confirming the large scatter in the central regions.

A powerful probe of the thermodynamics of the ICM is the gas entropy  $S = \frac{T_g}{n_e^{2/3}}$  (Ponman et al. (1999); Voit et al. (2002)). It has been shown (Ponman et al. (2003); Voit et al. (2005)) that the value of entropy in cluster cores usually follows a shallower profile than expected from a self-similar model, with a slope  $S \propto T^{0.65}$ . This suggests that gravitational heating cannot be the only process at work. Several interpretations have been proposed to understand the entropy profiles. Voit et al. ((2003); (2005)) suggested both pre-heating during gas infall and gas-to-galaxy feedback processes; Kay et al. ((2004)) proposed a simple gas feedback model which better reproduces the observed entropy properties; Borgani et al ((2005)) investigated the effect of SN feedback on the ICM, finding that SN-powered winds can be effective in increasing the ICM in the core, but cannot produce a durable or strong effect. Other feasible interpretations include AGN feedback (CIT.NEED.).

### 1.1.2.2 Cool core clusters

The self-similar model for radial ICM profiles holds beyond  $\sim 0.1 - 0.2R_{200}$ . Below this scale, a large scatter is seen in all relations, suggesting that more complex processes could be at work in cluster cores. As the ICM density in the core grows to very high values, the cooling time could likely drop below the cluster age. The

## 1 General framework

---

cooling flow model (see e.g. Fabian (1994)) shows that, due to radiative cooling, the central temperature would drop and the density accordingly grow to maintain the gas in hydrostatic equilibrium. As a consequence, the gas will also show a stronger emission and a more centrally-peaked profile. The model predicts mass deposition rates as high as  $1000 M_{\odot}/\text{yr}$ . Although lower central temperatures are indeed found in relaxed clusters, the gas does not show the cool ICM phase as expected from the cooling flow model (see Molendi & Pizzolato (2001); Böhringer et al. (2002); Peterson et al. (2003); Kaastra et al. (2004)). At the same time, the effects of strong interaction between the ICM and AGN activity in the core are observed, mainly from the central galaxy (Blanton (2004)). High-resolution *Chandra* images have shown huge cavities in the ICM connected with radio lobes from the central AGN, suggesting a direct interaction (McNamara et al. , David et al. , Fabian et al. (2003)). Modeling shows that the central AGN power output should be sufficient to compensate for the cooling flow (see Fabian (2003); Bregman (2004); and Voit (2005)).

### 1.1.3 Clusters and the large-scale structure

Detailed numerical simulations show that clusters tend to form at the intersection of filaments and sheets of matter in the evolving large-scale structure of the Universe: over time, matter falls along such structures and accretes into a cluster. The infall pattern is not random: paths show a correlation in time and are almost stable, so that matter is channeled into a cluster through filamentary structures with persistent geometry. Matter does not accrete in a steady and continuous way, but in clumps or somehow bound structures, which can be identified as infalling groups of galaxies or less massive clusters (Colberg et al. (1999)).

Filaments around clusters are hard to identify observationally, since they usually do not stand out as clear overdensities like clusters, and, thus, tend to be confused with the surroundings and the background. Early shallow X-ray observations could set upper limits to the X-ray luminosity of these structures (Briel & Henry (1995)), but deep imaging in X-ray or optical broad bands led to the discovery of an extended filamentary network around a few clusters at  $0.05 \leq z \leq 0.6$  (Kull & Böhringer (1999); Scharf et al. (2000); Kodama et al. (2001); Durret et al. (2003); Ebeling et al. (2004)).

## 1.2 X-ray surveys of clusters

The fact that galaxy clusters brightly shine in the X-ray sky is an advantage that has been employed to unambiguously detect them. As the X-ray emission of a cluster can be used to derive its temperature and mass (see e.g. Reiprich & Böhringer (2002)), it is possible to build X-ray selected cluster catalogues with a well-defined selection function almost directly related with the cluster mass. Cluster detection

in the X-rays also has additional intrinsic advantages. As the X-ray background is more homogeneous than the galaxy background, it is possible to subtract it in a more reliable way. Moreover, as the ICM emission scales with its squared density, superposition effects are minimised, and cluster are more easily detected with respect to the background.

The construction of statistically complete samples of X-ray selected galaxy clusters begun with the completion of the first X-ray all-sky surveys (HEAO-1 and ARIEL V, see Piccinotti et al. (1982); Kowalski et al. (1984)), that identified the 30 most luminous X-ray clusters. Observations with EINSTEIN and EXOSAT brought additional clusters for a total of  $\sim 50$  X-ray bright clusters (Lahav et al. (1989); Edge et al. (1990)). The analysis of deeper EINSTEIN observations brought the first deep X-ray cluster survey, EMSS (Gioia et al. (1990); Henry et al. (1992)), that allowed to explore for the first time the evolution of cluster abundance with redshift (Henry et al. (1992); Nichol et al. (1997)). It detected 105 clusters up to  $z \sim 0.8$  to a flux limit of  $1.3 \times 10^{-13} \text{ erg cm}^{-2} \text{ s}^{-1}$ . All later surveys stem from the ROSAT All-Sky Survey (RASS), the first all-sky survey conducted with an X-ray telescope (Trümper (1992), (1993)). Many cluster catalogues originate from this project (see Romer et al. (1994); Burns et al. (1996); Ebeling et al. (1997), (1997), (2000); and (2001); De Grandi et al. (1999); Henry et al. (1992); Ledlow et al. (1997); Böhringer et al. (2001); Cruddace et al. (2002)).

The ROSAT-ESO Flux-Limited X-ray (REFLEX) galaxy cluster survey (Böhringer (2001); (2004)) provides the largest homogeneously selected catalogue of X-ray selected clusters so far. It accounts for all galaxy clusters at  $\delta \leq 2.5$  deg and brighter than  $3 \times 10^{-12} \text{ erg cm}^{-2} \text{ s}^{-1}$  in the ROSAT [0.1-2.4] keV. The sample is made of 447 clusters with spectroscopically-confirmed redshifts, probing a large mass and luminosity range out to redshifts of order  $\sim 0.5$ . The X-ray luminosities in the sample range from about  $10^{42}$  to several  $10^{45} \text{ ergs s}^{-1}$ , i.e. from compact groups to the highest-mass clusters at  $z \gtrsim 0.3$ . The REFLEX survey has been used in many successful studies covering several different cluster properties and features. Among others, the analysis of the 2-point spatial correlation function, of the power spectrum on the cluster scale and of the luminosity function helped in ruling out high-density, EdS-type cosmological models in favor of  $\Lambda$ CDM models (Collins et al. (2000); Schuecker et al (2001), (2002), (2003) and (2003); Böhringer et al. (2004)). Spectroscopic follow-up allowed to obtain an estimate of the  $\sigma_v - L_X$  relation on scales from groups to massive clusters (Ortiz-Gil et al. (2004)).

Thanks to its properties, the REFLEX survey provides an ideal ground from which to draw specific subsamples of clusters according to precise criteria and free of biases.

## 1 General framework

---

### 1.2.1 The REFLEX-DXL Sample

The Distant X-ray Luminous (DXL) cluster sample was drawn from the REFLEX catalogue with the aim of composing an unbiased catalogue of X-ray luminous (i.e. massive) clusters at intermediate redshift (see Zhang et al. (2004), (2006)). The sample is made of the most luminous ( $L_X > 10^{45}$  ergs s<sup>-1</sup>) clusters in the redshift strip [0.27 – 0.31]. At this distance, the field of view of XMM-Newton allows to observe the cluster and its surroundings in an area of about 8×8 Mpc around the cluster. The REFLEX-DXL sample was born as an X-ray selected sample, among whose main goals (see Zhang et al. (2006)) were the determination of ICM properties like temperature structure and entropy; the determination of accurate cluster masses and gas mass fractions; the measure of the normalisation of ICM scaling relations; and to test the evolution of scaling relations and temperature by comparing the DXL members to nearby cluster samples. The clusters were covered with XMM-Newton dedicated observations in AO-1 and AO-3 and with optical follow-up with WFI and VIMOS for large-scale imaging and spectroscopy, respectively. Three supplementary clusters at redshifts of 0.22, 0.44 and 0.45 were also observed, being particularly bright and representative of high-mass systems. Although small, the DXL sample provides an unbiased and almost complete collection of high mass clusters. Their X-ray morphologies show a large range of dynamical states, allowing the study of different stages of cluster formation. In particular, out of 13 clusters, three very dramatic mergers are found: RXCJ0014.3-3022 (A 2744 or AC118), RXCJ0658.5-5556 (the “Bullet” cluster) and RXCJ1131.9-1955 (A 1300).

Results from X-ray analysis show that the clusters have a high degree of self-similarity in the scaled profiles of X-ray properties, such as temperature, surface brightness, entropy, gravitational mass and gas mass. These scaling relations have been found beyond  $0.2 - 0.3R_{500}$ . The average metallicity shows no significant evolution from local samples, agreeing with previous studies (see Tozzi et al. (2003); De Grandi et al. (2004); Pointecouteau et al. (2004); also see Balestra et al. (2007)). The temperature profiles are found to be in agreement with previous works, both from observations (Vikhlinin et al. (2005); Piffaretti et al. (2005)) and from simulations (Borgani et al. (2004)), with a peak around  $0.2 - 0.3R_{500}$  and only a mild decrease beyond  $0.3R_{500}$ . Observed surface brightness profiles agree with  $\beta$ -models with  $\beta \sim 2/3$  and are self-similar beyond  $0.2R_{500}$ . Entropy profiles show a similar slope to Ettori et al. ((2002)) and have central values higher in the merging clusters than in the relaxed systems.

### 1.3 Galaxy morphology, star-formation activity and interactions in clusters

**Table 1.1:** Deduced properties of the REFLEX-DXL clusters (from Zhang et al. 2006). Column (1): cluster name; Col. (2): central electron number density; Col. (3): central entropy; Cols. (4,5): cooling time and cooling radius; Col. (6):  $r_{500}$ ; Cols. (7–9): gas mass, total mass, and gas mass fraction at  $r_{500}$ .

RXCJ	$n_{e0}$ ( $10^{-3} \text{ cm}^{-3}$ )	$S_0$ ( $\text{keV cm}^2$ )	$t_c$ (Gyr)	$r_{\text{cool}}$ (Mpc)	$r_{500}$ (Mpc)	$M_{\text{gas},500}$ ( $10^{14} M_{\odot}$ )	$M_{500}$ ( $10^{14} M_{\odot}$ )	$f_{\text{gas},500}$
0014.3–3022	$3.7 \pm 0.2$	$421 \pm 37$	$14.1 \pm 0.6$	0.00	1.24	$1.0 \pm 0.2$	$7.4 \pm 2.9$	$0.142 \pm 0.024$
0043.4–2037	$5.8 \pm 0.4$	$293 \pm 17$	$10.2 \pm 0.3$	0.12	1.08	$0.6 \pm 0.1$	$4.8 \pm 1.8$	$0.120 \pm 0.023$
0232.2–4420	$14.0 \pm 0.1$	$279 \pm 10$	$10.3 \pm 0.2$	0.18	1.30	$0.9 \pm 0.2$	$8.4 \pm 2.4$	$0.105 \pm 0.023$
0303.7–7752	$6.0 \pm 0.4$	$311 \pm 24$	$10.3 \pm 0.4$	0.12	1.27	$0.8 \pm 0.1$	$7.7 \pm 2.3$	$0.101 \pm 0.022$
0307.0–2840	$10.2 \pm 0.3$	$265 \pm 16$	$10.5 \pm 0.3$	0.17	1.14	$0.6 \pm 0.1$	$5.5 \pm 1.1$	$0.113 \pm 0.029$
0437.1+0043	$10.1 \pm 0.4$	$223 \pm 14$	$10.2 \pm 0.3$	0.16	1.17	$0.5 \pm 0.1$	$6.1 \pm 2.2$	$0.081 \pm 0.020$
0516.7–5430	$2.9 \pm 0.2$	$403 \pm 24$	$16.7 \pm 0.4$	0.00	1.19	$0.8 \pm 0.2$	$6.4 \pm 2.1$	$0.122 \pm 0.029$
0528.9–3927	$10.6 \pm 0.4$	$280 \pm 16$	$10.3 \pm 0.3$	0.14	1.19	$0.9 \pm 0.1$	$6.4 \pm 1.5$	$0.135 \pm 0.028$
0532.9–3701	$13.3 \pm 0.5$	$337 \pm 23$	$10.4 \pm 0.3$	0.14	1.13	$0.6 \pm 0.1$	$5.4 \pm 1.7$	$0.107 \pm 0.024$
0658.5–5556	$6.1 \pm 0.2$	$354 \pm 16$	$10.1 \pm 0.2$	0.15	1.42	$1.8 \pm 0.3$	$11.0 \pm 6.8$	$0.161 \pm 0.018$
1131.9–1955	$5.8 \pm 0.3$	$307 \pm 18$	$10.0 \pm 0.3$	0.11	1.10	$0.8 \pm 0.2$	$5.2 \pm 3.0$	$0.160 \pm 0.030$
2308.3–0211	$9.2 \pm 0.3$	$296 \pm 22$	$10.1 \pm 0.3$	0.14	1.24	$0.7 \pm 0.1$	$7.4 \pm 1.8$	$0.089 \pm 0.022$
2337.6+0016	$5.7 \pm 0.3$	$372 \pm 21$	$12.3 \pm 0.3$	0.00	1.43	$0.8 \pm 0.1$	$10.9 \pm 2.6$	$0.074 \pm 0.016$
Mean	—	—	—	—	—	—	—	$0.116 \pm 0.007$

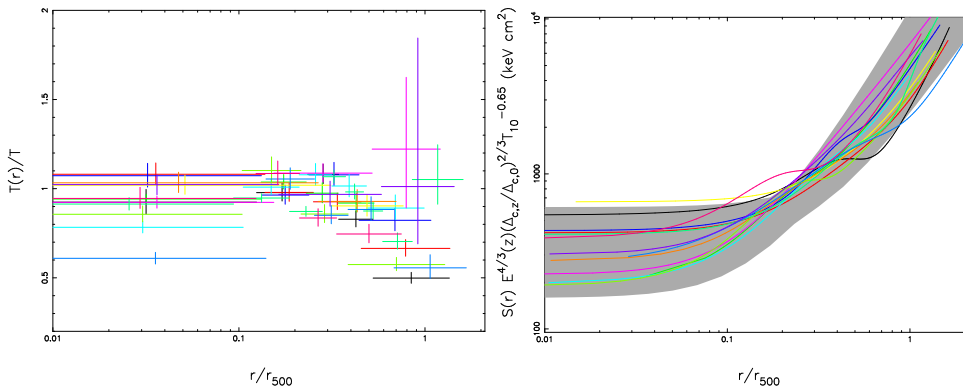


**Figure 1.2:** Left panel: scaled temperature profiles for the REFLEX-DXL sample showing the high degree of self-similarity. Right panel: comparison of the scaled entropy profile of DXL clusters with the same value from the Birmingham-Cfa cluster survey. Both plots from Zhang et al. 2006.

### 1.3 Galaxy morphology, star-formation activity and interactions in clusters

Galaxies in clusters do not independently evolve. As they live in a dense environment, they do indeed experience interactions with each other, with the ICM and with the cluster itself.

The existence of a correlation between the galaxy morphology or star-formation activity and the local density of the cluster environment, or with the radial distance from cluster centre, is well known since the '80s. Dressler ((1980)) studied the galaxy

## 1 General framework

---

populations of 55 nearby clusters to investigate the origin of the population gradients. His results showed that a clear dependence of galaxy morphology on the local density is found regardless of the dynamical state of the cluster or of its concentration: passively-evolving galaxies are preferentially found in the cluster densest regions (i.e. the core), while spirals prefer the lower density environment of the outskirts. Later re-analysis of the same data by Whitmore et al. ((1993)) showed that an even stronger relation is present, between galaxy morphology and cluster-centric radius. Referring to a characteristic optical cluster radius  $R_c^{opt} \sim 0.5$  Mpc, they show that the fraction of passive ellipticals rapidly grows to 60%-70% of the total below  $R_c^{opt}$ , while beyond it it drops to below 20%. Later work by Dressler et al. ((1997)) extended the knowledge relative to the morphology-density relation to higher redshifts by sampling 11 clusters between  $z = 0.36$  and  $z = 0.57$ . Their results showed that, although the morphology-density relation is well-established in all clusters in the local Universe, its extent is less evident at high redshift, where it is clearly detected only in regular, highly concentrated clusters. Although ellipticals are always found in large numbers (thus suggesting that they predate the formation age of spirals and irregulars), the relative fraction of spirals and irregulars increases with redshift.

The spatial segregation of different galaxy types in clusters is even more evident when star-formation activity is directly investigated. Butcher & Oemler (1978a), (1978b), (1984) already showed that intermediate-redshift clusters can have a larger fraction of blue galaxies than expected from the morphology-density relation (Butcher-Oemler effect, BO hereafter). These galaxies appeared from ground-based observations only as “fuzzy blobs”. Subsequent *Hubble space Telescope* (HST) observations allowed to identify these blue galaxies as low-luminosity spirals, part of which also show somewhat distorted shapes (Dressler et al. (1994)), suggesting that these blue galaxies are indeed undergoing star-forming activity. Later works by Abraham ((1996)) and Morris ((1998)), respectively on the rich clusters A 2390 ( $z \sim 0.22$ ) and MS 1621.5+2640 ( $z \sim 0.43$ ), showed that underneath the morphology-density relation lies an even more precise relation. The presence of radial gradients in the strengths of characteristic spectral features (namely the [OII] and  $H\delta$  lines and the 4000 Å break) suggested that the cluster assembly is gradual with almost continuous accretion of field galaxies and that star formation is gradually truncated during the accretion process. This effect is more evident in the higher-redshift cluster, suggesting that the BO effect and more in general the decreasing presence of spiral galaxies in clusters is due to a slow quenching of the star formation in the spirals. These results are confirmed by Balogh et al. ((1999)) through spectral index analysis of a sample of clusters at  $0.18 < z < 0.55$ . Their results suggest again that the increase in the mean star formation activity towards cluster outskirts can be interpreted as an age sequence: outer galaxies have experienced star formation more recently than galaxies in the core. Their interpretation was that the truncation of star formation in clusters may largely be a gradual process, perhaps due to the exhaustion of gas in the galaxy discs over



### 1.3 Galaxy morphology, star-formation activity and interactions in clusters

---

fairly long timescales. In this case, differential evolution may result because field galaxies can refuel their discs with gas from extended halos, thus regenerating star formation, while cluster galaxies may not have such halos and so continue to evolve passively. This scenario was confirmed through numerical simulations (Balogh et al. (2000)), confirming that the origin of radial gradients could lie in the relation between radial position and accretion time that results from assuming a hierarchical model of assembly for clusters. Gomez et al. ((2003)) confirmed the radial trend in local clusters using SDSS data, also pointing to the fact that the morphology-density relation alone cannot explain the observed star formation regimes in the low-density environment. Finn et al. ((2005)) observed similar behaviours in three high- $z$  clusters ( $\sim 0.75$ ) drawn from the EDisCS cluster sample.

Recently, Poggianti et al. ((2006)) extended this analysis through studies of a set of 16 clusters, 10 groups and a large number of field galaxies out to  $z \sim 0.8$ . The fraction of star-forming galaxies in clusters at  $z \gtrsim 0.4$  is found to be anti-correlated with the cluster velocity dispersion, i.e. with its mass. Groups are found to contain a larger fraction of star-forming galaxies than high-mass clusters. The strength of the [OII] emission is also found to be dependent on environment, with the largest equivalent widths being found in regions of higher star formation activity. They suggest that the star formation history of individual clusters might be largely dependent on the growth history of structures, with accretion events ruling the relative fraction of active galaxies. This could also provide a viable explanation for the BO effect, suggesting that clusters with evidence of younger accretion also show a larger fraction of younger galaxies.

#### 1.3.1 The interactions of cluster galaxies

Several explanations have been given on the galaxy scale to understand what drives both the observed morphological transformation, progressive star-formation quenching in disk galaxies and, on the other hand, the BO effect. Basically, two main types of interaction can be identified: gravitational interactions between galaxies (or between galaxies and the cluster as a whole) and interaction of galaxies with the ICM.

Shortly after the first detection of hot gas in clusters via X-ray observations, Gunn & Gott ((1972)) already addressed the issue of interaction between infalling galaxies and the ICM. They found that the interstellar material in a galaxy would feel the ram pressure of the intracluster medium as it moves through the cluster. A simple estimate of the effect assumes that the outer disk gas gets stripped off when the local restoring force in the disk is smaller than the ram pressure. Thus disks get stripped up to the so called “stripping radius” where the forces balance. Nulsen ((1982)) investigated the impact of viscosity, thermal conduction and turbulence in the wake of an infalling galaxy. They concluded that turbulent viscous stripping will be an

## 1 General framework

---

important mechanism for gas loss from cluster galaxies. This view has been extended and confirmed through 3D hydrodynamical simulations (see e.g. Roediger & Hensler (2004); Roediger & Brueggen (2006a); Roediger, Brueggen & Hoeft (2006b)), also analysing the role of disk inclination with respect to the ICM wind. Their results show that the effect of ram-pressure stripping will be at its maximum for angles close to edge-on. Conversely, Dressler & Gunn ((1983)) suggested that interaction with the ICM could compress the gas in the disk and induce star formation (also see Gavazzi et al. (1995)). Recent observations of the massive cluster A 1689 at  $z \sim 0.2$  (Cortese et al. (2007)) show two peculiar galaxies infalling with high velocity onto the main cluster. In the wakes of these galaxies, bright, compact blue knots and stellar streams are detected, suggesting that ram-pressure-induced star formation is happening in these blobs, thus confirming this scenario. Moreover, the two galaxies show different star formation regimes, as the smallest ( $\sim 0.1L^*$ ) has already ceased star formation, while the largest ( $\sim L^*$ ) is still actively forming star, suggesting that ram pressure stripping is more efficient in quenching star formation in small systems.

Dynamical-gravitational interactions of galaxies can be summarised in three main categories: mergers, close encounters and interactions with the cluster potential. The feasibility of galaxy-galaxy mergers as triggers for star formation activity and to fuel the BO effect has been addressed in several studies (Icke (1985); Miller (1988)), but following observations (see Oemler, Dressler & Butcher (1997)) show that merging is implausible, as the blue galaxy fraction in BO clusters is too high to be accounted for only through merging. Similarly, interaction with the cluster potential can provide enough tidal stress to induce star formation (see e.g. Byrd & Valtonen (1990); Valluri (1993)), but will be efficient only close to the core, where the potential has a cuspy profile and provides tidal forces strong enough. Star-forming galaxies are instead mainly found in the outer regions of clusters, where the cluster potential is shallower. An efficient mechanism through which it is possible to account for both star formation activity and morphological transition from spirals to spheroids is *galaxy harassment*, proposed by Moore et al. ((1996); (1999)). At high speeds, close encounters between galaxies can cause impulsive gravitational shocks. While massive spheroids will not be largely affected by such encounters, the effect on disk galaxies will mainly depend on the disk mass profile. Low surface brightness systems have shallow profiles and large disk scale-length. As a consequence, the effect of tidal shocks on their thin discs will be maximised. In single encounters, this means that the discs will be rearranged in a spheroidal shape. In the denser regions in the core, where multiple encounters can happen within short timescales, the multiple torques will completely disrupt the disk and the galaxies will be torn apart. On the other hand, high surface brightness disks and spirals with a dominant bulge have steep mass profiles and flat rotation curves, with orbital times short enough for the disk to respond almost adiabatically to the shock from rapid encounters. Consequently, tidal shocks cannot efficiently remove gas or induce morphological transitions, but will instead produce

## 1.4 The luminosity function of galaxies in clusters

---

disk instabilities that can funnel gas in the central regions (see also Lake et al. (1998)). As a consequence, these galaxies will undergo a period of enhanced star formation for about 1–2 Gyr. If, after this time, the galaxies enter the denser region of the core, there ram pressure could be efficient enough to strip the remaining gas, inducing an evolution to S0 type. It is important to stress that, although the effect of harassment will be at its maximum efficiency close to the core, already at the cluster outskirts it can generate strong morphological instabilities (see Moore et al. (1998); Mastropietro et al. (2005)).

## 1.4 The luminosity function of galaxies in clusters

The galaxy luminosity function (LF hereafter) (Schechter (1976)) is the record of the past star formation activity in a given galaxy population; hence, it is a powerful diagnostic tool to test different models of galaxy formation and evolution. Clusters of galaxies are ideal laboratories to investigate the LF thanks to the large number of almost coeval galaxies at the same distance and in a compact region of space. The study of the LF of clusters has two main purposes: the comparison of the LF shape in clusters and in the field, to obtain information on the influence of environment on the formation and overall statistics of cluster galaxies; and the investigation of differences in the LFs of different clusters, both at similar or different redshifts, as markers of the effect of evolution in the star formation of galaxies.

Many studies have been carried out to establish the properties of the LF for field and cluster galaxies, based either on individual clusters or on stacked cluster samples, to increase statistics and investigate the presence of a universal galaxy LF underlying the individual shapes of each cluster. The results of these studies have been discordant, partly due to different selection criteria for the samples and partly due to different background subtraction techniques. While several investigations have brought a picture of an universal cluster LF (Lugger (1986); Colless (1989); Paolillo et al. (2001); Popesso et al. (2005a)), other studies have highlighted clear differences in the LF of cluster and field, or of different clusters (Dressler (1978a); Lopez-Cruz (1997); Garilli et al. (1999); Goto et al. (2002); de Propris et al. (2003); Hansen et al. (2005)). The effect of evolution on the shape of the LF was investigated already by Dressler ((1978a); (1978b);(1978c) ), who noted that clusters with massive cD galaxies tend to have a steeper bright end of the LF and suggested that galaxy cannibalism in cluster cores could help in shaping the LF. Colless ((1989)) found evidence of a dimmer characteristic magnitude ( $M^*$ ) for clusters with low velocity dispersion. Lugger ( (1986)) compared the LF of inner and outer regions of different clusters and of a composite cluster sample, showing the presence of an excess of bright galaxies and a flattening of the bright end in the high-density regions and explaining it in terms of evolutionary models of galaxies. This result was later confirmed by Garilli

## 1 General framework

---

et al. ((1999)) on a mixed sample of Abell (optically selected) and X-ray selected clusters. Conversely, Paolillo et al. ((2001)) claimed that no significant change is found in the cluster outskirts with respect to the core, and de Propris et al. ((2003)) found strong differences in the LFs of the field and clusters.

The shape of the galaxy LF at the faint end has been another subject of controversy. Popesso et al. ((2005a)) analysed a sample of 97 clusters at  $z \leq 0.25$  - selected from the RASS-SDSS galaxy cluster catalogue - and proposed a universal cluster LF made of two components: a bright-end LF with a classical slope  $\alpha = -1.25$  in the SDSS *griz* bands, and a steeper faint-end LF ( $-21.1 \leq \alpha \leq -1.6$ ). The upturn in the LF slope happens at magnitudes fainter than  $-16+5\log(h)$  in the SDSS *g* band ( $-18.5+5\log(h)$  in the *z* band), where the population of dwarf galaxies sets in. A universal cluster LF may sound at odds with the morphology dependence of the LF for cluster galaxies (Binggeli et al. (1988)), given the existence of a morphology-density relation for galaxies (Dressler (1980)). A change in the LF shape with cluster-centric distance was observed in previous studies (Beijersbergen et al. (2002); Goto (2005); Hansen et al. (2005)). This radial dependence was also found in the RASS-SDSS sample by Popesso et al. ((2006)) and mainly ascribed to the effect of galaxy harassment on dwarf galaxies (see Moore et al. (1996)). Recently Barkhouse et al. ((2007)) have confirmed the dependence of the LF shape on the cluster-centric distance in a sample of 57 low-redshift Abell clusters. In particular, they find the LF to become shallower and dimmer with decreasing cluster-centric distance, which is attributed to the interaction between infalling galaxies and the intracluster medium (ICM) via ram-pressure stripping and tidal disruption in the cluster core.

### 1.5 Determination of cluster masses

Galaxy clusters mass is an important observable in cosmological applications. The number density of clusters beyond a given mass threshold, coupled with the evolution of abundance with redshift, provide strong constraints on cosmological parameters (see Rosati et al. (2002); Voit et al. (2005); and references therein). Galaxy clusters, being massive, bright objects that can be detected to redshifts of 1 and beyond, can thus provide very strong bounds on the evolution of structure. Their drawback lies in the fact that they can be extremely complex objects, difficult to model, and their masses can be affected by systematics. The drawback in using clusters for cosmological studies is their dynamical youth, which is the reason why clusters are often found far from dynamical equilibrium and sometimes show complex merger configurations. This makes difficult to obtain a perfect modeling of clusters, consequently their assessment can be affected by systematics. Thus, cluster mass determinations have always been taken with caution (see Biviano (2000) for a historical review).

Mass estimates based on the projected phase-space distribution of member galaxies

(i.e. based on spatial and velocity clustering) can be affected by the presence of interlopers in the cluster member sample, due to projection effects on the velocity axis (see, e.g., Lucey (1983); Borgani et al. (1997); Cen (1997)). Dynamical mass estimates can be wrong also if the cluster is far from virialization, for instance during a merger or a phase of accretion (see Girardi & Biviano (2002)). Dynamical friction or infalling motions can make galaxies biased tracers of the potential, again providing an erroneous mass estimate. Several combined analysis of simulated and observed clusters have been performed in the last years to understand the systematics and the reliability of cluster mass estimates entirely based on velocity dispersions. In particular, Biviano et al. ((2006)) studied accurately the efficiency and reliability of such methods by analysing a set of 62 simulated clusters and comparing them with observed clusters from ENACS (Biviano et al. (1996); Katgert et al. (1996)). Their results show that optical cluster mass estimates can be very reliable and the biases can be kept under control, provided that a relatively large number of objects is available and that specific prescriptions are followed.

Other methods have been devised to calculate cluster masses, but these can also be affected by biases. Lensing mass estimates are less affected by projection effects (Reblinsky & Bartelmann (1999); Clowe et al. (2004)), but are affected by the mass-sheet degeneracy that cannot always be disentangled (Cypriano et al. (2004)). Moreover, substructuring or elongation along the line of sight will also artificially increase the cluster mass determination.

X-ray data are considered even less biased estimators of mass, as shown extensively in Sect. 1.1.2. Still, nontrivial problems can arise in the case of peculiar clusters. In clusters undergoing merging events the X-ray luminosity and temperature can be boosted, leading to an overestimate of the cluster mass (see Ricker & Sarazin (2001); Barrena et al. (2002); Diaferio et al. (2005)). Violations of the condition of hydrostatic equilibrium, inaccurate modelling of the gas density profile and observational biases in the measure of the intra-cluster gas temperature, may lead to a sizeable underestimate of the cluster mass (Kay et al. (2004); Rasia et al. (2004)).

A combination of several, independent cluster mass estimates is thus likely to provide the most accurate results.

### 1.5.1 Mass-to-light ratios

Since the works of Zwicky (see e.g. (1933)), it is well known that the luminous matter associated with galaxies in clusters provides only a small part of the total cluster mass. The relative contribution of the dark matter component is usually specified in terms of the mass-to-light ratio ( $M/L$  hereafter), the total amount of mass relative to the total light within a given scale.

Pioneering analyses showed that  $M/L$  increases from the bright luminous parts of galaxies to cluster scales (Blumenthal et al. (1984), also see Faber & Gallagher

## 1 General framework

---

((1979)). This is well in agreement with models of biased galaxy formation, that naturally predict an increase of  $M/L$  with system mass (e.g., Bardeen et al. (1986)).

The question of the amount of  $M/L$  in clusters has been addressed for several years and brought different results. Early optical studies on small cluster samples pointed to high mean values of  $M/L$ . Dressler ((1978a)) found oscillating values of  $\sim 200\text{--}600h M_{\odot}/L_{\odot}$  in R band for a sample of 12 rich abell clusters. Faber & Gallagher ((1979)) found a high mean value of  $\sim 750h M_{\odot}/L_{\odot}$  in B band and  $\sim 580h M_{\odot}/L_{\odot}$  in V band. Huchra & Geller ((1982); (1984)) found a mean value of  $340h M_{\odot}/L_{\odot}$  in B band from a group sample from the CfA survey. Optical studies on single clusters indicated lower values: Chapman, Geller & Huchra ((1988)) found  $M/L_B = 194h M_{\odot}/L_{\odot}$  in the elongated cluster Abell 194 with a mass estimator based on cluster dynamics. Similarly, Eyles ((1991)) derived the X-ray mass of Perseus from EXOSAT measures, finding a  $M/L \sim 200h M_{\odot}/L_{\odot}$  in B band.

Later determinations based on larger samples showed smaller mean values. Carlberg et al. ((1996)) found a mean value of  $\sim 300h M_{\odot}/L_{\odot}$  in R band for CNOC1 clusters. They also suggest the possibility of an underlying constant  $M/L$ , as no significant trend was found with redshift in their sample. Adami et al. ((1998)) examined 29 X-ray selected clusters from the ENACS survey finding a robust mean value of  $424h M_{\odot}/L_{\odot}$  in the B band. In a more recent study within the Birmingham-CfA Cluster Survey, Sanderson & Ponman ((2003)) find a mean  $M/L_{B_j} \sim 350h M_{\odot}/L_{\odot}$  - scaled to  $M/L_{R_c} \sim 190h M_{\odot}/L_{\odot}$  - for a sample of 66 relaxed groups and clusters. They find no significant trend with X-ray luminosity and suggest that there is no trend of  $M/L$  with mass.

In the last years, better statistics from large samples and comparison with simulations have provided a better understanding of the relation between mass and luminosity. Girardi et al. ((2000); (2002)), using a large sample of 294 systems ranging from groups to massive clusters, have shown instead the presence of a trend, with mass increasing more than luminosity ( $M \propto L_B^{1.34}$ ). A similar trend is found by Lin et al. ((2004)) investigating the  $M/L$  in K. They also find that massive clusters have less galaxies per unit mass than small clusters or groups, suggesting galaxy-galaxy dynamical interactions as an explanation. Similarly, Popesso et al. ((2007)), using the RASS-SDSS sample of 217 clusters, find again a non linear trend between mass and light ( $L \propto M^{0.92}$ ) within  $R_{200}$ . Also, they find evidence of a non linear relation between cluster mass and number of galaxies, suggesting that this could be directly related to the relation between the cluster halo and the number of subhaloes.

### 1.6 The thesis: aims and methods

The goal of this thesis is to investigate the global properties and the galaxy populations in the massive clusters of the REFLEX-DXL sample through optical follow-up

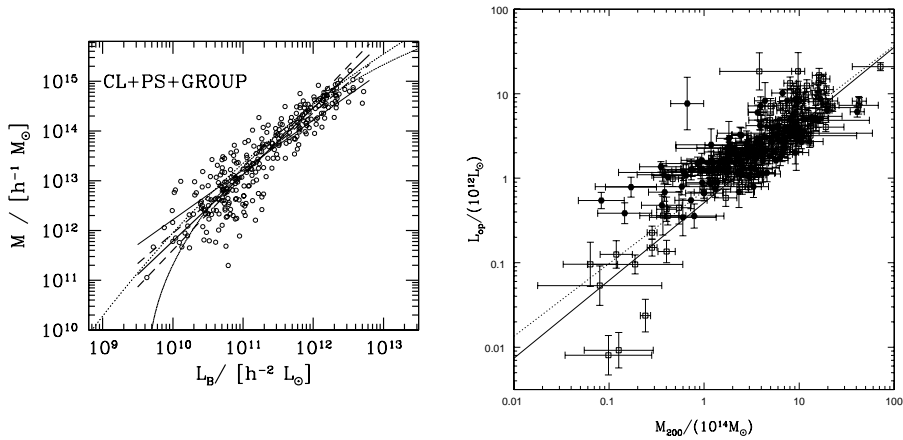


**Figure 1.3:** Detected trends between mass and light in different cluster samples. Left panel: combined sample of 264 clusters from girardi et al. 2002. Right panel: sample of 217 clusters from the RASS-SDSS cluster sample of Popesso et al. 2007.

and comparison with X-ray analysis. Among the many aims of this project, I will mainly address the relations between cluster dynamical state, interaction with the surrounding large-scale structure, evolution of the star formation activity and of the global galaxy population in these extremely massive systems.

To obtain the needed information, different types of observations have been carried on. Optical imaging was performed in the BVR optical bands, suitably chosen to map interesting spectral regions of cluster members through which different types of galaxies can be identified and photometric redshifts can be obtained. The observations were performed at the WFI (Wide Field Imager) instrument at the ESO2.2m Telescope. The advantage of this instrument is the large field of view (more than  $30'$ ), allowing to observe in a single exposure a region of about  $9 \times 9$  Mpc centred on the cluster (at  $z \sim 0.3$ ). This allows to detect and analyse both the cluster galaxy population and the possible neighbouring large-scale structure out to about three times the cluster virial radius. Analysis of these data was performed using both standard procedures and software and specifically tailored techniques that I developed with precise aims. Specifically, the cluster density maps were derived with an original algorithm flexible enough to be applied to very different data.

Spectroscopic follow-up was performed with VIMOS, a multi-object spectrograph mounted on VLT-UT3. The choice of this instrument was driven by both the large field of view and the powerful multiplexing capabilities. Indeed, with six VIMOS masks on a single cluster it was possible to obtain around (or more than) 1000 spectra per cluster field. This provided enough cluster member spectra to perform a reliable virial analysis, and to suitably map the star formation activity across the clusters

## 1 General framework

---

by spectral index analysis of the detected spectral features. A suitable number of background and foreground objects was also sampled, which was useful in properly calibrating photometric redshifts and assessing the intrinsic contamination on cluster members. Data reduction and analysis of these large data sets was carried on with public software (mainly the VIPGI data reduction tool) and with a sequence of dedicated, original techniques specifically developed to extract spectral information, for instance the determination of equivalent widths for such a large amount of data.

The thesis is organised as follows. chapter 2 shows the results of a pilot study of the DXL cluster RXCJ0014.3-3022, as published in Braglia, Pierini & Böhringer ((2007)). In this work, some of the main techniques were presented, with special emphasis on the determination of photometric redshifts and the study of their reliability by comparison with the available spectroscopic redshifts. It is shown that a combination of X-ray, dynamical analysis and optical photometry can provide a powerful and reliable tool to probe the large-scale structure surrounding the clusters and to identify interesting features. Specifically, the combined analysis allowed us to detect two high density filamentary structures that are interpreted as driving the large-scale accretion pattern on the cluster. Along these filaments, a strong increase in the star formation activity (to levels higher than in a comparison low density field) was found beyond the cluster virial radius, along with an unexpected population of bright star-forming galaxies. These results suggest that along the filaments, processes are at work that stress the infalling galaxies.

Chapter 3 addresses a complementary study of the star formation activity in two clusters from the DXL sample. The two chosen clusters, RXCJ0014.3-3022 and RXCJ2308.3-0211, are in opposite and extreme dynamical stages. The former is undergoing a major merger, while the latter is a relaxed cool core cluster. Combined large-scale structure analysis at the cluster redshifts and spectral index analysis allowed to detect clear, different trends in the star formation activity of these two massive systems. While RXCJ2308.3-0211 is confirmed as a globally old and relaxed system, with small amounts of star formation activity, RXCJ0014.3-3022 (a BO cluster) shows evidence of intense star formation activity along its large-scale filaments. It was also possible to confirm by spectral index analysis of cluster members the results published in Braglia et al. ((2007)), with respect to the increase in the star formation activity. This chapter reproduces the paper by Braglia, Pierini, Biviano & Böhringer, to be submitted to A&A.

Chapter 4 covers the detailed analysis of the same two clusters with respect to cluster dynamics, luminosity function and mass-to-light ratios. Virial analysis was used to determine the dynamical mass of the two cluster and compared with the X-ray derived value. The cluster LF was investigated, both for the two clusters and for interesting regions of both systems. In both cases, radial trends in the shape of the LF have been found, confirming previous studies. Along the filaments in RXCJ0014.3-3022, an even more dramatic transformation of the LF was found



beyond the cluster virial radius, where the shape of the LF is seen to suddenly flatten with no detectable cutting magnitude. The mass-to-light ratio for the two clusters was analyzed and compared with previous results, confirming the expected values from previous studies. This chapter reproduces the paper by Braglia, Biviano, Pierini & Böhringer, to be submitted to A&A.

Chapter 5 will include some final remarks and future prospects. Future directions and possible applications will be shown, as well as some interesting results coming from a newly started project.

### 1.6.1 Previous studies on the analyzed clusters

The two clusters studied through this work have been already known since the catalogues of Abell ((1958); (1965); (1989)) and are both part of their southern extensions. As very massive clusters, their properties have been already partly investigated in the past, although always limited to the cluster central regions (the inner Mpc). Our results extend and complete the available knowledge to larger distances. For comparison in the following chapters, here the main past results will be summarised for RXCJ0014.3-3022 and RXCJ2308.3-0211.

#### 1.6.1.1 RXCJ0014.3-3022

This cluster (A 2744 or AC118) has been subject of several optical studies, being a BO cluster. In an early study of four such clusters, including RXCJ0014.3-3022, Poggianti et al. ((1996)) analysed spectral lines and broad-band colours by means of an evolutionary synthesis model. They concluded that a substantial fraction of cluster galaxies is undergoing short but vigorous starburst episodes, which affect a substantial galactic mass fractions, typically 30% or more. Later on, HST-WFPC2 observations at 0.3''-spatial resolution and ground-based multi-object spectroscopy (MOS) in a central square region of about 1 Mpc on the side (Couch et al. (1998)) revealed a link between starburst activity and galaxy-galaxy interactions in three “Butcher-Oemler” clusters at  $z \sim 0.3$ , including RXCJ0014.3-3022. These authors concluded that the evolution of the overall cluster galaxy population is driven by several different physical processes. Colour-magnitude relation and luminosity function in the optical and near-infrared were successively determined by Busarello et al. ((2002)), Andreon ((2002)), and Merluzzi et al. ((2003)).

The latter studies targeted an almost four time wider region, which allowed the first evidence of substructure in the galaxy distribution in the central region of RXCJ0014.3-3022 to be covered. X-ray observations with *Chandra* led to the discovery of a shock discontinuity due to a major merger occurring at Mach number of  $\sim 1.2$  (Kempner & David (2004)). These authors suggested that the ongoing merging could be pumping energy into the central radio halo of the cluster (Giovannini et

## 1 General framework

---

al. (1999); Govoni et al. (2001)). In a recent analysis of the central radio halo and peripheral radio relic of RXCJ0014.3-3022, conducted with the VLA at 350 MHz and 1.4 GHz, Orrú et al. ((2007)) discovered that the flat spectrum regions of the radio halo are correlated with higher temperature in X-rays. This result supports the idea that a fraction of the gravitational energy, which is dissipated during mergers in heating the thermal plasma, is converted into re-acceleration of relativistic particles and amplification of the magnetic field. Indeed, the dynamical analysis of Boschin et al. ((2006)) confirmed the presence of substructure in the cluster central region, where two subcomponents with a mass ratio of 3:1 approach each other at a velocity along the line of sight in excess of  $3000 \text{ km s}^{-1}$ .

Recently we have extended the knowledge on the substructure and galaxy populations of the cluster beyond the cluster virial radius, which measures about 2.5 Mpc (Zhang et al. (2006)). In particular, deep XMM-*Newton* observations allowed to produce 2D maps of the entropy of the X-ray emitting gas at high signal-to-noise ratio (S/N), which revealed not only the shock region discovered by *Chandra* but also the presence of a low-entropy channel pointing outwards from the cluster core towards the South (Böhringer et al. (2006)). Finally, Böhringer et al. ((2006)) showed that the merging nature of the cluster induces a displacement of the distributions of galaxies and ICM for both subcomponents (similar to the famous “Bullet Cluster” in Clowe et al. (2006)).

### 1.6.1.2 RXCJ2308.3-0211

Fewer studies have been performed on this cluster (A 2537). This can be due to its position close to the galactic plane, where absorption is very large. Moreover, although it is a massive cluster, it is dimmer than RXCJ0014.3-3022.

Dahle et al. ((2002)) performed lensing analysis over a sample of clusters, including RXCJ2308.3-0211. The results of their shear analysis show that the cluster has a mass distribution partly different from the galaxy distribution, being elongated on the N–S axis, but the peaks of the two are well in accord. They also derive a mass value slightly below  $10^{15} M_{\odot}$ . Similarly, *Chandra* observations by Schmidt & Allen ((2007)) show an x-ray derived mass of about  $8 \times 10^{14} M_{\odot}$ , although with very large upper errorbars, suggesting an even larger mass. Both values are in agreement with the X-ray determination of Znaehg et al. ((2006)), where a mass of  $(7.4 \pm 1.8) \times 10^{14} M_{\odot}$  is found within  $R_{500}$ . Venturi et al. ((2007)) covered this cluster with GMT radio observations, not finding any clue of extended radio features. Only the cD shows a short radio tail.

## Bibliography

- [1958] Abell, G.O. 1958, ApJS, 3, 211
- [1965] Abell, G.O. 1965, ARA&A, 3, 1
- [1989] Abell, G.O. 1989, ApJS, 78, 150
- [1996] Abraham, R. G.; Smecker-Hane, T.A.; Hutchings, J. B.; Carlberg, R. G.; Yee, H. K. C.; Ellingson, E.; Morris, S.; Oke, J. B.; Rigler, M. 1996, ApJ, 471, 694
- [1998] Adami, C.; Mazure, A.; Katgert, P.; Biviano, A. 1998, A&A, 336, 63
- [2001] Allen, S.W., Fabian, A.C., Johnstone R.M., Arnaud K.A., Nulsen P.E.J. 2001, MNRAS, 322, 589
- [2002] Andreon, S. 2002, A&A, 382, 821
- [2007] Balestra, I.; Tozzi, P.; Ettori, S.; Rosati, P.; Borgani, S.; Mainieri, V.; Norman, C.; Viola, M. 2007, A&A, 462, 429
- [1999] Balogh, M.L.; Morris, .L.; Yee, H. K. C.; Carlberg, R. G.; Ellingson, E. 1999, ApJ, 527, 54
- [2000] Balogh, M.L.; Navarro, J.F.; Morris, S.L. 2000, ApJ, 540, 113
- [1986] Bardeen, J. M.; Bond, J. R.; Kaiser, N.; Szalay, A. S. 1986, ApJ, 304, 15
- [2002] Barrena, R.; Biviano, A.; Ramella, M.; Falco, E. E.; Seitz, S. 2002, A&A, 386, 816
- [1970] Bautz, L.P., & Morgan, W.W. 1970, ApJ, 162, L149
- [2007] Barkhouse, W.A.; Yee, H. K. C.; Lopez-Cruz, O. 2007, ApJ, 671, 1471
- [2002] Beijersbergen, M.; Schaap, W. E.; van der Hulst, J. M. 2002, A&A, 390, 817
- [1988] Binggeli, B., Sandage, A., Tamman, G.A. 1988, ARA&A, 26, 509
- [1996] Biviano, A.; Giuricin, G.; Katgert, P.; Mazure, A.; den Hartog, R.; Dubath, P.; Escalera, E.; Focardi, P.; et al. 1996, ApL&C, 33, 157

## Bibliography

---

- [2000] Biviano, A. 2000, in *Constructing the Universe with Clusters of Galaxies*, IAP 2000 meeting, Paris, France, July 2000, Florence Durret & Daniel Gerbal Eds.
- [2006] Biviano, A.; Murante, G.; Borgani, S.; Diaferio, A.; Dolag, K.; Girardi, M. 2006, *A&A*, 456, 23
- [2004] Blanton, E.L., in Reiprich T., Kempner J., Soker N., eds, *The Riddle of Cooling Flows in Galaxies and Clusters of Galaxies The Interaction of Radio Sources and X-Ray-Emitting Gas in Cooling Flows*, pp. 181+
- [1984] Blumenthal, G. R.; Faber, S. M.; Primack, J. R.; Rees, M. J. 1984, *Nature*, 311, 517
- [2004] Borgani, S.; Murante, G.; Springel, V.; Diaferio, A.; Dolag, K.; Moscardini, L.; Tormen, G.; Tornatore, L.; Tozzi, P. 2004, *MNRAS*, 348, 1078
- [2001] Böhringer, H., Voges, W., Huchra, J. P., McLean, B., Giacconi, R., Rosati, P., Burg, R., Mader, J., Schuecker, P., Simic, D., Komossa, S., Reiprich, T. H., Retzlaff, J., Trümper, J. 2001, *ApJS*, 129, 435
- [2002] Böhringer, H., Matsushita, K., Churazov, E., Ikebe, Y., Chen, Y. 2002, *A&A*, 382, 804
- [2004] Böhringer, H.; Schuecker, P.; Guzzo, L.; Collins, C. A.; Voges, W.; Cruddace, R. G.; Ortiz-Gil, A.; Chincarini, G.; et al. 2004, *A&A*, 425, 367
- [2006] Boehringer, Hans; Braglia, Filberto; Pierini, Daniele; Biviano, Andrea; Schuecker, Peter; Zhang, Yu-Ying; Finoguenov, Alexis; Pratt, Gabriel W.; Quintana, Hernan; Lynam, Paul D. 2006, *Msngr*, 123, 49
- [1997] Borgani, Stefano; da Costa, Luiz N.; Freudling, Wolfram; Giovanelli, Riccardo; Haynes, Martha P.; Salzer, John; Wegner, G. 1997, *ApJ*, 482L, 121
- [2005] Borgani, S., Finoguenov, A., Kay, S.T., Ponman, T.J., Springel, V., Tozzi, P., Voit, G.M. 2005, *MNRAS*, 361, 233
- [2006] Boschin, W.; Girardi, M.; Spolaor, M.; Barrena, R. 2006, *A&A*, 449, 461
- [2007] Braglia, F.; Pierini, D.; Böhringer, H. 2007, *A&A*, 470, 425
- [2004] Bregman, J.N. 2004, in Reiprich T., Kempner J., Soker N., eds, *The Riddle of Cooling Flows in Galaxies and Clusters of Galaxies Meeting Summary: Cluster Cooling Flows Become Modest*, pp. 327+
- [1995] Briel, U.G., & Henry, J.P. 1995, *A&A*, 302, L9

- [1996] Burns, J.O., Ledlow, M.J., Loken, C., Klypin, A., Voges, W., Bryan, G.L., Norman, M.L., White, R.A. 1996, ApJ, 467, 49
- [2002] Busarello, G.; Merluzzi, P.; La Barbera, F.; Massarotti, M.; Capaccioli, M. 2002, A&A, 389, 787
- [1978a] Butcher, H.; Oemler, A., Jr. 1978, ApJ, 219, 18
- [1978b] Butcher, H.; Oemler, A., Jr. 1978, ApJ, 226, 559
- [1984] Butcher, H.; Oemler, A., Jr. 1984, ApJ, 285, 426
- [1990] Byrd, G., Valtonen, M. 1990, ApJ, 350, 89
- [1996] Carlberg, R. G.; Yee, H. K. C.; Ellingson, E.; Abraham, R.; Gravel, P.; Morris, S.; Pritchett, C. J. 1996, ApJ, 462, 32
- [1972] Catura, C.R., Fisher, P.G., Johnson, M.M., Meyerott A.J. 1972, ApJ, 177, L1
- [1971] Cavaliere, A., Gursky, H., Tucker, W 1971, Nature, 231, 437
- [1976] Cavaliere, A., Fusco-Femiano, R. 1976, A&A, 49, 137
- [1997] Cen, R. 1997, ApJ, 485, 39
- [1988] Chapman, G. N. F.; Geller, M. J.; Huchra, J. P. 1988, AJ, 95, 999
- [2004] Clowe, D.; De Lucia, G.; King, L. 2004, MNRAS, 350, 1038
- [2006] Clowe, Douglas; Brada, Marua; Gonzalez, Anthony H.; Markevitch, Maxim; Randall, Scott W.; Jones, Christine; Zaritsky, Dennis 2006, ApJ, 648, 109
- [1999] Colberg, J. M., White, S. D. M., Jenkins, A., Pearce, F. R. 1999, MNRAS, 308, 593
- [1989] Colless, M. 1989, MNRAS, 237, 799
- [2000] Collins, C. A.; Guzzo, L.; Bhringer, H.; Schuecker, P.; Chincarini, G.; Crudele, R.; De Grandi, S.; MacGillivray, H. T.; Neumann, D. M.; Schindler, S.; Shaver, P.; Voges, W. 2000, MNRAS, 319, 939
- [1998] Couch, Warrick J.; Barger, Amy J.; Smail, Ian; Ellis, Richard S.; Sharples, Ray M. 1998, ApJ, 497, 188
- [2007] Cortese, L.; Marcillac, D.; Richard, J.; Bravo-Alfaro, H.; Kneib, J.-P.; Rieke, G.; Covone, G.; Egami, E.; Rigby, J.; Czoske, O.; Davies, J. 2007, MNRAS, 376, 157

## Bibliography

---

- [2002] Cruddace, R., Voges, W., Böhringer, H., Collins, C. A., Romer, A. K., MacGillivray, H., Yentis, D., Schuecker, P., Ebeling, H., De Grandi, S. 2002, ApJS, 140, 239
- [2004] Cypriano, Eduardo S.; Sodr, Laerte, Jr.; Kneib, Jean-Paul; Campusano, Luis E. 2004, ApJ, 613, 95
- [2002] Dahle, Haakon; Kaiser, Nick; Irgens, Ragnvald J.; Lilje, Per B.; Maddox, Steve J. 2002, ApJS, 139, 313
- [1999] De Grandi, S., Böhringer, H., Guzzo, L., Molendi, S., Chincarini, G., Collins, C., Cruddace, R., Neumann, D., Schindler, S., Schuecker, P., Voges, W. 1999, ApJ, 514, 148
- [2001] De Grandi, S., & Molendi, S. 2001, ApJ, 551, 153
- [2004] De Grandi, S.; Etori, S.; Longhetti, M.; Molendi, S. 2004, A&A, 419, 7
- [2003] De Propriis, Roberto; Colless, Matthew; Driver, Simon P.; Couch, Warrick; Peacock, John A.; Baldry, Ivan K.; Baugh, Carlton M.; Bland-Hawthorn, Joss; et al. 2003, MNRAS, 342, 725
- [2005] Diaferio, A.; Geller, M.J., Rines, K.J. 2005, ApJ, 628, 97
- [1978a] Dressler, A. 1978, ApJ, 222, 23
- [1978b] Dressler, A. 1978, ApJ, 223, 765
- [1978c] Dressler, A. 1978, ApJ, 226, 55
- [1980] Dressler, A. 1980, ApJS, 42, 565
- [1983] Dressler, A., Gunn, J.E. 1983, ApJ, 270, 7
- [1994] Dressler, A.; Oemler, A., Jr.; Butcher, H.R.; Gunn, J.E. 1994, ApJ, 430, 107
- [1997] Dressler, A.; Oemler, A.Jr.; Couch, W.J.; Smail, I.; Ellis, R.S.; Barger, A.; Butcher, H.; Poggianti, B.M.; Sharples, R.M. 1997, ApJ, 490, 577
- [2003] Durret, F., Lima Neto, G. B., Forman, W., Churazov, E. 2003, A&A, 403, L29
- [1997] Ebeling, H., Edge, A.C., Fabian, A.C., Allen, S.W., Crawford, C.S., Böhringer, H. 1997, ApJ, 479, 101
- [1997] Ebeling, H., Edge, A.C., Böhringer, H., Allen, S.W., Crawford, C.S., Fabian, A.C., Voges, W., Huchra, J.P. 1998, MNRAS, 301, 881

- [2000] Ebeling, H., Jones, L.R., Perlman, E., Scharf, C., Horner, D., Wegner, G., Malkan, M., Fairley, B.W., Mullis, C.R. 2000, *ApJ*, 534, 133
- [2001] Ebeling, H., Edge, A.C., Henry, J.P. 2001, *ApJ*, 553, 668
- [2004] Ebeling, H., Barrett, E., Donovan, D. 2004, *ApJ*, 609, L49
- [1990] Edge, A.C., Stewart, G.C., Fabian, A.C., Arnaud, K. A. 1990, *MNRAS*, 245, 559
- [2002] Ettori, S.; De Grandi, S.; Molendi, S. 2002, *A&A*, 391, 841
- [1991] Eyles, C. J.; Watt, M. P.; Bertram, D.; Church, M. J.; Ponman, T. J.; Skinner, G. K.; Willmore, A. P. 1991, *ApJ*, 376, 23
- [1979] Faber, S. M.; Gallagher, J. S. 1979, *ARA&A*, 17, 135
- [1994] Fabian, A.C., 1994, *ARA&A*, 32, 277
- [2003] Fabian, A.C. 2003, in Avila-Reese V., firmani C., Frenk C.S., Allen C., eds, *Revista Mexicana de Astronomia y Astrofisica Conference Series Vol. 17 of Revista Mexicana de Astronomia y Astrofisica, Vol. 27, Cluster Cores and Cooling Flows*, pp. 303-313
- [1966] Felten, J.E., Gould, J.R., Stein, W.A., Woolf, N.J. 1966, *ApJ*, 146, 955
- [2005] Finn, Rose A.; Zaritsky, Dennis; McCarthy, Donald W., Jr.; Poggianti, Bianca; Rudnick, Gregory; Halliday, Claire; Milvang-Jensen, Bo; Pell, Roser; Simard, Luc 2005, *ApJ*, 630, 206
- [1999] Garilli, B., Maccagni, D., Andreon, S. 1999, *A&A*, 342, 408
- [1995] Gavazzi, G., Randone, I., Branchini, E. 1995, *ApJ*, 438, 590
- [1984] Geller, M. J.; Huchra, J. P. 1984, *ApJS*, 54, 442
- [1998] Ghigna, S., Moore, B., Governato, F., Lake, G., Quinn, T., Stadel, J. 1998, *MNRAS*, 300, 146
- [1990] Gioia, I.M., Maccacaro, T., Schild, R.E., Wolter, A., Stocke, J.T., Morris, S.L., Henry, J. P. 1990, *ApJS*, 72, 567
- [1999] Giovannini, G.; Tordi, M.; Feretti, L. 1999, *NewA*, 4, 141
- [2000] Girardi, Marisa; Borgani, Stefano; Giuricin, Giuliano; Mardirossian, Fabio; Mezzetti, Marino 2000, *ApJ*, 530, 62

## Bibliography

---

- [2002] Girardi, Marisa; Manzato, Patrizia; Mezzetti, Marino; Giuricin, Giuliano; Limboz, Fsun 2002, ApJ, 569, 720
- [2000] Gladders, Michael D.; Yee, H. K. C. 2000, AJ, 120, 2148
- [2001] Gladders, Michael D.; Yee, H. K. C. 2001, ASPC, 232, 126
- [2003] Gómez, Percy L.; Nichol, Robert C.; Miller, Christopher J.; Balogh, Michael L.; Goto, Tomotsugu; Zabludoff, Ann I.; Romer, A. Kathy; Bernardi, Mariangela; et al. 2003, ApJ, 584, 210
- [2005] Goto, Tomotsugu; Postman, Marc; Cross, Nicholas J. G.; Illingworth, G. D.; Tran, K.; Magee, D.; Franx, M.; Bentez, N.; et al. 2005, ApJ, 621, 188
- [2002] Goto, Tomotsugu; Okamura, Sadanori; McKay, Timothy A.; Bahcall, Neta A.; Annis, James; Bernard, Mariangela; Brinkmann, Jonathan; Gmez, Percy L. 2002, PASJ, 54, 515
- [2001] Govoni, F.; Feretti, L.; Giovannini, G.; Bhringer, H.; Reiprich, T. H.; Murgia, M. 2001, A&A, 376, 803
- [1972] Gunn, J.E., Gott, J.R.III 1972, ApJ, 176, 1
- [1997] van Haarlem, M. P.; Frenk, C. S.; White, S. D. M. 1997, MNRAS, 287, 817
- [2005] Hansen, Sarah M.; McKay, Timothy A.; Wechsler, Risa H.; Annis, James; Sheldon, Erin Scott; Kimball, Amy 2005, ApJ, 633, 122
- [1992] Henry, J.P., Gioia, I.M., Maccacaro, T., Morris, S.L., Stocke, J.T., Wolter, A. 1992, ApJ, 386, 408
- [1982] Huchra, J. P.; Geller, M. J. 1982, ApJ, 257, 423
- [1985] Icke, V. 1985, A&A, 144, 115
- [2004] Kaastra, J.S., Tamura, T., Peterson, J.R., Bleeker, J.A.M., Ferrigno, C., Kahn S.M., Paerels F.B.S., Piffaretti, R., Branduardi-Raymont, G., Böhringer, H. 2004, A&A, 413, 415
- [1996] Katgert, P.; Mazure, A.; Perea, J.; den Hartog, R.; Moles, M.; Le Fevre, O.; Dubath, P.; Focardi, P.; et al. 1996, A&A, 310, 8
- [2004] Kay, S.T., Thomas, P.A., Jenkins, A., Pearce, F.R. 2004, MNRAS, 355, 1901
- [2004] Kempner, Joshua C.; David, Laurence P. 2004, MNRAS, 349, 385
- [1962] King, I.R. 1962, AJ, 74, 804



- [2001] Kodama, T., Smail, I., Nakata, F., Okamura, S., Bower, R. G. 2001, *ApJ*, 562, 9
- [2007a] Koester, Benjamin P.; McKay, Timothy A.; Annis, James; Wechsler, Risa H.; Evrard, August E.; Rozo, Eduardo; Bleem, Lindsey; Sheldon, Erin S.; Johnston, David 2007, *ApJ*, 660, 221
- [2007b] Koester, B. P.; McKay, T. A.; Annis, J.; Wechsler, R. H.; Evrard, A.; Bleem, L.; Becker, M.; Johnston, D.; et al. 2007, *ApJ*, 660, 239
- [1984] Kowalski, M.P., Cruddace, R.G., Wood, K.S., Ulmer, M.P. 1984, *ApJS*, 56, 403
- [1999] Kull, A., Böhringer, H. 1999, *A&A*, 341, 23
- [1989] Lahav, O., Fabian, A.C., Edge, A.C., Putney, A. 1989, *MNRAS*, 240, 753
- [1998] Lake, G., Katz, N., Moore, B. 1998, *ApJ*, 495, 152
- [1997] Ledlow, M., Burns, J., Owen, F., Voges, W. 1997, *AAS*, 18912212
- [2004] Lin, Yen-Ting; Mohr, Joseph J.; Stanford, S. Adam 2004, *ApJ*, 610, 745
- [2000] Lobo, C.; Iovino, A.; Lazzati, D.; Chincarini, G. 2000, *A&A*, 360, 896
- [1997] Lopez-Cruz, O. 1997, Ph.D. Thesis
- [1983] Lucey, J.R. 1983, *MNRAS*, 204, 33
- [1986] Lugger, P.M. 1986, *ApJ*, 303, 535
- [2005] Mastropietro, C., et al. 2005, *MNRAS*, 364, 607
- [2003] Merluzzi, P.; La Barbera, F.; Massarotti, M.; Busarello, G.; Capaccioli, M. 2003, *A&A*, 589, 147
- [1988] Miller, R.H., Smith, B.F. 1988, in *The few body problem; Proceedings of the 96th IAU Colloquium, Turku, Finland, June 14-19, 1987 (A89-12451 02-90)*. Dordrecht, Kluwer Academic Publishers, 1988, p. 353-359
- [1976] Mitchell, R.J., Culhane, J.L., Davidson, P.J., Ives, J.C. 1976, *MNRAS*, 127, 29
- [2001] Molendi, S., Pizzolato, F. 2001, *ApJ*, 560, 194
- [1996] Moore, B., et al. 1996, *Nature*, 379, 613
- [1998] Moore, B., Lake, G., Katz, N., 1998, *ApJ*, 495, 139

## Bibliography

---

- [1999] Moore, B., Lake, G., Quinn, T., Stadel, J. 1999, MNRAS, 304, 465
- [1998] Morris, S.L.; Hutchings, J. B.; Carlberg, R. G.; Yee, H. K. C.; Ellingson, E.; Balogh, M.L.; Abraham, R. G.; Smecker-Hane, T.A. 1998, ApJ, 507, 84
- [2004] Mushotzky, R.F. 2004, in Mulchaey J.S., Dressler A., Oemler A., eds, Clusters of Galaxies: Probes of Cosmological Structure and Galaxy Evolution Clusters of Galaxies: An X-ray Perspective, pp. 123+
- [1996] Navarro, J.F., Frenk, C.S., White, S.D.M. 1996, ApJ, 462, 563
- [1996] Navarro, J.F., Frenk, C.S., White, S.D.M. 1997, ApJ, 490, 493
- [1997] Nichol, R.C., Holden, B.P., Romer, A.K., Ulmer, M.P., Burke, D.J., Collins, C.A. 1997, ApJ, 481, 644
- [1982] Nulsen, P.E.J. 1982, MNRAS, 198, 1007
- [1997] Oemler, A.Jr., Dressler, A., Butcher, H.R. 1997, ApJ, 474, 561
- [2007] Orrú, E.; Murgia, M.; Feretti, L.; Govoni, F.; Brunetti, G.; Giovannini, G.; Girardi, M.; Setti, G. 2007, A&A, 467, 943
- [2004] Ortiz-Gil, A.; Guzzo, L.; Schuecker, P.; Bhringer, H.; Collins, C. A. 2004, MNRAS, 348, 325
- [1999] Olsen, L. F.; Scodreggio, M.; da Costa, L.; Slijkhuis, R.; Benoist, C.; Bertin, E.; Deul, E.; Erben, T.; et al. 1999, A&A, 345, 363
- [2001] Paolillo, M.; Andreon, S.; Longo, G.; Puddu, E.; Gal, R. R.; Scaramella, R.; Djorgovski, S. G.; de Carvalho, R. 2001, A&A, 367, 59
- [2003] Peterson, J.R., Kahn, S.M., Paerels, F.B.S., Kaastra, J.S., Tamura, T., Bleeker, J.A.m., Ferrigno, C., Jernigan, J.G., 2003, ApJ, 590, 207
- [1982] Piccinotti, G., Mushotzky, R.F., Boldt, E.A., Holt, S.S., Marshall, F.E., Serlemitsos, P.J., Shafer, R.A. 1982, ApJ, 253, 485
- [2005] Piffaretti, R., Jetzer, P., Kaastra, J.S., Tamura, T. 2005, A&A, 433, 101
- [2004] Pointecouteau, E.; Arnaud, M.; Kaastra, J.; de Plaa, J. 2004, A&A, 423, 33
- [1996] Poggianti, B. M.; Barbaro, G. 1996, A&A, 314, 379
- [2006] Poggianti, Bianca M.; von der Linden, Anja; De Lucia, Gabriella; Desai, Vandana; Simard, Luc; Halliday, Claire; Aragn-Salamanca, Alfonso; Bower, Richard; et al. 2006, ApJ, 642, 188

- [1999] Ponman, T.J., Cannon, D.B., Navarro, J.F., 1999, *Nature*, 397, 135
- [2003] Ponman, T.J., Sanderson, A.J.R., Finoguenov, A. 2003, *MNRAS*, 249, 662
- [2005a] Popesso, P.; Böhringer, H.; Romaniello, M.; Voges, W. 2005, *A&A*, 433, 415
- [2005b] Popesso, P.; Biviano, A.; Böhringer, H.; Romaniello, M.; Voges, W. 2005, *A&A*, 433, 431
- [2006] Popesso, P.; Biviano, A.; Böhringer, H.; Romaniello, M. 2006, *A&A*, 445, 29
- [2007] Popesso, P.; Biviano, A.; Böhringer, H.; Romaniello, M. 2007, *A&A*, 464, 451
- [1996] Postman, Marc; Lubin, Lori M.; Gunn, James E.; Oke, J. B.; Hoessel, John G.; Schneider, Donald P.; Christensen, Jennifer A. 1996, *AJ*, 11, 615
- [2007] Pratt, G.W., Böhringer, H., Croston, J.H., Arnaud, M., Borgani, S., Finoguenov, A., Temple, R.F. 2007, *A&A*, 461, 71
- [2004] Rasia, E., Tormen, G., Moscardini, L. 2004, *MNRAS*, 351, 237
- [1999] Reblinsky, K., Bartelmann, M. 1999, *A&A*, 345, 1
- [2002] Reiprich, T., Böhringer, H., 2002, *ApJ*, 567, 716
- [2001] Ricker, P.M., Sarazin, C.L. 2001, *ApJ*, 561, 621
- [2004] Roediger, E., Hensler, G. 2004, *Astron. Nachr.*, 325, 54
- [2005] Roediger, E., Brüggem, M. 2005, *Astron. Nachr.*, 326, 509
- [2006a] Roediger, E., Brüggem, M. 2006, *MNRAS*, 369, 567
- [2006b] Roediger, E., Brüggem, M., Hoeft, M. 2006, *MNRAS*, 371, 609
- [1994] Romer, A.K., Collins, C.A., Böhringer, H., et al. 1994, *Nature*, 372, 75
- [1971] Rood, H.J., & Sastry, G.N. 1971, *PASP*, 83, 313
- [2002] Rosati, P., Borgani, S., Norman, C. 2002, *ARA&A*, 40, 539
- [2003] Sanderson, A. J. R.; Ponman, T. J. 2003, *MNRAS*, 345, 1241
- [2000] Scharf, C., Donahue, M., Voit, G.M., Rosati, P., Postman, M. 2000, *ApJ*, 528, 73
- [1976] Schechter, P. 1976, *ApJ*, 203, 297
- [2007] Schmidt, R. W.; Allen, S. W. 2007, *MNRAS*, 379, 209

## Bibliography

---

- [1998] Schuecker, P.; Boehringer, H. 1998, *A&A*, 339, 315
- [2001] Schuecker, P.; Bhringer, H.; Guzzo, L.; Collins, C. A.; Neumann, D. M.; Schindler, S.; Voges, W.; De Grandi, S.; Chincarini, G.; Cruddace, R.; Mller, V.; Reiprich, T. H.; Retzlaff, J.; Shaver, P. 2001, *A&A*, 368, 86
- [2002] Schuecker, P., Guzzo, L., Collins, C.A., Böhringer, H. 2002, *MNRAS*, 335, 807
- [2003] Schuecker, P., Böhringer, H., Guzzo, L., Collins, C.A. 2003, *A&A*, 368, 86
- [2003] Schuecker, P., Böhringer, H., Collins, C.A., Guzzo, L. 2003, *A&A*, 398, 867
- [2003] Tozzi, P.; Rosati, P.; Etti, S.; Borgani, S.; Mainieri, V.; Norman, C. 2003, *ApJ*, 593, 705
- [1992] Trümper, J. 1992, *Royal Astron. Soc. Quart. J.*, 33, 165
- [1993] Trümper, J. 1993, *Science*, 260, 1769
- [1993] Valluri, M. 1993, *ApJ*, 408, 57
- [2007] Venturi, T.; Giacintucci, S.; Brunetti, G.; Cassano, R.; Bardelli, S.; Dallacasa, D.; Setti, G. 2007, *A&A*, 463, 937
- [2005] Vikhlinin, A. Markevitch, M., Murray, S.S., Jones, C., Forman, W., Van Speybroeck, L. 2005, *ApJ*, 628, 655
- [2002] Voit, G.M., Bryan, G.L., Balogh, M.L., Bower, R.G., 2002, *ApJ*, 576, 601
- [2003] Voit, G.M., Balogh, M.L., Bower, R.G., Lacey, C.G., Bryan, G.L. 2003, *ApJ*, 593, 272
- [2005] Voit, G.M. 2005, *Reviews of Modern Physics*, 77, 207
- [1993] Whitmore, B.C., Gilmore, D.M., Jones, C. 1993, *ApJ*, 407, 489
- [2004] Zhang, Y.-Y.; Finoguenov, A.; Bhringer, H.; Ikebe, Y.; Matsushita, K.; Schuecker, P. 2004, *A&A*, 413, 49
- [2006] Zhang, Y.-Y., et al. 2006, *A&A*, 456, 55
- [1933] Zwicky, F. 1933, *Helvetica Physica Acta*, 6, 110
- [1961-1968] Zwicky, F., Herzog, E., Wild, P., Karpowicz, M., Kowal, C.T. 1961-1968, *Catalogues of Galaxies and Clusters of Galaxies*, Vol. 1-6 (Caltech, Pasadena)

# 2

## Transformation of galaxy colours along cluster-feeding filaments

*...or...* **Flaming, bright galaxies along the filaments of A 2744**

Braglia, F., Pierini, D., Böhringer, H. 2007, A&A 470, 425

The existence of a lumpy, large-scale filamentary structure is at the basis of the current paradigm of cosmic formation and evolution of clusters. The star-formation history of galaxies falling into a cluster is altered as a result of the environmental stresses. We investigate the relation between substructure and properties of the galaxy population in a  $30' \times 30'$  region centred on the massive merging cluster A 2744 at  $z \sim 0.3$ . Multi-object spectroscopy at low resolution and BVR photometry are used to detect the presence of substructure through a Dressler–Schectman analysis and the photometric redshift technique, respectively. Galaxies at the same photometric redshift of the cluster are divided into red and blue according to their distribution in the B-R vs. R colour–magnitude diagram. We identify two large-scale filaments associated with A 2744. Along these filaments, the blue-to-red galaxy number ratio increases together with the cluster-centric distance but peaks slightly beyond the cluster virial radius. The filaments host a population of bright, large (i.e. more luminous than  $R^*$  for the main body of the cluster and with angular sizes of 13–22  $h_{70}^{-1}$  kpc) blue galaxies that is hardly found among galaxies lying in a neighbouring low-density environment at the same redshift of the cluster. These results can be interpreted as a manifestation of galaxy harassment.

### 2.1 Introduction

Detailed numerical simulations show that clusters form at the intersection of filaments and sheets of matter in the evolving large-scale structure of the Universe (e.g., Colberg et al. (1999)). These infall-pattern features are correlated in time and appear to be lumpy rather than homogeneous. Thus they define preferred directions from which clusters are fed with lumps of matter.

The existence of extended filamentary structures and voids in the large-scale spatial distribution of local galaxies is known since the advent of redshift surveys (Davis et al. (1982)). Later X-ray observations detected the emission from the hot ( $10^5$ – $10^7$  K) gas in filaments of nearby clusters (Briel & Henry (1995); Kull & Böhringer (1999); Scharf et al. (2000); Durret et al. (2003)).

In addition, optical observations established the existence of a correlation between the morphology or star-formation rate of a galaxy and the local galaxy density or cluster-centric distance (Dressler (1980); Whitmore et al. (1993); Dressler et al. (1997); Balogh et al. (1999); Poggianti et al. (1999)). In particular, the spectral-index analysis for galaxies of the CNOC1 cluster sample at  $z \sim 0.3$  demonstrated that the radial increase in star-formation activity means that the last episode of star formation occurred more recently in galaxies farthest from the cluster centre (Balogh et al. (1999)). Different mechanisms can establish this pattern and, thus, the observed difference in star-formation activity between cluster and field galaxies (e.g., Abraham et al. (1996); Morris et al. (1998); Balogh et al. (1999)). They include ram-pressure stripping by the intracluster medium (ICM) (e.g., Gunn & Gott (1972); Quilis et al. (2000)), close encounters (Barnes (1992)), “galaxy harassment” (Moore et al. (1996)) and “strangulation” (Larson et al. (1980)).

Determining the relative importance of these mechanisms requires probing galaxy properties as a function of the infall-region topology and mass of a cluster. In this pilot study, we investigate A 2744 (AC 118 or RXCJ0014.3-3022) out of the REFLEX-DXL (Distant X-ray Luminous) catalogue. This is a homogeneous, unbiased sample drawn from the REFLEX survey (Böhringer et al. (2001)) comprising the thirteen most luminous clusters at  $z = 0.27$ – $0.31$  in the Southern hemisphere, with X-ray ( $[0.1$ – $2.4]$  keV) luminosities in excess of  $10^{45} h_{70}^{-1} \text{ erg s}^{-1}$  (Zhang et al. (2006)). Multiple evidence shows that the main body of A 2744 is a merging system (Boschin et al. (2006) and references therein). In a preliminary analysis (Böhringer et al. (2006)), the comparison of X-ray and optical properties suggested the presence of two filamentary structures stemming out of the main body of the cluster. Here we present a more accurate kinematical analysis of the cluster and investigate the galaxy populations associated with these filaments.

## 2.2 Data description and reduction

Imaging in the B-, V-, and R-passbands was carried out using the wide-field imager (WFI) on the ESO/MPG-2.2m telescope at La Silla, Chile in September 2000, with a seeing of  $\sim 1''$ . The WFI data were reduced using the data reduction system developed for the ESO Imaging Survey (EIS, Renzini & da Costa (1997)) and its associated EIS/MVM image processing library version 1.0.1 (*Alambic*, Vandame (2004))<sup>1</sup>. Source detection and photometry were performed with *SExtractor* (Bertin & Arnouts (1996)). Source photometry was extracted in fixed circular apertures ( $2''$  wide for the determination of photometric redshifts) or in a flexible (Kron-like, Kron (1980)) elliptical aperture with a Kron-factor of 2.5. Magnitudes were calibrated to the Johnson–Cousins system using standard stars (Landolt (1992)), corrected for galactic extinction (Schlegel et al. (1998)), and expressed in the AB system. The photometric catalogue is complete down to  $R \sim 23.5$  and contains objects across a field of  $1/4$  of a square degree.

Multi-object spectroscopy was performed with VLT-VIMOS in low resolution ( $R = 200$ ) mode (LR-Blue grism) in September 2004. With a slit-width of  $1''$ , the expected uncertainty on the observed velocities is  $250\text{--}300 \text{ km s}^{-1}$ . Comparison with previously known redshifts in the same region gives a mean error of  $276 \text{ km s}^{-1}$ , in agreement with the value estimated by Le Fèvre et al. (2005) for the same LR-Blue grism. This is enough to establish the membership of a galaxy and the presence of large-scale structure for a massive cluster like A 2744. Objects with  $I \leq 22.5$  were selected as targets for spectroscopy from VLT-VIMOS pre-imaging of a  $24' \times 22'$  field. This limiting magnitude corresponds approximatively to an  $I^* + 3$  galaxy at the redshift of the cluster (0.3068, see Couch et al. (1998)). The adopted selection criterion prevents a bias against cluster members with specific star-formation histories (i.e., colours). Thus, it also prevents the completeness of the spectroscopic sample from being dependent on the local galaxy density, given the known relation between this density and the star-formation rate of a galaxy. The spectroscopic observations provided about 900 spectra. These data were reduced using the dedicated software VIPGI<sup>2</sup>.

Throughout the paper we adopt a  $\Lambda$ CDM cosmology where  $\Omega_m = 0.3$ ,  $\Omega_\Lambda = 0.7$ , and  $h_{70} = H_0 / 70 \text{ km s}^{-1} \text{ Mpc}^{-1} = 1$ .

<sup>1</sup>*Alambic* is a publicly available software designed to automatically transform raw images from single/multi-chip optical/infrared cameras into reduced images for scientific use.

<sup>2</sup>VIPGI (VIMOS Interactive Pipeline and Graphical Interface) (Scodreggio et al. (2005)) is developed by the VIRMOS Consortium to handle the reduction of the VIMOS data for the VVDS (VIMOS VLT Deep Survey, Le Fèvre et al. (2005)).

### 2.3 Analysis

#### 2.3.1 Evidence of large-scale structure

Spectroscopic redshifts were first converted into velocities according to Danese et al. ((1980)). We then applied a recursive  $3\sigma$  clipping algorithm to the subsample of galaxies selected in a velocity interval of  $10,000 \text{ km s}^{-1}$  width centred on the known redshift of the cluster. As a result, we identified 134 cluster members. This number was increased by additional 60 cluster members identified from redshifts available in the *NED*, mostly lying within 1 Mpc from the centre of the cluster. The ensuing mean redshift of the cluster ( $0.3068 \pm 0.006$ ) is in excellent agreement with previous determinations. The total number of 194 spectroscopic cluster members is twice as large as the number considered in the analysis of Boschin et al. ((2006)). Furthermore, it probes an area almost four times as large.

We determine a rest-frame velocity dispersion of the cluster equal to  $1509 \text{ km s}^{-1}$ . If A 2744 were a dynamically relaxed system, its velocity dispersion and virial radius<sup>3</sup> would give a dynamical mass equal to  $3.3 \times 10^{15} h_{70}^{-1} M_{\odot}$ . However, a Kolmogorov–Smirnov (KS) test reveals that the distribution of radial velocities has only a 0.02% probability to be gaussian. This is consistent with A 2744 being a merging system. Combining galaxy velocity and position information (Dressler & Schectman (1988)), we identify two very prominent substructures, lying at  $9.3'$  to the NW and  $8.2'$  to the S with respect to the cluster main body. These substructures are external but contiguous to those identified by Boschin et al. ((2006)). They find counterparts in the structures seen in the hot-gas entropy map (Finoguenov et al. (2005)) as remarked in Böhringer et al. ((2006)). In particular (see Fig. 1), we find that the NW structure corresponds to a clump of 23 objects with a velocity distribution characterised by a mean relative velocity of  $+566 \text{ km s}^{-1}$ , a dispersion of  $428 \text{ km s}^{-1}$  and a positive skew. We picture these galaxies as infalling from the near side of the cluster. Conversely, the S structure corresponds to a tighter clump of 15 objects, with a mean relative velocity of  $-738 \text{ km s}^{-1}$  and a dispersion of  $318 \text{ km s}^{-1}$ . This suggests infall from the far side of the cluster.

We run extended Monte Carlo simulations over our spectroscopic sample, reshuffling the redshifts of the objects while maintaining their positions as in Dressler & Schectman ((1988)) and adding a random gaussian error with sigma equal to the dispersion found. We also run the same test by generating a gaussian velocity distribution. Comparison of the DS-test deviation distributions shows that the inclusion of errors is not sufficient to change the overall behaviour: the two distributions are always consistent, the mean KS statistical parameter being 0.57, to be confronted with a rejection threshold of 0.88. Conversely, comparison of the true redshift distribution with the gaussian case shows that the two distributions differ not only in

---

<sup>3</sup> $R_{\text{Vir}} = 2.5 h_{70}^{-1} \text{ Mpc}$ , from the X-ray analysis of Zhang et al. ((2006)).



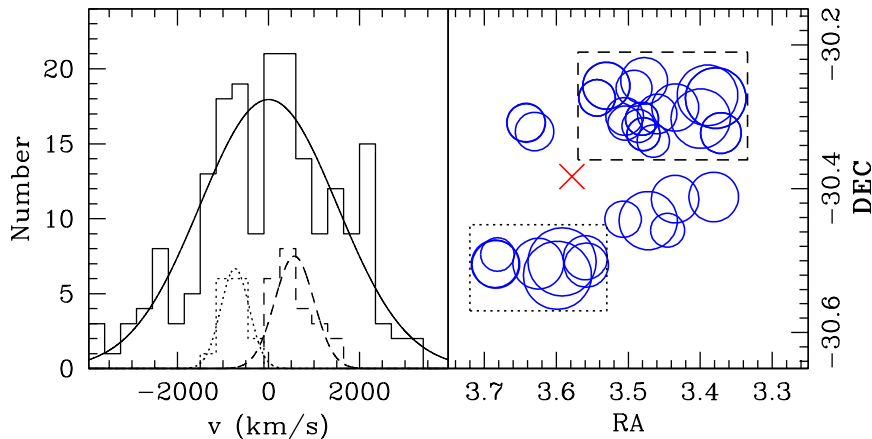


**Figure 2.1:** Left: velocity distribution for different regions of A 2744, i.e.: the overall system (*solid line*), with a velocity dispersion of  $1509 \text{ km s}^{-1}$ ; the substructure to the NW (*dashed line*), with a mean velocity of  $566 \text{ km s}^{-1}$  and a dispersion of  $428 \text{ km s}^{-1}$ ; the substructure to the S (*dotted line*), with a mean velocity of  $-738 \text{ km s}^{-1}$  and a dispersion of  $314 \text{ km s}^{-1}$ . Right: Dressler-Schectman test for the spectroscopic cluster members; the dashed- and dotted-line boxes outline respectively the NW and S substructures detected as very significant deviations from the overall velocity distribution. The red cross marks the cluster X-ray centre.

velocity, but also in the distribution of DS deviations (we obtain a KS parameter of 0.81, against a threshold for rejection of 0.53). The spatial location of the highly deviating peaks does not change position, so they are clearly robust against the size of velocity errors. This is mainly due to the statistical nature of the DS test, which looks for deviations of whole clumps of galaxies by comparing the velocity mean and dispersion of individual groups with the overall velocity dispersion of the cluster. So the effect of errors of individual velocities is smeared down.

In order to map these structures beyond the area covered by spectroscopy, we determine photometric redshifts for the whole photometric catalogue with the *HyperZ* code (Bolzonella et al. (2000)). Photo- $z$  solutions are trained on the available spectroscopic redshifts (about 800 non-stellar objects in the redshift range  $[0, 0.85]$ ), so to select the most efficient templates at the cluster redshift. We divide our spectro-photometric sample into red and blue objects on the basis of the cluster red sequence as described in Sect. 3.2. Then, we separate objects into bright and faint, where we define as “bright” the galaxies that are equally or more luminous than the characteristic magnitude for the main body of the cluster, i.e.,  $R^* \sim 19.6 \pm 0.3$  (Busarello et al. (2002)). For the resulting 4 catalogues we check independently which templates

## 2 Transformation of galaxy colours along cluster-feeding filaments

---

to use for the photo- $z$  determination, running *HyperZ* over the same redshift range. Galaxies at the distance of the cluster are then identified as objects in the photo- $z$  range [0.28,0.40]. This corresponds to the  $1\sigma$  interval centred on the mean photometric redshift (0.34) of the spectroscopic cluster members. The rms uncertainty is 0.06 at the spectroscopic redshift of A 2744. We see a somewhat wider spread for blue objects, as can be expected; nevertheless, the cluster stands clearly out in the photo- $z$  distribution (see Fig. 2.2). The  $\chi^2$  distribution for random objects from the samples exhibits always a single minimum (and thus a single solution).

We check the occurrence of catastrophic failures (i.e., wrong identifications) running *HyperZ* over the spectro-photometric catalogue with increasing redshift ranges (from [0,0.85] to [0,6]). This is done for both red and blue objects independently. No catastrophic failure is found up to  $z \sim 1.5$ . From this result and the relatively bright magnitude limit of the sample ( $R \sim 23.5$ ), we adopt a safe range of [0,1] for the photo- $z$  determination across the whole field.

To check the robustness of this assumption against contamination from high- $z$  outliers, we apply the same photometric redshift analysis over a simulated catalogue of objects in the chosen magnitude range and with a suitable redshift distribution. A sample of  $\sim 30000$  mock objects is thus created with the *HyperZ* routine *make\_catalogue* down to  $R = 23.5$  and with a redshift distribution consistent with deep, magnitude-selected spectroscopic surveys (VVDS-Deep, Le Fèvre et al. (2005)) to replicate as much as possible a natural redshift distribution over the field of view.

We run *HyperZ* with the selected templates over the simulated catalogue constrained to the redshift range [0,1]; the result is shown in Fig. 2.3. While we see (as expected) some contamination from outliers, the wrong identifications mainly lie outside the photometric redshift range of the cluster (0.28–0.4).

In this simulation we did not take into account the presence of the cluster at  $z = 0.3068$ , as we want to assess the pure contamination from background objects. Comparing the number of interlopers with the photometric cluster members (5759 objects within the cluster photo- $z$  range) shows that the contamination is still quite low (1.8% for high- $z$  red objects, 3.2% for high- $z$  blue objects and 6.1% for blue foreground objects). Thus, we conclude that the effect of contamination in the cluster redshift range is negligible.

For the 5759 objects at the distance of the cluster, divided into a red subsample and a blue one (see Sect. 3.2), we determine separate number density maps. As Fig. 2.4 shows, the bulk of the red objects sits in the main body of the cluster, as expected. However, two extensions of red objects are clearly seen towards the same NW and S directions defined by the structures identified by the Dressler–Schechter analysis. On the other hand, the blue objects are almost evenly spread across the imaged region. A closer look reveals a chain of highly significant overdensities of blue objects stemming out of the S extension of red objects and turning to the SW. This is very suggestive of an extended, lumpy filament as simulations predict. An extended

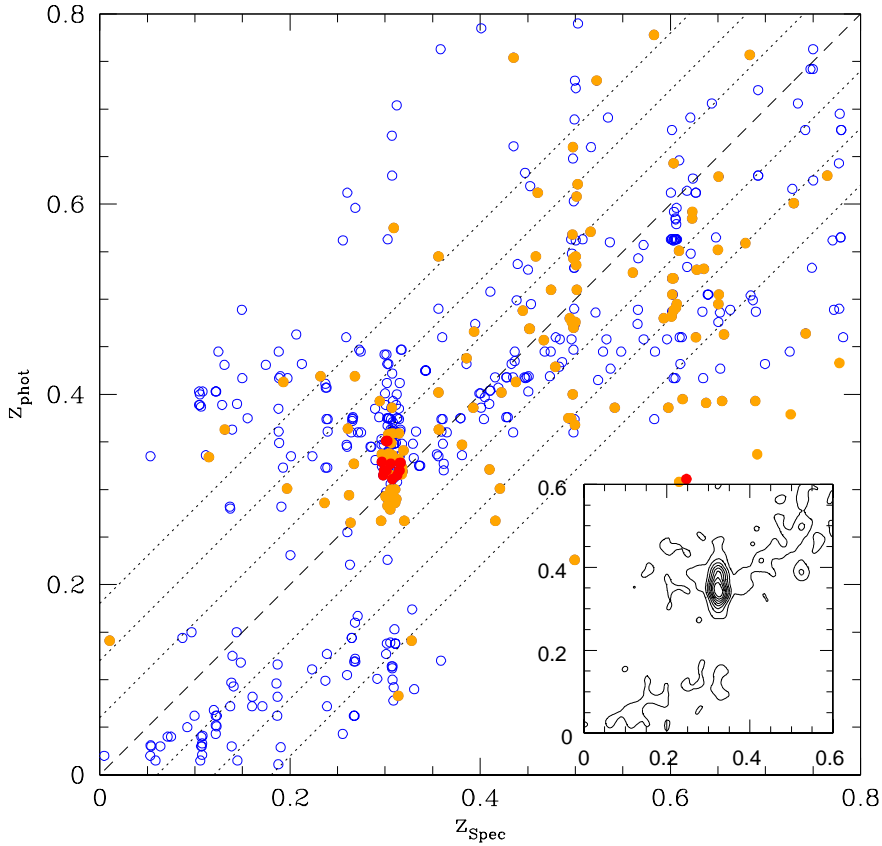


**Figure 2.2:** Comparison of spectroscopic and photometric redshifts. Orange dots: faint red galaxies; red dots: bright red galaxies; blue circles: blue galaxies. The dashed lines show the  $1\sigma$ ,  $2\sigma$  and  $3\sigma$  intervals, where we take as  $\sigma$  the spread of the photo- $z$  at the cluster redshift. The lower right insert shows a region of the same distribution as a contour plot to highlight the density (almost 200 points) in the cluster region.

filament in the NW direction is less evident.

### 2.3.2 Star formation along the large-scale structure

As a zero-point for the description of the star-formation activity in the region of A 2744, we take the red sequence of the likely massive, old, passively evolving galaxies in the B-R vs. R colour-magnitude diagram. Here it is defined as the locus of galaxies with  $17 \leq R \leq 20$  and  $B-R \sim 2.2$  within a cluster-centric distance of  $3'$  (i.e., about

## 2 Transformation of galaxy colours along cluster-feeding filaments

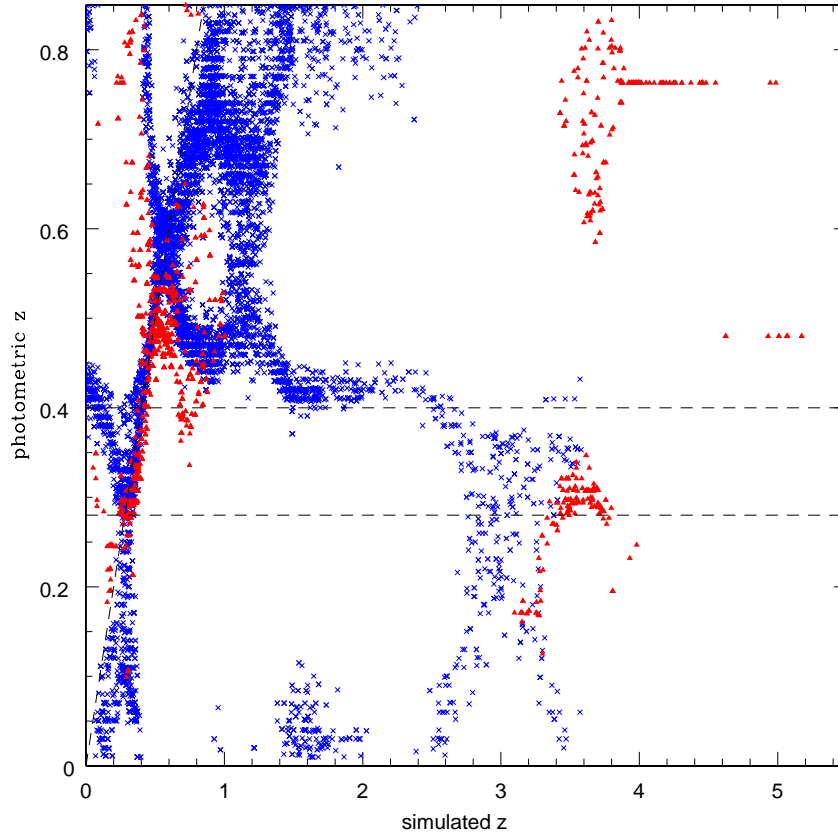


**Figure 2.3:** Simulated contamination from high- $z$  outliers. Red triangles represent old, passively evolving galaxies; blue crosses, star-forming galaxies. The dashed lines mark the cluster region in redshift space. Three main sources of contamination are identified: high- $z$  red galaxies (105 objects, contamination of 6.9%); high- $z$  blue galaxies (185 objects, contamination of 1.7%); and foreground blue galaxies (349 objects, contamination of 3.2%).

800 kpc). Then we divide the total sample of 5759 galaxies at the distance of the cluster into a red subsample and a blue one. An object is classified as blue if its B-R colour is bluer than that of a mean red-sequence object with the same R-magnitude at more than the  $3\sigma$  level.

Furthermore, we define two circular sectors with a  $60^\circ$  aperture and radii from  $3'$  to  $15'$  which encompass the two filaments. A third circular sector with a  $90^\circ$  aperture and radii from  $6'$  to  $18'$  defines an area equivalent to the sum of the previous two regions where no structure is evident. This third region represents the comparison

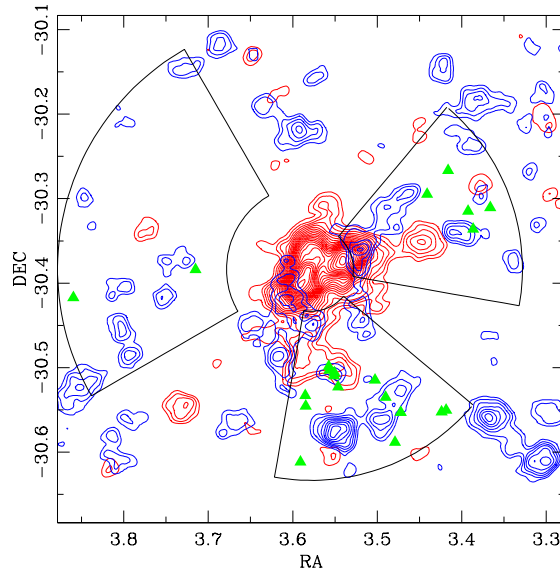


**Figure 2.4:** Density contours for red and blue galaxies at the distance (photo- $z$ ) of the cluster, in multiples of background RMS. The red objects density map shows the non-relaxed main body of the cluster and the head of the filamentary structures towards the S and NW. The blue objects map shows the presence of regions of high density in the outskirts of the cluster. In particular, two high density regions toward the S and NW lie on the extension of the substructures emerging from the cluster main body. The regions delimiting the two filaments and the “field” are also shown. Triangles mark the position of the luminous blue galaxies.

“field” at the same redshift of the cluster. Down to the completeness limit, there are 570 and 500 objects in the S and NW circular sectors, respectively, against a total of 796 in the field. Hence the significance of the average overdensity is equal to  $9\sigma$  and  $5\sigma$  for the S and NW circular sectors, respectively, and to  $10\sigma$  overall. The overdensity is driven by faint galaxies:  $15\sigma$  and  $11\sigma$  for the red and blue galaxies with  $R^* < R \leq 23.5$ , respectively, against  $6\sigma$  and  $5\sigma$  for the red and blue galaxies with  $R \leq R^*$ , respectively.

Figure 2.5 reproduces the B-R vs. R colour-magnitude diagram for galaxies in these three regions. Luminous, red galaxies exhibit similar, tight colour-magnitude relations. In the higher-density regions, red galaxies with  $17 \leq R \leq 20$  define a red-sequence that is shifted bluewards by  $0.012 \pm 0.003$  mag with respect to the red-sequence in the main body of the cluster. As for the population of blue galaxies, a KS-test run for bins of 0.5 R-mag and the full B-R colour range shows a very significant ( $9\sigma$ ) overabundance of galaxies with  $17.6 \leq R \leq 19.3$  and  $0.8 \leq B-R$

## 2 Transformation of galaxy colours along cluster-feeding filaments

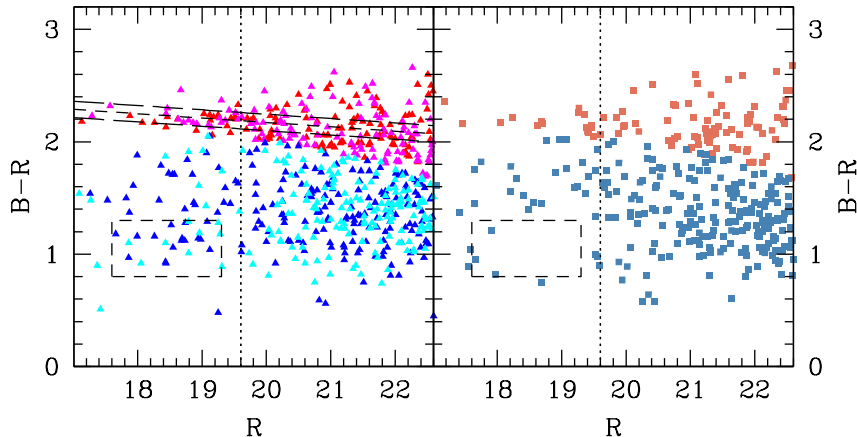


**Figure 2.5:** Colour-magnitude diagram for the galaxies in the filaments (left) or in the field (right). The population of the two filaments is represented in different colours: red objects appear in red (S filament) and magenta (NW filament), blue objects in blue (S filament) and cyan (NW filament). The signature of a red sequence can clearly be seen for the filaments, as well as the peculiar population of blue galaxies, in the dashed box; this population is not matched in the field. In each panel, the dashed vertical line marks the value of  $R^*$  for the main body of the cluster.

$\leq 1.3$  in the higher-density regions. This does not simply mirror the overabundance of luminous, blue galaxies there.

These bright, blue (and, thus, star-forming) galaxies are large systems, as confirmed visually by eye-ball estimation of their angular sizes to about  $3\text{--}5''$  (i.e. about  $13\text{--}22 h_{70}^{-1}$  kpc). They lie mostly in or close to overdensities of blue objects and around or beyond the cluster virial radius  $R_{\text{vir}}$  (about  $9'$  or 2.5 Mpc). Out of these 19 luminous, blue galaxies, only three can be part of interacting pairs, whereas all are surrounded by several small companions.

Finally, we note that the relative fraction of blue galaxies increases moving outwards along the regions containing the filaments (see Fig. 4), possibly because the number of blue galaxies decreases less rapidly than the number of red galaxies. However, in the southern region a sudden increase of blue galaxies contributes to the peak in the blue-to-red galaxy number ratio at a cluster-centric distance of about  $1.2 R_{\text{vir}}$ . This peak is significant with respect to the relative fraction of blue galaxies in the field.

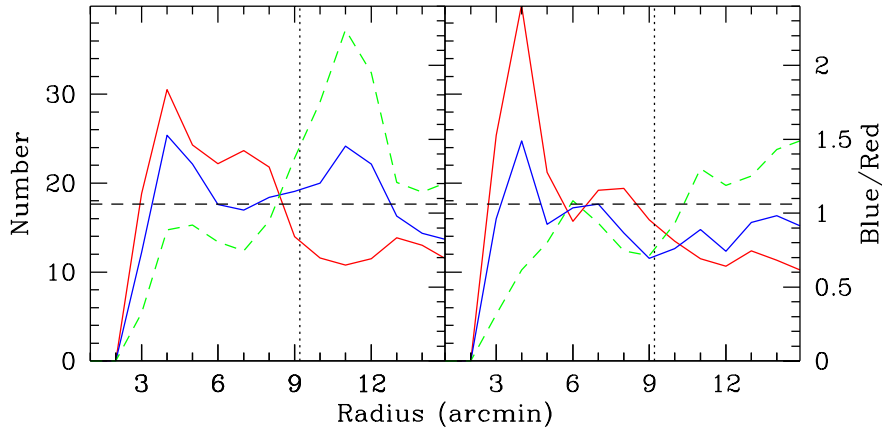


**Figure 2.6:** Radial trend of the galaxy population in the filaments, in bins of  $1'$  width (left: S filament; right: NW filament). The galaxy number reads on the left margin, the blue-to-red ratio on the right one). Along with the trend of the two populations (red and blue lines), the ratio of blue-to-red galaxies is shown (dashed green line) and compared with the mean value in the field (horizontal dashed line). Beyond the virial radius (vertical dotted line), a sudden increase in the ratio is seen, up to twice the field value.

## 2.4 Discussion and conclusions

In conjunction with the seminal study of Böhringer et al. ((2006)), our analysis strongly suggests the presence of two large-scale filaments associated with the massive merging cluster A 2744 at  $z = 0.3068$ . Similar evidence exists for other clusters at intermediate redshifts (Kodama et al. (2001); Ebeling et al. (2004)). On the other hand, the existence of a lumpy, large-scale filamentary structure is at the basis of the current paradigm of cosmic formation and evolution of clusters (e.g., Colberg et al. (1999)).

We investigate star formation in galaxies selected in two regions encompassing the large-scale filaments of A 2744 and in an equivalent, wide region where the density of galaxies at the (photometric) redshift of the cluster is significantly lower (the field). The overdensity in the filaments is driven by the population of galaxies fainter than  $R^*$  (as determined by Busarello et al. ((2002)) in the main body of the cluster), whatever their B-R colour. However, the blue-to-red galaxy number ratio increases with increasing cluster-centric distance along the filaments but peaks at about  $1.2 R_{\text{Vir}}$ . This result is consistent with and complementary to the established existence of a radial dependence of azimuthal averages of cluster galaxy properties like colours or

## 2 Transformation of galaxy colours along cluster-feeding filaments

---

emission-line strengths (e.g. Balogh et al. (1999); Lewis et al. (2002); Gómez et al. (2003); Finn et al. (2005)). It is also consistent with the result that the relative fraction of blue galaxies peaks between 1 and 2  $R_{\text{vir}}$  in the nearby Shapley and Pisces-Cetus superclusters (Haines et al. (2006); Porter & Raychaudhury (2007)).

A 2744 is a merging cluster, where the mass-ratio of the sub-components is about 3:1 (Boschin et al. (2006)). A qualitative comparison between the *Chandra* X-ray map (Kempner & David (2004)), exhibiting a signature of a bow-shock, and recent model renditions of shock heating in cluster mergers (McCarthy et al. (2007)) suggests that merging started less than 2 Gyr before the observed epoch. The primary shock could not travel to distances as large as the virial radius of the cluster. Hence the galaxy population along the filaments of A 2744 has not been affected by this large-scale merging event.

In their seminal spectroscopic study of the galaxy population in the core region of this cluster, Couch et al. ((1998)) find that the majority of star-forming galaxies is generally made of systems involved in major mergers but of modest luminosity, even in this brightened phase. These galaxies are interpreted as the progenitors of dwarf systems once they fade. Interestingly, we find that the filaments of A 2744 host a population of luminous, large (i.e. brighter than  $R^*$  and with sizes of 13–22  $h_{70}^{-1}$  kpc), blue galaxies that hardly exists in the field. Hence these galaxies can either retain or gain gas while they are falling into the main body of the cluster.

Galaxy harassment (Moore et al. (1996)) is a suitable physical explanation for the enhanced star formation inferred for these sparse, luminous, blue galaxies found at distances close to the virial radius of A 2744, where the density of the ICM is low. As envisioned by Moore et al. ((1999)), high-surface brightness disc galaxies and galaxies with luminous bulges do not experience a significant removal of material nor a transformation in Hubble type under the influence of high-speed, close encounters with substructure (including bright galaxies) and strong tidal shocks from the global cluster potential. However, their discs will be heated and undergo instabilities that can funnel gas (if any initially) into the central regions (Lake et al. (1998)). Galaxy harassment can generate morphological instabilities in galaxies already at the outskirts of a cluster (Moore et al. (1998); Mastropietro et al. (2005)). In the core of the cluster, ram pressure can strip all the residual gas from discs and drive a morphological transformation into S0's, as speculated by Moore et al. ((1999)). Alternatively, this can happen there once the shock associated with the large-scale merging decelerates and discs can cross it (see Roettiger et al. (1996)). Therefore, the luminous, blue galaxies along the filaments of A 2744 can be analogous to the progenitors of the S0–Sb galaxies in the core of the cluster that completed their last major episode of star formation 1–2 Gyr before the observed epoch (Couch et al. (1998)).



## Bibliography

- [1996] Abraham, R. G., et al. 1996, ApJ, 471, 694
- [1999] Balogh, M. L. et al. 1999, ApJ, 527, 54
- [1992] Barnes, J. E. 1992, ApJ, 393, 484
- [1996] Bertin, E., & Arnouts, S. 1996, A&AS, 117, 393
- [2001] Böhringer, H., et al. 2001, A&A, 369, 826
- [2006] Böhringer, H., et al. 2006, The Messenger, 123, 49
- [2000] Bolzonella, M., Miralles, J.-M., & Pelló, R. 2000, A&A, 363, 476
- [2006] Boschini, W., Girardi, M., Spolaor, M., & Barrena, R. 2006, A&A, 449, 461
- [1995] Briel, U. G., & Henry, J. P. 1995, A&A, 302, L9
- [2002] Busarello, G., et al. 2002, A&A, 389, 787
- [1999] Colberg, J. M., White, S. D. M., Jenkins, A., & Pearce, F. R. 1999, MNRAS, 308, 593
- [1998] Couch, W. J., et al. 1998, ApJ, 497, 188
- [1980] Danese, L., de Zotti, G., & di Tullio, G. 1980, A&A, 82, 322
- [1982] Davis, M., Huchra, J., Latham, D. W., & Tonry, J. 1982, ApJ, 253, 423
- [1980] Dressler, A. 1980, ApJ, 236, 351
- [1988] Dressler, A., Shectman, S. A. 1988, AJ, 95, 985
- [1997] Dressler, A., et al. 1997, ApJ, 490, 577
- [2003] Durret, F., Lima Neto, G. B., Forman, W., & Churazov, E. 2003, A&A, 403, L29
- [2004] Ebeling, H., Barrett, E., & Donovan, D. 2004, ApJ, 609, L49

## Bibliography

---

- [2005] Finn, R. A., et al. 2005, ApJ, 630, 206
- [2005] Finoguenov, A., Böhringer, H., & Zhang, Y.-Y. 2005, A&A, 442, 827
- [2003] Gómez, P. L., et al. 2003, ApJ, 584, 210
- [1972] Gunn, J. E., & Gott, J. R., III 1972, ApJ, 176, 1
- [2006] Haines, C.P., et al., 2006, MNRAS, 371, 55
- [2004] Kempner, J. C., & David, L. P. 2004, MNRAS, 349, 385
- [2001] Kodama, T., et al. 2001, ApJ, 562, L9
- [1980] Kron, R. G. 1980, ApJS, 43, 305
- [1999] Kull, A., & Böhringer, H. 1999, A&A, 341, 23
- [1998] Lake, G., Katz, N., & Moore, B. 1998, ApJ, 495, 152
- [1992] Landolt, A. U. 1992, AJ, 104, 340
- [1980] Larson, R. B., Tinsley, B. M., & Caldwell, C. N. 1980, ApJ, 237, 692
- [2005] Le Fèvre, O., et al. 2005, A&A, 439, 845
- [2002] Lewis, I., et al. 2002, MNRAS, 334, 673
- [2005] Mastropietro, C., et al. 2005, MNRAS, 364, 607
- [2007] McCarthy, I. G., et al. 2007, astro-ph/0701335
- [1996] Moore, B., et al. 1996, Nature, 379, 613
- [1998] Moore, B., Lake, G., & Katz, N., 1998, ApJ, 495, 139
- [1999] Moore, B., Lake, G., Quinn, T., & Stadel, J. 1999, MNRAS, 304, 465
- [1998] Morris, S. L., et al. 1998, ApJ, 507, 84
- [1999] Poggianti, B., et al., 1999, ApJ, 518, 576
- [2007] Porter, S. C., & Raychaudhury, S. 2006, MNRAS, 375, 1409
- [2000] Quilis, V., Moore, B., & Bower, R. 2000, Science, 288, 1617
- [1997] Renzini, A., & da Costa, L. 1997, The Messenger, 87, 23
- [1996] Roettiger, K., Burns, J. O., & Loken, C. 1996, ApJ, 473, 651

- [2000] Scharf, C., et al. 2000, ApJ, 528, L73
- [1998] Schlegel, D. J., Finkbeiner, D. P., & Davis, M. 1998, ApJ, 500, 525
- [2005] Scodreggio, M., et al. 2005, PASP, 117, 1284
- [2004] Vandame, B. 2004, PhD thesis, University of Nice-Sophia Antinopolis
- [1993] Whitmore, B. C., Gilmore, D. M., & Jones, C. 1993, ApJ, 407, 489
- [2006] Zhang, Y.-Y., et al. 2006, A&A, 456, 55

## Bibliography

---

# 3

## Evolution of the star formation activity across massive galaxy clusters

### 3.1 Introduction

X-ray emitting clusters signpost the largest amounts and concentrations of (cold) dark matter (CDM) in bound systems. At the same time, they provide large samples of coeval galaxies within a well-defined environment. This allows to study how galaxy properties, like star formation rate (SFR), behave as a function of the local matter/galaxy density.

Detailed numerical simulations show that clusters tend to form at the intersection of filaments and sheets of matter in the evolving large-scale structure of the Universe: over time, matter falls along such structures and accretes into a cluster. The infall pattern is not random: paths show a correlation in time and are almost stable, so that matter is channeled into a cluster through filamentary structures with persistent geometry. Matter does not accrete in a steady and continuous way, but in clumps and bound structures, which can be identified as infalling groups of galaxies or less massive clusters (Colberg et al. (1999)).

Filaments around clusters are hard to identify observationally, since they do not usually stand out as clear overdensities like clusters, and thus tend to be confused with the surroundings and the background. Early shallow X-ray observations could set upper limits to the X-ray luminosity of these structures (Briel & Henry (1995)), but deep imaging in X-ray or optical broad bands led to the discovery of an extended filamentary network around a few clusters at  $0.05 \leq z \leq 0.6$  (Kull & Böhringer

### 3 Evolution of the star formation activity across massive galaxy clusters

---

(1999); Scharf et al. (2000); Kodama et al. (2001); Durret et al. (2003); Ebeling et al. (2004); also see Werner et al. (2008)).

The galaxy population in cluster-feeding filaments can be expected to be somewhat different from those in the cluster main body as well as from the adjacent field, being filaments an environment of transition between low and extremely high density regimes. Consistently, observations have shown a clear correlation between galaxy morphology or SFR and local density or cluster-centric distance (Dressler et al. (1997); Whitmore, Gilmore & Jones (1993); Balogh et al. (1997)). The past and present star formation activities of galaxies appear to be different in low and high density environments already at intermediate redshifts (Abraham et al. (1996); Morris et al. (1998); Poggianti et al. (2006)). From a spectral index analysis of galaxies in 15 X-ray luminous clusters at  $0.18 < z < 0.55$ , Balogh et al. ((1999)) concluded that the increase in the observed star formation activity of galaxies towards the outer regions of a cluster is consistent with an age sequence: galaxies in the cluster outskirts have experienced star formation phases more recently than galaxies in the cluster innermost regions. Their interpretation was that the truncation of star formation in clusters may largely be a gradual process, perhaps due to the exhaustion of gas in the galaxy discs over fairly long timescales. In this case, differential evolution may result because field galaxies can refuel their discs with gas from extended halos, thus regenerating star formation, while cluster galaxies may not have such halos and so continue to evolve passively.

Recently, Böhringer et al. ((2006)) and Braglia et al. ((2007), hereafter BPB07) provided evidence for the presence of two filaments stemming out of the main body of the cluster RXCJ 0014.3–3022 (alias Abell 2744, AC 118) and extending beyond the cluster virial radius, making use of X-ray and optical data. This is one of the 13 clusters at  $z = 0.27–0.31$  with X-ray luminosities exceeding  $10^{45}$  erg cm<sup>-2</sup> s<sup>-1</sup>, selected from the ROSAT-ESO-Flux-Limited-X-ray (REFLEX) cluster survey (Böhringer et al. (2001a)) and observed with XMM-*Newton*, which make the Distant X-ray Luminous (DXL) cluster sample (Zhang et al. (2006)). It is also a major-merger system (e.g., Boschin et al. (2006)) and a “Butcher–Oemler” cluster (Butcher & Oemler (1978a), (1978b), (1984)). The blue galaxies in the cluster core, that are more abundant in this system compared to present-day massive clusters, are mostly systems involved in major mergers but subluminescent even in this brightened phase; in their faded state they appear destined to become dwarfs (Couch et al. (1998)). On the other hand, along the filaments of Abell 2744, BPB07 found evidence for luminous galaxies with boosted star formation activity with respect to their counterparts in the field.

Similar studies conducted with different approaches are confirming the picture of an increased star formation activity along filaments in the outskirts of clusters: for instance, Fadda et al. ((2007)) found a similar effect in another Abell cluster, where a large amount of obscured star formation was detected through *Spitzer* data. Porter

## 3.2 Data description and reduction procedures

---

et al. ((2007); (2008)) also found a similar activity increase along filaments in superclusters and showed that the largest part of the star formation increase lies in subluminescent systems ( $M_B < -20$ ).

The presence of these two distinct galaxy populations with abnormal SFRs in two distinct regions of the cluster and the wealth of optical and X-ray data make of the merging cluster Abell 2744 an interesting laboratory to study how several different physical processes affect galaxy evolution in different cluster environments. We also chose from our sample the cluster Abell 2537, a cool core (and thus likely relaxed) cluster, to obtain a complementary view of how star formation activity is related to cluster dynamics and environment.

The analysis presented here shows how combining X-ray observations, wide-field optical photometry and multi-object spectroscopy fosters the understanding of the link between large-scale structure, substructure, and star formation history in representative samples of galaxy clusters at intermediate-redshifts (e.g., Böhringer et al. (2001b), (2006); (2007); BPB07; Pierini et al. (2008)). Results from a similar analysis for the whole REFLEX-DXL sample will be presented in future papers of this series.

This first paper presents in detail data reduction and analysis techniques, in addition to the specific results obtained for RXCJ0014.3-3022 (Abell 2744,  $z=0.3068$ ) and RXCJ2308.3-0211 (Abell 2537,  $z=0.2966$ ). It is organised as follows: Sect. 2 provides information on the available data and data reduction; Sects. 3 and 4 describe the construction of the photometric and spectroscopic catalogues, respectively. Sect. 5 contains the main results, i.e. spectral index analysis for a representative sample of cluster galaxies, morphology comparison of the two clusters and results on the star-formation activity. The results are discussed in Sect. 6; conclusions are summarized in Sect. 7.

Hereafter we adopt a  $\Lambda$ CDM cosmology where  $\Omega_m = 0.3$ ,  $\Omega_\Lambda = 0.7$ , and  $h_{70} = H_0/70 \text{ km s}^{-1} \text{ Mpc}^{-1} = 1$ .

## 3.2 Data description and reduction procedures

### 3.2.1 Spectroscopic data

Multi-object spectroscopy in the cluster field was performed with the VIMOS instrument mounted at the Nasmyth focus B of VLT-UT3 *Melipal* at Paranal Observatory (ESO), in Chile.

VIMOS (VIvisible Multi-Object Spectrograph) is a visible (360 to 1000 nm) wide field imager and multi-object spectrograph. It is made of four identical arms with a field of view of  $7' \times 8'$  and a  $0.205''$  pixel size each, separated by a gap between each quadrant of  $2'$ . The total field of view (FOV) is  $4 \times 7' \times 8'$ . Each arm is equipped

### 3 Evolution of the star formation activity across massive galaxy clusters

---

with 6 grisms providing a spectral resolution ranging from 200 to 2500 and with one EEV CCD  $4k \times 2k$ .

The data presented here have been collected under the ESO Large Programme 169.A-0595 (PI: H. Böhringer) carried out in visitor and service modes in ESO G.O. time. This program addresses the coverage of 7 out of 13 DXL cluster members with VIMOS spectroscopic observations in low resolution mode, with the aim of maximizing the number of spectroscopic cluster members in a wide region centred around the X-ray centroid of the cluster.

Both clusters were observed from August 14 to August 16, 2004 for a total of about 4.4 hours each.

Since the main aim of the project was to study cluster dynamics, galaxy populations and star-formation activity in the least biased way, target pre-selection was not based on a colour criterion; instead, I-band pre-imaging was chosen to provide as close as possible a selection in stellar mass by using a red band, avoiding biases due to specific star-formation activity. In fact, I-band probes emission from stellar populations mostly older than 1-2 Gyrs at  $z \sim 0.3$ . At the same time, this choice allows to sample different environments with equal probability, given the existence of a correlation between density and star-formation activity (Dressler (1980); Whitmore et al. (1993)).

Preimaging was executed adopting three different pointings with two ditherings of  $15''$  each, in order to allow the most complete coverage of the cluster central region, a good coverage of the cluster outskirts and sufficient overlap for the cross-shaped gaps between the CCDs. The three pointings are thus aligned in the E-W direction and partly overlapping, providing a total continuous coverage of about  $34'$  in R.A. and  $20'$  in DEC. This corresponds to an uninterrupted coverage of the cluster out to  $2.7h_{70}^{-1}$  Mpc and a fairly good coverage of the outskirts out to  $4.6 h_{70}^{-1}$  Mpc at the clusters redshift. Fig. 3.1 shows the exact pointing pattern used for both clusters.

Exposure times of 8 minutes per preimaging pointing allowed a complete sampling of galaxies down to  $I \sim 22.5$ , i.e. about  $I^*+2$  at the cluster redshift (see Couch et al. (1998)). This exposure time and the light collecting area of an 8-meter class telescope make a complete sampling of bright galaxies in the cluster possible and provide a good census of faint systems.

For each pointing position, two VIMOS masks were prepared using the VMMPS tool from ESO<sup>1</sup>, based on the I-band magnitude of the targets. Objects were classified as bright or faint if  $17 \leq I \leq 19$  or  $19 < I \leq 21.5$ , respectively. We then flagged bright galaxies as compulsory, leaving instead the software free to choose faint galaxies to maximize the number of objects in each mask. This approach allowed to obtain spectra for most of the bright objects in this region, while avoiding any possible bias on the overall target selection. This also allowed to select objects roughly above or

---

<sup>1</sup><http://www.eso.org/observing/p2pp/OSS/VMMPS>



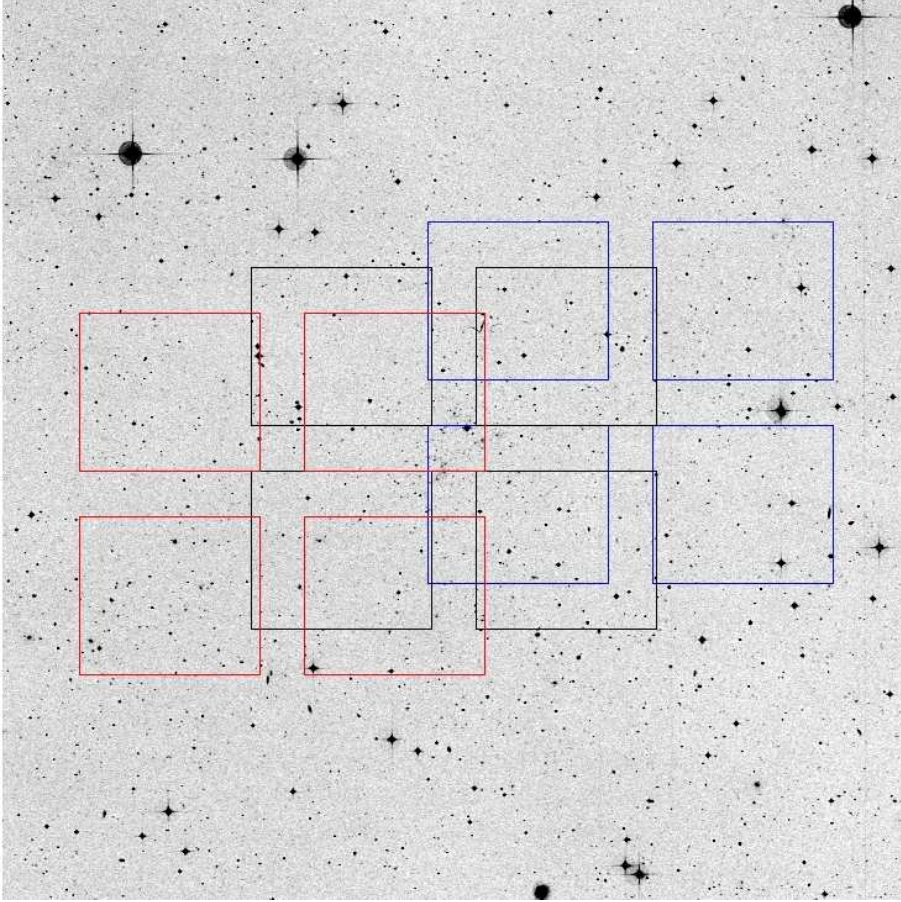


**Figure 3.1:** Pointing strategy for the VIMOS observations, overlaid onto the DSS field centred on RXCJ 0014.3-3022. Each differently coloured set of four boxes represents one pointing, with the VIMOS quadrants aligned on the E-W direction.

below the luminosity function's characteristic magnitude  $I^*$ . Exposure times were chosen to provide S/N ratios of at least 10 for bright objects and 5 for faint ones: this converts to 6 minute exposures for bright objects masks and 82 minute exposures for faint ones. In total, each cluster was thus covered by six masks (three for bright objects and three for faint ones).

Slits were defined for the LR-Blue grism, which provides spectral coverage of (observed frame) 370-670 nm region with a spectral resolution of about 200 for  $1''$  slits. At the cluster redshift, it samples the region from 283 to 513 nm, thus allowing important spectral features like the [OII], [OIII],  $H_\beta$ ,  $H_\gamma$  and  $H_\delta$  emission lines, the  $\text{CaII}_{H+K}$  absorption lines and 4000 Å break to be detected. All these spectral fea-

### 3 Evolution of the star formation activity across massive galaxy clusters

---

tures provide powerful tools to evaluate the redshift of the targets up to redshifts of about 0.8. Furthermore, the multiplexing capability of the LR-Blue grism enables to stack up to 4 spectra along the spectral dispersion direction; thus, it is possible to collect up to 150-200 spectra per mask, depending on the brightness and position of the targets. The slits were designed using a width of  $1''$  and a sky region of  $3''$  to provide a suitable sky subtraction, while completely covering the observed object.

These data were reduced mainly using the dedicated software VIPGI <sup>2</sup>. VIPGI is a complete data reduction environment specifically developed to handle and reduce imaging, spectroscopic and IFU data collected with VIMOS. Its capabilities and quality have been tested against the reduction of many tens of thousands spectra from the VVDS and are thoroughly explained in the aforementioned publications. In addition to bias and flatfield correction, multiplex spectra identification, sky subtraction, spectral reduction and wavelength calibration, VIPGI is also capable of data editing and redshift evaluation based on single- and multiple-line fitting by manually selecting candidate lines to be matched with available line catalogues.

Data reduction has been performed using the standard approach, as described in the VIPGI manual and in Scodreggio et al. (2005). Adjustment of first guesses for wavelength calibration was usually fairly quick: after checking the line catalogue, which was always found in good agreement with the observed spectra, a small shift of 1 to 3 pixels (i.e. about 4 to 15  $\text{\AA}$  at the resolution of the LR-Blue grism) was enough to correct the first guess. None of the quadrants was found to be tilted or rotated. The complete adjustment of the calibration arcs was usually performed with a small shift of less than 5 pixels (i.e. about 20  $\text{\AA}$ ) on the dispersion direction. A master bias frame was obtained, where possible, by combining all the available biases from the night; rejection of overscan areas and/or bad pixels was done by standard  $3\text{-}\sigma$  clipping through the data cube defined by the biases. Spectra detection, based on the adjusted arc calibration, was also run using standard recipe parameters. Wavelength calibration, after manual correction of shifted lines slit by slit, shows typical dispersion RMS of order 1.5  $\text{\AA}$ .

As the spectroscopic observing blocks (OBs hereafter) were defined as jittered observations, three frames per mask were collected; thus, a combined reduction is performed with the *Reduce Sequence of Observations* tool of VIPGI. This avoids confusion with noise and residuals from bias removal and flat-field correction and enables detection of fainter than expected objects. The minimum object detection level is set to  $3\sigma$  for bright and faint objects alike; sky subtraction was based on a fit with a 3rd-order polynomial over each single frame instead of using a simple median over the stacked frame group. This was found to give a better estimation of the sky

---

<sup>2</sup>VIPGI (VIMOS Interactive Pipeline and Graphical Interface) (Scodreggio et al.(2005)) is developed by the VIRMOS Consortium to handle the reduction of the VIMOS data for the VVDS (VIMOS VLT Deep Survey, Le Fèvre et al. (2005))

## 3.2 Data description and reduction procedures

---

and to provide a more solid spectral detection: with a median-based sky subtraction, up to 15% of the objects can be lost in case of faint object masks. Also, no *ABBA* (i.e. mutual subtraction of frames to extract the fringing pattern) combination method was used, as no fringing affects this grism. Spectra were then extracted using Horne's algorithm (Horne (1986)). Standard parameters for object detection and deblending (i.e. disentangling of multiple spectra falling in the same slit) were used, as they were found to provide a robust extraction.

After data reduction, all the spectra were checked by eye to look for residual sky contamination or hot pixels lying directly on top of the spectra, presence of ghosts arising from the superposition of different spectral orders and other artifacts, and to check whether all the objects had been successfully extracted. Typical continuum S/N ratios of 4 or more and high significance ( $S/N \gg 10$ ) spectral features enable a clear determination of spectral types and provide an unambiguous way to determine redshifts.

These were mainly determined via internal VIPGI algorithms (both the EZ<sup>3</sup> package and manual detection and fit of spectral features). After a blind run over all the spectra, redshifts were checked one by one, correcting wrong determinations where necessary (this can arise from identification of residual sky lines with galaxy emission lines, mainly the [OII] line at  $\lambda = 3727\text{\AA}$ ). Non-detections (i.e. signals too faint to extract a reliable spectrum, their typical mean S/N ratios being lower than 3) were flagged for removal and were only used to evaluate the mean spectral noise, which amounts to about 20 counts per pixel. The blue region ( $\lambda < 5000\text{\AA}$ ) of the spectrum is found to be slightly noisier than the red region. For comparison, the faintest reliably detected spectra have continuum fluxes from 100 to 500 counts/pixel depending on spectral type, and the presence of spectral features with high S/N ratios.

### 3.2.2 Photometric data

Optical photometry was carried out using the wide-field imager (WFI) mounted at the Cassegrain focus of ESO/MPG-2.2m telescope at La Silla, Chile. WFI is a focal reducer-type mosaic camera which consists of  $4 \times 2$  CCD chips with  $2048 \times 4096$  pixels with a scale of  $0''.238/\text{pixel}$ , giving a FOV of  $8'.12 \times 16'.25$  for each chip. The chips are separated by gaps of  $23''.8$  and  $14''.3$  along the RA and Dec directions, respectively. Hence the full FOV of WFI is  $34' \times 33'$  with a filling factor of 95.9%.

The data presented in this paper were obtained as part of a programme carried out in visitor and service modes (P.I.: H. Böhringer) during MPG observing time. In particular, observations of RXCJ 0014.3-3022 and RXCJ 2308.3-0211 were performed in the B, V, and R passbands in photometric conditions from September 27, 2000 through September 30, 2000. They were split into OBs defining a sequence of eight

---

<sup>3</sup><http://cosmos.iasf-milano.inaf.it/pandora/>

### 3 Evolution of the star formation activity across massive galaxy clusters

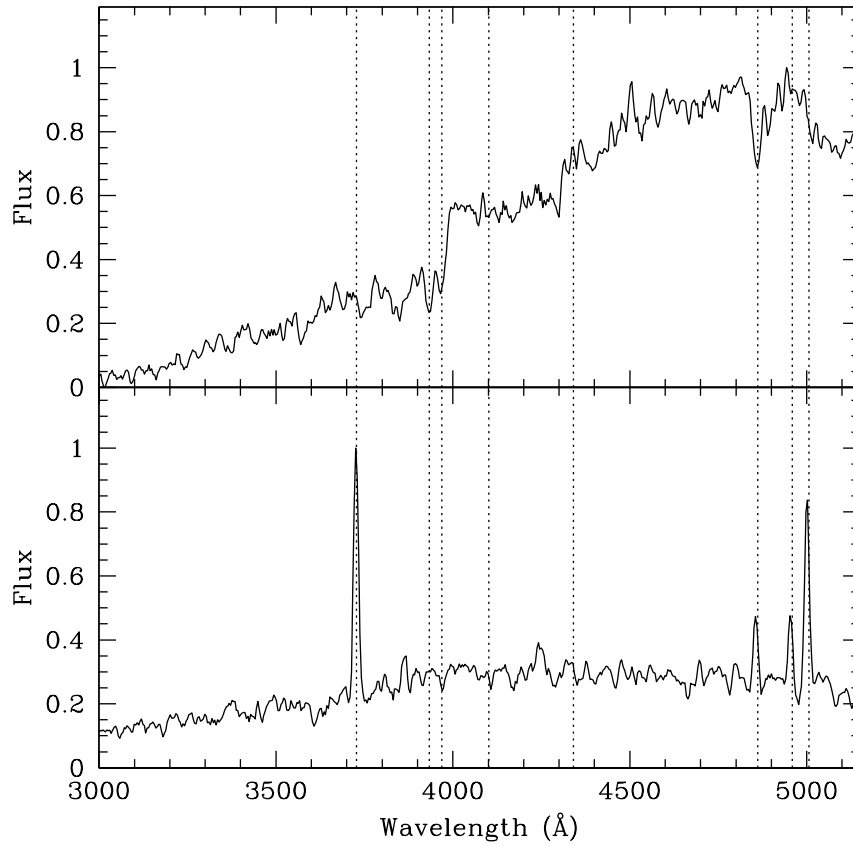


**Figure 3.2:** Examples of rest-frame spectra from two cluster members of RXCJ2308.3-0211, with spectral features marked. Top panel: a typical spectrum for an elliptical galaxy. The absorption features of  $\text{CaII}_{H+K}$  at 3933.7 and 3968.5  $\text{\AA}$  are clearly visible, as well as the absorption from  $\text{H}_\beta$  at 4861.3  $\text{\AA}$ . Bottom panel: spectrum of an emission line galaxy with evident emission from  $[\text{OII}]$  at 3727.5  $\text{\AA}$ ,  $\text{H}_\beta$  and the double emission line due to  $[\text{OIII}]$  at 4958.9 and 5006.8  $\text{\AA}$ , suggesting an amount of nuclear activity. Both spectra are scaled to their maximum value for ease of comparison.

dithered sub-exposures. Total exposure times are listed in Table 1. Filter curves can be found in Arnouts et al. ((2001)) and on the web page of the la Silla Science Operations Team<sup>4</sup>.

Standard star observations were executed in all the four nights of science obser-

<sup>4</sup><http://www.la.silla.eso.org/lasilla/sciops/2p2/E2p2M/WFI/filters>

### 3.2 Data description and reduction procedures

---

vations. They consist of a total of 16 standard star OBs per filter, targeting three Landolt fields (Landolt (1992)).

The WFI data were reduced using the data reduction system developed for the ESO Imaging Survey (EIS, Renzini & da Costa (1997)) and its associated EIS/MVM image processing library version 1.0.1 (*Alambic*, Vandame 2004). *Alambic* is a publicly available<sup>5</sup> software designed to automatically transform raw images from single/multi-chip optical/infrared cameras into reduced images for scientific use. In addition to the standard bias-subtraction, flatfield correction and trimming, the EIS/MVM image processing pipeline performs background estimation, de-fringing (if needed), astrometric calibration, minimization of chip-to-chip variations in sensitivity, and detection/masking of satellite tracks. All these steps are described in detail in previous publications (Arnouts et al. (2001); Vandame (2004); Mignano et al. (2007); Pierini et al. (2008)) and, thus, are skipped here. However, we note that the astrometric calibration was derived using the GSC2.2 reference catalogue and a distortion model described by a second order polynomial. Its precision is 0.2 arcsec but the internal accuracy is about 70 mas (see Mignano et al. (2007)).

Magnitudes were calibrated to the Johnson-Cousins system using Landolt ((1992)) standard stars whose magnitudes were obtained using a 10 arcsec-wide circular aperture, which proved to be adequate by monitoring the growth curve of all the measured stars. Photometric standards were observed over a rather broad range of airmasses. Science frames of several science targets were taken at the best airmass, whereas the photometric solutions used to calibrate reduced images were obtained from merging all the measurements of standard stars for each passband. The number of non-saturated Landolt stars per field did not allow independent solutions to be determined for each of the eight chips of WFI. Hence calibration had to rely on solutions based on measurements taken across all chips.

Despite the fact that the EIS data reduction system includes a photometric pipeline for the automatic determination of photometric solutions, these were determined interactively using the *IRAF*<sup>6</sup> task *fitparams*. This choice allows interactive rejection of individual measurements, stars, and chips. Photometric solutions with minimum scatter were obtained through a two-parameter linear fit to about 200 photometric points per passband, the extinction coefficient being set equal to that listed in the “definitive” solution obtained by the 2p2 Telescope Team<sup>7</sup>. In general, zeropoints and colour terms are consistent with those obtained by the 2p2 Telescope Team or

---

<sup>5</sup>at [http://www.eso.org/science/eis/survey\\_release.html](http://www.eso.org/science/eis/survey_release.html)

<sup>6</sup>*IRAF* is the Image Reduction and Analysis Facility, a general purpose software system for the reduction and analysis of astronomical data. IRAF is written and supported by the IRAF programming group at the National Optical Astronomy Observatories (NOAO) in Tucson, Arizona. NOAO is operated by the Association of Universities for Research in Astronomy (AURA), Inc. under cooperative agreement with the National Science Foundation.

<sup>7</sup>available at <http://www.ls.eso.org/lasilla/Telescopes/2p2T/E2p2M/WFI/zeropoints/>

### 3 Evolution of the star formation activity across massive galaxy clusters

**Table 3.1:** The photometric solutions available in this work. The table lists: in Col. 1 the passband; in Cols. 2 – 4 the zeropoint in the Vega magnitude system ( $ZP$ ), the extinction coefficient ( $k$ ), and the colour term ( $CT$ ) together with their errors. These “best fit” parameters were obtained from a two-parameter fit to about 200 measurements across the WFI field for each passband, the extinction coefficient being fixed.

Passband	$ZP$	$k$	$CT$
$B$	$24.66 \pm 0.005$	0.22	$0.26 \pm 0.007$
$V$	$24.23 \pm 0.006$	0.11	$-0.15 \pm 0.012$
$R$	$24.50 \pm 0.007$	0.07	$-0.02 \pm 0.015$

**Table 3.2:** The “definitive” photometric solutions obtained by the 2p2 Telescope Team from observations of standard stars in perfectly photometric nights, where a bunch of standard fields were moved around each chip of WFI. All parameters were fitted simultaneously as free parameters, with good airmass and colour range, and around 300 stars per fit. The table below gives the average solutions over all chips.

Passband	$ZP$	$k$	$CT$
$B$	$24.81 \pm 0.05$	$0.22 \pm 0.015$	$0.25 \pm 0.01$
$V$	$24.15 \pm 0.04$	$0.11 \pm 0.01$	$-0.13 \pm 0.01$
$R$	$24.47 \pm 0.04$	$0.07 \pm 0.01$	$0.00 \pm 0.00$

by the ESO DEEP Public Survey (DPS) team (Mignano et al. (2007)), as shown by the comparison between Tables 2, 3, and 4.

Finally, we emphasize that the CCD-to-CCD gain variations were corrected with *Alambic* using median background values sampled in sub-regions bordering adjacent CCDs, but no illumination correction was applied. This may lead to relative zeropoint offsets from the centre to the borders of the image of up to 10%, according to the

**Table 3.3:** The table below gives median values for all the photometric solutions based on three-parameter fits obtained by the ESO DPS team.

Passband	$ZP$	$k$	$CT$
$B$	24.58	0.22	0.24
$V$	24.23	0.19	-0.04
$R$	24.49	0.08	-0.01

## 3.2 Data description and reduction procedures

---

*still experimental* method to derive a zeropoint correction map designed by Selman ((2004)).

Source detection and photometry are based on SExtractor (Bertin & Arnouts (1996)). A common configuration file was used for each of the three band catalogues with a minimum number of adjustments to be made for individual images. For each image the appropriate values for the seeing and magnitude zeropoints as well as the weight-map associated with each image, produced by *Alambic*, are used. The BVR images were matched to the worst seeing using the *IRAF* task *psfmatch* for each target. Other parameters are the same for all catalogues. The deepest R-band image was used as the detection image, where sources are defined by an area with a minimum number of 5 pixels above a threshold of  $1\sigma$  of the background counts. Source photometry was extracted in fixed circular apertures (from  $1''.2$  to  $10''$  in diameter) or in a flexible (Kron-like, Kron (1980)) elliptical aperture with a Kron-factor of 2.5 and a minimum radius of 3.5 pixels. Kron-like magnitudes are used hereafter in the analysis. Background values were taken directly from the background map, which was obtained from a bi-cubic-spline interpolation over all the sub-areas with a size of 64 pixels (i.e.  $15''.2$ ) after median-filtering over  $5\times 5$  meshes. The object magnitudes were corrected for galactic extinction<sup>8</sup> according to the Schlegel et al. ((1998)) Galactic reddening maps (from *NED*) and converted to the AB system according to the response function of the optical system (see Alcalá et al. (2004)). Finally, we note that the output catalogues contain a large number of spurious objects but they are pruned for fake sources by hand before the photometric redshifts are determined.

The depth and quality of these catalogues was assessed by the comparison of the galaxy number counts in the field with those in the literature (REF.NEED!) as well as by the comparison of the stellar number counts with those expected from the model of stellar population synthesis of the Galaxy by Robin et al. ((2003)).

### 3.2.3 UV data

To complement our data set with information on the UV emission of observed galaxies, the GALEX data archive was scanned via the MultiMission Archive at Space Telescope Science Institute (MAST<sup>9</sup>). Data for the regions of both clusters were extracted from the All Sky Imaging Survey (GR3 data release); only magnitude information was collected.

When multiple detection of the same object from overlapping pointings were available, the object magnitude was calculated as the weighted mean over multiple detections. Cross-identification of GALEX sources with objects in our fields was largely unambiguous. Where multiple objects were present within the radius of the GALEX

---

<sup>8</sup>At present, this correction is applied to the magnitudes of all objects, including stars.

<sup>9</sup><http://galex.stsci.edu>

### 3 Evolution of the star formation activity across massive galaxy clusters

---

PSF, the bluest object from our catalogue (i.e., with smaller (B-R) colour) was identified as the UV source.

#### 3.2.4 X-ray data

RXCJ 0014-3023 was observed with *XMM-Newton* in AO-1 as part of the REFLEX-DXL cluster sample (see Zhang et al. (2006) for a detailed description of the full data reduction). The cluster was observed with thin filter for the three EPIC detectors; MOS data were collected in Full Frame (FF) mode, while *pn* data were taken in Extended Full Frame (EFF). The total exposure time for RXCJ0014-3023 was of 18.3 ks.

### 3.3 Photometric catalogues

For each cluster, both spectroscopic and photometric catalogues were built; their cross-correlation provided a spectro-photometric sample.

Preparation of photometric catalogues was trained on RXCJ0014.3-3023, a cluster already investigated (see BPB07). The initial photometric catalogue for this cluster, already cleaned and pruned for stellar objects and spurious detections, contains 23900 objects with *R*-band magnitudes between 14 and 27. Many objects are beyond the completeness limit set by the exposure times used; these faint objects tend to have large errors in their magnitude and colour determinations.

Completeness magnitude was assessed by comparison with deep fields (see McCracken et al. (2003)). It was defined as the magnitude at which the observed counts reach 50% of the expected numbers. To evaluate the influence of the cluster galaxy population in each observed field, we compared the number counts both on the full field and in a low density region, assumed relatively clean of cluster galaxies (see Sect. 3.5.1 for an extended discussion). As Fig. 3.3 shows, results for both samples show consistent results, with the limiting magnitude being set around  $R = 23.5$  for both clusters. The influence of cluster galaxies is assumed to be negligible at this magnitude, where field galaxies dominate the counts. Conversely, the presence of the cluster can account for the discrepancy found at bright magnitudes ( $R < 22$ ), where the cluster galaxy population is predominant. To ensure a safe determination of photometric redshifts, we also checked magnitude errors corresponding to this limit. For magnitudes brighter than  $R = 23.5$ , the colour error is almost always below 0.2 mags, the typical error being of order  $\Delta(B - R) = 0.05$  mag. As can be seen from the error distribution in RXCJ0014.3-3022 shown in Fig. 3.4, only 248 objects (i.e., 0.02% of the selected sample) have  $(B - R)$  errors greater than 0.2 mag, and these are associated with objects at the faint end of our sample ( $R > 21.4$ , with a mean  $R = 23.05$ ).



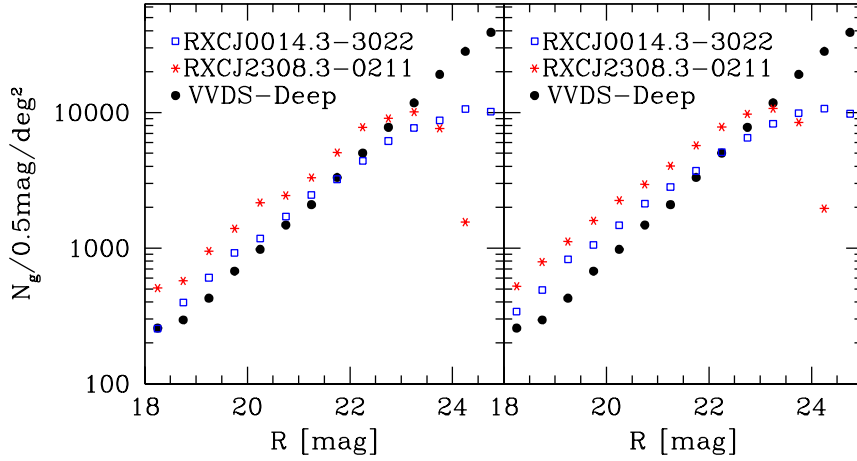


**Figure 3.3:** Normalized number counts for both clusters, compared with the VVDS-Deep derived counts of McCracken et al. 2003. Left panel shows number counts in a low density region of each cluster. Right panel shows the number counts for the full field of view for each cluster.

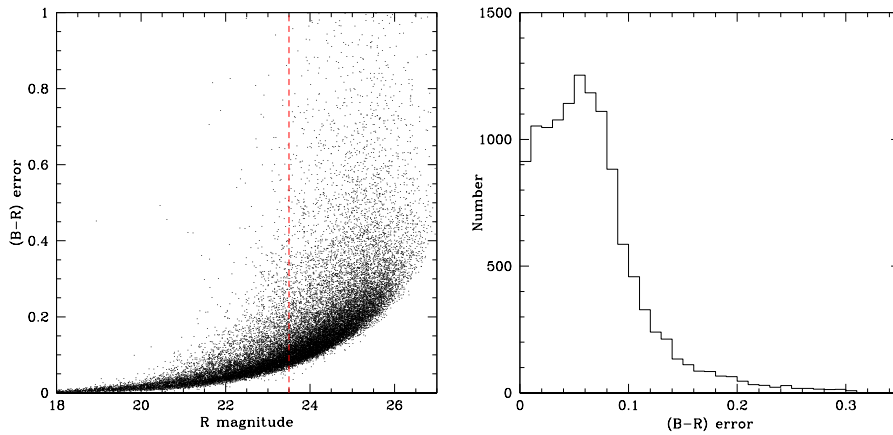


**Figure 3.4:** Left: distribution of colour ( $B - R$ ) errors vs.  $R$  magnitude for RXCJ0014.3-3022. The vertical dashed line marks the chosen selection limit. Right: distribution of errors for objects with  $R \leq 23.5$ ; as can be seen from the plot, almost all of them lie below 0.2 mag, with the typical error of order 0.05 mag.

### 3 Evolution of the star formation activity across massive galaxy clusters

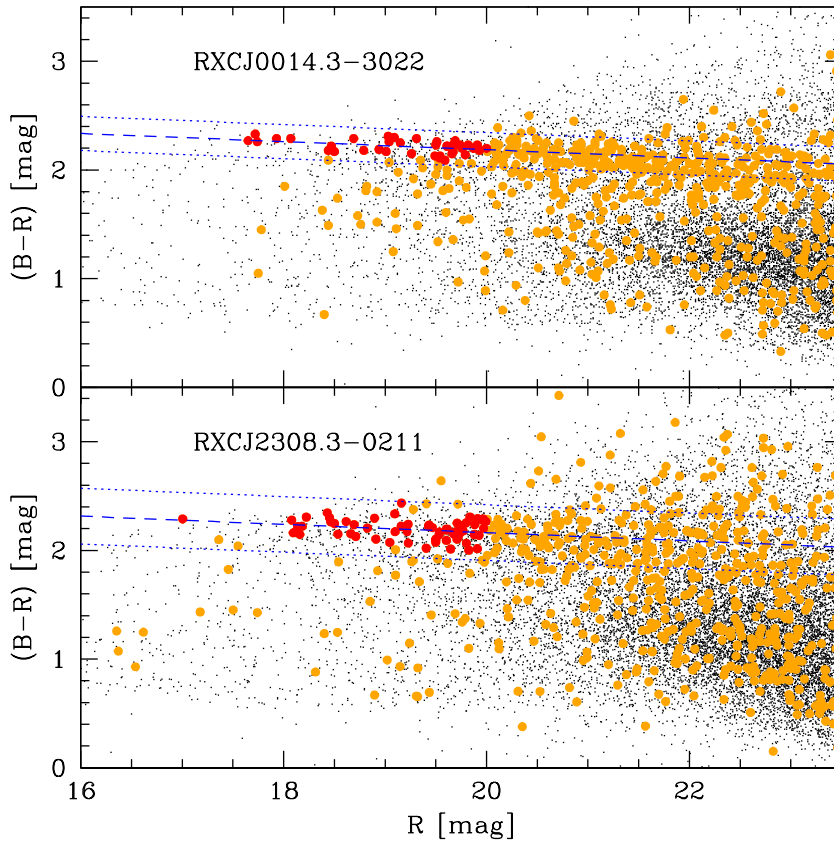
---

Fig. 3.3 shows a different decrease in number counts for the two clusters at faint magnitudes. This must be ascribed to a combination of seeing and galactic absorption. In fact, RXCJ0014.3-3022 was observed with a relatively good seeing of  $\sim 0.9''$  and lies in a sky region far from the Galactic Plane, thus detection of very faint objects was more likely thanks to smaller absorption and better resolution. On the other hand, RXCJ2308.3-0211 lies near to the Galaxy and was observed with a seeing of about  $1.2''$ , thus detection of very faint object is intrinsically more difficult in this case and counts drop consequently faster. For magnitude brighter than the completeness limit, detection is not heavily affected by these effects. The two magnitude-limited catalogues show in fact comparable numbers: 14409 objects for RXCJ0014.3-3022, 14820 for RXCJ2308.3-0211. To statistically confirm this, we compared the two distributions over the full field of view with a Kolmogorov-Smirnov test, resulting in a robust agreement between the two distributions (the rejection probability being 7.1%).

The operational catalogues were used to build the colour-magnitude diagrams down to the limiting magnitude already discussed. The CM diagrams clearly display in both cases the clusters red sequence, with on average, comparable (B-R) colours of about 2.2 mag (observed frame). The red sequence was fitted in both cases using a recursive  $3\text{-}\sigma$  clipping linear regression algorithm. Starting from all objects with  $17 \leq R \leq 20$  and within a distance of  $3'$  from the nominal centre (i.e., the X-ray coordinates of the centroid) of each cluster, the selected objects were fitted via linear regression and any object lying more than  $3\sigma$  away from the fit was rejected at each iteration. The algorithm converged in both cases, providing two very similar equations for the red sequence fit (see the following subsections).

Two subcatalogues were then extracted on the basis of the relative colour with respect to the red sequence. Specifically, objects are flagged as red if they lie within  $3\sigma$  of the red sequence, or as blue if their (B-R) colour value is lower than this limit (i.e. more than  $3\sigma$  away). This selection is based on the observation that at the clusters' redshifts the B and R bands sample, respectively, the rest-frame  $[3022\text{-}3940] \text{ \AA}$  and  $[4247,6045] \text{ \AA}$  spectral regions, where important galactic spectral features lie ([OII] being the most prominent emission line in the B band). Moreover, the two filters bracket the  $4000\text{ \AA}$  break, thus mapping its position and assessing unambiguously whether an object lies on the red sequence. Thus, comparison of the (B-R) colour for cluster galaxies offers strong constraints on their star-formation regime. Fig. 3.5 shows the distribution of galaxies for the regions of the two clusters in the (B-R) vs. R space, from  $R=17$  (the magnitude of the clusters BCG) to our operational limit. The fit to the red-sequence is shown, and both the cluster red sequence and the field "blue cloud" can be easily seen in both cases.

Photometric redshifts were calibrated against available spectra and determined using the well-tested *HyperZ* code by Bolzonella et al. ((2000)). As already extensively discussed in BPB07, the filter choice allows to achieve a relatively good precision on



**Figure 3.5:** Observed colour-magnitude diagram for the regions centred on RXCJ0014-3023 (upper panel) and RXCJ2308.3-0211 (lower panel). Orange points mark the position in the  $(B-R)$  vs.  $R$  plane of the galaxies within  $3'$  from the cluster X-ray centre: most of these points lie as expected along the cluster red-sequence. Red circles mark the galaxies chosen for the fit; the red sequence fit is shown in dashed blue lines with the fit  $3\text{-}\sigma$  scatter.

the photometric redshift determination, despite the fact that only three filters are used.

The separation between blue and red galaxies provided guidance in selecting the best-fitting templates while minimizing the danger of wrong identification (i.e., wrong spectral type). Specifically, while red galaxies were only fitted with passively-evolving templates (E and S0 types), blue objects were fitted with spiral and irregular templates. To assure the correctness of this method, we also determined the photometric redshift without any constraints on the spectral template, finding an overall

### 3 Evolution of the star formation activity across massive galaxy clusters

---

agreement between the results of the two methods. Default synthetic non-evolving templates for E, S0, Sa, Sb, Sc, Sd and Im galaxies were found to give the best results.

#### 3.3.1 RXCJ0014.3-3022

The red sequence was fitted on 41 objects selected with a recursive algorithm; the fit equation is:

$$(B - R) = (2.935 \pm 0.238) - (0.037 \pm 0.003) \times R \pm 0.052$$

where the errors on each parameter, as well as the scatter of the fit, are also shown. The color-magnitude diagram does not show a clear, single BCG or cD galaxy dominating over other red sequence galaxies: a tight bunch of 5 galaxies populates the red sequence between  $R = 17.5$  and  $R = 18$ , four of which form two visible pairs of BCGs associated with the two X-ray subcomponents of this cluster (see Pierini et al. (2008)). These are correctly identified with the brightest galaxies lying in the central part of the cluster.

Based on our training, cluster photometric members were then selected as those with photometric redshift between 0.28 and 0.4, i.e., within 0.06 (our dispersion value at the cluster redshift) from the mean  $z_{phot} = 0.34$ .

The final photometric cluster catalogue comprises 3698 objects, 1409 of which are red and 2289 are blue objects.

We note that the cluster exhibits a mean photometric redshift slightly higher than the spectroscopic one. Although the two values are consistent within the photometric redshift error, it is important to understand why this discrepancy arises.

We find that the large scatter is mainly due to blue galaxies, whose photometric redshifts are on average higher and exhibit a larger scatter. We already evaluated contamination from outliers (especially background objects with correct photo- $z$ ) to be rather low (below 10%, cfr. BPB07). Thus, contamination is not heavily affecting our results, nor the globally correct identification of cluster members.

On the other hand, large peculiar velocities are found in this cluster, up to order 4000 km/s; although this is usually a small effect, this can still produce a difference in redshift of order 0.02. At the cluster redshift of 0.3068, the [OII] emission line falls in the B band, just bluewards of the border with the V filter; thus, a difference in peculiar velocity can push the line across the boundary and in the V band. As a consequence, the photometric redshift of cluster star-forming galaxies with high peculiar velocities will be higher and this, combined with the intrinsic scatter, can provide redshifts up to 0.4. For passively evolving cluster members, the 4000 Å break is correctly sampled, as it falls right in the middle of the V band and in fact the agreement between photometric and spectroscopic redshifts for red cluster members is proven to be quite good.

### 3.3.2 RXCJ2308.3-0211

The red sequence was based on 64 robustly selected objects; the corresponding fit is given by the equation:

$$(B - R) = (2.933 \pm 0.323) - (0.038 \pm 0.003) \times R \pm 0.085$$

The fit shows a strong similarity with the other cluster, although with a slightly larger scatter; this can be ascribed to the red sequence being more populated in this cluster.

The cluster single BCG is clearly visible and separated by other red sequence galaxies by a full magnitude; this is what can be expected from an evolved, relatively undisturbed cluster. The catalogue was pruned of some galaxies lying around bright stars, that were masked to avoid wrong photometry due to the stars glare.

Photometric cluster members for this cluster were selected as having photometric redshift between 0.23 and 0.35 in photo-z; the mean cluster redshift is found to be 0.29, again with a typical error of 0.06. The different redshift range can be explained considering the position of typical spectral features. As this cluster has a slightly lower redshift of 0.2966, it is likely that, even accounting for the scatter due to peculiar velocities, the [OII] line stays in the B band for all cluster members. The consequence is thus a more precise determination of photometric redshift for blue objects, as the emission line is encompassed by the B band unambiguously. Hence the mean cluster redshift is correctly recovered for both blue and red galaxies in RXCJ2308.3-0211.

The final catalogue has a total of 4109 cluster members, 2361 of which are flagged as red and 1748 as blue galaxies.

## 3.4 Spectroscopic catalogues

### 3.4.1 Cluster membership

Cluster members were identified from the available spectroscopic catalogue starting from a relatively broad interval, centred on the mean cluster redshift and with a width of 0.05. This is a fairly large value, corresponding to a velocity interval of about 10000 km/s in the cluster reference frame, but it to avoids the loss of high-speed cluster members. At the same time, this redshift range still enables unambiguous rejection of any other structure on the foreground or background.

Cluster membership was checked from this starting catalogue using the biweight estimators introduced in Beers et al. ((1990)) and applied successfully in many different studies (see for instance Biviano et al. (1992); Girardi et al. (1993); Adami et al. (1998a); Girardi et al. (1998); Biviano et al. (2006)). Peculiar velocities were calculated applying the usual correction for velocity errors and relativistic correction

### 3 Evolution of the star formation activity across massive galaxy clusters

---

(Danese, De Zotti & di Tullio (1980)), rejecting afterwards all objects with peculiar velocities larger than  $\pm 4000$  km/s. The algorithm of Den Hartog & Katgert ((1996), (2004)) was then applied for removal of interlopers, by sampling the position of candidate cluster members in the projected phase space (peculiar velocity vs. radial distance). The cluster X-ray centroid was used as reference in these calculations. For a more extended discussion on this method, see Biviano et al. ((2006)) and Braglia et al. 2008b (in prep.).

The spectroscopic catalogue is then cross-correlated with the photometric one to re-identify galaxies and associate colours and spectral information. Cross-correlation was based on matching spectroscopic targets and photometric objects coordinates; as the two exposures have almost the same seeing ( $\sim 1''$ ), no correction was taken into account for this. The resulting spectro-photometric catalogue confirms that all our detected spectroscopic targets have R-band magnitudes brighter than 23.5, as already estimated from the instrument ETCs.

#### 3.4.2 RXCJ0014.3-3023

The initial reduced spectroscopic catalogue comprises objects sampled with a total of 545 slits over the full area of observation. 147 slits contained more than one object (up to 5), for a total of 872 detections. 262 detections were found to be too faint for a reliable spectrum to be extracted and were flagged as non-detections, while 64 ended up being serendipitous faint stars.

Of the 546 detected objects, 43 were found to be repeatedly observed galaxies; these were useful in calculating redshift and velocity errors. A mean velocity error of  $294 \pm 50$  km/s is estimated, in good agreement with the VVDS value of 276 km/s using the same VIMOS instrumental setup. The distribution of redshift errors is plotted in fig. 3.6.

The final spectroscopic catalogue comprises 512 detected non-stellar objects, covering the I-magnitude range from 19 to about 22.5 out to a redshift of  $0.85^{10}$ .

To expand our spectroscopic catalogue, we checked publicly available spectroscopic redshifts from *NED*, finding a total of 101 additional objects around the cluster redshift. These objects are mainly brighter than  $R = 22.0$ , as assessed after cross-correlation of these additional data with the WFI photometric catalogue; still, some objects have R magnitudes fainter than this value (see Fig. 3.7). We also found 24 already observed objects in the redshift interval [0.06, 0.35]. They allowed us to assess the external error of our redshifts, which is on average  $276$  km/s  $\pm$   $55$  km/s, consistent with our internal error.

The resulting cluster member catalogue comprises 190 different objects. The colour-magnitude diagram for this sample reassuringly shows the red-sequence of

---

<sup>10</sup>Three additional high-redshift quasars were detected at  $z = 1.02$ ,  $z = 2.51$  and  $z = 3.08$ .

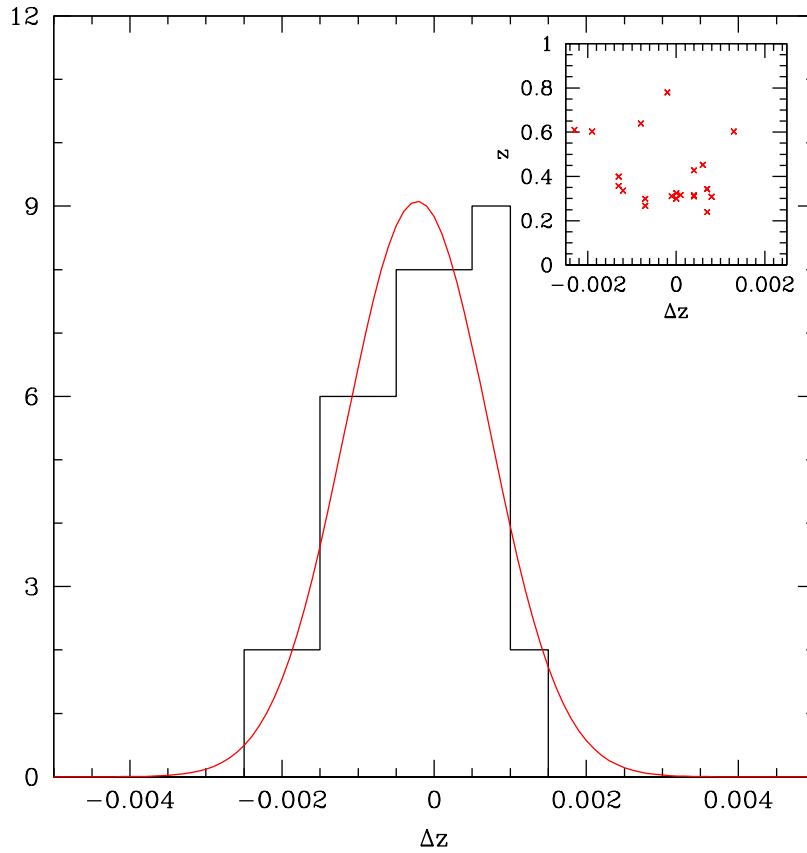


**Figure 3.6:** Distribution of redshift errors for multiply-observed galaxies in the field of RXCJ0014.3-3022. The distribution and its gaussian fit are shown in the main plot. The upper right inset shows the redshift errors (in abscissae) plotted against redshift, showing no clear correlation of errors with redshift. Most of the multiple detections come from the cluster’s redshift slice around  $z=0.3$ .

the cluster; we fit it using the same selection criteria and algorithm as for the photometric catalogue ( $17 \leq R \leq 20$  within  $3'$  from the X-ray centre), obtaining the best fit as:

$$(B - R) = (3.023 \pm 0.277) - (0.042 \pm 0.004) \times R \pm 0.049$$

As figure 3.7 shows, the spectroscopic members fits are almost identical to the photometric one and, although the former one shows a slightly lower constant term, they coincide within the errors.

### 3 Evolution of the star formation activity across massive galaxy clusters

---

Intriguingly, some very blue objects ( $B-R \leq 1$ ) can be detected even within the central 3 arcminutes, which correspond to about 800 kpc at the cluster redshift. This suggests the presence of enhanced star-formation activity in the cluster, as already shown in BPB07 (see also Couch et al. (1998)). It must however be noted that, in principle, the presence of part of these galaxies could also be due to phase-space projection of background or foreground field galaxies in the cluster position.

#### 3.4.3 RXCJ2308.3-0211

A larger number of objects were covered with slits in this cluster. The starting catalogue comprises a total of 1122 slits, 424 of which proved to be multiple detections for a total number of 1522 collected spectra. A total of 446 detections were too faint to properly evaluate a redshift, while 64 were identified as faint stars. In the end, 1012 identified galaxy spectra were collected in the redshift range  $[0, 0.85]^{11}$ , 104 of which were found to be multiple observations. The intrinsic redshift error was again calculated from the multiple observations and was found to be  $254 \pm 49$  km/s, in good agreement with both VVDS and our previous determination.

The final spectroscopic catalogue for RXCJ2308.3-0211 holds 902 identified VIMOS spectra. No public redshift data were found to complement our sample. The final cluster catalogue comprises 269 cluster members.

The fit of the cluster red sequence results in the equation:

$$(B - R) = (3.026 \pm 0.748) - (0.043 \pm 0.013) \times R \pm 0.114$$

As shown in Fig. 3.7, the fits to the two red sequences are practically identical, although, as in the case of the fit of photometric data, the scatter is larger for RXCJ2308.3-0211. The spectrum from the BCG is not present in the plot, as this galaxy was not covered by a slit during target selection. Interestingly, the same kind of blue galaxies detected in RXCJ0014.3-3022 is not seen here, which suggests an intrinsic lower star formation activity in RXCJ2308.3-0211.

In both clusters, the fit to the spectroscopic members is well in agreement with the fit from photometric members. Hereafter, the photometric fit to the red sequence will always be used, as this is based on larger statistics.

The spectroscopic members catalogues for the two clusters are provided in Appendices B and C, complete with photometric information from WFI imaging and spectral indices (see Section 3.5.2).

---

<sup>11</sup>Plus six high-redshift quasars at redshifts of 1.09, 1.32, 2.01, 2.04, 2.14 and 3.16.



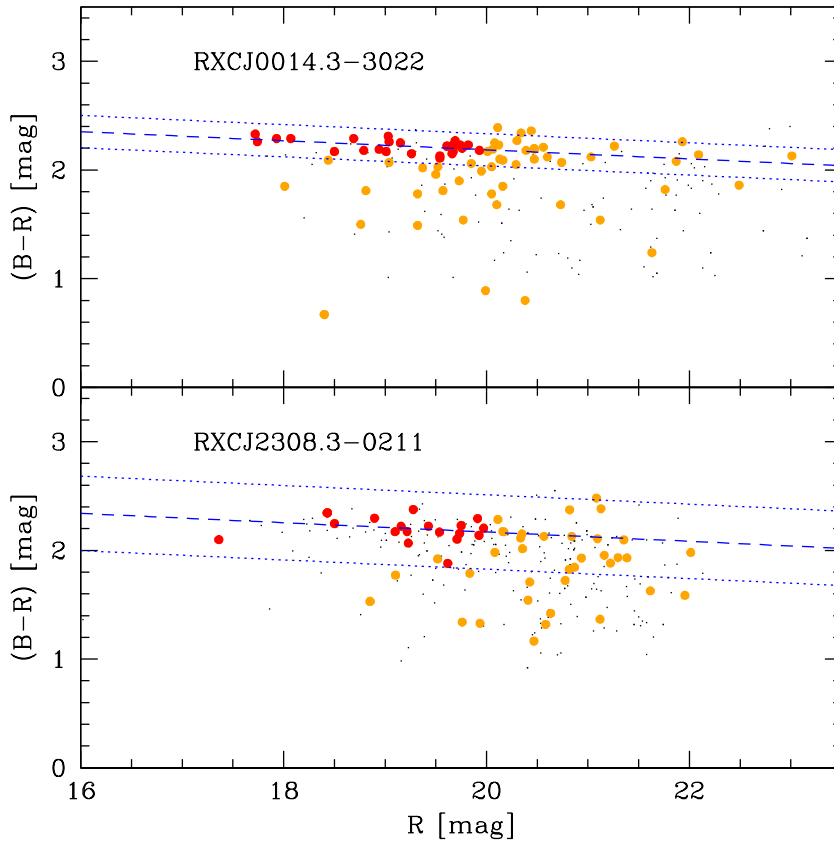


**Figure 3.7:** colour-magnitude diagram for the spectroscopic members of both clusters. Orange points mark the objects selected within 3 arcminutes for the fit to the red sequence, while red points mark the objects actually used for the fit. The dashed line shows the fit to the red-sequence, with the fit dispersion shown by the dotted lines; the photometric fit is not shown, as it almost perfectly superposes to the spectroscopic determination, although with somewhat smaller scatter.

## 3.5 Results

### 3.5.1 Cluster morphology

To obtain a global picture of the clusters, surface density maps were derived to look for evidence of substructure and large-scale structures. The algorithm used to derive density maps is extensively described in Appendix A.

For each cluster, member galaxy density maps were calculated independently for

### 3 Evolution of the star formation activity across massive galaxy clusters

catalogue	N. objects	Mean BG	RMS
RXCJ0014.3-3022 (all)	3698	32.37	10.31
RXCJ0014.3-3022 (red)	1409	9.70	4.28
RXCJ0014.3-3022 (blue)	2289	21.91	6.90
RXCJ0014.3-3022 (spec.)	190	1.90	3.03
RXCJ2308-0211 (all)	4109	44.72	14.74
RXCJ2308-0211 (red)	2361	23.26	9.52
RXCJ2308-0211 (blue)	1748	20.10	7.52
RXCJ2308-0211 (spec.)	269	1.18	5.01

**Table 3.4:** Background evaluation results for the different subcatalogues of cluster members, for both clusters. Values are always given in units of number of galaxies per square Mpc.

the full catalogue and for the red and blue subcatalogues; in all three cases, the same smoothing scale for background calculation and final spike cleaning is used, with a gaussian kernel of  $100''$ . The maps were always extracted with the same resolution (mesh width of  $10''$ ) to directly compare results. Density maps were also calculated for the spectroscopic catalogues, although these cover only a fraction of the field observed with WFI. Since less objects are available from the spectroscopic catalogues, the mesh width and smoothing scale have been increased to  $20''$  and  $250''$ , respectively, to ensure convergence and to avoid occurrence of spikes due to undersampling. Table 3.5.1 gives results for background calculation for all catalogues used. Hereafter, the background r.m.s. is used as standard unit to estimate overdensities.

#### 3.5.1.1 RXCJ0014.3-3022

As already shown in BPB07, RXCJ0014.3-3022 shows two prominent filamentary structures to the NW and S, extending beyond the cluster main body. There we mapped the trend of star formation activity from the cluster core outwards along these filaments. Hereafter the main large-scale features of the cluster, already discussed in BPB07, will briefly be reviewed and updated.

Out of the full cluster catalogue we selected the regions of the core and the two filaments, together with a control low-density “field” region. Table 3.5.1.1 shows the geometrical selection criteria (additional to observed magnitude and photo-z) for the subcatalogues; cluster-centric radius is given in arcminutes and azimuthal zero angle is towards west (right in the image files). Area is given in square arcminutes.

The two filaments hold about the same number of objects, although the southern one seems denser (see the density maps in Fig. 3.8), whereas the NW filament looks more like a relatively high-density chain of lumps than a continuous filamentary structure (as in the case of southern filament). The core region has almost the same

Region	Radius	Angle	Objects	Area
Cluster core	$0' \leq r \leq 3'$	$0' \leq \theta \leq 360$	304	$9\pi$
NW filament	$3' < r \leq 15'$	$-10' \leq \theta \leq 50$	359	$36\pi$
S filament	$3' < r \leq 15'$	$260' \leq \theta \leq 320$	374	$36\pi$
BG field	$6' < r \leq 18'$	$120' \leq \theta \leq 210$	488	$72\pi$

**Table 3.5:** Definition of regions of interest in RXCJ0014.3-3022. Areas are expressed in square arcminutes.

number of objects as the filaments, but contained in one fourth of their area, while the field has about 1.3 times the filaments' objects in an area twice as wide. Hereafter, we will always refer to the cluster regions and local field as they are defined in table 5.

The cluster shows a non-relaxed shape in all maps. Its main body is elongated in the NW-SE direction, joining the two main clumps of galaxies, and contains lots of extensions. Among them, the two principal ones to the NW and S extend out to about  $9'$ , equivalent to 2.44 Mpc at the cluster redshift. These two filamentary structures reach the image borders. The southern one shows a twisting, clumpy extension of loosely connected high-density blobs, while the western one extends to the NW quadrant with a collection of more scattered overdense peaks. Other, less prominent peaks are scattered across the field.

The central part of the cluster clearly stands out in the red objects density map. Two main clumps of galaxies lie in the centre: they are associated with the two pairs of BCGs lie (see Pierini et al. (2008)). A third clump, slightly less dense, lies to the N and contains a similarly bright and red galaxy as the BCG pairs. Two limited extensions of red galaxies jutting out from the cluster body are clearly visible to the NW and to the S. An additional, isolated density peak to the SE of the cluster reveals the presence of a secondary group of galaxies at the cluster redshift. This group could well be connected to the cluster via a slightly overdense channel of red galaxies, suggesting the presence of another thread in the cosmic web of this cluster.

The structure emerging from the blue object density map is more complex. An overdensity of objects is evident in the cluster very centre; it lies exactly between the three peaks detected in the red map. The presence of star-forming (i.e. blue) objects in the cluster core has been already detected in Couch et al. ((1998)) and to a lesser extent by our spectral index analysis (see Sect. 3.5.2). Its extent could be ascribed to the ongoing merger. A significant overdensity of blue objects is also detected in two secondary peaks just trailing the two main peaks of red objects in the centre. In particular, the blue clump to the NW is led by an X-ray bow-shock detected with *Chandra* (see Kempner & David (2004)). This suggests that this shock shields infalling galaxies from the cluster ICM and allows them to continue their normal star

### 3 Evolution of the star formation activity across massive galaxy clusters

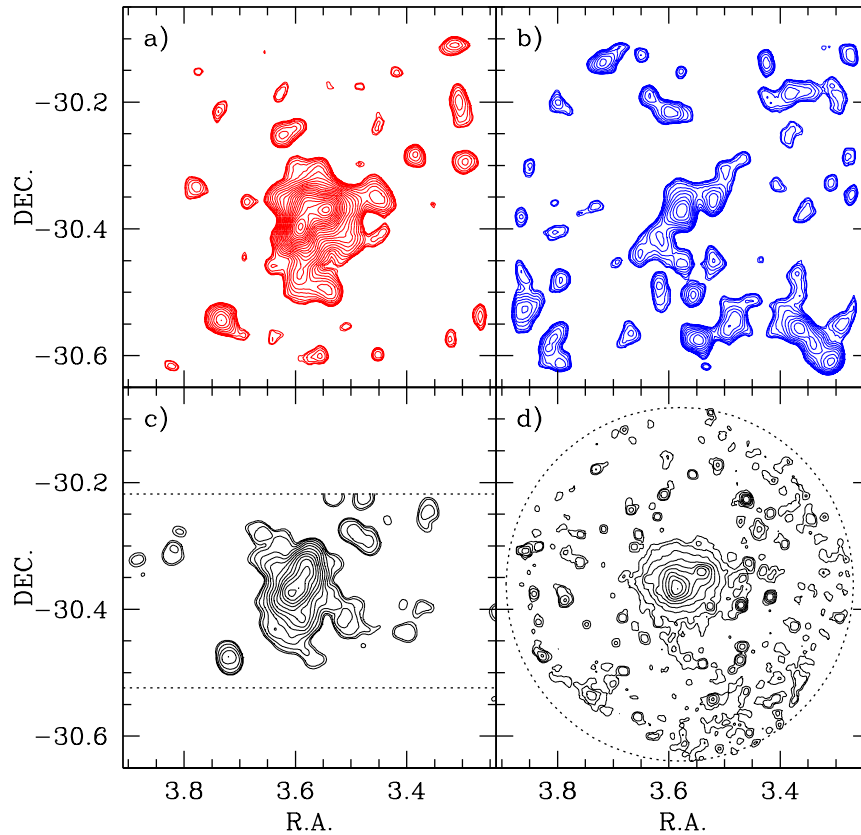


**Figure 3.8:** Density maps and X-ray imaging for RXCJ0014.3-3022. Panels a) and b) show respectively the density maps of red and blue photometric cluster members. Panel c) shows the spectroscopic cluster members density maps, where the dotted lines mark the approximate extent of the VIMOS combined pointings. Panel d) shows the X-ray emission imaged with XMM-Newton, with the dotted circle marking the border of the satellite FOV. The lowest contour is at 5 r.m.s. of background for all maps.

formation. A similar clump is seen trailing the SE peak, although no X-ray shock was detected here. Finally, blue objects largely trace the filaments, extending them beyond the cluster X-ray  $R_{200}$  (2.52 Mpc), as already discussed in BPB07.

The overall picture is confirmed by the limited spectroscopic information and the X-ray image (see Fig. 3.8). In particular, the southern filament detected in the photometric member maps is well matched in both spectroscopic and X-ray maps by an elongated and partially lumpy extension to the south that precisely follows the

Region	Radius	Angle	Objects	Area
Cluster core	$0' < r \leq 3'$	$0 \leq \theta \leq 360$	258	$9\pi$
Inner outskirts	$3' < r \leq 6'$	$0 \leq \theta \leq 360$	293	$27\pi$
Outer outskirts	$6' < r \leq 9'$	$0 \leq \theta \leq 360$	429	$45\pi$
BG field (1)	$9' < r \leq 19'$	$200' \leq \theta \leq 240$	255	$31.1\pi$
BG field (2)	$9' < r \leq 19'$	$300' \leq \theta \leq 350$	228	$38.9\pi$

**Table 3.6:** Definition of regions of interest in RXCJ2308.3-0211. Areas are expressed in square arcminutes.

shape of the filament.

### 3.5.1.2 RXCJ2308.3-0211

The overall morphology of RXCJ2308.3-0211 is largely different from that of RXCJ0014.3-3022. There, the position of the one and only BCG coincides with the X-ray centroid and the peak emission (see Pierini et al. (2008)). Indeed, this is a cool core cluster (e.g. Pratt et al. 2008, in prep.), where the X-ray emission is centrally peaked and circularly symmetric.

However, the optical aspect is richer than the X-ray. In particular, to the north of the cluster two galaxy groups can be easily spotted. These two groups are at the same photometric redshift of the cluster, as confirmed by their red sequences. The two groups are at about  $4'$  from each other, about 1.2 Mpc at the cluster redshift, and lie  $15'$  from the core of RXCJ2308.3-0211 (i.e., 4.1 Mpc). The two groups are mainly traced by red objects and seem to be detected in X-rays, although at the edge of the XMM FOV. They could be part of a larger structure, partly elongated in the E-W direction and partly extending towards the cluster. The presence of this bridge of red galaxies is suggested by the spectroscopic member density map, where an extension is seen towards N and the overdense bridge. An additional overdensity of spectroscopic members just E of the main cluster is also seen traced by red objects. This is (as shown from Dressler-Schechtman analysis) likely a group still not connected to the cluster (Braglia et al. 2008b, in prep.). Conversely, almost no overdensity of blue objects is found, but for a sequence of blobs jutting out of the cluster core towards NE, almost reaching  $R_{200}$  (2.44) Mpc.

Similarly to RXCJ0014.3-3022, we define interesting regions in RXCJ2308.3-0211. As the cluster does not show evident substructure, we divide it in a core and two concentric circular annuli to sample the outskirts at increasing cluster-centric radii. A comparison background field is also selected as the sum of the two zones with lowest surface density. The regions are summarized in Table 4.4.3:

The two background regions together have the same area and number of objects than the background field for RXCJ0014.3-3022. This is important to directly com-

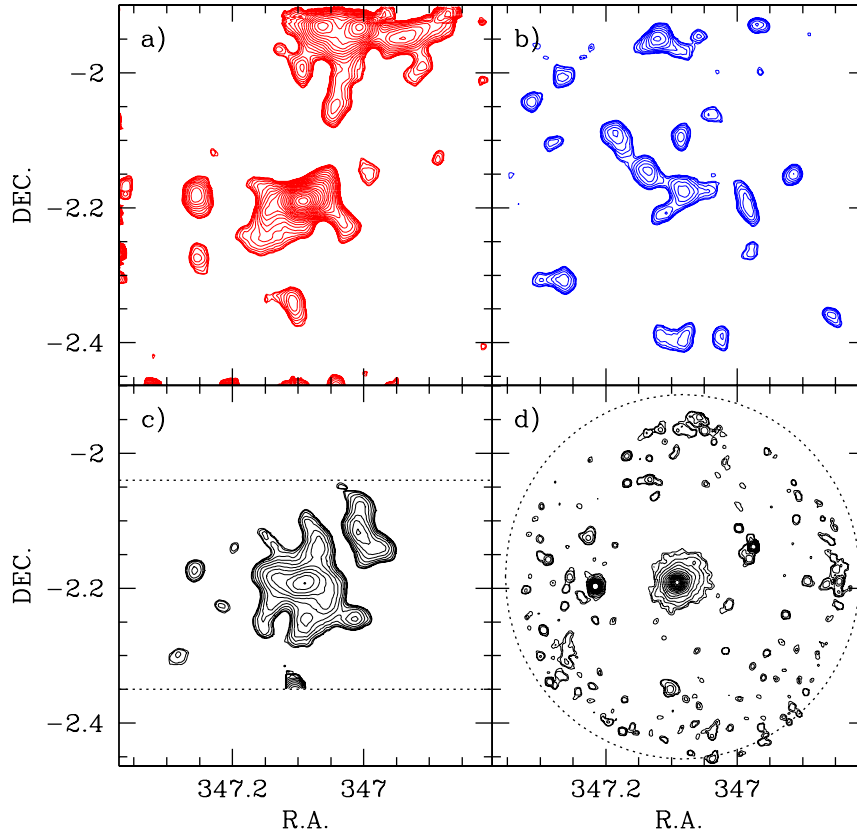


**Figure 3.9:** Density maps and X-ray emission for the different catalogues available for RXCJ2308.3-0211. Panels a) and b) show respectively the density maps of red and blue photometric cluster members. Panel c) shows the spectroscopic cluster members density maps, where the dotted lines mark the approximate extent of the VIMOS combined pointings. Panel d) shows the X-ray emission imaged with XMM-Newton, with the dotted circle marking the border of the satellite FOV. The lowest contour is at 5 r.m.s. of background for all maps.

pare the global properties of the two clusters with respect to a common ground, i.e. background fields with comparable statistics. The full cluster is defined as the sum of the three concentric regions, bringing a total of 980 objects within  $9'$ . For comparison, RXCJ0014.3-3022 has 1016 objects within the same radius.

### 3.5.2 Spectral index analysis

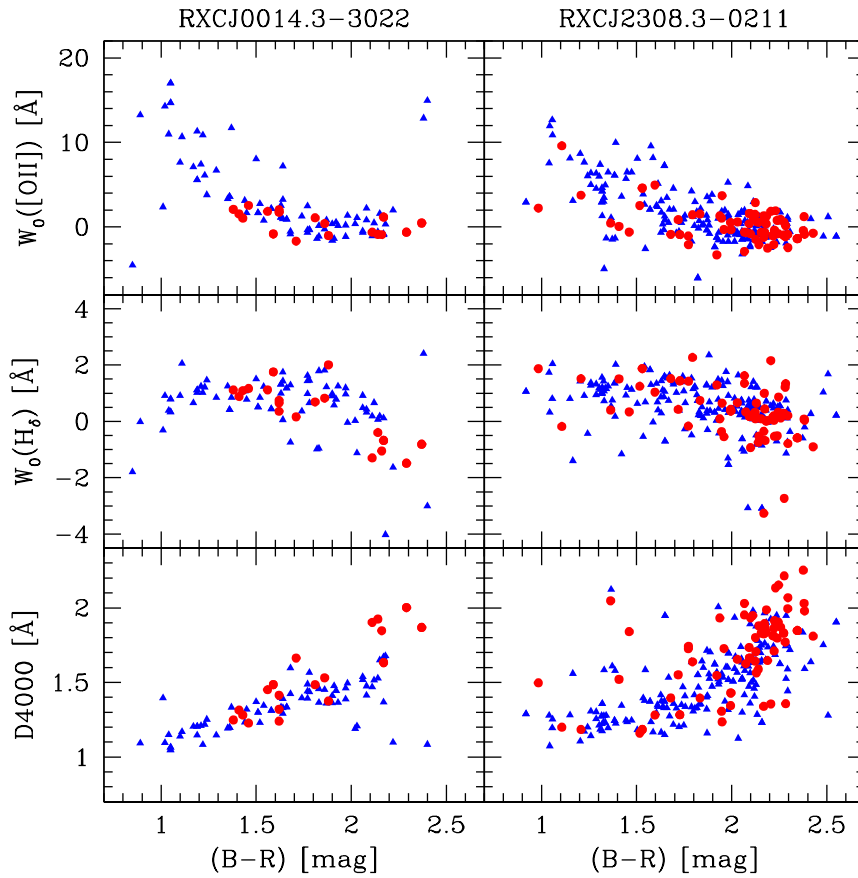
The star-formation histories of individual cluster members can be constrained through a spectral index analysis (e.g. Balogh et al. (1999)). VIMOS spectra with  $S/N > 4$  allowed us to robustly determine the strength of the 4000Å break ( $D4000$ ), and the equivalent widths of the  $H_\delta$  photospheric absorption line ( $W_0(H_\delta)$ ) and the  $[OII]$  nebular emission line ( $W_0([OII])$ ). In particular,  $D4000$  is particularly sensitive to the presence of old (i.e.,  $\geq 1-2$  Gyr), passively evolving stellar populations;  $W_0(H_\delta)$  is sensitive to episodes of star formation in the last Gyr by measuring the presence of A-type stars;  $W_0([OII])$  gives an estimate of the present SFR (i.e., on timescales of  $\leq 0.01$  Gyr). The combined use of the diagnostic diagrams  $W_0(H_\delta)$ – $W_0([OII])$  and  $W_0(H_\delta)$ – $D4000$  limits misinterpretations arising from the absence of corrections for intrinsic extinction by dust or additional line emission affecting  $W_0([OII])$  and  $W_0(H_\delta)$ , respectively.

Figure 3.10 reproduces the behaviour of each spectral index as a function of the observed  $B - R$  colour (uncorrected for internal extinction) for the spectroscopic cluster member galaxies. In this section, all plots will have the same colour-shape coding, chosen to underline different types of galaxies in each cluster and to allow direct comparison between the two clusters and the different diagrams. Thus, blue triangles will be used to mark faint galaxies, red dots for the bright ones.

A clear trend with colour can be clearly seen in both clusters for the  $W_0([OII])$  and  $D4000$  spectral indices. Values of  $EW(OII)$  decrease with increasing values of  $(B-R)$ . This is consistent with a change from actively star-forming (blue) galaxies to passively evolving spectral types. For  $(B-R) < 1.5$ ,  $EW(OII)$  is almost stable beyond 0 with a clear increase towards large values for very blue colours ( $(B-R) < 1.2$ ), confirming star-formation activity; on the other hand, at  $(B-R) \sim 2$  its mean value is of order 0, typical of passive systems. Conversely,  $D4000$  intensity steadily increases from blue to red colours, as expected if moving from star-formation systems to old stellar populations. For  $(B-R) \sim 2$ ,  $D4000$  is significantly beyond 1.5 and increasing rapidly towards redder colours. Although with a somewhat larger scatter, a feeble trend can also be detected in  $W_0(H_\delta)$  from higher values (i.e., more absorbed) for bluer objects to lower or negative values for redder objects. This could be due to contamination from nebular emission, which we did not take into account in the calculation of our spectral indices.

We empirically determine threshold values for the three spectral indices, which will be used to discriminate different star-formation regimes, by combining colour and spectroscopy information. Specifically, mean values for  $EW(OII)$ ,  $D4000$  and  $W_0(H_\delta)$  are calculated from red-sequence objects, as representative of passively-evolving systems; objects are then defined as passively evolving if they lie within  $3\sigma$  from the mean. We thus define objects as passively evolving if they have  $[OII]$  equivalent widths lower than 4.85 in the  $[EW(OII), W_0(H_\delta)]$  plane, or if they have

### 3 Evolution of the star formation activity across massive galaxy clusters



**Figure 3.10:** Distribution of spectral indices against galaxy (B-R) colour for RXCJ0014.3-3022 (left column) and for RXCJ2308.3-0211 (right column). The notations are explained in Sect. 5.2. The values of  $EW(OII)$  and  $D4000$  are found to be well correlated with galaxy colours, showing a steady increase of  $D4000$  for redder systems and a decrease in  $EW(OII)$ . A less evident trend of  $W_0(H_\delta)$  can still be noticed.

$D4000$  in excess of 1.4 in the  $[D4000, W_0(H_\delta)]$  plane. This approach is similar to the definition found in Barger et al. ((1996)) and Balogh et al. ((1999)), but adapted to our specific case to better describe galaxies based on the definition of red sequence, i.e. the locus of passively evolving systems at the clusters redshift. The values found are comparable to those from Balogh et al. ((1999)), or Dressler et al. ((1999)), who similarly tailored the thresholds to their data-sets. For the  $W_0(H_\delta)$  index we assume instead the same definitions as previously applied: a lower limit of  $0 \text{ \AA}$  and an upper limit of  $5 \text{ \AA}$  to discriminate between different regimes in star-forming galaxies. It is



**Table 3.7:** Definitions in the  $[W_0(OII), W_0(H_\delta)]$  plane

Definition	$W_0(OII)$	$W_0(H_\delta)$
PEV (passive)	$< 4.85$	$\leq 5$
SF (star-forming)	$\geq 4.85$	$\in [0, 5]$
SSB (short starburst)	$\geq 4.85$	$< 0$

**Table 3.8:** Definitions in the  $[D4000, W_0(H_\delta)]$  plane

Definition	$D4000$	$W_0(H_\delta)$
PEV (passive)	$\geq 1.4$	$\leq 5$
SF (star-forming)	$< 1.4$	$\in [0, 5]$
SSB (short starburst)	$< 1.4$	$< 0$

worth noting that our thresholds are in good agreement with ones in the literature, i.e.  $W_0([OII]) = 5\text{\AA}$  and  $D4000 = 1.45\text{\AA}$ . We will use our definitions for these two indices, as better tuned to our data.

These definitions allow to flag galaxies as a function of their star-formation regime, as defined from their position in the  $[W_0([OII]), W_0(H_\delta)]$  and  $[D4000, W_0(H_\delta)]$  planes. Since we do not detect extreme values of  $W_0(H_\delta)$  in our sample, we will only use the following definitions (see also tables 3.7 and 3.8), consistent with previous works (for an extended explanation, see Balogh et al. ((1999))).

*Passive galaxies (PEV):* galaxies not currently undergoing significant star formation activity, mainly ellipticals and S0. They are defined by  $W_0(H_\delta) < 5$  and  $W_0([OII]) \leq 4.85$ , or  $D4000 \geq 1.4$ .

*Star-forming galaxies (SF):* galaxies undergoing significant star formation activity since at least several hundred million years, mainly late-type spirals and starburst galaxies. These are identified by  $0 < W_0(H_\delta) < 5$  and  $W_0([OII]) > 4.85$ , or  $D4000 < 1.4$ .

*Short starburst galaxies (SSB):* galaxies currently undergoing a short-lived, intense episode of star formation (i.e.,  $\leq 200$  Myr), with strong nebular emission. These galaxies have  $W_0(H_\delta) < 0$  and  $W_0([OII]) > 4.85$ , or  $D4000 < 1.4$ .

As shown in Fig. 3.11, RXCJ0014.3-3022 and RXCJ2308.3-0211 host galaxy populations with rather different distributions in the diagnostic plots  $W_0(H_\delta)$ – $W_0([OII])$  and  $W_0(H_\delta)$ – $D4000$ .

In particular, RXCJ0014.3-3022 exhibits a larger fraction of objects with large  $W_0([OII])$  and star-forming systems, which confirms the presence of the Butcher-Oemler effect in this cluster.

To assess if the galaxy populations in the two clusters are significantly different, a diagnostic two-dimensional Kolmogorov-Smirnov test was run on their distribution in both planes. As a result, the probability that the two distributions are drawn from

### 3 Evolution of the star formation activity across massive galaxy clusters

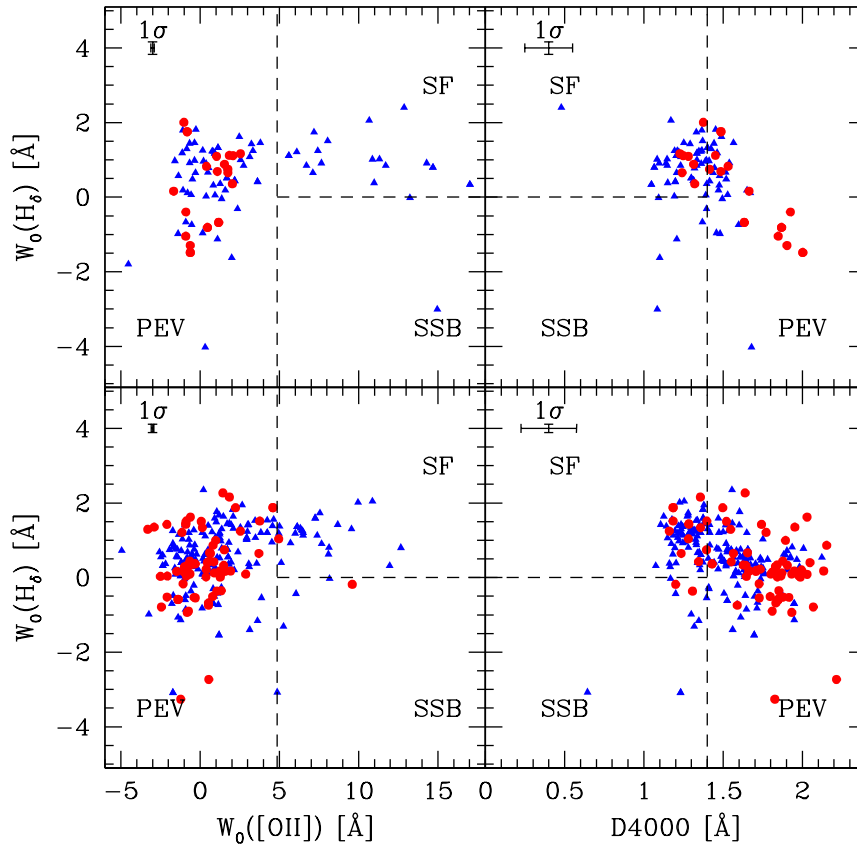


**Figure 3.11:** Distribution of spectral indices for the two clusters. Top row shows the members of RXCJ0014.3-3022; bottom row shows the members of RXCJ2308.3-0211. The dashed lines mark the position of boundary values for the different spectral indices to discriminate different star formation regimes (see Tables 3.7 and 3.8). Average error values are shown in the top left corner of each plot. Note that the error on  $W_0([OII])$  is rather small in the diagram scale.

the same parent population is absolutely negligible: 0.02% in the  $[D4000, W_0(H_\delta)]$  plane, 0.41% in the  $[EW(OII), W_0(H_\delta)]$ . We want to recall that the two spectroscopic samples were built with the same selection function (cfr. Sect. 3.2.1). We attribute this significant difference to the largely different dynamical state and morphology of the two clusters (see Sect. 3.5.1 and Braglia et al. 2008b, in prep.). As an independent test, we consider the galaxy distribution in the (FUV-V) vs.  $D4000$  plane (cfr. Moran et al. (2007)). For our spectroscopic sample (FUV-V) colours were calculated from our total magnitudes and archival GALEX data. In absence of

GALEX FUV detections, we assumed  $3\sigma$  lower limits on the UV magnitude, based on the completeness magnitude of the two fields.

Fig. 3.12 shows the (FUV-V) vs.  $D4000$  plots for both clusters, where galaxies are flagged as star-forming or passive according to their [OII] emission. RXCJ0014.3-3022 has a larger number of UV-detected objects than RXCJ2308.3-0211 (12 objects in the first cluster, 7 in the second). As our spectroscopic catalogue for RXCJ0014.3-3022 contains 101 objects, against 269 in RXCJ2308.3-0211, this suggests that an intrinsically larger fraction of objects are actively forming stars in the first cluster. Most of the FUV-detected galaxies in RXCJ0014.3-3022 lie close to the cluster core and in the region of the southern filament, where our density maps reveal the presence of blue clumps of galaxies.

A more complete picture is obtained when lower limits on the (FUV-V) colour are considered. Fig. 3.12 shows that in RXCJ2308.3-0211 the bulk of spectroscopic members avoid the region with (FUV-V) $<2$ , whatever the value of  $D4000$ . Conversely, RXCJ0014.3-3022 hosts a non-negligible population of galaxies with  $D4000 < 1.6$  and (FUV-V) $<2$  mag.

It is now interesting to compare the behaviour of spectral indices of individual galaxies in the two clusters as a function of cluster-centric radius, as shown in Fig. 3.13.

In RXCJ0014.3-3022, the radial trend of  $W_0([OII])$  shows a strong and localized increase of the star formation activity at  $R_{200}$ . This recalls our results in BPB07, where we found a sharp peak in the blue-to-red galaxies ratio along the two filaments connected to the cluster. Here this is confirmed by spectroscopy (see also the next section), suggesting that the filaments really begin to interact with the cluster at this distance through an intense increase of the star formation. The brightest cluster members always show small or negligible  $W_0([OII])$ . The distribution of  $D4000$  shows again a sharp change across  $R_{200}$ . The number of galaxies with  $D4000 > 1.4$  increases towards the center, whereas beyond  $R_{200}$  no galaxy shows a strong break, its value suddenly dropping.

The distribution of spectral indices for RXCJ2308-0211 shows different features. The radial behaviour of  $W_0([OII])$  shows that the largest part of cluster members is no more forming stars. All but one bright galaxy lie below the threshold value for this index, and the few objects still showing signs of star formation are scattered both below and beyond  $R_{200}$ . The radial distribution of  $D4000$  shows this cluster as largely dominated by passively evolving galaxies. Although slightly larger values are found towards the center, high values of  $D4000$  are found also beyond  $R_{200}$ , both for bright and faint galaxies.

The presence of bright passive galaxies outside  $R_{200}$  for RXCJ2308-0211 suggests that in this region massive galaxies could be moving towards a passive sequence already beyond the cluster structure. The separation between bright and faint galaxies is evident in the radial plot of  $D4000$ , where the two populations are largely segre-

### 3 Evolution of the star formation activity across massive galaxy clusters

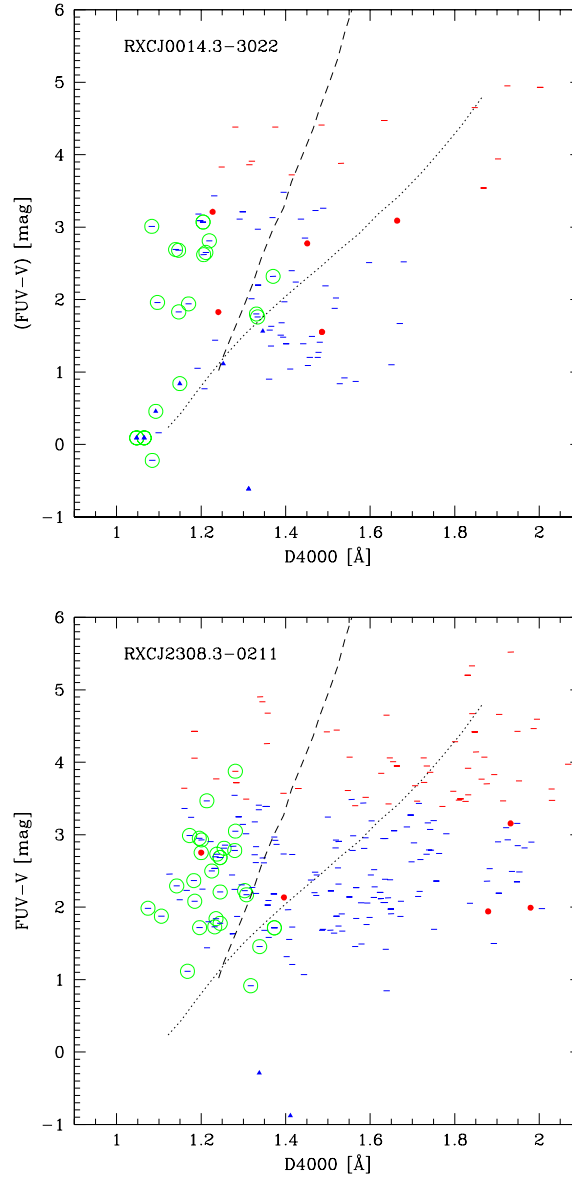


**Figure 3.12:** Distribution in the (FUV-V) vs.  $D4000$  plane for the two clusters. In addition to the usual coding for this section, red and blue bars mark lower limits for bright and red galaxies, respectively. Green circles mark galaxies with significant (i.e.,  $> 4.85$ ) [OII] emission. The dashed and dotted lines mark respectively a starvation and a truncation evolutionary track, similarly to Moran et al. ((2007)).

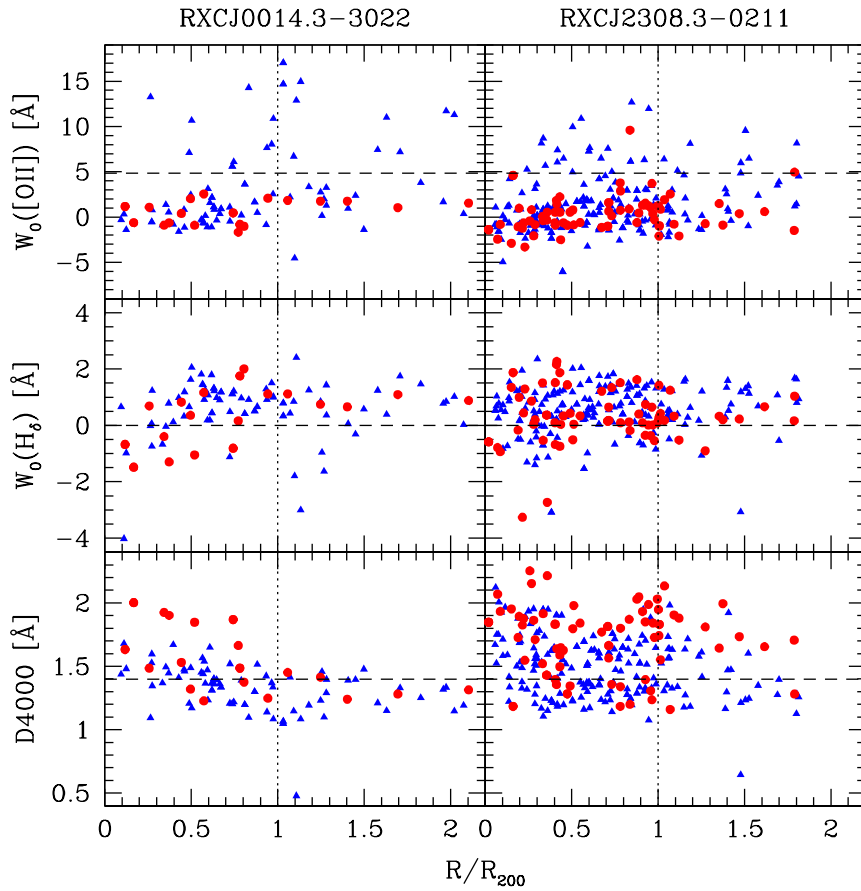


**Figure 3.13:** Radial dependence of spectral indices for the two clusters. The left column shows the radial behavior of the three measured indices for RXCJ0014.3-3022; the right one shows the same for RXCJ2308.3-0211. The horizontal dashed lines mark the characteristic values for the spectral indices, while the vertical dotted line marks the scaled position of  $R_{200}$  for each cluster.

gated. This is in agreement with previous works (Kodama et al. (2001) and (2003); Balogh et al. (1997)). In particular, Balogh et al. ((1997)) found that star formation is generally suppressed out to  $2R_{200}$ .

### 3.5.2.1 Environmental dependence of spectral indices

To better check and confirm our already published findings of an increase in the star-formation activity along filaments in RXCJ0014.3-3022, equivalent widths are plotted against cluster-centric radius for the cluster core, the filaments and the comparison

### 3 Evolution of the star formation activity across massive galaxy clusters

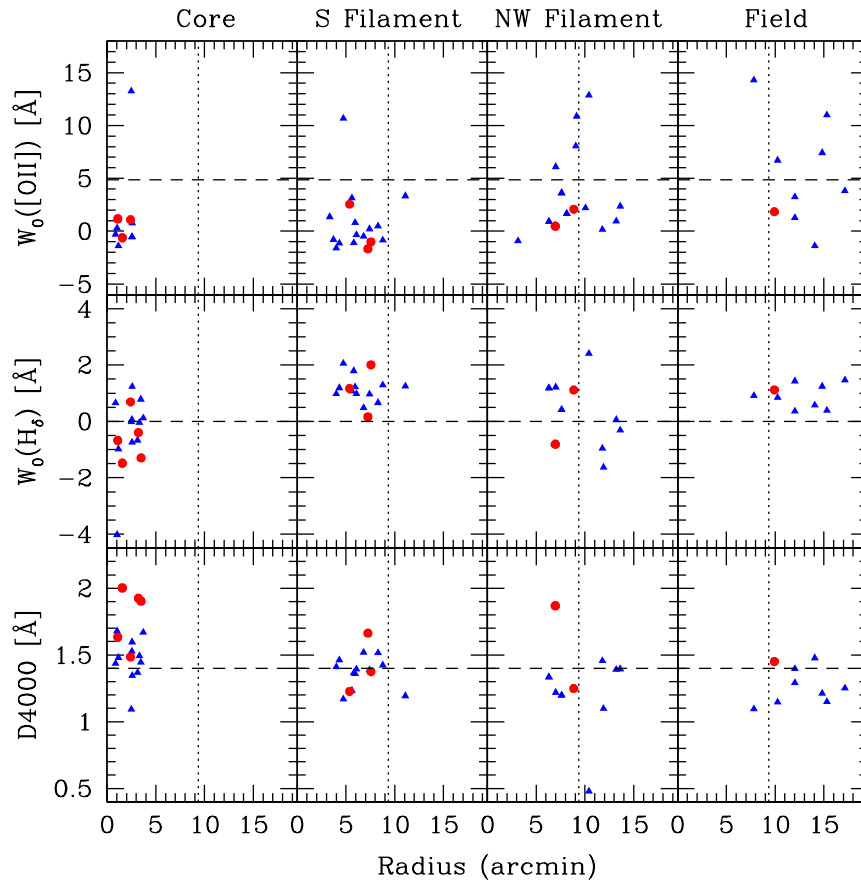


**Figure 3.14:** Radial dependence of spectral indices in the different regions of RXCJ0014.3-3022. Cluster-centric distance is expressed in arcminutes, to directly compare with the definitions given in Section 3.5.1. Notations are as in Fig. 3.13.

field (cfr. Fig. 3.14).

The cluster core shows a population rather typical of a cluster: galaxies have large values of  $D4000$  and negligible [OII] emission. Still, at least one object is intensely forming stars; this is found to be a small, compact galaxy just outside the largest density peak in the center. Analysis on the two planes of the spectral indices shows that all but two objects are indeed star forming galaxies, with the most prominent being at the boundary between normal star formation and short starburst. This suggests that in the core of this cluster, short-lived and young episodes of star formation can still happen. This is likely associated with strong gravitational stresses (see Couch et al. (1998)).

The southern filament is mostly outside the region targeted by VIMOS (see BPB07 and Sect. 3.5.1). Thus, we cannot spectroscopically confirm the star-formation mode of the “flaming giants” discovered by BPB07, which are mostly located along this filament but beyond  $R_{200}$  (i.e.,  $\sim 9.4'$ ). According to our density maps, up to  $R_{200}$  the cluster shows mostly a population of passively evolving galaxies. This is also confirmed by the spectral index analysis. A slight but systematic decrease in the values of  $D4000$  suggests the presence of a population somewhat younger than in the core. In the northern filament, several galaxies are found to be actively star forming across the cluster  $R_{200}$ , while beyond and below this distance the population is again more typical of a cluster in the distribution of  $W_0([OII])$ . However, the values of  $D4000$  are sensibly lower, suggesting again younger systems. The position of these galaxies with respect to the spectral indices confirms them as star-forming galaxies, with a small fraction of short-starbursts.

The comparison field is rather quiet, with a single bright and passive galaxy and several low-luminosity star-forming galaxies. Analysis of the spectral indices shows that the field is made of a mix of passive and mildly-to-high star-forming systems. No clear trends with radius is found, confirming this region as a fair sample of the field unaffected by the cluster. Also no short-starbursts are found, suggesting that the star formation in the field is quietly evolving without noticeable interaction with structures. New observations are currently under completion to spectroscopically sample 1200-1400 additional galaxies in this region to robustly map the star formation activity across the cluster core and filaments and beyond  $R_{200}$ .

Although no specific regions of interest are detected in RXCJ2308.3-0211 which are also covered by spectroscopy, it is still possible to better examine the radial behaviour of spectral indices referring to the regions defined and discussed in Sect. 3.5.1. Thus, equivalent widths are plotted against cluster-centric radius in the regions of the cluster core, inner outskirts and outer outskirts, as well as for the comparison field.

From Fig. 3.15 it is possible to notice that active star-forming systems are almost exclusively represented by faint galaxies. Their presence in the core is practically negligible, while for increasing cluster-centric radii it is possible to see a slight increase of their fraction. Also, the mean value of  $W_0([OII])$  is slightly increasing from the core to the outskirts. This is in good agreement with previous findings (i.e. Balogh et al. (1999)) and suggests the presence of age sequences in the radial distribution of galaxies in evolved clusters. Accordingly, typical values of  $D4000$  show a small decrease with increasing cluster-centric radius, confirming that in the core are found on average older galaxies. Although the field coverage is scarce, it is still possible to detect the signature of the cluster in its galaxy population, suggesting that the whole region surrounding RXCJ2308.3-0211 is globally evolved. In particular, the mean values of  $D4000$  show that massive galaxies outside the cluster  $R_{200}$  are already old (i.e. have large values of  $D4000$ ). A population of younger galaxies is also found,

### 3 Evolution of the star formation activity across massive galaxy clusters

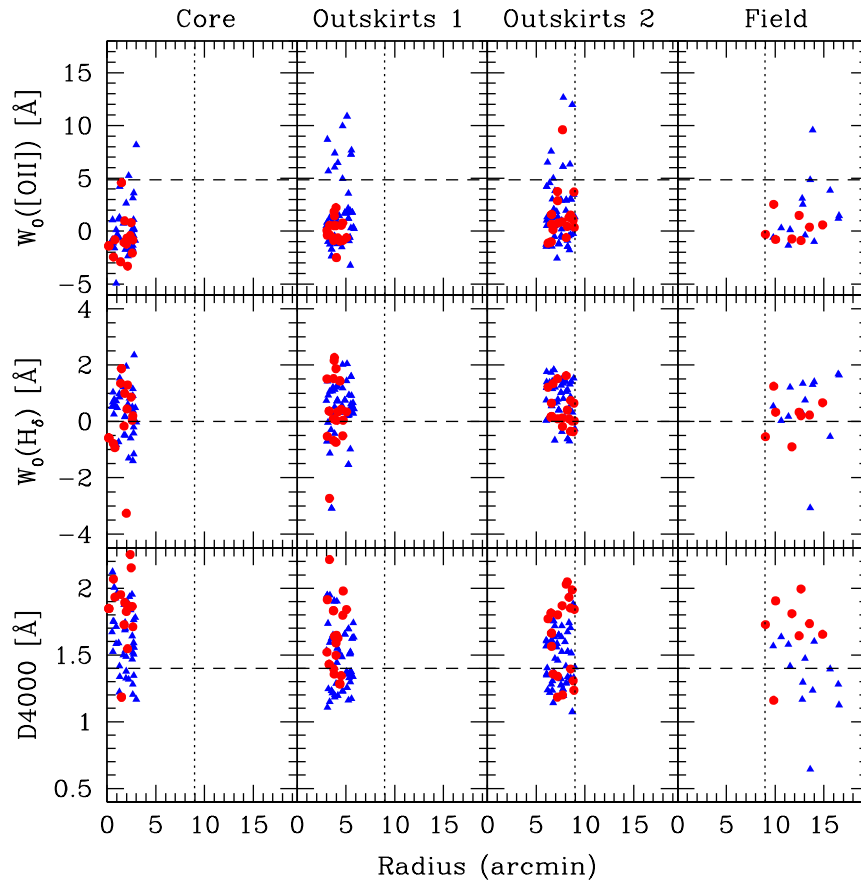


**Figure 3.15:** Radial dependence of spectral indices in the different regions of RXCJ2308.3-0211. Cluster-centric distance is expressed in arcminutes, to directly compare with the definitions given in Section 3.5.1. Notations are as in Fig. 3.13.

although with no significant star-formation activity.

### 3.6 Discussion

A comparison of spectral indices for cluster members shows large differences in the galaxy populations of the two systems. RXCJ0014.3-3022 shows a larger fraction of actively star-forming systems, with more extreme regimes (i.e., higher values of  $W_0[OII]$ ), while RXCJ2308.3-0211 shows a population typical of well evolved clusters, with higher values of  $D4000$  and an overall passively evolving population.

Specifically, RXCJ0014.3-3022 reveals a sudden increase in the star formation



regime around  $R_{200}$  along its filamentary structure. This increase is concentrated in a very thin region across  $R_{200}$  and confirms our previous results from photometry (see Braglia et al. (2007)). Along the filaments and just inside  $R_{200}$ , we find a population of relatively young systems that are no more forming stars. This suggests that these galaxies could be what has been classified as passive spirals, i.e. stellar disks largely depleted of gas. These could become the S0's found in cluster cores, in agreement with our infall interpretation. Indeed, as galaxies approach the cluster, a sudden increase in their intrinsic star formation rate can be detected via their [OII] emission. As these galaxies enter the cluster, interaction with the denser ICM can lead to gas loss via ram-pressure stripping, leaving these galaxies with an intermediate age population of stars without the fuel needed to trigger newer star formation. This is also supported by the radial trend of spectral indices, that confirms in this cluster a rapid transformation in the characteristics of galaxies across  $R_{200}$ . While below this scale cluster galaxies are quite typical of a cluster environment, beyond it a sudden lack of passive systems and a rapid increase in the star formation activity is noticed.

Part of the UV-detected objects show significant star formation activity (i.e., large values of  $W_0[OII]$ ) and accordingly very blue (FUV-V) colour. Also, many objects, both with UV detection and without, lie in a region of the diagram expected to be populated mainly by truncated systems, i.e. galaxies where the star formation was abruptly stopped on short timescales at an intermediate age (less than 7 Gyrs, marked in Fig. 3.12 with a dashed line; cfr. Moran et al. (2007)). These objects still present relatively small  $D4000$  values ( $<1.3$ ), but no more significant UV emission, and have been classified as passive spirals. Conversely, the upper right part of the diagram, i.e. the region where passive galaxies are expected to lie, is not heavily populated. This is the region where galaxies end while following a natural, undisturbed evolution, with their gas being progressively consumed in timescales of several Gyrs. These galaxies follow the starvation (dotted) track shown in Fig. 3.12, from the lower left part of the diagram (where blue galaxies with large [OII] emission are found) to the upper right, where galaxies have turned red and have strong  $D4000$  absorptions. All this suggests that the galaxy population of RXCJ0014.3-3022 is still relatively young, or is being rejuvenated.

This can be explained considering the effect of the ongoing merger and of the large-scale structure of this cluster. It compares well with other complementary findings. In particular, Couch et al. ((1998)) found a population of distorted, star-forming galaxies in the central region of RXCJ0014.3-3022: their results suggests that the strong tidal interactions in the cluster core can increase the star formation activity, thus rejuvenating the galaxy stellar population. At the same time, our interpretation of an increased star formation activity along the infall directions provides a natural way to extend the rejuvenation to larger cluster-centric radii.

Moreover, comparison of spectral indices with observed (B-R) colour reveals an

### 3 Evolution of the star formation activity across massive galaxy clusters

---

additional population of galaxies (see Fig. 3.10). Specifically, while the largest part of galaxies follows a well defined track in the  $D4000$  vs. (B-R) plane (with redder galaxies also having higher values of  $D4000$ ), some very red galaxies (with colour even redder than the red sequence) can be noticed with low ( $< 1.2$ ) values of  $D4000$ . Indeed, in the last years, mid-infrared observations with *Spitzer* have revealed strongly obscured star-forming systems in clusters (see Saintonge et al. (2008) and references therein). It has been shown that Butcher-Oemler clusters and merging or interacting clusters are likely to hide an even larger fraction of luminous infrared galaxies, i.e. dusty star-forming systems. This is directly connected with the evolutionary state of the cluster, as these galaxies are mainly found in clusters assembling from the cosmic web (Tran et al. (2005); Loh et al. (2008)).

On the other hand, RXCJ2308.3-0211 appears as an undisturbed cluster. Its population of passive galaxies is rich and well established in both bright and faint systems. No remarkable interaction with the cosmic web is found, but a bridge of red galaxies connecting to two groups. This bridge is almost depleted of blue galaxies, and also the few sampled spectra from this region show no signs of active star formation.

The radial behavior also shows a well populated cluster with a dominating fraction of passively evolving galaxies and only a few systems still actively forming stars. Remarkably, while inside  $R_{200}$  the galaxy population is well mixed with respect to luminosity, beyond  $R_{200}$  a luminosity segregation is seen in the radial behavior (see Fig. 3.13). This suggests that in this field, massive galaxies are already following a passive evolution even outside the cluster. This, together with the cluster relaxed morphology, suggests an indeed old system, whose galaxy population could have formed earlier than RXCJ0014.3-3022 and evolved relatively undisturbed.

The (FUV-V) vs.  $D4000$  diagram for RXCJ2308.3-0211 (see Fig. 3.12) also reveals an older system. Not many galaxies are detected in UV, neither show intense star formation activity from  $W_0([OII])$ . The few detected objects are located in the outer regions of the cluster and are loosely scattered, not being directly related to the few blue overdensities found in the density maps. The largest part of the galaxies, both detected and undetected in UV, lie in regions of the diagram that suggest an undisturbed evolution towards passively evolving systems. The upper right part of the diagram is indeed largely populated, while the lower left, where young and active systems are found, is almost completely empty. Still, a non negligible fraction of objects lies well separated in the upper left region, where truncated systems are found. Although only one object is actually detected in this region, it suggests that also in this cluster a population of truncated systems is found. Overall, this cluster shows an older galactic population, with no detectable blue objects and lots of passively evolving systems. RXCJ2308.3-0211 is a cool core cluster, which suggests that the cluster was globally undisturbed in the last Gyrs: such a kind of system is indeed expected to be mainly populated by passive galaxies, whose star formation history was relatively undisturbed.

The high-luminosity end of the colour-magnitude diagrams for the two clusters are also significantly different and reveal different dynamical stages, with RXCJ2308.3-0211 showing a single, bright BCG, with characteristics of a cD, dominating the cluster core and brighter by a full magnitude than other red sequence objects. On the other hand, RXCJ0014.3-3022 shows no single BCG, but instead a tight group of five bright galaxies, all lying in an intermediate region between other red sequence objects and the magnitude expected for a single BCG or cD galaxy. This can be interpreted as the bright core galaxies being still climbing the red sequence, on the road of merging together to form a single, massive cD dominating the cluster core in the future.

### 3.7 Conclusions

We use multi-wavelength data analysis to describe the dynamical and galaxy population state of two massive clusters out to large radii. For RXCJ2308.3-0211 this is the first study of this kind, while in the case of RXCJ0014.3-3022 we complement the already extended knowledge on the central regions of this cluster.

The two clusters show opposite dynamical stages, as witnessed by their X-ray morphologies. RXCJ0014.3-3022 is known to be a major merger and a strong Butcher-Oemler system, RXCJ2308.3-0211 is instead a cool core cluster. This is confirmed from analysis of the optical morphology and colour-magnitude diagrams. In RXCJ0014.3-3022, we find a substructured cluster and two large-scale filaments appearing to be driving the merger itself and the feeding of matter. No single BCG is found, instead five bright galaxies dominate the central region. On the other hand, RXCJ2308.3-0211 has a relaxed shape, with a well defined central peak (matching the X-ray peak) where the one and only BCG lies. No obviously actively interacting regions are seen, the only one being a filament composed of mainly passively evolving galaxies, connecting the main cluster with another structure also dominated by red galaxies.

We find a clear link between the dynamical stage of the clusters and their galaxy populations. Specifically, RXCJ0014.3-3022 shows an overall increased star formation activity, with a sharp change right across  $R_{200}$ : while star-forming systems reveal maximal activity at this distance, the fraction of passively evolving galaxies rapidly drops from the core to  $R_{200}$ , where those galaxies are basically disappearing. Also, RXCJ0014.3-3022 reveals a larger number of UV-emitting galaxies and an overall young population, with very blue UV-optical colour and less evolved systems. On the other hand, RXCJ2308.3-0211 shows a galaxy population largely composed of passively evolving ellipticals, with only a few star-forming systems. Also, we find that beyond  $R_{200}$  a form of luminosity segregation can be detected in the spectral index distribution, suggesting that massive galaxies could already be following passive evolution outside the cluster. This is also confirmed by an overall lack of

### 3 Evolution of the star formation activity across massive galaxy clusters

---

UV emission and a galaxy population of well evolved galaxies, as confirmed by redder UV-optical colour and larger values of  $D4000$ . Thus, the region surrounding RXCJ2308.3-0211 appears to be intrinsically older than RXCJ0014.3-3022, suggesting that RXCJ2308.3-0211 could have collapsed earlier and not been disturbed during its evolution.

We also detect a tight dependence of star formation activity with local environment. The spectral index analysis for filaments in RXCJ0014.3-3022 shows in fact that along these structures the star formation activity is suddenly triggered across  $R_{200}$ . This fit in the scenario in which galaxy clusters form by accretion of matter from the field; during accretion, disk galaxies infalling through the filaments experience short, intense star formation episodes, mainly driven by galaxy harassment processes. As galaxies reach the cluster main body, their residual gas is stripped, transforming them in lenticulars and S0. If galaxies can reach the core undisturbed by the ICM, they can fall into the centre and experience additional star formation activity due to tidal interaction with the giant ellipticals in the core, before being tidally disrupted.

Last, we find evidence of an even larger fraction of star-forming galaxies being present in RXCJ0014.3-3022. These systems, not identified in optical as star-forming galaxies due to their apparent colour, could well be explained as obscured star-forming galaxies, where large amounts of dust absorb UV and optical emission. These systems are identified as lying on the red sequence or redwards, but having low values of  $D4000$ , suggesting that their colour is mainly due to obscuration.

## Bibliography

- [1996] Abraham, R. G., Smecker-Hane, T. A., Hutchings, J. B., et al. 1996, *ApJ*, 471, 694
- [1998a] Adami, C., Mazure, A., Biviano, A., Katgert, P., & Rhee, G. 1998a, *A&A*, 331, 493
- [1998b] Adami, C., Mazure, A., Katgert, P., & Biviano, A. 1998b, *A&A*, 336, 63
- [2004] Alcalá, J. M., Pannella, M., Puddu, E., et al. 2004, *A&A*, 428, 339
- [2002] Andreon, S., 2002, *A&A*, 382, 821
- [2001] Arnouts, S., Vandame, B., Benoist, C., et al. 2001, *A&A*, 379, 740
- [1976] Avni, Y., 1976, *ApJ*, 210, 642
- [1999] Baade, D., Meisenheimer, K., Iwert, O., et al. 1999, *Msngr*, 95, 15
- [1988] Balluch, M. 1988, *A&A*, 200, 58
- [1997] Balogh, M. L., Morris, S. L., Yee, H. K. C., Carlberg, R. G., & Ellingson, E. 1997, *ApJ*, 488, 75
- [1999] Balogh, M. L., Morris, S. L., Yee, H. K. C., Carlberg, R. G., & Ellingson, E. 1999, *ApJ*, 527, 54
- [1966] Baker, N. 1966, in *Stellar Evolution*, ed. R. F. Stein, & A. G. W. Cameron (Plenum, New York), 333
- [1996] Barger, A. J., Aragón-Salamanca, A., Ellis, R. S., et al. 1996, *MNRAS*, 279, 1
- [2007] Barkhouse, W. A., Yee, H. K. C., & López-Cruz, O. 2007, *ApJ*, 671, 1471
- [1990] Beers, T. C., Flynn, K., & Gebhardt, K. 1990, *AJ*, 100, 32
- [2002] Beijersbergen, M., Hoekstra, H., van Dokkum, P. G., & van der Hulst, T. 2002, *MNRAS*, 329, 385

## Bibliography

---

- [1996] Bertin, E., & Arnouts, S. 1996, *A&A*, 117, 393
- [1988] Binggeli, B., Sandage, A., & Tamman, G. A. 1988, *ARA&A*, 26, 509
- [1992] Biviano, A., Girardi, M., Giuricin, G., Mardirossian, F., & Mezzetti, M. 1992, *ApJ*, 396, 35
- [2006] Biviano, A., Murante, G., Borgani, S., et al. 2006, *A&A*, 456, 23
- [2001a] Böhringer, H., Schuecker, P., Guzzo, L., et al. 2001a, *A&A*, 369, 826
- [2001b] Böhringer, H., Schuecker, P., Lynam, P., et al. 2001b, *Msngr*, 106, 24
- [2004] Böhringer, H., Schuecker, P., Guzzo, L., et al. 2004, *A&A*, 425, 367
- [2006] Böhringer, H., Braglia, F., Pierini, D., et al. 2006, *Msngr*, 123, 49
- [2007] Böhringer, H., Schuecker, P., Pratt, G. W., et al. 2007, *A&A*, 469, 363
- [1983] Bohlin, R. C., Jenkins, E. B., Spitzer, L. Jr., et al. 1983, *ApJS*, 51, 277
- [2000] Bolzonella, M., Pelló, R., & Miralles, J. M. 2000, *A&A*, 363, 476
- [2006] Boschin, W., Girardi, M., Spolaor, R., & Barrena, R., 2006, *A&A*, 449, 461
- [2007] Braglia, F., Pierini, D., & Böhringer, H. 2007, *A&A*, 470, 425 (BPB07)
- [1995] Briel, U. G., & Henry, J. P. 1995, *A&A*, 302, L9
- [2002] Busarello, G., Merluzzi, P., La Barbera, F., Massarotti, M., & Capaccioli, M. 2002, *A&A*, 389, 787
- [1978a] Butcher, H., & Oemler, A. Jr., 1978a, *ApJ*, 219, 18
- [1978b] Butcher, H., & Oemler, A. Jr., 1978b, *ApJ*, 226, 559
- [1984] Butcher, H., & Oemler, A. Jr., 1984, *ApJ*, 285, 426
- [1996] Carlberg, R. G., Yee, H. K. C., Ellingson, E., et al. 1996, *ApJ*, 462, 32
- [1988] Chapman, G. N. F., Geller, M. J., & Huchra, J. P. 1988, *AJ*, 95, 999
- [2006a] Clowe, D., Bradač, M., Gonzalez, A. H., et al. 2006a, *ApJ*, 648, L109
- [2006b] Clowe, D., Schneider, P., Aragón-Salamanca, A., et al. 2006b, *A&A*, 451, 395
- [1999] Colberg, J. M., White, S. D. M., Jenkins, A., & Pearce, F. R., 1999, *MNRAS*, 308, 593

- [1989] Colless, M., 1989, MNRAS, 237,799
- [1998] Couch, W. J., Barger, A. J., Smail, I., Ellis, R. S., & Sharples, R. M. 1998, ApJ, 497, 188
- [1969] Cox, A. N., & Stewart, J. N. 1969, Academia Nauk, Scientific Information 15, 1
- [1980] Cox, J. P. 1980, Theory of Stellar Pulsation (Princeton University Press, Princeton) 165
- [1980] Danese, L., de Zotti, G., & di Tullio, G. 1980, A&A, 82, 322
- [1996] den Hartog, R., & Katgert, P. 1996, MNRAS, 279, 349
- [2003] de Propris, R., Colless, M., Broadhurst, T., et al. 2003, MNRAS, 342, 725
- [1978a] Dressler, A. 1978a, ApJ, 222, 23
- [1978b] Dressler, A. 1978b, ApJ, 223, 765
- [1980] Dressler, A. 1980, ApJ, 236, 351
- [1983] Dressler, A., & Gunn, J. E. 1983, ApJ, 270, 7
- [1988] Dressler, A., & Shectman, S. A. 1988, AJ, 95, 985
- [1997] Dressler, A., Oemler, A. Jr., Couch, W. J., et al. 1997, ApJ, 490, 577
- [1999] Dressler, A., Smail, I., Poggianti, B. M., et al. 1999, ApJS, 122, 51
- [2003] Durret, F., Lima Neto, G. B., Forman, W., & Churazov, E. 2003, A&A, 403, L29
- [2004] Ebeling, H., Barrett, E., & Donovan, D. 2004, ApJ, 609, L49
- [1991] Eyles, C. J., Watt, M. P., Bertram, D., et al. 1991, ApJ, 376, 23
- [1979] Faber, S. M., & Gallagher, J. S. 1979, ARA&A, 17, 135
- [2007] Fadda, D., Biviano, A., Marleau, F.R., Storrie-Lombardi, L.J., Durret, F., ApJ, 672, L9
- [1995] Fukugita, M., Shimasaku, K., & Ichikawa, T. 1995, PASP, 107, 945
- [1999] Garilli, B., Maccaagni, D., & Andreon, S. 1999, A&A, 342, 408
- [2003] Gavazzi, G., Cortese, L., Boselli, A., et al. 2003, ApJ, 597, 210

## Bibliography

---

- [1999] Giovannini, G., Tordi, M., & Feretti, L. 1999, *New Astron.*, 4, 141
- [1993] Girardi, M., Biviano, A., Giuricin, G., Mardirossian, F., & Mezzetti, M. 1993, *ApJ*, 404, 38
- [1998] Girardi, M., Giuricin, G., Mardirossian, F., Mezzetti, M., & Boschini, W. 1998, *ApJ*, 505, 74
- [2000] Girardi, M., Borgani, S., Giuricin, G., Mardirossian, F., & Mezzetti, M., 2000, *ApJ*, 530, 62
- [2002] Girardi, M., Manzato, P., Mezzetti, M., Giuricin, G., & Limboz, F. 2002, *ApJ*, 569, 720
- [2003] Gómez, P. L., Nichol, R. C., Miller, C. J., et al. 2003, *ApJ*, 584, 210
- [2005] Goto, T. 2005, *MNRAS*, 359, 1415
- [2002] Goto, T., Okamura, S., McKay, T. A., et al. 2002, *AJ*, 123, 1807
- [2001] Govoni, F., Feretti, L., Giovannini, G., et al. 2001, *A&A*, 376, 803
- [2005] Hansen, S. M., McKay, T. A., Wechsler, R. H., et al. 2005, *ApJ*, 633, 122
- [1986] Horne, K. 1986, *PASP*, 98, 609
- [1992] Landolt, A. U. 1992, *AJ*, 104, 340
- [2005] Le Fèvre, O., Vettolani, G., Garilli, B., et al. 2005, *A&A*, 439, 845
- [2004] Lin, Y.-T., Mohr, J. J., & Stanford, S. A. 2004, *ApJ*, 610, 745
- [2008] Loh, Y., Ellingson, E., Yee, H.K.C., Gilbank, D.G., Gladders, M.D., Barrientos, L.F., 2008, *ApJ*, 680, 214
- [1997] Lopez-Cruz, O., Yee, H. K. C., Brown, J. P., Jones, C., & Forman, W. 1997, *ApJ*, 475, 97
- [1986] Lugger, P. M. 1986, *ApJ*, 303, 535
- [2004] Katgert, P., Biviano, A., Mazure, A. 2004, *ApJ*, 600, 675
- [2004] Kempner, J. C., & David, L. 2004, *MNRAS*, 349, 385
- [2001] Kodama, T., Smail, I., Nakata, F., Okamura, S., Bower, R. G. 2001, *ApJ*, 562, L9



- [2003] Kodama, T., Smail, I., Nakata, F., Okamura, S., Bower, R. G. 2003, *ApJ*, 591, 169
- [1980] Kron, R. G. 1980, *ApJS*, 43, 305
- [1999] Kull, A., & Böhringer, H. 1999, *A&A*, 341, 23
- [2007] Mahdavi, A., Hoekstra, H., Babul, A, Balam, D. D., & Capak, P. L. 2007, *ApJ*, 668, 806
- [2003] McCracken, H. J., Radovich, M.; Bertin, E., Mellier, Y., Dantel-Fort, M., Le Fèvre, O., Cuillandre, J. C., Gwyn, S., Foucaud, S., Zamorani, G. 2003, *A&A*, 410, 17
- [2003] Merluzzi, P., La Barbera, F., Massarotti, M., Busarello, G., & Capaccioli, M. 2003, *ApJ*, 589, 147
- [2007] Mignano, A., Miralles, J.-M., da Costa, L., et al. 2007, *A&A*, 466, 541
- [1980] Mizuno, H., 1980, *Prog. Theor. Phys.*, 64, 544
- [1996] Mohr, J. J., Geller, M. J., Fabricant, D. G., et al. 1996, *ApJ*, 470, 724
- [1996] Moore, B., Katz, N., Lake, G., Dressler, A., & Oemler, A. Jr. 1996, *Nature*, 379, 613
- [1998] Moore, B., Lake, G., & Katz, N. 1998, *ApJ*, 495, 139
- [1999] Moore, B., Lake, G., Quinn, T., & Stadel, J. 1999, *MNRAS*, 304, 465
- [2007] Moran, S.M., Ellis, R.S., Treu, T., Smith, G.P., Rich, M., Smail, I. 2007, *ApJ*, 671, 1503
- [1998] Morris, S. L., Hutchings, J. B., Carlberg, R. G., et al. 1998, *ApJ*, 507, 84
- [1965] Nelder, J. A., & Mead, R. 1965, *Computer Journal*, 7, 308
- [2007] Okabe, N., & Umetsu, K. 2007, preprint, astro-ph/0702649
- [1974] Oke, J. B. 1974, *ApJS*, 27, 21
- [1998] Oke, J. B., Postman, M., & Lubin, L. M. 1998, *AJ*, 116, 549
- [2007] Orrú, E., Murgia, M., Feretti, L., et al. 2007, *A&A*, 467, 943
- [2001] Paolillo, M., Andreon, S., Longo, G., et al. 2001, *A&A*, 367, 59
- [2008] Pierini, D., Zibetti, S., Braglia, F., et al. 2008, *A&A*, 483, 727

## Bibliography

---

- [1993] Pisani, A. 1993, MNRAS, 265, 706
- [1996] Pisani, A. 1996, MNRAS, 278, 697
- [1996] Poggianti, B. M., & Barbaro, G. 1996, A&A, 314, 379
- [1999] Poggianti, B. M., Smail, I., Dressler, A., et al. 1999, ApJ, 518, 576
- [2006] Poggianti, B. M., von der Linden, A., De Lucia, G., et al. 2006, ApJ, 642, 188
- [2004] Popesso, P., Böhringer, H., Brinkmann, J., Voges, W., & York, D. G. 2004, A&A, 423, 449
- [2005a] Popesso, P., Böhringer, Romaniello, M., & Voges, W. 2005a, A&A, 415, 429
- [2005b] Popesso, P., Biviano, A., Böhringer, Romaniello, M., & Voges, W. 2005b, A&A, 433, 431
- [2006] Popesso, P., Biviano, A., Böhringer, H., & Romaniello, M. 2006, A&A, 445, 29
- [2007] Popesso, P., Biviano, A., Böhringer, H., & Romaniello, M. 2007, A&A, 464, 451
- [2007] Porter, S.C., Raychaudhury, S., 2007, MNRAS, 375, 1409
- [2008] Porter, S.C., Raychaudhury, S., Pimblet, K.A., Drinkwater, M.J., 2008, preprint, arXiv:0804.4177
- [1997] Renzini, A., & da Costa, L. 1997, Msngr, 87, 23
- [2003] Robin, A. C., Reylé, C., Derrière, S., & Picaud, S. 2003, A&A, 409, 523
- [2002] Sakai, S., Kennicutt, R. C. Jr., van der Hulst, J. M., & Moss, C. 2002, ApJ, 578, 842
- [2008] Saintonge, A., Tran, K.V.H., Holden, B.P. 2008, preprint, arXiv:0806.2157
- [2003] Sanderson, A. J. R., & Ponman, T. J. 2003, MNRAS, 345, 1241
- [2000] Scharf, C., Donahue, M., Voit, G. M., Rosati, P., & Postman, M. 2000, ApJ, 528, L73
- [1976] Schechter, P. 1976, ApJ, 203, 297
- [1998] Schlegel, D. J., Finkbeiner, D. P., & Davis, M. 1998, ApJ, 500, 525
- [2005] Scodreggio, M., Franzetti, P., Garilli, B., et al. 2005, PASP, 117, 1284

- [2004] Selman, F. J. 2004, in *Optimizing Scientific Return for Astronomy through Information Technologies*, ed. P. J. Quinn, & A. Bridger (SPIE 5493) 453
- [2007] Sheldon, E. S., Johnston, D. E., Masjedi, M., et al. 2007, preprint, astro-ph/0709.1162
- [1992] Terlevich, R. 1992, in *ASP Conf. Ser. 31, Relationships between Active Galactic Nuclei and Starburst Galaxies*, ed. A. V. Filippenko, 13
- [2005] Tran, K.-V. H., van Dokkum, P., Illingworth, G.D., Kelson, D., Gonzalez, A., Franx, M., 2005, *ApJ*, 619, 134
- [1987] Tscharnuter, W. M. 1987, *A&A*, 188, 55
- [2004] Vandame, B. 2004, PhD thesis, University of Nice-Sophia Antinopolis
- [2008] Werner, N. et al. 2008, *A&A*, 482, 29
- [1993] Whitmore, B.C., Gilmore, D., & Jones, C. 1993, *ApJ*, 407, 489
- [1996] Yee, H. K. C., Ellingson, E., & Carlberg, R. G. 1996, *ApJS*, 102, 269
- [1980] Yorke, H. W. 1980, *A&A*, 86, 286
- [2004] Zhang, Y.-Y., Finoguenov, A., Böhringer, H., et al., 2004, *A&A*, 413, 49
- [2006] Zhang, Y.-Y., Böhringer, H., Finoguenov, A., et al. 2006, *A&A*, 456, 55
- [1997] Zheng, W., Davidsen, A. F., Tytler, D., & Kriss, G. A. 1997, preprint

## Bibliography

---

# 4

## Connecting dynamical state and galaxy populations in massive clusters

### 4.1 Introduction

X-ray emitting clusters signpost the largest amounts and concentrations of (cold) dark matter (CDM) in bound systems. At the same time, they provide large samples of coeval galaxies within a well-defined environment. This allows us to study how galaxy properties, like star formation rate (SFR) and luminosity function (LF), behave as a function of the local matter/galaxy density, and how the total mass-to-stellar luminosity ratio ( $M/L$ ) depends on the mass  $M$  of a bound system.

Detailed numerical simulations show that clusters tend to form at the intersection of filaments and sheets of matter in the evolving large-scale structure of the Universe: over time, matter falls along such structures and accretes into a cluster. The infall pattern is not random: paths show a correlation in time and are almost stable, so that matter is channeled into a cluster through filamentary structures with persistent geometry. Matter does not accrete in a steady and continuous way, but in clumps or somehow bound structures, which can be identified as infalling groups of galaxies or less massive clusters (e.g. Colberg et al. (1999)).

The galaxy LF is the integrated record of the past star formation activity in a given galaxy population; hence, it is a powerful diagnostic tool to test different models of galaxy formation and evolution. Many studies have been carried out to establish the properties of the LF for field and cluster galaxies, based either on individual clusters or on cluster samples (to increase statistics and investigate the presence of

## 4 Connecting dynamical state and galaxy populations in massive clusters

---

a universal galaxy LF). They lead to opposite results: the existence of different field and cluster LFs (Dressler (1978a); Lopez-Cruz et al. (1997); Garilli et al. (1999); Goto et al. (2002); Hansen et al. (2005)) against a universal LF (Lugger (1986); Colless (1989); Paolillo et al. (2001); de Propris et al. (2003)). In particular, the shape of the galaxy LF at the faint end has been subject of controversy. Popesso et al. ((2005a)) analysed a sample of 97 clusters at  $z \leq 0.25$  - selected from the RASS-SDSS galaxy cluster catalogue - and proposed a universal cluster LF made of two components: a bright-end LF with a classical slope  $\alpha = -1.25$  in the SDSS *griz* bands, and a steeper faint-end LF ( $-2.1 \leq \alpha \leq -1.6$ ). The upturn in the LF slope happens at magnitudes fainter than  $-16+5\log(h)$  in the SDSS *g* band ( $-18.5+5\log(h)$  in the *z* band), where the population of dwarf galaxies sets in. A universal cluster LF may sound at odds with the morphology dependence of the LF for cluster galaxies (Binggeli et al. (1988)), given the existence of a morphology-density relation for galaxies (Dressler (1980)). A change in the LF shape with cluster-centric distance was observed in previous studies (Beijersbergen et al. (2002); Goto (2005); Hansen et al. (2005)). This radial dependence was also found in the RASS-SDSS sample by Popesso et al. ((2006)) and mainly ascribed to the effect of galaxy harassment on dwarf galaxies (see Moore et al. (1996)). Recently Barkhouse et al. ((2007)) have confirmed the dependence of the LF shape on the cluster-centric distance in a sample of 57 low-redshift Abell clusters. In particular, they find the LF to become shallower and dimmer with decreasing cluster-centric distance, which is attributed to the interaction between infalling galaxies and the intracluster medium (ICM) via ram-pressure stripping and tidal disruption in the cluster core.

If the cluster optical luminosity accounts for the evolution in number and luminosity of the galaxy population, the cluster mass mostly accounts for the amount of dark matter that has been bound to the system through time. Hence, the cluster  $M/L$  measures the relative efficiency of these two processes. Early optical studies pointed to high mean values of  $M/L$  in small samples of clusters:  $M/L_B \sim 750h M_\odot/L_\odot$  or  $M/L_V \sim 580h M_\odot/L_\odot$  (Faber & Gallagher (1979)) and  $M/L_R \sim 200-600h M_\odot/L_\odot$  (Dressler (1978a)). Later optical studies indicated lower values:  $M/L_B \sim 190h M_\odot/L_\odot$  in Abell 194 (Chapman, Geller, & Huchra (1988)) and  $M/L_B \sim 200h M_\odot/L_\odot$  in Perseus (Eyles (1991)). Similar values were found when an X-ray estimate of cluster mass is used instead of the virial mass estimate:  $M/L_B \sim 400h M_\odot/L_\odot$  in 29 ENACS clusters (Adami et al. (1998b)),  $M/L_R \sim 300h M_\odot/L_\odot$  in CNOC1 clusters (Carlberg et al. (1996)). In a more recent study, Sanderson & Ponman ((2003)) find a mean  $M/L_{B_j} \sim 350h M_\odot/L_\odot$  - scaled to  $M/L_{R_c} \sim 190h M_\odot/L_\odot$ . for a sample of 66 relaxed groups and clusters. With better statistics and a deeper sampling of the group-mass regime ( $10^{12} < M < 10^{14} M_\odot$ ), trends between  $M/L$  and  $M$  or  $L$  have been found, whether cluster masses are estimated from the galaxy velocity dispersion (Girardi et al. (2000); Girardi et al. (2002)) or from X-ray observables (Popesso et al. (2007); see also Lin et al. (2003), (2004) for the cluster

## 4.2 The data and cluster member catalogues

---

mass-to-near-infrared luminosity ratio).

This paper is organised as follows. In Sect. 4.2 the available data, their properties and treatment are briefly summarized. Sect. 4.3 introduces the dynamical analysis performed on the two clusters and shows the results. Sect. 4.4 covers the study of the luminosity function and its dependence on different cluster regions, the determination of total cluster luminosity and the evaluation of mass-to-light ratio. Results are discussed in Sect. 4.5.

In this paper we adopt a  $\Lambda$ CDM cosmology where  $\Omega_m = 0.3$ ,  $\Omega_\Lambda = 0.7$ , and  $h_{70} = H_0/70 \text{ km s}^{-1} \text{ Mpc}^{-1} = 1$ .

## 4.2 The data and cluster member catalogues

Data reduction and catalogue preparation was extensively presented in Braglia et al. (2008a, in prep.). Thus, herein only a short review will be given.

Optical spectroscopy was performed with VIMOS in low resolution mode (LR-Blue grism), efficiently sampling the observed-frame 360-670 nm spectral range with a mean spectral resolution of 200. At the clusters redshift, this is the region where interesting spectral features (namely [OII], [OIII],  $H_\beta$ ,  $H_\gamma$ ,  $H_\delta$ ,  $\text{CaII}_{H+K}$  and 4000 Å break) are found. This enables an unambiguous determination of peculiar velocity and star formation activity in cluster members. Typical velocity errors were found to be in good agreement with previous determinations from VVDS for the same instrumental setup (cfr. Le Fèvre et al. (2005), where a mean value of  $276 \text{ km s}^{-1}$  is found).

Cluster spectroscopic membership was determined using the technique extensively explained in Biviano et al. ((2006)). For a better determination of cluster members and a more precise virial analysis (see Sect. 4.3), each galaxy was assigned a statistical weight to correct for uneven sampling of the cluster region (see Sect. 4.2.1). Where available, archival spectra from *NED* were added to our spectroscopic catalogues. This was only possible for RXCJ0014.3-3022, for which 101 additional redshifts (89 of which proved to be consistent with the cluster one) were available. The spectroscopic catalogue was then cross-correlated with the photometric one to re-identify galaxies and associate colours and spectral information. For RXCJ0014.3-3022, additional available redshifts were also retrieved from *NED* and added to our data. The final spectroscopic member catalogues for the two clusters have 190 objects for RXCJ0014.3-3022 and 292 objects for RXCJ2308.3-0211. The cluster spectroscopic red sequences were fitted through recursive  $3\text{-}\sigma$  clipping linear regression and found to be in good agreement with each other (see Braglia et al. 2008a, in prep.).

Optical photometry in BVR bands was performed with WFI. Photometric catalogues, complete down to  $R = 23.5$ , were constructed for both clusters. The clusters photometric red sequences were fitted through recursive  $3\text{-}\sigma$  clipping linear regres-

## 4 Connecting dynamical state and galaxy populations in massive clusters

---

sion and found to be in good agreement with each other and with the spectroscopic red sequences. Objects were flagged as red or blue according to their position with respect to the red sequence in the (B-R) vs. R diagram (red if within  $3\sigma$  from the red sequence, blue if more than  $3\sigma$  bluer than the red sequence). Photometric redshifts were calibrated against available spectroscopic redshifts and were found to have a typical error of  $\Delta z_{phot} = 0.06$  at the clusters redshift of  $\sim 0.3$ . Photometric redshifts were then used to select photometric cluster members, resulting in two catalogues with comparable numbers of cluster members: 3698 for RXCJ0014.3-3022, 4109 for RXCJ2308.3-0211. RXCJ0014.3-3022 has a slightly higher redshift but a much larger fraction of blue galaxies. Its mean photometric redshift of 0.34 results in a higher value than the spectroscopic redshift of 0.3068, owing to the coupling of these properties with the filter functions (see the discussion in Braglia et al. 2008a). Consistently, RXCJ2308.3-0211, with a largely red galaxy population (i.e. passively evolving ellipticals), has a photometric redshift of 0.29, well in agreement with the spectroscopically confirmed value of 0.2966. Absolute magnitudes were calculated in the B, V and R band as:

$$M = m - DM(z_{phot}) - K(z_{phot})$$

where  $DM(z_{phot})$  is the distance modulus and  $K(z_{phot})$  is the K-correction, both functions of the photometric redshift of the galaxy. The K-correction was calculated from the filter response curve and the spectral template providing the best fit to the photometry of the object. Where available, optical photometry was complemented with archival GALEX photometric data of the two observed regions, to obtain a clearer picture of the star formation activity in the two clusters.

### 4.2.1 Statistical weighting of spectroscopic cluster members

Since spectra were obtained only for a fraction of available targets and in an unevenly covered part of the cluster region, it is necessary to correct for incompleteness and selection effects by assigning a statistical weight to each object in the spectroscopic catalogue. This allows to more precisely account for incompleteness in the calculation of mass and other dynamics-related quantities (see Sect. 4.3).

Statistical weights were calculated by comparing the catalogues of photometric cluster members (as defined from photo-z classification) and candidate spectroscopic cluster members, for each cluster. All spectroscopic redshifts within 0.05 of each cluster mean redshift were selected; this allows all potential cluster members to be accounted, while minimizing contamination from outliers. Similarly to Yee et al. (1996) and following works, we define the statistical weight of a spectroscopic cluster member as the inverse of its selection function:

$$w(x, y, m) = (S(x, y, m))^{-1}$$



## 4.2 The data and cluster member catalogues

---

where the  $S(x, y, m)$  depends on galaxy position  $(x, y)$  in the field of view and galaxy magnitude  $m$ . This last variable accounts for the cluster's population: as faint galaxies outnumber bright ones, it is usually possible to sample a larger fraction of bright cluster members than faint ones. Moreover, our spectroscopic observation strategy produces an intrinsic better coverage of the cluster core than of the outskirts.

From the photometric catalogue only objects falling in the combined VIMOS window pattern were selected. This automatically corrects for the different unevenness of spectral sampling at different cluster-centric radii and for the larger relative number of photometric members (available for a wider region) with respect to spectroscopic ones. Objects in the two catalogues (spectroscopic and photometric) were then divided into bright and faint ones, using the characteristic  $R^*$  of RXCJ0014.3-3022 as cutting magnitude ( $R^* = 19.6$ , see Busarello et al. (2002)). The weight calculation was performed in circular annuli centred on the X-ray centroid of each cluster. To obtain a stabler sampling of the outskirts and a finer sampling in the core, quadratic increases of annular radii were chosen according to the formula  $R = (x/2)^2$  arcmin, with  $x$  running from 0 to 10. In this way, the core is sampled with smaller areas, while in the outskirts large annuli compensate for undersampling. In each annulus, the ratio of spectroscopic to photometric members was calculated, independently for bright and faint objects. This is taken as the selection function in each annulus, and each spectrum in that region is assigned this value of  $S(x, y, m)$ . In principle, a colour selection function could be applied to further refine the weights, however the spectroscopic target selection strategy (the I-band pre-imaging) was aimed at homogeneously selecting galaxies without introducing biases towards star-formation activity (i.e., colour). Hence, the effect of colour on the selection function can be neglected without any risk for over- or under-weighting. Moreover, this is shown to be a minor effect in many cases, the associated correction term having an almost constant value of  $\sim 1$  across different fields and galaxy populations (see Yee et al. (1996)). This approach provides a natural way to easily evaluate both the effect of geometrical distribution, via the radial slicing, and the influence of magnitude selection, which is particularly evident in the centre where a larger number of bright galaxies are sampled with respect to the outskirts.

Fig. 4.1 shows that bright objects have on average lower weights than faint ones. This is due to the target selection, since bright objects were flagged as mandatory in the VIPGI selection process (see Braglia et al. 2008a) and as such were more efficiently sampled over the cluster area. The radial distribution of weights also shows that in the central region of the clusters objects were sampled with greater efficiency and thus have smaller weights. This is again due to the observation strategy, where the cores were covered with multiple VIMOS masks to ensure a complete coverage of cluster members in these regions. Objects in RXCJ2308.3-0211 have smaller weights, as more spectra were collected in this cluster, especially in the outskirts.

In Fig. 4.2 the spatial distribution of weights of cluster members is shown for each

## 4 Connecting dynamical state and galaxy populations in massive clusters

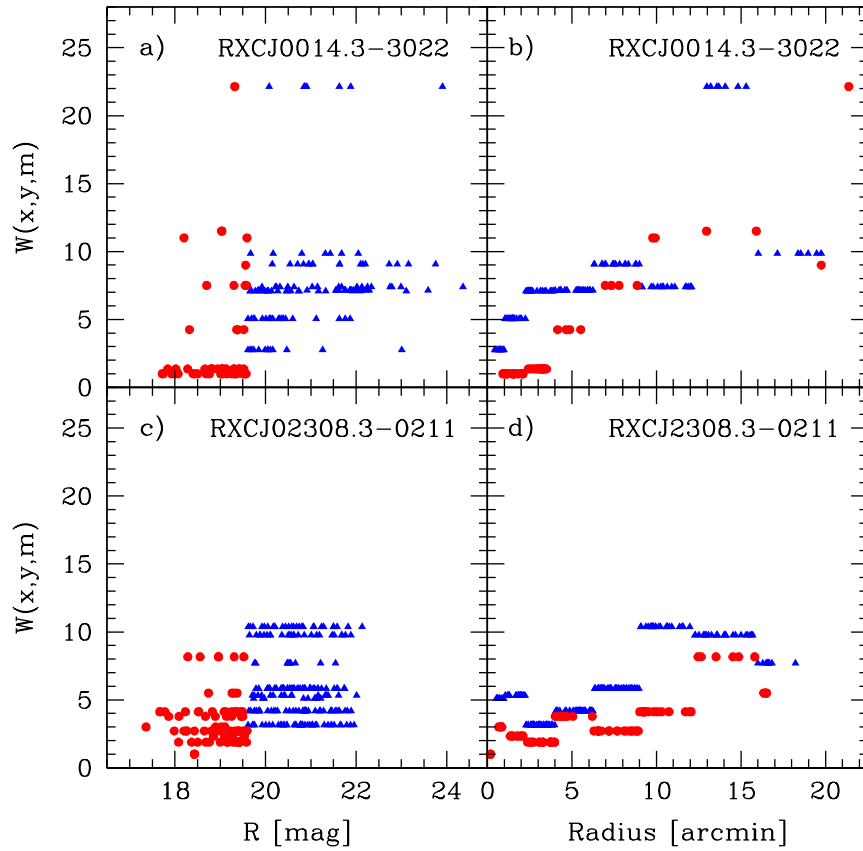


**Figure 4.1:** Distribution of weights versus R magnitude and cluster-centric distance for RXCJ0014.3-3022 (panels a and b) and for RXCJ2308.30-0211 (panels c and d). Red dots mark the bright objects, blue triangles the faint ones.

cluster. Galaxies are marked depending on the value of their weight with respect to the mean weight,  $\bar{w}$ , equal to 6.3 for RXCJ0014.3-3022 and to 5.2 for RXCJ2308.3-0211 (this value is only used here to provide an internal definition of “low” and “high” weight in each cluster and does not play a role in the following analysis). Objects with low weights ( $w \leq \bar{w}$ ) are mainly found in the better sampled inner regions of the clusters, whereas those with high weights ( $w > \bar{w}$ ) are more commonly found in the outskirts. This is particularly evident in RXCJ0014.3-3022, where the outskirts lack an even coverage. A few very high weight objects ( $w > 2\bar{w}$ ) are also found in the very outer regions of RXCJ0014.3-3022. Conversely, low weight objects in RXCJ2308.3-0211 are found to larger cluster-centric radii and no very high weight objects are

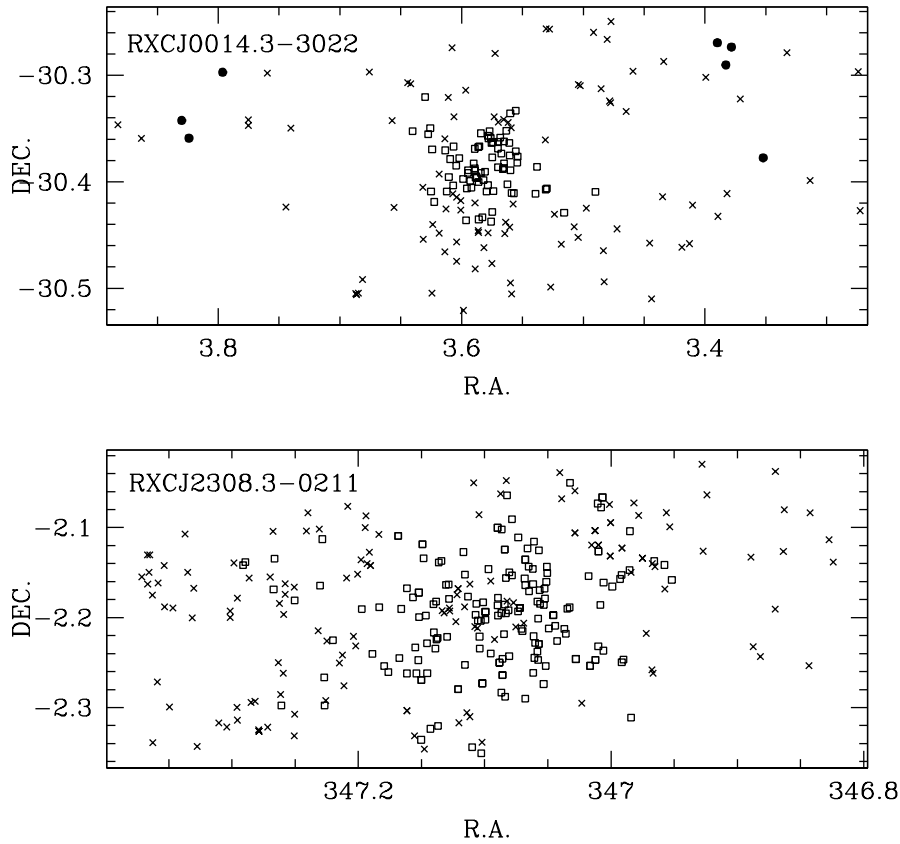


**Figure 4.2:** Spatial distribution of weights for cluster members of RXCJ0014.3-3022 (top panel) and RXCJ2308.3-0211 (bottom panel). Low weight objects (empty squares) are mainly concentrated in the central regions where sampling is more efficient, while heavier objects (crosses) lie in the outer part. In the outskirts of RXCJ0014.3-3022, some very high weight objects (filled circles) are also found.

found.

### 4.3 Dynamics

A first-order dynamical analysis for RXCJ0014.3-3022 was performed in BPB07. A double-peaked velocity structure was identified with high significance with a very high velocity dispersion. A Dressler-Schechtman (DS) analysis was then run on the cluster members to locate the presence of substructuring: we were able to detect two

## 4 Connecting dynamical state and galaxy populations in massive clusters

---

interesting dynamical substructures corresponding to the two large-scale filaments connected to the cluster. From their velocity difference, we argued that the NW filament is infalling from behind into the cluster with a velocity component towards the observer, while the S filament is apparently falling into the cluster from our direction, with negative radial velocity. The cluster mass was also roughly calculated from the total velocity dispersion to several  $10^{15} M_{\odot}$ . However, this value should be considered a guess of the order of magnitude of the mass, as it was calculated assuming a spherical, relaxed cluster.

In this section the mass and dynamical parameters will be calculated with greater precision for each cluster, making use of all cluster member redshifts available and using the virial analysis extensively illustrated in Biviano et al. ((2006)) and already applied in several other studies (see for instance Girardi et al. (1998) and Popesso et al. (2007)). Hereafter, the X-ray centroid of each cluster is used as effective cluster centre for our analysis. Candidate cluster members were first identified by applying in succession the biweight estimator of Beers et al. ((1990)), the weighted gap selection of Girardi et al. ((1993)) and finally the den Hartog & Katgert procedure (REF.NEED.) to check the position of galaxies in the projected phase space. A preliminary virial analysis and a DS test were then run on all selected objects. This enabled us to identify objects that, although lying at the same redshift of the cluster and within its velocity dispersion, could belong to different structures unbound to the cluster (i.e. isolated groups at the cluster redshifts). In both clusters a small concentration of such objects was found, corresponding to regions where a small group was seen in the optical images and galaxy density maps (see Braglia et al. 2008a, in prep.). These objects have DS parameter larger than 3 and lie in both cases beyond the clusters  $R_{200}$ , confirming that they are dynamically unrelated. Rejection of these objects (16 from RXCJ0014.3-3022, 23 from RXCJ2308.3-0211) was found to give smaller errors on velocity dispersions and mass estimate (by about 20%) and a lower value of  $R_{200}$  ( $\sim 10\%$  smaller values). After this additional rejection, the virial analysis was applied on the two resulting cluster member catalogues of 164 and 269 robustly selected members (for RXCJ0014.3-3022 and RXCJ2308.3-0211, respectively).

The results of the virial analysis were found to be sensitive to the choice of different parameters. The best working parameters were thus determined by trial and comparison of results on the two catalogues. The results appear to be mainly affected by the choice of the limiting radius for detection of the main velocity peak and of the aperture radius within which the virial analysis is performed. Another important parameter is whether only red (i.e. passively evolving) galaxies should be used in the calculation of velocity dispersion and mass. This is found to be heavily dependent on the cluster, with RXCJ2308.3-0211 being less affected than RXCJ0014.3-3022 by this parameter. Other variables have a smaller effect, namely the influence of centering method (whether obtained by biweighting the galaxy positions and velocities or from

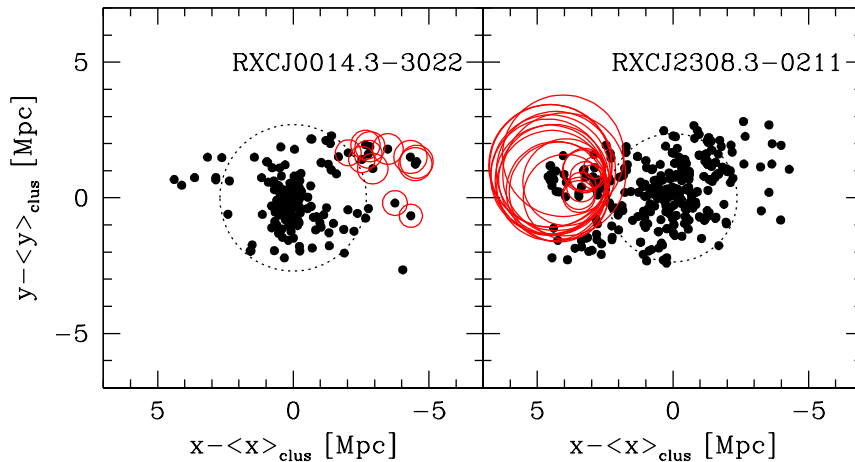


**Figure 4.3:** Dressler-Schechtman analysis for the two clusters. Red circles are centred on candidate members with high ( $\geq 3$ ) DS parameter. The circle radii are proportional to  $e^{P_{DS}}$ , where  $P_{DS}$  is the DS parameter.

X-ray derived data) and the inclusion or exclusion of literature-drawn redshifts for RXCJ0014.3-3022 that only probe the cluster central Mpc.

Biweighting and weighted gap techniques were chosen to isolate cluster members, rejecting afterwards interlopers with combined den Hartog and Katgert procedure and DS test analysis, as already explained. The X-ray centroid was always used as nominal cluster centre. The harmonic radius was calculated accounting for individual weights for each galaxy. Errors were estimated using the jackknife analysis. The red objects were used to actually determine velocity dispersions and dynamical masses, as they are likely to be less affected by large-scale infall motion, are largely free of interlopers and are expected to more suitably probe the cluster potential (see Biviano et al. (2006)). For each cluster, we determined the values of total velocity dispersion,  $R_{200}$  and  $M_{200}$  with all available red galaxies from our spectroscopic catalogues. A radial mass profile was also extracted using only galaxies within multiple radii of  $0.1R_{200}$ , starting from  $0.2R_{200}$ . Fig. 4.4 shows the velocity distribution for cluster members (already pruned of outliers) in the two clusters.

#### 4.3.1 RXCJ0014.3-3022

The rest-frame velocity distribution for RXCJ0014.3-3022 shows two peaks with broad wings where peculiar velocities can exceed  $4000 \text{ km s}^{-1}$  (see also Boschin et al. (2006); Braglia et al. (2007)). This distribution is reflected both in the red

## 4 Connecting dynamical state and galaxy populations in massive clusters

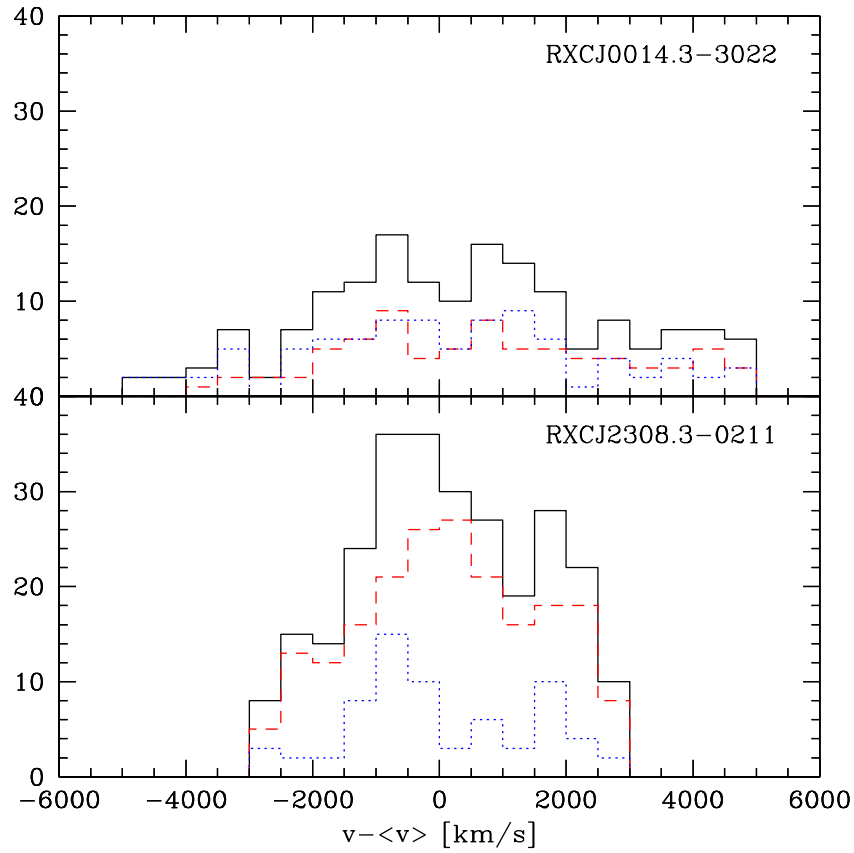


**Figure 4.4:** Rest-frame peculiar velocity distributions for the two observed clusters. The continuous black histogram shows the distribution of all cluster members. The dashed red and dotted blue histograms represent respectively the velocity distribution of red and blue cluster members, as defined with respect to the cluster red sequence.

and blue galaxies. This cluster is known as an ongoing major merger: Boschin et al. ((2006)) calculated a mass ratio of 3:1 for the two main components in the core.

With the parameters discussed above, a total of 117 red cluster members were used for the virial analysis. We found for  $r_{200}$  a value of  $2.69h_{70}^{-1}$  Mpc and a mean velocity dispersion for the full cluster of  $(1405 \pm 81)$  km/s. The total mass within  $r_{200}$  is found to be  $(2.708 \pm 0.378) \times 10^{15} h_{70}^{-1} M_{\odot}$ <sup>1</sup>. For comparison, the total mass

<sup>1</sup>The extrapolated cluster mass within  $4.82h_{70}^{-1}$  Mpc (where the farthest cluster member lies) is  $(5.34 \pm 1.02) \times 10^{15} h_{70}^{-1} M_{\odot}$ . This value, though, relies on a large extrapolation beyond  $r_{200}$ , thus

within  $r_{200}$  obtained from velocity dispersion alone is  $(3.490 \pm 0.384) \times 10^{15} h_{70}^{-1} M_{\odot}$ . The concentration parameter for the NFW halo profile with the velocity dispersion found is 3.23. The error on the mass is relatively large ( $\Delta M/M=0.14$ ). This suggests that the cluster is dynamically very complicated, with substructures and an overall non relaxed state that makes the mass estimate difficult. This is also evident from the very large value of the velocity dispersion and of its error (about 6%). For comparison, making use of all available cluster members (161 objects) provides the following values:  $R_{200} = 2.87 h_{70}^{-1}$  Mpc,  $M_{200} = (2.707 \pm 0.297) \times 10^{15} h_{70}^{-1} M_{\odot}$  and  $\sigma_v = (1326 \pm 64)$  km/s.

The X-ray mass of the cluster was estimated in Zhang et al. (2006). To obtain a determination as unaffected as possible by the merger, the X-ray substructure seen in XMM-Newton data (and corresponding to one of the two peaks detected from the galaxy density maps) was cut from the analysis. This gave a mass estimate of  $(7.4 \pm 2.9) \times 10^{14} h_{70}^{-1} M_{\odot}$  within 1.24 Mpc (i.e.  $R_{500}$  as derived from X-ray data) from the X-ray centroid. Limiting our analysis to the same region (and excluding the cluster members identified as part of the southern filament to avoid contamination from secondary structures), we find a dynamical mass of  $(1.062 \pm 0.159) \times 10^{15} h_{70}^{-1} M_{\odot}$ , with a velocity dispersion of  $1136 \pm 74$  km/s: thus, within  $R_{500}$  a loose agreement between optical and X-ray masses is found, although with a relatively large error (the dynamical mass within  $R_{500}$  being about 40% higher than the X-ray mass). The higher mass found by dynamical analysis has to be ascribed to the merger and its boosting effect on the velocity dispersion in the core. X-ray mass was derived assuming the ICM in hydrostatic equilibrium. However, due to the ongoing merger, it is likely that this assumption is no more valid. As already shown in Rasia et al. ((2004)), different gas models can provide different mass estimates by up to 40% around  $R_{200}$ . Thus, considering for instance incomplete ICM thermalization (likely in the case of a major merger), the observed discrepancy in the two mass determinations could drop to 10%, i.e. well within errors. With available data, it was also possible to derive the mass profile and velocity dispersion profile within  $1.5R_{200}$ , i.e.  $4.035 h_{70}^{-1}$  Mpc. The profiles are shown in Fig. 4.5. The mass profile is in relatively good agreement with a NFW profile outwards of  $0.5R_{200}$  within the error limits. The deviation at smaller radii is mainly due to lack of more redshifts in the central region of the cluster.

#### 4.3.2 RXCJ2308.3-0211

RXCJ2308.3-0211 is a typical relaxed, dynamically old cluster. The velocity distribution of its red galaxies is symmetric and peaked at zero, whereas the asymmetric peaks are mainly due to the few blue galaxies in its outskirts. For this cluster 195

---

it will not be used: we will always refer to the cluster mass at  $r_{200}$ .

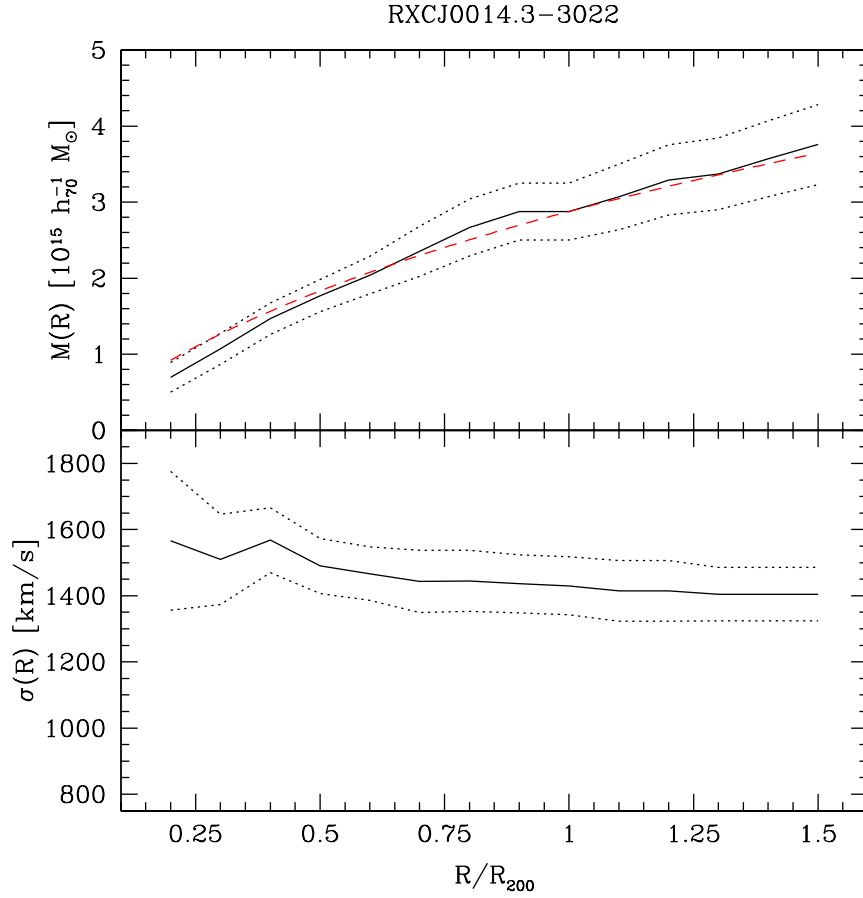


**Figure 4.5:** Radial behaviour of dynamical mass (top panel) and velocity dispersion (bottom panel) for RXCJ0014.3-3022. Dotted lines show  $1\text{-}\sigma$  errors. Superposed (red dashed line) to the radial mass profile is a NFW profile with concentration parameter  $c = 3$ .

red cluster members were used for the virial analysis. We calculate a dynamical mass of  $(1.396 \pm 0.139) \times 10^{15} h_{70}^{-1} M_{\odot}$  within  $R_{200} = 2.38 h_{70}^{-1}$  Mpc. The velocity dispersion is  $(869 \pm 36)$  km s $^{-1}$  and the mass inferred from velocity dispersion alone is  $(0.989 \pm 0.099) \times 10^{15} h_{70}^{-1} M_{\odot}$ . The concentration parameter for the NFW halo is 3.74. The use of all cluster members (i.e. red and blue galaxies) provides rather similar values, which confirms this cluster being largely virialized and unaffected by large-scale interactions or groups of interlopers. For comparison, the values obtained with all 269 cluster members are  $R_{200} = 2.45 h_{70}^{-1}$  Mpc,  $M_{200} = (1.512 \pm 0.106) \times 10^{15} h_{70}^{-1} M_{\odot}$  and  $\sigma_v = (868 \pm 27)$  km/s. Also for this cluster the mass estimate and the



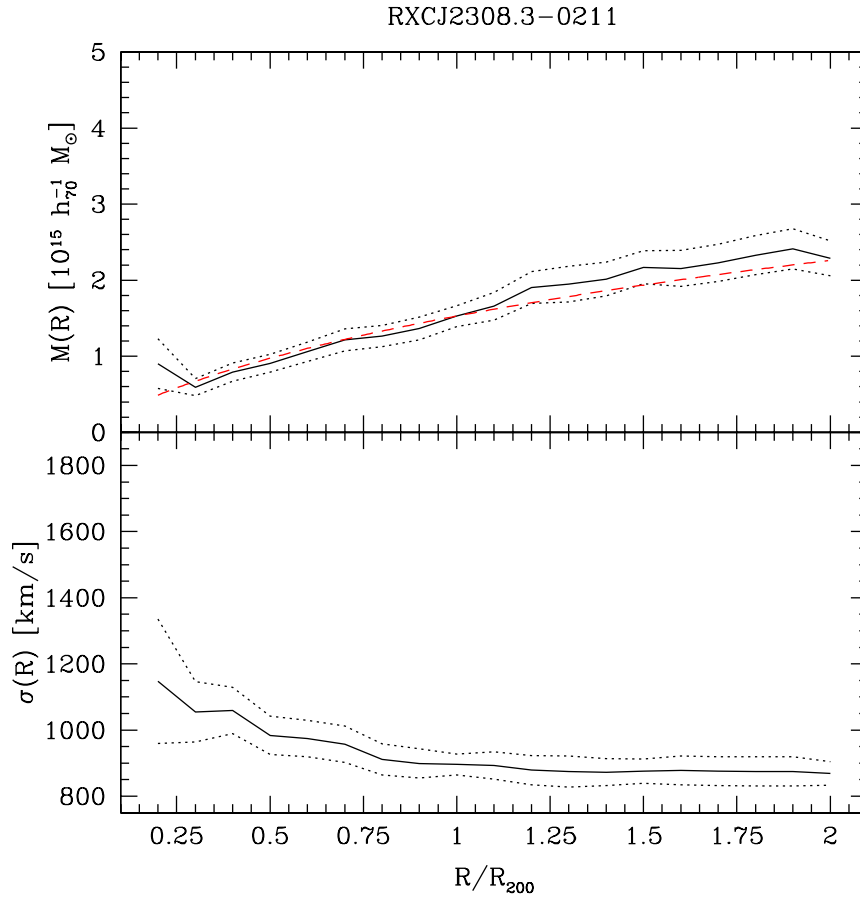


**Figure 4.6:** Radial behaviour of dynamical mass (top panel) and velocity dispersion (bottom panel) for RXCJ2308.3-0211. Dotted lines show  $1\text{-}\sigma$  errors. Superposed (red dashed line) to the radial mass profile is a NFW profile with concentration parameter  $c = 3$ .

velocity dispersion are largely unreliable in the inner  $0.5R_{200}$ . This is again due to lack of enough spectra in the central region.

The X-ray mass of the cluster (see Zhang et al. (2006)) is  $(7.4 \pm 1.8) \times 10^{14} h_{70}^{-1} M_{\odot}$  within an X-ray derived  $R_{500}$  of 1.24 Mpc. Within the same radius, the dynamical analysis provides a mass of  $(9.56 \pm 1.24) \times 10^{14} h_{70}^{-1} M_{\odot}$ . Although this value is still about 30% higher than the X-ray value, the two values are in agreement within errors. The available redshifts allowed us to derive the radial mass profile and velocity dispersion out to  $2R_{200}$ , corresponding to  $4.76 h_{70}^{-1}$  Mpc. The profiles are shown in Fig. 4.6.

### 4.4 Optical luminosity function

The luminosity function is derived in the B, V, and R bands for all the photometric member galaxies of each cluster, for interesting regions of each cluster, and in the neighbouring low-density region (i.e., the field) at the cluster redshift. This field is used to estimate and correct for the contamination from residual foreground or background interlopers which can affect different cluster regions, since the typical uncertainty of photo- $z$ 's corresponds to large values of the systemic velocity along the line of sight. As shown by Popesso et al. ((2004)), the choice of a local region as a comparison field leads to a fair determination of the background, which does not affect the estimate of luminosity function parameters.

Our photometry is complete down to  $R = 23.5$ , which corresponds to a rest-frame R-band absolute magnitude  $M_R$  in the range between -17.5 and -18 (as a function of the  $k$ -correction) at the distance of the two clusters. Hence, it does not probe the dwarf galaxy population of the clusters (cfr. Popesso et al. (2004), (2005a)), although it reaches  $\sim R^* + 4$ . Therefore, we can describe the galaxy luminosity function at the cluster redshift with a single Schechter function (Schechter (1976)). This LF is expressed in terms of the absolute magnitude as:

$$n(M)dM = N^*k \times [10^{(M^*-M)(\alpha+1)}]e^{[-10^{-0.4(M^*-M)}]},$$

where  $k = 0.4 \log 10$ ,  $M^*$  is the characteristic absolute magnitude,  $\alpha$  is the slope of the faint end, and  $N^*$  acts as a normalization parameter (see Colless (1989); Barkhouse et al. (2007)). The statistical scatter of counts is assumed to follow a Poissonian distribution, i.e.:  $\sigma_N = \sqrt{N(m)}$ .

In general, the LF is fitted to the data by standard  $\chi^2$  minimization, where:

$$\chi^2 = \sum_i \frac{(N_i - n(M_i))^2}{\sigma_i^2}.$$

Here  $N_i = N_i^{clus} - N_i^{bg}$ , i.e., the net galaxy counts in each magnitude bin (i.e., the total number of objects minus the number of objects in the field for the  $i$ -th magnitude bin), whereas  $n(M_i)$  is the expected number of objects in the  $i$ -th bin from the Schechter function, and  $\sigma_i$  is the uncertainty of the counts in the same bin, given by:

$$\sigma_i = \sqrt{(N_i^{clus} + N_i^{bg})}.$$

Solutions (i.e., the best-fit parameters) were found by means of the IDL routine *AMOEBA*, which performs multi-dimensional minimization using the Nelder–Mead (Nelder & Mead (1965)) simplex method in parameters space. This method can generally be less efficient than other algorithms (e.g., the Powell's derivatives method)

and may require a larger number of iterations; however, it does not require the computations of derivatives. The dependence of convergence on bin width was explored: the result is found to be slightly dependent on binning for widths smaller than 0.4 mag. In particular, for widths smaller than 0.2 mag convergence is not reached owing to extremely noisy counts. A bin width of 0.5 mag was chosen since it provides a robust and detailed sampling of the galaxy distribution as a function of magnitude. The convergence of the fit was reached in less than 10 iterations.

An initial guess for each fit parameter was supplied; it was selected from a reasonably large region of the parameter space, centred on typical values available in the literature. This allowed to test the robustness of the minima found by the algorithm against initial conditions. Multiple trials were found to unerringly converge to the same best-fit values. The uncertainty of each best-fit parameter was backwards-calculated after convergence using the technique explained in Avni ((1976)). This technique works as follow: for each parameter (i.e.,  $\alpha$  and  $M^*$ ), the  $1\sigma$  error is found by projecting the confidence contour of  $\Delta\chi = 2.3$  (i.e., the contour width for a set of two parameters) on the parameter space around the minimum, after minimizing with respect to  $N^*$ . The ensuing errors are found to be globally symmetric, at the  $1\sigma$  level, with respect to the minimum.

### 4.4.1 Total cluster luminosity

The luminosity of each galaxy, expressed in  $L_{\odot}$ , was derived from the galaxy absolute magnitude (see Sect. 4.2). Conversion from absolute magnitude to absolute luminosity in units of solar luminosities ( $L_{\odot}$ ) was calculated with the same method originally introduced in Fukugita et al. ((1996)) and applied in several studies (e.g. Popesso et al. (2004)). For better comparison with previous works, the total luminosity was converted from AB system to classical Vega magnitudes using standard conversions for the filters used. We also calculated conversion factors from the rather anomalous WFI filters (particularly the #844  $R_C/162$  filter, for which a large leak is known beyond  $\lambda = 11000 \text{ \AA}$ ) into standard Johnson filters. The conversion factor was calculated again adopting the same technique of Fukugita et al. ((1996)). Specifically, the Vega SED model (spectral type A0V,  $T_{eff} = 9520 \text{ K}$ ) from Kurucz Spectral Atlas was convolved with the BVR filters of Johnson and the conversion factor was derived from the ratio of these quantities with the corresponding Vega absolute magnitudes in the WFI BVR filters.

For each cluster, the total luminosity was calculated with three different methods. Firstly, the total cluster luminosity was calculated by summing all cluster member luminosities (see for instance Miller et al. (2005)). Only galaxies classified as photometric cluster members were summed. The total optical luminosity of the field galaxy population is normalized in order to account for the different areas occupied by the field and the cluster as a whole, and then subtracted from the optical luminosity of

## 4 Connecting dynamical state and galaxy populations in massive clusters

---

the full cluster photometric sample. Uncertainties were calculated from photometric errors as for the standard error propagation theory. Typical error values are of order of a few percent of the total luminosity. This method provides a reliable evaluation of the cluster total luminosity down to the magnitude limit, although it does not provide a way to compensate for this incompleteness.

For comparison, the total luminosity can also be derived from the shape of the luminosity function. This method has the advantage of providing an intrinsic correction for incompleteness, although the errors are usually larger. The total cluster luminosity is thus calculated by integration of the LF and extrapolation to the faint end:

$$L_{tot} = \sum_i n_i(M) L_i(M) + \int_{M_{lim}}^{\infty} n(M) L(M) dM,$$

where the sum is performed over all magnitude bins of the LF fit,  $L_i(M)$  is the luminosity (in units of  $L_{\odot}$ ) in the  $i$ -th magnitude bin, and the integral is the incompleteness correction, which compensates for the magnitude limit of our sample. This correction corresponds to a small fraction of the total luminosity: it lies around 3% of the total luminosity, with a small increase from the R to the B band. This behaviour is mainly due to the dimming of the knee of the LF from R to B band, which produces a shift of the LF across the magnitude limit, with the consequence of increasing the correction factor. The uncertainty on the total optical luminosity of the cluster is calculated from the errors in the LF, taking into account the noise from background subtraction:

$$\Delta L = \left( \sum_i (\sigma_i^N(M)^2 + \sigma_i^{BG}(M)^2) \right)^{1/2} L_i(M).$$

The typical error obtained with this method is of the order of 10% of the total luminosity.

Finally, a third method, also discussed in Popesso et al. ((2004)), is applied. It adopts the best-fit parameters of the LF to calculate the total optical luminosity of a cluster according to the following formula:

$$L = L^* (N_{clus} / \Delta_i) \Gamma(2 + \alpha).$$

where we added to the original equation an additional term  $1/\Delta_i$  ( $\Delta_i$  being the bin width, in our case 0.5 mag) to correct for the different normalization adopted in this work. This method can not compensate for background contamination; however we can assume that the photo- $z$  selection and the further background subtraction have minimized the impact of background contamination on the LF best-fit parameters. Hence, the uncertainty is carried by the uncertainty affecting these parameters. Consistently, the typical statistical error is obtained by computing the value of the

## 4.4 Optical luminosity function

Region	Radius	Angle	Objects	Area
Cluster core	$0' \leq r \leq 3'$	$0' \leq \theta \leq 360'$	304	$9\pi$
NW filament	$3' < r \leq 15'$	$-10' \leq \theta \leq 50'$	359	$36\pi$
S filament	$3' < r \leq 15'$	$260' \leq \theta \leq 320'$	374	$36\pi$
BG field	$6' < r \leq 18'$	$120' \leq \theta \leq 210'$	488	$72\pi$

**Table 4.1:** Definition of regions of interest in RXCJ0014.3-3022. Areas are expressed in square arcminutes.

function along the  $1\sigma$  ellipsoid in the parameter space  $\alpha-M^*$ . The typical errors from this method amount to 20% of the total cluster luminosity.

Comparison of results of the three methods shows an overall agreement of the three determinations. Method 3 always gives larger errors and slightly ( $\sim 5\% - 10\%$ ) larger luminosities. In the B band, the discrepancy is larger, since less objects are detected and their photometric errors are larger. Since method 1 (the direct sum over galaxies) gives the smallest errors, we will only use this as our actual luminosity determination. We also add the incompleteness correction derived from method 2 (i.e. from the luminosity function) to obtain a better determination of the total cluster luminosity.

### 4.4.2 Luminosity function parameters for RXCJ0014.3-3022

Overall the cluster environment comprises its core and the two filaments (see Braglia et al. (2007) and Braglia et al. 2008a). Here a third region is associated with it: an annular ring centred on the X-ray centroid and limited by radii of 3 and 5 arcmin, excluding the filaments. This region extends to where the overdensity of red galaxies is still significant at more than  $5\sigma$ . It contains 128 objects, bringing the total number of cluster members to 1165. The regions are summarized in Table 4.4.2:

We determine the luminosity function in each of the rest-frame B, V, and R bands for the cluster environment, the cluster core, the filaments, and the field. Best-fit parameters, uncertainties, and values of the reduced  $\chi^2$  (i.e., the value of  $\chi^2$  divided by the degrees of freedom of the fit minus the number of parameters,  $\nu - p$ ) are listed in Table 4.4.2 for the individual bands and the individual regions. Figure 4.7 reproduces the LF as a function of broad-band filter and surveyed regions, while Fig. 4.8 shows the associated error contours in the parameter space. Both Table 4.4.2 Fig. 4.8 show that the best-fit solutions are robust. For the cluster as a whole, our best-fit values for slopes and characteristic magnitudes of the LFs in V and R bands are consistent with those quoted by Busarello et al. ((2002)), within the errors. The number of objects is similar (i.e., 1165 vs. 1206), but the combination of photo- $z$  selection and robust characterization of the background allow smaller uncertainties to be reached for the best-fit parameters listed in Table 4.4.2.

## 4 Connecting dynamical state and galaxy populations in massive clusters

Region	N.Objects	R band				
		$\alpha$	$\Delta\alpha$	$M^*$	$\Delta M^*$	$\chi^2/(\nu - p)$
Full cluster	1165	-0.89	0.03	-22.51	0.21	3.46/9
Core	304	-0.78	0.06	-21.91	0.29	5.98/9
NW filament	359	-0.91	0.12	-22.69	0.59	4.21/7
S filament	374	-0.94	0.09	-23.09	0.73	3.00/9
Field	488	-1.07	0.01	-23.13	0.28	12.37/9
		V band				
		$\alpha$	$\Delta\alpha$	$M^*$	$\Delta M^*$	$\chi^2/(\nu - p)$
Full cluster	1165	-0.92	0.03	-22.14	0.23	8.34/9
Core	304	-0.93	0.04	-22.16	0.34	5.88/8
NW filament	359	-0.84	0.09	-22.69	0.29	4.86/6
S filament	374	-0.99	0.08	-23.70	0.72	8.70/8
Field	488	-1.17	0.01	-23.58	0.23	5.33/9
		B band				
		$\alpha$	$\Delta\alpha$	$M^*$	$\Delta M^*$	$\chi^2/(\nu - p)$
Full cluster	1165	-0.95	0.02	-21.88	0.19	4.44/9
Core	304	-0.90	0.04	-21.36	0.29	8.42/9
NW filament	359	-1.02	0.05	-22.79	0.35	10.74/7
S filament	374	-0.98	0.06	-22.87	0.43	5.25/8
Field	488	-1.19	0.01	-23.40	0.23	4.39/9

**Table 4.2:** Summary of luminosity function parameters for RXCJ0014.3-3022 and its components in the B, V and R bands.

There is a robust evidence for the slope of the faint end of the LF to flatten moving from the field to the cluster environment. At the same time, the characteristic magnitude becomes fainter. This holds for all bands. The difference is more evident when comparing the field to the cluster core. Accordingly, the distribution of the fit parameters in the parameter space (see Fig. 4.8) describes, within error contours, an almost continuous evolution of the values of the fit from the field through the filaments towards the core. These results are consistent with previous ones, whether they were obtained for this cluster or for other systems at different redshifts.

The new result is that the LF in the filaments exhibits characteristic parameters that are in between those of the field and the cluster core. In fact, the fit to the filaments shows unexpectedly large contours, even in comparison with those of other regions with similar number of objects. The contours for the cluster, core and field have well-defined and limited regions in the parameters space, confirming the robust-

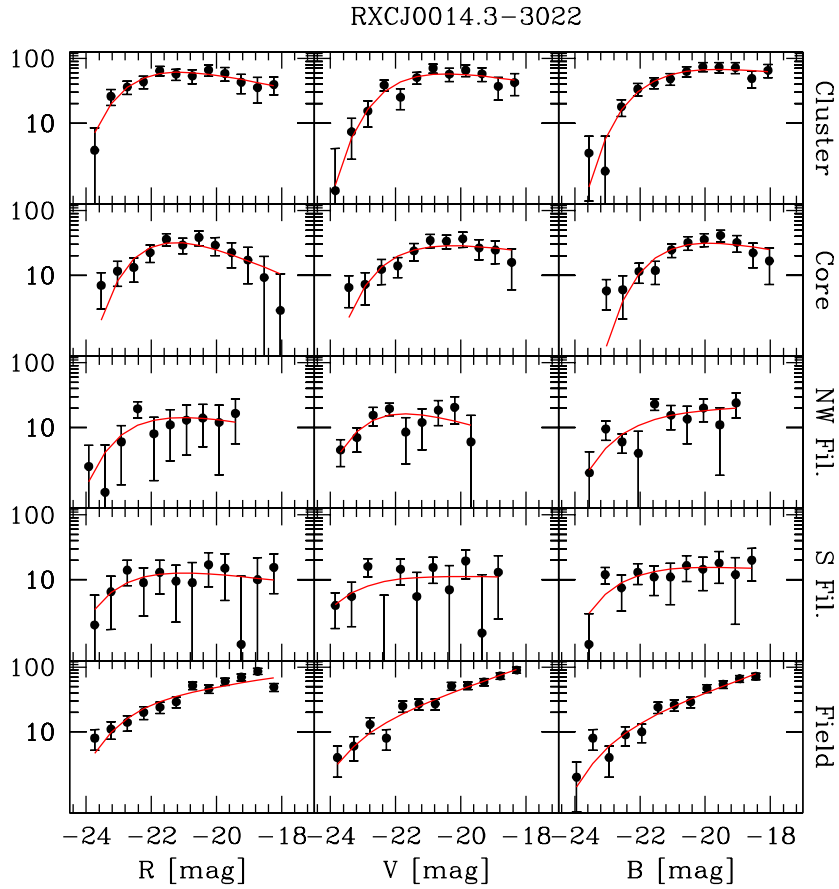


**Figure 4.7:** Luminosity functions of the cluster RXJ0014.3-3022 and for its components. Left column is for R band, central column for V band and right column for B band. From top to bottom, the background-corrected magnitude distribution of cluster members and Schechter function best fit are shown for the full cluster sample, cluster core, NW filament, S filament and field.

ness of the fit. On the other hand, the filaments contours have large and irregular shapes. This is also reflected in the bumpy distributions shown in Fig. 4.7. This suggests that the best-fit could be not a single function, but a combination of different behaviours. In Braglia et al. ((2007)) a sudden increase in the blue-to-red objects was found in the outer part of the filaments. The increase is dramatically evident in the denser southern filament, while the northern one shows a gentler trend still towards high values. Based on this results, luminosity functions for the inner and outer part of the filaments are independently re-fitted to check whether the popula-

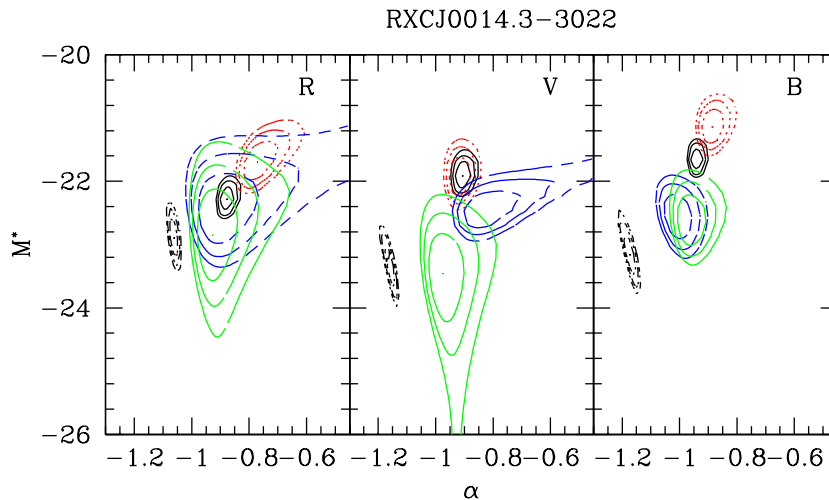


**Figure 4.8:** Error contours for the fits of all regions of RXCJ0014.3-3022. From left to right, the panels show results for the R, V and B band respectively. Black continuous contours are for the full cluster, black dashed contours for the field, red dotted for the core, blue short dashed for the N filament and green long dashed for the S filament. In the R and V band, the filament error contours are large and irregular, shrinking only in the B band to comparable values and areas. The full cluster and its core always show well-defined and compact contours, as the field does. The field contours are well separated from the cluster and its components, and in V and B basically occupy the same region in the parameters space.

tion in the two parts can be different. To obtain higher counts for a better fit the two filaments are stacked together to form a composite filament, whose population is then splitted with respect to cluster-centric radius. The inner and outer part of the composite are defined as below or beyond a radius of  $8'$ , respectively. This value is chosen to separate the filament sections where the ratio of blue-to-red galaxies is below or beyond the typical field values (cfr. Fig. 6 in BPB07). At the cluster's redshift, it corresponds to about 2.2 Mpc or  $0.82 R_{200}$ .

The inner part of the composite filament shows a luminosity function globally comparable with the main cluster. Although errors are still relatively large, the error contours now are smooth and well-defined. Thus, we can consider the inner part of the filaments as following the overall population in the cluster. The same result is seen if the LF is evaluated for each filament's inner part, although uncertainties become larger. The outer part proves instead difficult to fit with a Schechter function, appearing instead as an almost flat distribution of objects across the full magnitude



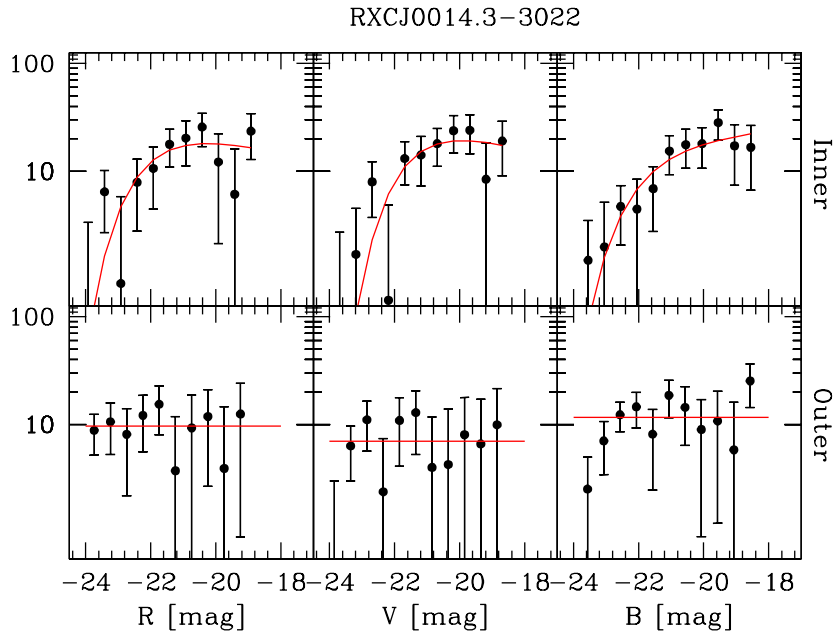


**Figure 4.9:** Luminosity functions for the composite filament in RXCJ0014.3-3022. From left to right, the plots for the three bands (R, V and B respectively) are shown. Top row shows the LF for the inner part of the filament, where galaxies follow the overall trend of the cluster population. Bottom row is instead the magnitude distribution for the outer filaments, where the shape of the LF is globally transformed. Overplotted to the points in the bottom panels is the mean count value.

Region	R		V		B	
	L	$\Delta L$	L	$\Delta L$	L	$\Delta L$
Full cluster	2.290	0.028	1.337	0.038	0.786	0.028
Core	0.910	0.014	0.514	0.019	0.279	0.014
NW Filament	0.256	0.013	0.154	0.018	0.099	0.013
S Filament	0.926	0.014	0.578	0.019	0.374	0.013

**Table 4.3:** Total luminosity and errors for RXCJ0014.3-3022 and for its components in the R, V and B bands. All luminosities are expressed in multiples of  $10^{13}L_{\odot}$ .

interval sampled.

The total luminosity is calculated for the full cluster environment, as well as for each cluster component (core, NW filament and S filament). Table 4.4.2 lists the values of

## 4 Connecting dynamical state and galaxy populations in massive clusters

---

Band	M/L	$\Delta$ M/L
B	370	58
V	214	32
R	124	18

**Table 4.4:** M/L ratio and error for RXCJ0014.3-3022, calculated in the three bands at  $R_{200}$ . All values are expressed in units of  $M_{\odot}/L_{\odot}$ . Errors are calculated by standard error propagation.

the total optical luminosity and associated errors for the cluster and its components in each band. The full cluster luminosity also accounts for contribution from the additional annulus around the core. These results provide a consistent picture of RXCJ0014.3-3022 as an extremely large system: its total optical luminosity is at the very high end of the values reported for clusters at intermediate redshifts (e.g. Popesso et al. (2004)). The southern filament, that we already know to be denser and richer in blue galaxies (see Braglia et al. (2007); Braglia et al. 2008, in prep.), has a total luminosity about three times of the north-western filament, and is found to be brighter than the core in B band by about 35%. The total optical luminosity decreases from the R band to the B band. This is not surprising, as for cluster galaxies (i.e., at  $z \sim 0.3$ ) R band samples a region of the spectrum mainly powered by old stars, while B band samples the region bluewards of the 4000 Å break, where the largest part of the emission is due to younger stars. Thus, mainly actively star-forming galaxies (i.e. a fraction of the total number of galaxies in the cluster) will contribute to the radiation detected in the B band.

### 4.4.2.1 Cluster mass-to-light ratio

The results obtained from the study of dynamics and the behaviour of the LF in the different cluster components can be easily combined to obtain a reliable evaluation of the cluster mass-to-light (M/L) ratio in the three bands and to examine its dependence with radius. The value of M/L ratio within  $R_{200}$  (as determined from dynamical analysis) is given in Table 4.4.2.1:

We calculate the radial behaviour of the M/L ratio in the three bands from the cluster core to its outskirts ( $1.5R_{200}$ ). The total cluster luminosity is calculated within concentric radii in the same way as for the dynamical mass (constant bin of  $0.1R_{200}$ , starting from  $0.2R_{200}$ ; cfr. Sect. 4.3) and considering all cluster photometric members (the core with additional objects out to 5' and the two filaments). The M/L ratio is constant within errors below  $0.5R_{200}$  and beyond  $0.7R_{200}$  (a slight decreasing trend is barely noticeable in the B band), whereas it increases steadily by about 40% in between (i.e., within 0.54 Mpc). Interestingly, this is the region where the two filaments connect to the cluster main body and their population is dominated by red

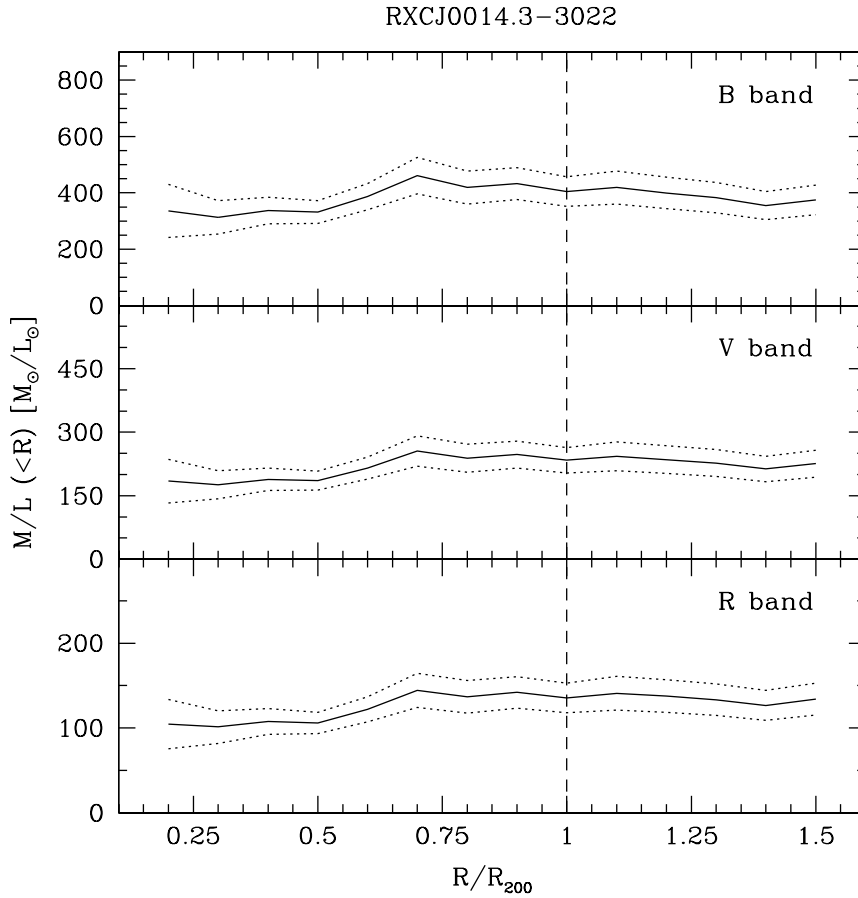


**Figure 4.10:** Radial behaviour of M/L ratio for RXCJ0014.3-3022 in the three bands. The vertical dashed line marks the position of  $r_{200}=2.69$  Mpc. Top panel, B band; middle panel, V band; bottom panel, R band.

galaxies (see Braglia et al. (2007), 2008a).

The differential mass-to-light radial profile (i.e.,  $\delta M(R)/\delta L(R)$ ) provides a more precise picture of the M/L profile of the cluster (see e.g. Rines et al. (2000)). The profile obtained is shown in Fig. 4.11. In all bands, the differential M/L profile is seen to be decreasing (within errors) for increasing cluster-centric radii below  $0.85R_{200}$ , as already shown in several previous works (e.g. Katgert et al. (1994); Rines et al. (2000) and (2001); Biviano & girardi (2003)). However, beyond  $0.85R_{200}$  a sudden increase in the M/L ratio is detected. This distance precisely corresponds to the region where Braglia et al. ((2007); also see Braglia et al. 2008a, in prep.) found a strong increase in the star formation activity of galaxies belonging to the two

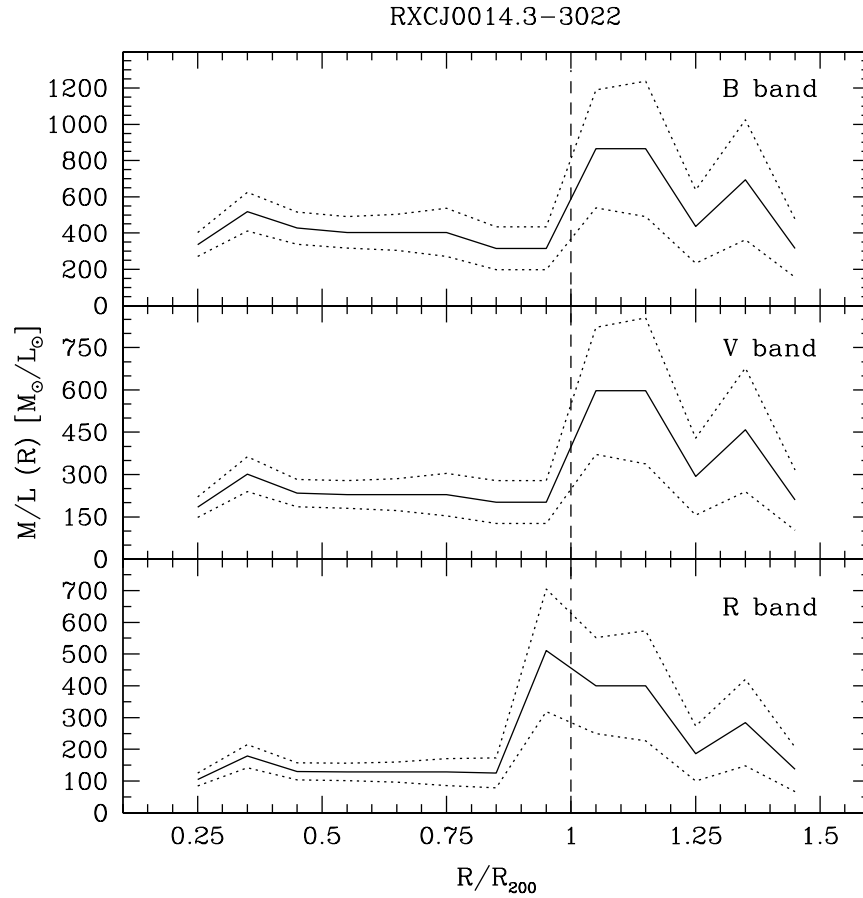


**Figure 4.11:** Radial behaviour of differential M/L ratio for RXCJ0014.3-3022 in the three bands. The vertical dashed line marks the position of  $r_{200}=2.69$  Mpc. Top panel, B band; middle panel, V band; bottom panel, R band.

filaments, both from colour information and spectral index analysis. Thus, we suggest that this increase in the M/L ratio is due to the presence of the two filaments that bring new matter into the cluster. This is also partly in agreement with the excess mass and luminosity profiles found by Sheldon et al. ((2007)) in clusters drawn from the MaxBCG sample, where they found a steady increase in the deprojected radial M/L ratio profile using weak lensing mass profiles.

#### 4.4.3 Luminosity function parameters for RXCJ2308.3-0211

The cluster RXCJ2308.3-0211 was divided (see Braglia et al. 2008a) in a core and two concentric circular annuli, plus an overdense region to the north of the cluster

#### 4.4 Optical luminosity function

Region	Radius	Angle	Objects	Area
Cluster core	$0' \leq r \leq 3'$	$0 \leq \theta \leq 360$	258	$9\pi$
Inner outskirts	$3' < r \leq 6'$	$0 \leq \theta \leq 360$	293	$27\pi$
Outer outskirts	$6' < r \leq 9'$	$0 \leq \theta \leq 360$	429	$45\pi$
BG field (1)	$9' < r \leq 19'$	$200' \leq \theta \leq 240$	255	$31.1\pi$
BG field (2)	$9' < r \leq 19'$	$300' \leq \theta \leq 350$	228	$38.9\pi$

**Table 4.5:** Definition of regions of interest in RXCJ2308.3-0211. Areas are expressed in square arcminutes.

where two galaxy groups are found. A comparison field was also selected as the sum of two low-density regions. The regions are summarized in Table 4.4.3:

The two background regions together have the same area and number of objects than the background field for RXCJ0014.3-3022. The full cluster is defined as the sum of the three concentric regions, for a total of 980 objects within  $9'$ . This corresponds to about  $1.2 R_{200}$  at the cluster redshift of 0.2966 (for comparison, RXCJ0014.3-3022 has 1016 objects within the same radius). An interesting high-density region was identified northwards of RXCJ2308.3-0211, where two galaxy groups are found within an overall higher density region with hints of X-ray emission (see Braglia et al. 2008a). Thus, we also derive the luminosity function for the two combined galaxy groups, which lie in the rectangular region defined by  $346.843 \leq \text{R.A.} \leq 347.173$ ,  $-1.995 \leq \text{DEC.} \leq -1.899$ . In this region, 552 objects are found on an area of  $\sim 114$  square arcminutes, which corresponds to about half the mean surface density in the cluster core.

We determine the luminosity function in each of the rest-frame B, V, and R bands for the cluster environment, its concentric components and the group structure. Best-fit parameters, uncertainties, and values of the reduced  $\chi^2$  are listed in Table 4.4.3 for individual bands and individual regions. Figure 4.12 reproduces the LF as a function of broad-band filter and surveyed regions, while Fig. 4.13 shows the associated error contours in the parameter space. The cluster core and inner outskirts show comparable values in slope and cutoff magnitude. These values also agree within errors with the fit for the core of RXCJ0014.3-3022. Interestingly, the group structure shows similar values than the cluster in both parameters, albeit the slope of the faint end is slightly steeper. The fit to the background in the B band is affected by a sudden drop beyond  $B=-22$ . This same drop is not seen in the V and R bands and must be ascribed to a severe incompleteness produced by the large absorption in the B band in the region of RXCJ2308.3-0211. Removing objects brighter than  $B=-22$  restores values in agreement with the V and R bands. The fit to the outer outskirts shows anomalous values. After removing a single bin in the V band at  $V=-22$  where counts drop to 0 (likely due to undersampling after background subtraction), the fit parame-

## 4 Connecting dynamical state and galaxy populations in massive clusters

Region	N.Objects	R band				
		$\alpha$	$\Delta\alpha$	$M^*$	$\Delta M^*$	$\chi^2/(\nu - p)$
Full cluster	980	-0.89	0.03	-21.71	0.25	3.13/9
Core	258	-0.74	0.08	-21.41	0.30	2.50/9
Inner outskirts	293	-0.79	0.12	-21.96	0.45	2.28/8
Outer outskirts	429	-1.18	0.02	-27.43	0.58	1.86/7
Field	483	-1.10	0.01	-23.57	0.26	10.05/9
Group structure	552	-0.92	0.03	-22.12	0.32	5.30/9
		V band				
		$\alpha$	$\Delta\alpha$	$M^*$	$\Delta M^*$	$\chi^2/(\nu - p)$
Full cluster	980	-0.87	0.04	-21.56	0.20	8.52/8
Core	258	-0.76	0.09	-20.89	0.31	0.82/7
Inner outskirts	293	-0.83	0.11	-22.16	0.41	3.33/6
Outer outskirts	429	-1.20	0.02	-25.32	0.67	6.13/7
Field	483	-1.07	0.01	-22.99	0.28	5.70/8
Group structure	552	-0.91	0.04	-23.00	0.32	2.99/8
		B band				
		$\alpha$	$\Delta\alpha$	$M^*$	$\Delta M^*$	$\chi^2/(\nu - p)$
Full cluster	980	-0.97	0.02	-21.56	0.19	9.67/8
Core	258	-0.80	0.07	-20.69	0.25	3.99/7
Inner outskirts	293	-0.91	0.07	-21.37	0.40	1.62/8
Outer outskirts	429	-1.14	0.02	-23.37	0.41	1.81/8
Field	483	-1.07	0.02	-22.19	0.23	3.40/9
Group structure	552	-1.03	0.02	-22.19	0.22	2.27/7

**Table 4.6:** Summary of luminosity function parameters for RXCJ2308.3-0211 and its components in the B, V and R bands.

ters in the B, V and R bands in this region show a steep slope and an extremely bright  $M^*$ . Thus, a Schechter function does not hold in this region, where the luminosity distribution is better described by power law. The parameter positions in Fig. 4.13 show that the inner regions, group structure and field define again a sequence in the parameter space from the field towards the cluster core. Conversely, the outermost regions of the cluster lie outside this sequence and show very irregular contours.

The total luminosity is calculated for the full cluster environment, as well as for each cluster component (core, inner outskirts, outer outskirts). For comparison, the total luminosity is also calculated for the group structure. Table 4.4.3 lists the values of the total optical luminosity and associated errors for the cluster and its components in

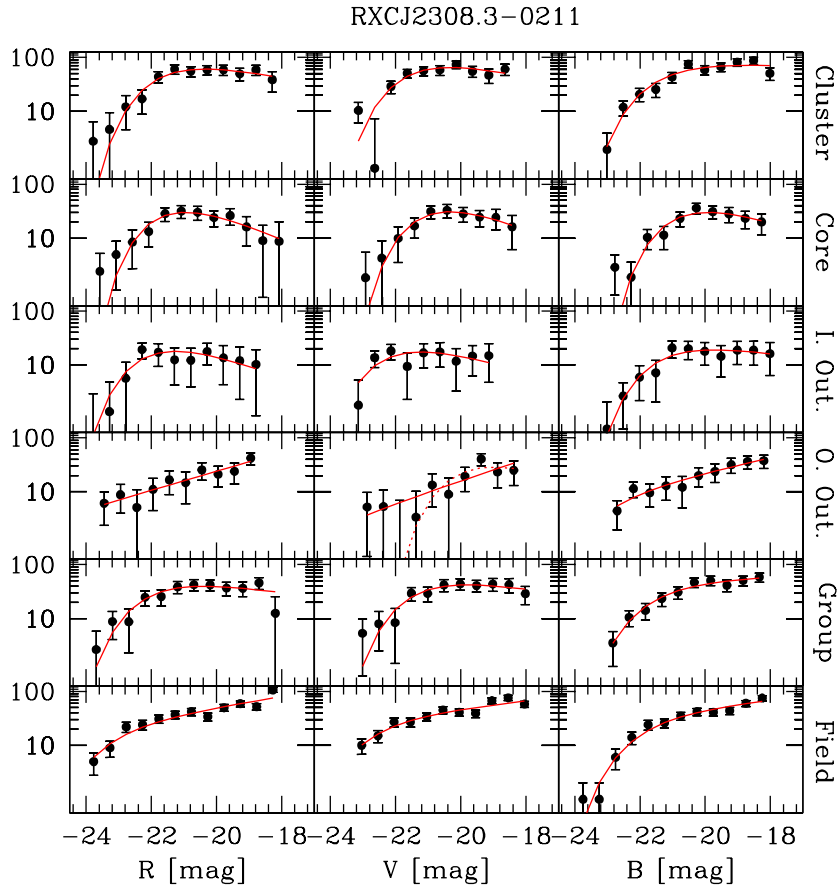


**Figure 4.12:** Luminosity functions of RXJ2308.3-0211 and its components. Left column is for R band, central column for V band and right column for B band. From top to bottom, the background-corrected magnitude distribution of cluster members and Schechter function best fit are shown for the full cluster sample, cluster core, inner outskirts, outer outskirts, group structure and field. The panel relative to the outer outskirts in V band also shows with a dashed red line the result of the fit if the zero counts bin at  $V=-22$  is taken into account.

each band. Again, the total luminosity monotonically decreases towards bluer bands, as expected. Large luminosity errors are seen in the V and B band, due to the larger photometric errors in these bands. The total luminosity confirms RXJ2308.3-0211 as a large system, with a luminosity just below  $10^{13}L_{\odot}$ . More than 55% of the total cluster luminosity is contained within the central  $3'$ , i.e. about  $800 h_{70}^{-1}$  kpc at the cluster redshift. This was already noticed from the galaxy density map (cfr. Braglia et al. 2008a, in prep.) and agrees with the cluster having a strong cool core in X-

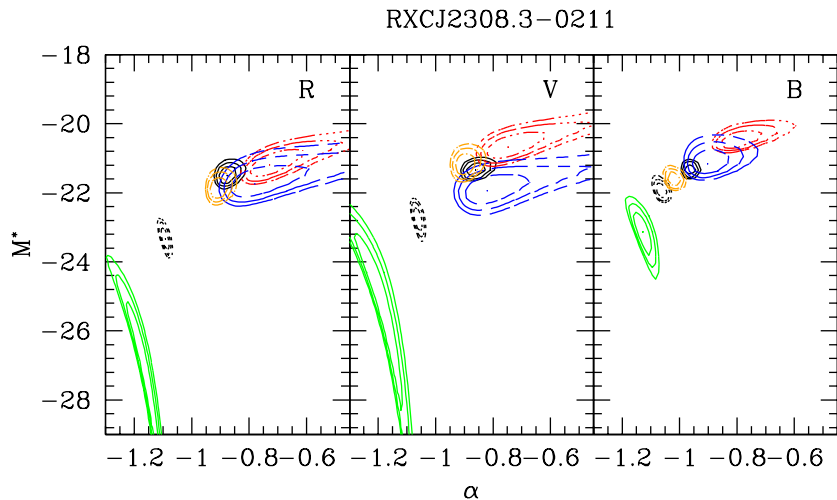


**Figure 4.13:** Error contours for the fits of all regions of RXCJ2308.3-0211. From left to right, the panels show results for the R, V and B band respectively. Black continuous contours are for the full cluster, black dashed contours for the field, red dotted for the core, blue short dashed for the inner outskirts, green long dashed for the outer outskirts and orange for the group structure. The full cluster always shows well-defined and compact contours, as the field and the group structure do. The field contours are well separated from the cluster and its components, and in R and V basically occupy the same region in the parameters space.

rays. The remaining 45% of the luminosity is distributed in the outskirts, suggesting that the luminosity density is steadily decreasing from the core to the edge of the cluster. The group structure has a total luminosity of about 80% of the total cluster luminosity, confirming this extended structure as quite massive. It is worth to remind here that a hint of X-ray emission is detected in the XMM-Newton images, although the structure lies at the very edge of the field of view.

#### 4.4.3.1 Cluster mass-to-light ratio

We derive the mass-to-light ratio for RXCJ2308.3-0211 with the same techniques already explained. The value of the M/L ratio within  $R_{200}$  (as determined from dynamical analysis) is given in Table 4.4.3.1. We also calculate the radial behaviour of the M/L ratio (shown in Fig. 4.14) in the three bands from the cluster core to its outskirts ( $1.2R_{200}$ ). The M/L ratio for this cluster is seen to slowly but monotonically decrease from the core to the outskirts. This is in agreement with the aforementioned works where the M/L profile of both observed and simulated clusters is seen to



Region	R		V		B	
	L	$\Delta L$	L	$\Delta L$	L	$\Delta L$
Full cluster	0.923	0.009	0.560	0.078	0.318	0.046
Core	0.513	0.005	0.293	0.042	0.169	0.041
Inner outskirts	0.236	0.005	0.144	0.043	0.081	0.041
Outer outskirts	0.221	0.006	0.124	0.047	0.077	0.042
Group structure	0.753	0.008	0.446	0.065	0.259	0.045

**Table 4.7:** Total luminosity and errors for RXCJ2308.3-0211, its components and the group structure in the R, V and B bands. All luminosities are expressed in multiples of  $10^{13}L_{\odot}$ .

Band	M/L	$\Delta M/L$
B	221	26
V	135	16
R	82	8

**Table 4.8:** M/L ratio and error for RXCJ2308.3-0211, calculated in the three bands at  $R_{200}$ . All values are expressed in units of  $M_{\odot}/L_{\odot}$ . Errors are calculated by standard propagation.

decrease with increasing cluster-centric radii. Again, we also calculate the differential M/L profile (shown in Fig. 4.15) for this cluster for a better description. This is almost monotonically decreasing, in agreement with previous works, excluding the innermost bin where low statistics do not allow a reliable determination of the M/L ratio.

## 4.5 Discussion

Both clusters are confirmed as very large systems with total masses in excess of  $10^{15} M_{\odot}$  within  $R_{200}$ . The virial analysis also confirms the very different dynamical state of the two clusters, in agreement with their X-ray and optical morphology. The virial mass estimate was compared with the value derived from X-ray temperature (see Zhang et al. (2006)). In both cases, the dynamical estimate is larger by about 30% than the X-ray derived value, although the latter has larger errors. RXCJ0014.3-3022 is confirmed as a major merger (as already pointed out in Boschin et al (2006)), whose velocity dispersion is boosted towards very high values (e.g. 1405 km/s). Its nontrivial dynamical state can also be inferred from the very high X-ray temperature ( $kT = 10.1 \pm 0.3$  keV). Conversely, RXCJ2308.3-0211 appears as a more relaxed cluster, as expected from its X-ray morphology, revealing a bright cool core. In the case of RXCJ0014.3-3022, we suggest that the extreme dynamical state could be taken into

## 4 Connecting dynamical state and galaxy populations in massive clusters

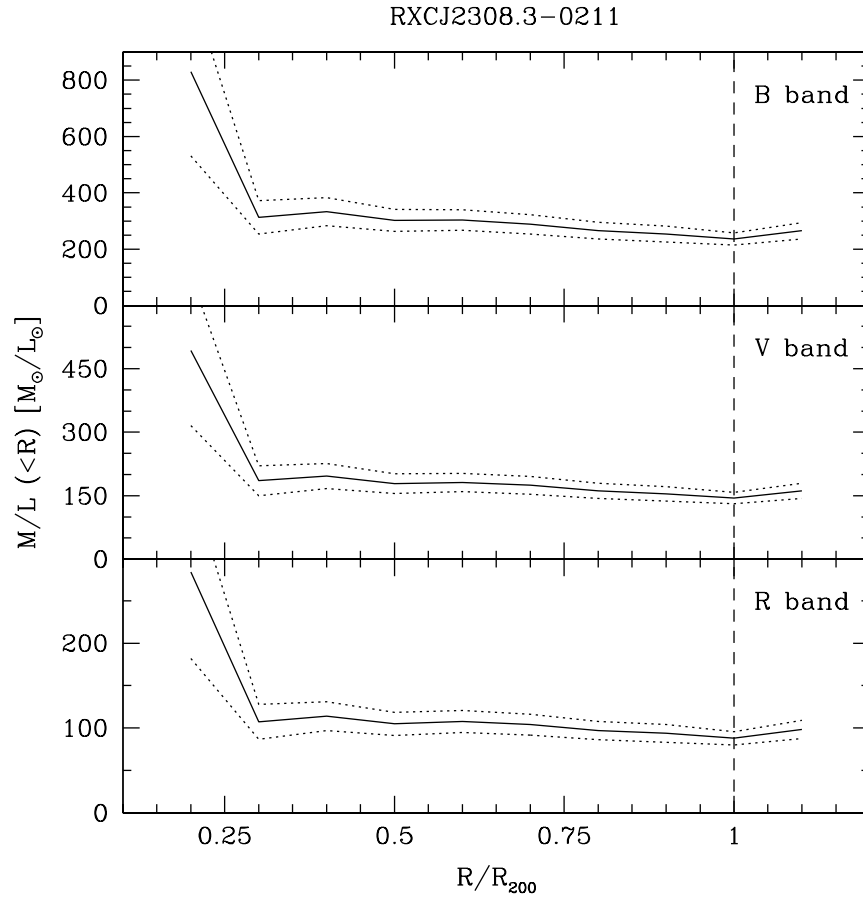


**Figure 4.14:** Radial behaviour of  $M/L$  ratio for RXCJ2308.3-0211 in the three bands. The vertical dashed line marks the position of  $r_{200} = 2.38$  Mpc. Top panel, B band; middle panel, V band; bottom panel, R band.

account assuming a non thermalized ICM, which would lower the discrepancy. Mass estimates from X-rays shows that the total mass of RXCJ2308.3-0211 is comparable with the mass of the main component of RXCJ0014.3-3022. We confirm this also via virial analysis, and other works (e.g. Boschin et al (2006)) find agreeing results. This confirms the picture of RXCJ0014.3-3022 as a 3:1 major merger between a massive cluster (of mass comparable to RXCJ2308.3-0211) and a smaller infalling system. If we assume the total mass estimate from dynamics as reliable, then the masses of the two merging systems can be calculated as about  $2 \times 10^{15}$  and  $7 \times 10^{14} M_{\odot}$ , in good agreement with the values of Boschin et al. ((2006)).

The total cluster luminosities were also calculated, also confirming these two clus-

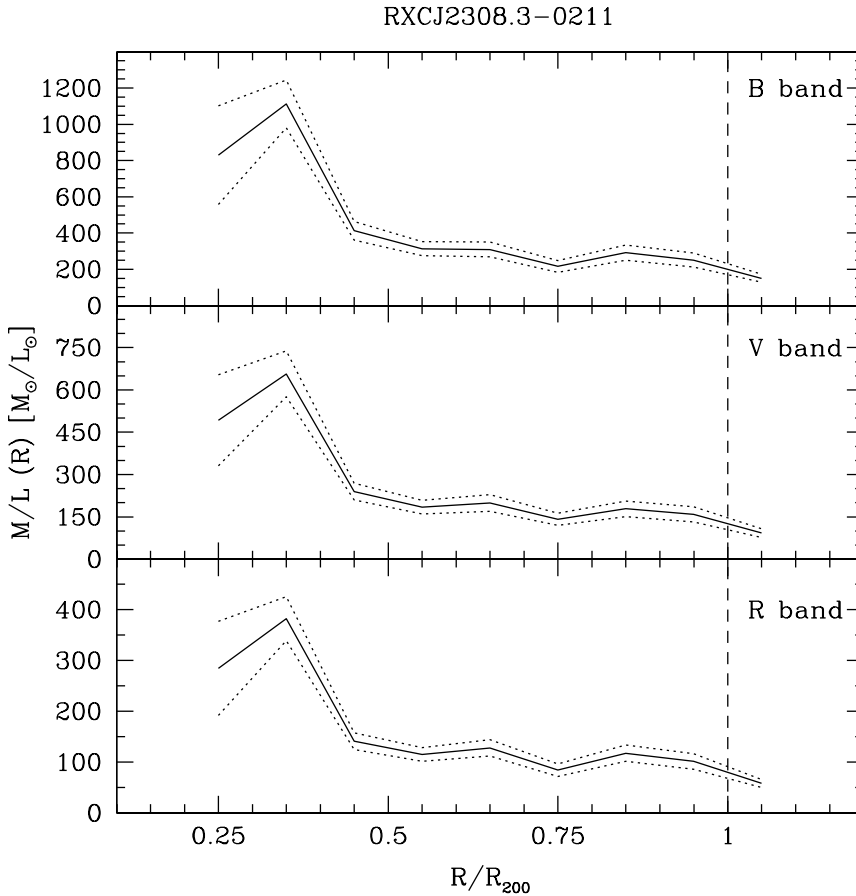


**Figure 4.15:** Radial behaviour of differential M/L ratio of RXCJ2308.3-0211 in the three bands. The vertical dashed line marks the position of  $r_{200}=2.38$  Mpc. Top panel, B band; middle panel, V band; bottom panel, R band.

ters as extremely large systems. They both lie at the bright end of the luminosity distribution of clusters (see e.g. Popesso et al. (2004)). RXCJ0014.3-3022 stands out as the most luminous system, with a total R band luminosity 2.5 larger than RXCJ2308.3-0211 and a core luminosity almost equal to the total luminosity of RXCJ2308.3-0211. On the other hand, RXCJ2308.3-0211 appears to be more concentrated, with more than half of the luminous matter lying in its core (i.e. the inner 800 kpc). It is important to remember here that RXCJ0014.3-3022 is undergoing a major merger, thus its total luminosity is basically the sum of two clusters, currently lying in the central region of the system. Moreover, the filaments were also taken into account in the luminosity calculation, adding a non-negligible fraction of luminosity

## 4 Connecting dynamical state and galaxy populations in massive clusters

---

to the total. Comparison of the M/L ratios for the two clusters shows that in every band RXCJ0014.3-3022 has a ratio about 1.5-1.6 larger than RXCJ2308.3-0211, as expected for a larger system. Comparison with the observational results of Girardi et al. ((2000); (2002)) shows that the two clusters lie within their M/L<sub>B</sub> relation, confirming it in the highest mass and luminosity region. The same is also true for the relations found by Popesso et al ((2007)).

The LF shape of RXCJ0014.3-3022 is in good agreement with previous works done on the cluster main body (Andreon (2002); Busarello et al. (2002); Merluzzi et al. (2003)). This confirms the reliability of selecting cluster members for the evaluation of the LF by means of photometric redshift selection as an alternative to rely on global background subtraction. The LF is seen to become steeper from the core to the outskirts, with a brightening of the characteristic luminosity  $M^*$  in the filaments by about a magnitude. Also, in the southern filament, where the star-formation activity is more intense, it is rather difficult to find a good fit to the Schechter function. Analysis of the combined galaxy population of the two filaments reveals that, while the inner part of the filaments shows a good agreement with the global cluster LF, the outer parts cannot be fitted at all with a Schechter function, showing instead an almost flat distribution of galaxies across at least 6 magnitudes. This confirms from a different point of view the increased star-formation activity in the filaments outer regions and could well explain the presence of the *flaming giants* in the filaments. As already explained in Braglia et al. ((2007)), the global change in the SFR can be interpreted in the light of galaxy-galaxy or galaxy-cluster harassment (see Moore et al. (1998) and (1999)): spiral galaxies infalling from the field into the cluster first experience fast encounters with neighbours and then begin to feel the cluster potential. This will trigger intense and short-lived starburst episodes via gravitational instabilities in the galaxy disks. Other galaxies, experiencing a slower infall, could feel feebler but long-lived interactions with their neighbours, resulting in extended tidal damage. This will again fuel star formation episodes, if gas is still present. A small part of the infalling galaxies is also likely to undergo mergers, prohibited in the core where high speed encounters rule but likely to happen in these transition regions. This will again result in an enhanced star formation activity.

This picture helps explaining the sudden transformation of the LF across the cluster  $R_{200}$ : galaxies begin to feel the cluster environment at about this distance, where the effect of galaxy harassment (being mainly due to cluster galaxies, as explained) is stronger and mergers are likely to happen. As a consequence, these galaxies will also become more luminous, climbing the luminosity function, crossing  $M^*$  and overpopulating the bright end at the expenses of the faint tail. Moreover, as the effect of harassment on faint galaxies ( $R > -18$ ) is total disruption by gravitational tides, the faint region of the LF will not be replenished from the reservoir of dwarf galaxies. The net effect will be a flattening of the LF. Later on, when galaxies fall towards the core with larger velocities and begin to feel the cluster potential and dense ICM,

tidal heating (i.e. interaction with the cluster potential) and ram pressure stripping (depletion of gas in the disks due to pressure of the ICM) will suddenly quench the star formation and restore the shape of the cluster luminosity function.

The M/L of RXCJ0014.3-3022 shows an intriguing and complicated radial behaviour. The integrated M/L ratio is basically flat over the full range examined, excluding a region of increase between  $0.5R_{200}$  and  $0.7R_{200}$ . This is the region where the two filaments connect to the cluster main body. Kneib et al. ((2003)) have found an almost flat M/L profile in the merging cluster CL0024+1654: this suggests that a flat radial profile could be related to an unrelaxed dynamical state of the cluster. The differential M/L ratio shows a peak around  $0.25R_{200}$  ( $\sim 680$  kpc at the cluster redshift), with an increase of about 50% with respect to the mean value in the inner region of the cluster. This is the distance where the secondary X-ray peak is found in the XMM-Newton images (see Braglia et al. 2008a). Böhringer et al. ((2006)) and Pierini et al. ((2008)) showed that in this peak the X-ray gas trails the clump of galaxies driving the infall from the NW. This suggests that this peak in the M/L is the signature of the X-ray gas. Beyond  $0.4R_{200}$ , the differential M/L shows typical values for clusters and in good agreement with RXCJ2308.3-0211. However, beyond  $0.9R_{200}$  a sudden increase is detected, i.e. in the region where the filament enters the cluster and the galaxy population undergoes the already discussed changes. This suggests that in the outer region of the filaments a much larger fraction of diffuse matter is present, which is not directly detected but only inferred from its dynamical signature in the mass determination and velocity dispersion of galaxies. Fig. 4.11 shows that this increase begins closer to the core in the R band, at the same distance where the inner, red section of the filament ends. The increase could thus be related to the matter content of the filament, suggesting that in the outer region of the filaments there is a large fraction of diffuse, undetectable matter. It could be partly in the form of diffuse intergalactic gas, too cold to be detected in X-rays, and partly the dark matter structure defining the backbone of the filament itself.

The X-ray map of RXCJ0014.3-3022 (see Braglia et al. 2008a) shows a low-luminosity X-ray tail that follows tightly the shape of the southern filament out to about  $R_{200}$ , where it disappears. In the same region, the galaxy density grows and the LF is seen to become similar to the cluster. This suggests that, in addition to witnessing the transformation of galaxies towards the cluster population,  $R_{200}$  could be the distance where the diffuse baryonic matter condenses in the warm-hot intergalactic medium detected as the X-ray tail in the filament (also see Zappacosta et al. (2005); Mannucci et al. (2007); Werner et al. (2008)).

The LF of RXCJ2308.3-0211 shows overall values well in agreement with similar works. We find a global trend of the LF with cluster-centric radius. While in the core of the cluster and in the surrounding region the LF shows typical values (with a shallow slope and an  $R^*$  slightly fainter than -22), in the outskirts (i.e. beyond  $0.7R_{200}$ ) the LF is seen to suddenly steepen. This suggests that even in the outskirts

## 4 Connecting dynamical state and galaxy populations in massive clusters

---

of a stable and relaxed cluster as RXCJ2308.3-0211 transformation processes can be present. Both Popesso et al. ((2005a)) and Barkhouse et al. ((2007)) already found that the shape of the LF has on average a dependence on cluster-centric radius, ranging from a dimmer  $M^*$  and a shallower slope of the faint end in the cluster centre, to steeper slopes and brighter  $M^*$  in the outskirts. This is well explained assuming that galaxies being accreted on the cluster have their star formation activity truncated by interaction with the ICM (thus dimming the characteristic magnitude) and then are tidally disrupted and/or cannibalized in the core by gravitational interaction with the giant ellipticals, producing a decrease in the population of faint systems in the central regions. Moreover, we detect another evidence of changes of the galaxy population in the outskirts of RXCJ2308.3-0211. Indeed, no evident knee (i.e. no characteristic  $M^*$ ) can be derived for the LF in the outermost regions of the cluster and the galaxy distribution is better described there assuming a simple power law. This could be due to a combination of accretion processes and dynamics in the cluster. Although no evident filaments or accretion patterns in specific directions are detected in this cluster, it is likely that accretion from the field is still taking place, possibly as a gentle, almost spherical infall from the field on the cluster. As galaxies enter the cluster and are progressively quenched, they are likely to be dragged to the core by dynamical friction. This will mostly be efficient for larger system, that drift faster toward the central regions, while smaller galaxies are likely to linger in the outskirts for longer times. The consequence will be a depletion of the bright end and thus a loss of the characteristic shape of the LF.

RXCJ2308.3-0211 shows a radial M/L ratio in good agreement with previous works (e.g. Katgert et al. (1994); Rines et al. (2000) and (2001); Biviano & Girardi (2003)), with a steady radial decrease from the core to the outskirts. This is quite evident in the differential M/L ratio, where values range from  $\sim 300 M_{\odot}/L_{\odot}$  in the inner regions to  $\sim 80 M_{\odot}/L_{\odot}$  in the R band. This confirms, along with the dynamical analysis and optical/X-ray morphology (see Braglia et al. 2008a), this cluster as a dynamically old system. The central peak in the M/L ratio must be ascribed to the population of old galaxies dominating the core, whose high M/L is reflected in the overall value of the cluster.

### 4.6 Conclusions

We use multi-wavelength data analysis to describe the dynamics and galaxy population of two massive clusters in opposite dynamical stages: the merging cluster RXCJ0014.3-3022 (A 2744) and the cool core cluster RXCJ2308.3-0211 (A 2537).

We detect evident transformations in the shape of the luminosity function in interesting regions of the two clusters. In both cases, a steepening of the faint end and a brightening of the characteristic magnitude is seen on average with increas-

ing cluster-centric distance. In the case of RXCJ0014.3-3022, the change is detected along two large-scale filaments driving the infall of matter on the cluster. Below the cluster  $R_{200}$  the populations of the filaments represent the typical cluster distribution. However, in the outskirts a Schechter function does not hold and the galaxy population has an almost flat distribution. We suggest that galaxy-galaxy interactions (galaxy harassment, extended tidal stress, mergers) and galaxy-cluster interactions (tidal heating, ram pressure stripping) can explain the observed transformation. For RXCJ2308.3-0211, the transformation takes place continuously from the core to the outskirts. In the outermost regions, the galaxy population is better described by a simple power law. In this case, the effect is most probably due to depletion of the bright end due to drifting of the most massive galaxies towards the core.

The clusters mass-to-light ratios are examined for the two clusters. RXCJ2308.3-0211 follows the predicted behaviour expected for clusters, confirming it as a dynamically old and well evolved system. RXCJ0014.3-3022 shows peculiar properties. In the inner regions the irregular shape can be ascribed to the ongoing merger and to the observed displacement between galaxies and gas. Across and beyond  $R_{200}$  we detect a strong and sudden increase in the M/L in all bands by as much as a factor 3. This suggests that the outskirts could have a much larger fraction of undetected matter, partly in the form of cold gas and mostly as dark matter defining the filament.

## 4 Connecting dynamical state and galaxy populations in massive clusters

---



## Bibliography

- [1996] Abraham, R. G., Smecker-Hane, T. A., Hutchings, J. B., et al. 1996, *ApJ*, 471, 694
- [1998a] Adami, C., Mazure, A., Biviano, A., Katgert, P., & Rhee, G. 1998a, *A&A*, 331, 493
- [1998b] Adami, C., Mazure, A., Katgert, P., & Biviano, A. 1998b, *A&A*, 336, 63
- [2004] Alcalá, J. M., Pannella, M., Puddu, E., et al. 2004, *A&A*, 428, 339
- [2002] Andreon, S., 2002, *A&A*, 382, 821
- [2001] Arnouts, S., Vandame, B., Benoist, C., et al. 2001, *A&A*, 379, 740
- [1976] Avni, Y., 1976, *ApJ*, 210, 642
- [1999] Baade, D., Meisenheimer, K., Iwert, O., et al. 1999, *Msngr*, 95, 15
- [1988] Balluch, M. 1988, *A&A*, 200, 58
- [1997] Balogh, M. L., Morris, S. L., Yee, H. K. C., Carlberg, R. G., & Ellingson, E. 1997, *ApJ*, 488, 75
- [1999] Balogh, M. L., Morris, S. L., Yee, H. K. C., Carlberg, R. G., & Ellingson, E. 1999, *ApJ*, 527, 54
- [1966] Baker, N. 1966, in *Stellar Evolution*, ed. R. F. Stein, & A. G. W. Cameron (Plenum, New York), 333
- [1996] Barger, A. J., Aragón-Salamanca, A., Ellis, R. S., et al. 1996, *MNRAS*, 279, 1
- [2007] Barkhouse, W. A., Yee, H. K. C., & López-Cruz, O. 2007, *ApJ*, 671, 1471
- [1990] Beers, T. C., Flynn, K., & Gebhardt, K. 1990, *AJ*, 100, 32
- [2002] Beijersbergen, M., Hoekstra, H., van Dokkum, P. G., & van der Hulst, T. 2002, *MNRAS*, 329, 385

## Bibliography

---

- [1996] Bertin, E., & Arnouts, S. 1996, *A&A*, 117, 393
- [1988] Binggeli, B., Sandage, A., & Tamman, G. A. 1988, *ARA&A*, 26, 509
- [1992] Biviano, A., Girardi, M., Giuricin, G., Mardirossian, F., & Mezzetti, M. 1992, *ApJ*, 396, 35
- [2003] Biviano, A., & Girardi, M. 2003, *ApJ*, 585, 205
- [2006] Biviano, A., Murante, G., Borgani, S., et al. 2006, *A&A*, 456, 23
- [2001a] Böhringer, H., Schuecker, P., Guzzo, L., et al. 2001a, *A&A*, 369, 826
- [2001b] Böhringer, H., Schuecker, P., Lynam, P., et al. 2001b, *Msngr*, 106, 24
- [2004] Böhringer, H., Schuecker, P., Guzzo, L., et al. 2004, *A&A*, 425, 367
- [2006] Böhringer, H., Braglia, F., Pierini, D., et al. 2006, *Msngr*, 123, 49
- [2007] Böhringer, H., Schuecker, P., Pratt, G. W., et al. 2007, *A&A*, 469, 363
- [1983] Bohlin, R. C., Jenkins, E. B., Spitzer, L. Jr., et al. 1983, *ApJS*, 51, 277
- [2000] Bolzonella, M., Pelló, R., & Miralles, J. M. 2000, *A&A*, 363, 476
- [2006] Boschin, W., Girardi, M., Spolaor, R., & Barrena, R., 2006, *A&A*, 449, 461
- [2007] Braglia, F., Pierini, D., & Böhringer, H. 2007, *A&A*, 470, 425 (BPB07)
- [1995] Briel, U. G., & Henry, J. P. 1995, *A&A*, 302, L9
- [2002] Busarello, G., Merluzzi, P., La Barbera, F., Massarotti, M., & Capaccioli, M. 2002, *A&A*, 389, 787
- [1978a] Butcher, H., & Oemler, A. Jr., 1978a, *ApJ*, 219, 18
- [1978b] Butcher, H., & Oemler, A. Jr., 1978b, *ApJ*, 226, 559
- [1984] Butcher, H., & Oemler, A. Jr., 1984, *ApJ*, 285, 426
- [1996] Carlberg, R. G., Yee, H. K. C., Ellingson, E., et al. 1996, *ApJ*, 462, 32
- [1988] Chapman, G. N. F., Geller, M. J., & Huchra, J. P. 1988, *AJ*, 95, 999
- [2006a] Clowe, D., Bradač, M., Gonzalez, A. H., et al. 2006a, *ApJ*, 648, L109
- [2006b] Clowe, D., Schneider, P., Aragón-Salamanca, A., et al. 2006b, *A&A*, 451, 395

- [1999] Colberg, J. M., White, S. D. M., Jenkins, A., & Pearce, F. R., 1999, MNRAS, 308, 593
- [1989] Colless, M., 1989, MNRAS, 237,799
- [1998] Couch, W. J., Barger, A. J., Smail, I., Ellis, R. S., & Sharples, R. M. 1998, ApJ, 497, 188
- [1969] Cox, A. N., & Stewart, J. N. 1969, Academia Nauk, Scientific Information 15, 1
- [1980] Cox, J. P. 1980, Theory of Stellar Pulsation (Princeton University Press, Princeton) 165
- [1980] Danese, L., de Zotti, G., & di Tullio, G. 1980, A&A, 82, 322
- [1996] den Hartog, R., & Katgert, P. 1996, MNRAS, 279, 349
- [2003] de Propriis, R., Colless, M., Broadhurst, T., et al. 2003, MNRAS, 342, 725
- [1978a] Dressler, A. 1978a, ApJ, 222, 23
- [1978b] Dressler, A. 1978b, ApJ, 223, 765
- [1980] Dressler, A. 1980, ApJ, 236, 351
- [1983] Dressler, A., & Gunn, J. E. 1983, ApJ, 270, 7
- [1988] Dressler, A., & Shectman, S. A. 1988, AJ, 95, 985
- [1997] Dressler, A., Oemler, A. Jr., Couch, W. J., et al. 1997, ApJ, 490, 577
- [1999] Dressler, A., Smail, I., Poggianti, B. M., et al. 1999, ApJS, 122, 51
- [2003] Durret, F., Lima Neto, G. B., Forman, W., & Churazov, E. 2003, A&A, 403, L29
- [2004] Ebeling, H., Barrett, E., & Donovan, D. 2004, ApJ, 609, L49
- [1991] Eyles, C. J., Watt, M. P., Bertram, D., et al. 1991, ApJ, 376, 23
- [1979] Faber, S. M., & Gallagher, J. S. 1979, ARA&A, 17, 135
- [1995] Fukugita, M., Shimasaku, K., & Ichikawa, T. 1995, PASP, 107, 945
- [1996] Fukugita, M., Ichikawa, T., Gunn, J.E., Shimasaku, K., Schneider, D.P. 1996, AJ, 111, 4

## Bibliography

---

- [1999] Garilli, B., Maccaagni, D., & Andreon, S. 1999, *A&A*, 342, 408
- [2003] Gavazzi, G., Cortese, L., Boselli, A., et al. 2003, *ApJ*, 597, 210
- [1999] Giovannini, G., Tordi, M., & Feretti, L. 1999, *New Astron.*, 4, 141
- [1993] Girardi, M., Biviano, A., Giuricin, G., Mardirossian, F., & Mezzetti, M. 1993, *ApJ*, 404, 38
- [1998] Girardi, M., Giuricin, G., Mardirossian, F., Mezzetti, M., & Boschin, W. 1998, *ApJ*, 505, 74
- [2000] Girardi, M., Borgani, S., Giuricin, G., Mardirossian, F., & Mezzetti, M., 2000, *ApJ*, 530, 62
- [2002] Girardi, M., Manzato, P., Mezzetti, M., Giuricin, G., & Limboz, F. 2002, *ApJ*, 569, 720
- [2003] Gómez, P. L., Nichol, R. C., Miller, C. J., et al. 2003, *ApJ*, 584, 210
- [2005] Goto, T. 2005, *MNRAS*, 359, 1415
- [2002] Goto, T., Okamura, S., McKay, T. A., et al. 2002, *AJ*, 123, 1807
- [2001] Govoni, F., Feretti, L., Giovannini, G., et al. 2001, *A&A*, 376, 803
- [2005] Hansen, S. M., McKay, T. A., Wechsler, R. H., et al. 2005, *ApJ*, 633, 122
- [1986] Horne, K. 1986, *PASP*, 98, 609
- [2003] Kneib, J.P., Hudelot, P., Ellis, R.S., Treu, T., Smith, G.P., Marshall, P., Czoske, O., Smail, I., Natarajan, P. 2003, *ApJ*, 598, 817
- [1992] Landolt, A. U. 1992, *AJ*, 104, 340
- [2005] Le Fèvre, O., Vettolani, G., Garilli, B., et al. 2005, *A&A*, 439, 845
- [2003] Lin, Y.-T., Mohr, J. J., & Stanford, S. A. 2003, *ApJ*, 591, 749
- [2004] Lin, Y.-T., Mohr, J. J., & Stanford, S. A. 2004, *ApJ*, 610, 745
- [1997] Lopez-Cruz, O., Yee, H. K. C., Brown, J. P., Jones, C., & Forman, W. 1997, *ApJ*, 475, 97
- [1986] Lugger, P. M. 1986, *ApJ*, 303, 535
- [1994] Katgert, P., Biviano, A., & Mazure, A. 1994, *ApJ*, 600, 657

- [2004] Kempner, J. C., & David, L. 2004, MNRAS, 349, 385
- [2001] Kodama, T., Smail, I., Nakata, F., Okamura, S., & Bower, R. G. 2001, ApJ, 562, L9
- [1980] Kron, R. G. 1980, ApJS, 43, 305
- [1999] Kull, A., & Böhringer, H. 1999, A&A, 341, 23
- [2007] Mahdavi, A., Hoekstra, H., Babul, A, Balam, D. D., & Capak, P. L. 2007, ApJ, 668, 806
- [2007] Mannucci, F., Bonnoli, G., Zappacosta, L., Maiolino, R., Pedani, M. 2007, A&A, 468, 807
- [2003] Merluzzi, P., La Barbera, F., Massarotti, M., Busarello, G., & Capaccioli, M. 2003, ApJ, 589, 147
- [2005] Miller, C.J., Nichol, R.C., Reichart, D., Wechsler, R.H., Evrard, A.E., Annis, J., McKay, T.A., Bahcall, N.A., Bernardi, M., Boehringer, H., Connolly, A.J., Goto, T., Kniazev, A., Lamb, D., Postman, M., Schneider, D.P., Sheth, R.K., Voges, W. 2005, ApJ, 130, 968
- [2007] Mignano, A., Miralles, J.-M., da Costa, L., et al. 2007, A&A, 466, 541
- [1980] Mizuno, H., 1980, Prog. Theor. Phys., 64, 544
- [1996] Mohr, J. J., Geller, M. J., Fabricant, D. G., et al. 1996, ApJ, 470, 724
- [1996] Moore, B., Katz, N., Lake, G., Dressler, A., & Oemler, A. Jr. 1996, Nature, 379, 613
- [1998] Moore, B., Lake, G., & Katz, N. 1998, ApJ, 495, 139
- [1999] Moore, B., Lake, G., Quinn, T., & Stadel, J. 1999, MNRAS, 304, 465
- [1998] Morris, S. L., Hutchings, J. B., Carlberg, R. G., et al. 1998, ApJ, 507, 84
- [1965] Nelder, J. A., & Mead, R. 1965, Computer Journal, 7, 308
- [2007] Okabe, N., & Umetsu, K. 2007, preprint, astro-ph/0702649
- [1974] Oke, J. B. 1974, ApJS, 27, 21
- [1998] Oke, J. B., Postman, M., & Lubin, L. M. 1998, AJ, 116, 549
- [2007] Orrú, E., Murgia, M., Feretti, L., et al. 2007, A&A, 467, 943

## Bibliography

---

- [2001] Paolillo, M., Andreon, S., Longo, G., et al. 2001, *A&A*, 367, 59
- [2008] Pierini, D., Zibetti, S., Braglia, F., et al. 2008, *A&A*, submitted
- [1993] Pisani, A. 1993, *MNRAS*, 265, 706
- [1996] Pisani, A. 1996, *MNRAS*, 278, 697
- [1996] Poggianti, B. M., & Barbaro, G. 1996, *A&A*, 314, 379
- [1999] Poggianti, B. M., Smail, I., Dressler, A., et al. 1999, *ApJ*, 518, 576
- [2006] Poggianti, B. M., von der Linden, A., De Lucia, G., et al. 2006, *ApJ*, 642, 188
- [2004] Popesso, P., Böhringer, H., Brinkmann, J., Voges, W., & York, D. G. 2004, *A&A*, 423, 449
- [2005a] Popesso, P., Böhringer, Romaniello, M., & Voges, W. 2005a, *A&A*, 415, 429
- [2005b] Popesso, P., Biviano, A., Böhringer, Romaniello, M., & Voges, W. 2005b, *A&A*, 433, 431
- [2006] Popesso, P., Biviano, A., Böhringer, H., & Romaniello, M. 2006, *A&A*, 445, 29
- [2007] Popesso, P., Biviano, A., Böhringer, H., & Romaniello, M. 2007, *A&A*, 464, 451
- [2004] Rasia, E., Tormen, G., & moscardini, L. 2004, *MNRAS*, 351, 237
- [1997] Renzini, A., & da Costa, L. 1997, *Msngr*, 87, 23
- [2000] Rines, K., Geller, M.J., Diaferio, A., Mohr, J., Wegner, G.A. 2000, *AJ*, 120, 2338
- [2001] Rines, K., Geller, M.J., Kurtz, M.J., Diaferio, A., Jarrett, T.H., Huchra, J.P. 2001, *ApJ*, 561, L41
- [2003] Robin, A. C., Reylé, C., Derrière, S., & Picaud, S. 2003, *A&A*, 409, 523
- [2002] Sakai, S., Kennicutt, R. C. Jr., van der Hulst, J. M., & Moss, C. 2002, *ApJ*, 578, 842
- [2003] Sanderson, A. J. R., & Ponman, T. J. 2003, *MNRAS*, 345, 1241
- [2000] Scharf, C., Donahue, M., Voit, G. M., Rosati, P., & Postman, M. 2000, *ApJ*, 528, L73

- [1976] Schechter, P. 1976, *ApJ*, 203, 297
- [1998] Schlegel, D. J., Finkbeiner, D. P., & Davis, M. 1998, *ApJ*, 500, 525
- [2005] Scodreggio, M., Franzetti, P., Garilli, B., et al. 2005, *PASP*, 117, 1284
- [2004] Selman, F. J. 2004, in *Optimizing Scientific Return for Astronomy through Information Technologies*, ed. P. J. Quinn, & A. Bridger (SPIE 5493) 453
- [2007] Sheldon, E. S., Johnston, D. E., Masjedi, M., et al. 2007, preprint, *astro-ph/0709.1162*
- [1992] Terlevich, R. 1992, in *ASP Conf. Ser. 31, Relationships between Active Galactic Nuclei and Starburst Galaxies*, ed. A. V. Filippenko, 13
- [1987] Tscharnuter, W. M. 1987, *A&A*, 188, 55
- [2004] Vandame, B. 2004, PhD thesis, University of Nice-Sophia Antinopolis
- [2008] Werner, N. et al. 2008, *A&A*, 482, 29
- [1993] Whitmore, B.C., Gilmore, D., & Jones, C. 1993, *ApJ*, 407, 489
- [1996] Yee, H. K. C., Ellingson, E., & Carlberg, R. G. 1996, *ApJS*, 102, 269
- [1980] Yorke, H. W. 1980, *A&A*, 86, 286
- [2005] Zappacosta, L., Maiolino, R., Finoguenov, A., Mannucci, F., Gilli, R., Ferrara, A. 2005, *A&A*, 434, 801
- [2004] Zhang, Y.-Y., Finoguenov, A., Böhringer, H., et al., 2004, *A&A*, 413, 49
- [2006] Zhang, Y.-Y., Böhringer, H., Finoguenov, A., et al. 2006, *A&A*, 456, 55
- [1997] Zheng, W., Davidsen, A. F., Tytler, D., & Kriss, G. A. 1997, preprint

## Bibliography

---



# 5

## Concluding remarks

In this chapter I will summarise the main achievements and results of my thesis. It was born with the general aim of characterising the galaxy population and the overall properties of the REFLEX-DXL clusters, a small but complete and unbiased sample of high-mass clusters. Its X-ray characteristics have been already studied and presented in detail in the work conducted in our research group at MPE by Y.Y. Zhang. With the results presented here, I demonstrate how a smart combination of several complementary observation techniques can provide a rich and complete view of the processes at work in galaxy clusters and of how clusters interact with the surrounding environment. This allows to characterise in unprecedented detail the interactions of clusters as a whole and of the galaxies within clusters with their environment.

The combined use of different data and techniques, i.e. X-ray morphology, dynamical tests and analysis of local optical overdensities has proven to be a powerful source of information. This was tested on a very complex and active system, the merging Butcher-Oemler cluster RXCJ0014.3-3022 (or A 2744). In this rich cluster, X-ray morphology revealed two colliding components, revealing an ongoing merger of a massive cluster with a smaller mass system. This was confirmed both by the velocity distribution, that revealed a clear bimodality, and by dynamical analysis via Dressler-Schechtman test, that allowed to identify two additional substructures to the S and NW of the main cluster body. Analysis of galaxy overdensities at the cluster redshift revealed, in the same positions as the dynamical inhomogeneities, two large-scale filaments extending well beyond the cluster virial radius. This demonstrates that

## 5 Concluding remarks

---

combination of multi-wavelength data can help in revealing the undergoing dynamics that help shaping the clusters. Along the newly found filaments, it was possible to detect through photometric data a change in the galaxy population. This change takes abruptly place across the virial radius, revealing a sharp transition from the old galaxy population typical of clusters to a population of luminous blue systems, i.e. galaxies where star formation is actively taking place. Comparison of the mean colour ratios shows that the mean star formation rate along the filaments is even higher than in the field at the same redshift. This suggests that peculiar processes act along the accretion paths of clusters that increase in a dramatic way the star formation activity of infalling galaxies. Moreover, a population of compact and luminous galaxies showing very blue colours also is detected only in the outer regions of the filaments. These galaxies are unexpected and provide evidence of an even larger enhancement of the star formation in some systems. To better understand their properties, new observations will be needed and are indeed under completion by now, thanks to a new proposal accepted for VIMOS observation of these peculiar systems.

Adding specific spectroscopic information and photometric data in the UV can provide even deeper and more precise information about the processes affecting the star formation activity in clusters. I confirmed this by analysing again the cluster RXCJ0014.3-3022 and comparing it with another DXL cluster, the cool core system RXCJ2308.3-0211. Comparison of two very different systems also allowed to understand how the global cluster state affects the star formation in each particular galaxy. Optical cluster morphology and colour-magnitude diagrams can already provide precious information about the dynamical stage of a cluster and its age: while the cool core (i.e. old and relaxed) cluster shows basically no large-scale interactions, no significant blue galaxy population and a well-defined cD galaxy dominating the core, the merging cluster clearly shows inhomogeneities (i.e. two filamentary structures connected with the two main merging bodies), several “blue blobs” populated by blue galaxies and a collection of dominating galaxies none of which really stands out as a BCG. This suggests that in RXCJ0014.3-3022 the BCG, like the cluster itself, is still in formation and will be born from the merging of the multiple bright galaxies in the central regions.

Spectral index analysis provides a direct insight into the stellar activity of galaxies. With this tool, it was possible to confirm the increase in the star formation activity along the filaments, already suggested by the increase of the blue fraction of galaxies. The increase is spectroscopically confirmed by the increasing trend in the [OII] emission and the decrease of the 4000Å break strength, confirming that galaxies in the filaments are overall younger than in the core. This is also revealed independently by comparing D4000 with the UV emission. On the other hand, the cool core cluster RXCJ2308.3-0211 shows an older galaxy population, with rare [OII] emission

---

confirming the lack of star formation activity. Also comparison of UV colours shows that the population in this cluster is old and well evolved, and that the cluster likely did not undergo any significant star formation activity in the last billions of years. The star formation activity is also found to be strongly dependent on the environment, confirming the colour segregation already seen from optical photometry of the filaments in RXCJ0014.3-3022. Lastly, hints of obscured star formation is seen from the presence of very red galaxies with spectroscopic evidence of young age, suggesting that these galaxies could be dusty star forming spirals not detected due to their internal absorption.

The determination of the cluster luminosity function also provides a complementary way to investigate the galaxy population, this time from a statistical point of view. In both clusters, the luminosity function shape is found to be largely dependent on local environment, with a clear steepening towards the outskirts. In the case of RXCJ2308.3-0211, the increase is a relatively gentle function of cluster-centric radius, suggesting an evolutionary track from the outskirts to the core. As galaxies flow from the field to the high-density regions of the inner cluster, they undergo more and more frequently gravitational interactions that tend to deplete the faint end of the LF, with a consequent flattening in the cluster core. For RXCJ0014.3-3022, the change is even more specific and dramatic. Indeed, while in the core the LF appears rather typical of a cluster, along the filaments a very sharp change is detected beyond  $R_{200}$ . The LF undergoes a sudden flattening beyond this distance and a characteristic  $M^*$  is not detected, confirming again that peculiar processes are at work in these external regions. Galaxies in the filaments are seen to have a flat distribution across several orders of magnitude in luminosity, suggesting that these processes are globally transforming the infalling systems. Again, galaxy-galaxy interactions, and mainly harassment, can provide a suitable explanation for the rearrangement of the galaxy distribution.

The combination of luminosity information with mass information from the virial analysis can also provide precious information about cluster dynamics and inner processes. In fact, the radial dependence of differential  $M/L$  shows that the merging cluster shows abrupt, sharp changes in the relative proportions of light and mass, precisely beyond  $R_{200}$ . This confirms independently that in the very regions where matter flows in clusters, unexpected processes can happen that affect the galaxy population on a global scale.

Future developments of this work are numerous and different. Of course, a first aim will be completing the analysis of all DXL clusters. As the DXL sample provides an almost unbiased selection of high-mass clusters, it will provide an unique opportunity to study and understand how clusters can be different, and to search for the specific physical processes that shape the galaxy population in these massive systems.

## 5 Concluding remarks

---

Specific results will also suggest new channels of investigation and new opportunities to enrich the already expanding knowledge of clusters. This is already seen with the “flaming giants” detected in RXCJ0014.3-3022: new VIMOS observations are right now under completion and will help in identifying these peculiar galaxies and in understanding the processes at work on these systems. These galaxies are also under analysis with even different analysis, under a newly started collaboration with E. Valentjin and G. Verdoes Klein at the Kapteyn Institute. This project addresses the morphological analysis of the “flaming giants” with dedicated softwares and is aimed at describing their shapes, to confirm the feasibility of galaxy harassment as their origin. Preliminary results already show the presence of vestigial spiral arms, suggesting that these galaxies originated from compact spirals.

The future availability of deep wide-field or all-sky optical surveys (i.e. Pan-STARRS, Dark Energy Survey on CTIO, KIDS on ESO-VST and VIKING on ESO-VISTA) will provide an opportunity to test the methods developed here on very large data sets, given the availability of X-ray data to complement optical data, which will be made available by the future all-sky X-ray surveys (for instance eROSITA). This will allow to understand even better the interaction between galaxies and environment in clusters and to extend this analysis at different mass scales, to directly compare the relative efficiency of the observed processes with respect to the cluster mass and surrounding large-scale structure.

Comparison with semi-analytical models could provide another interesting thread of investigation, as comparison of results from observations will help in refining the recipes used in cosmological simulations to track the evolution of clusters and cluster galaxies. The results obtained with this work and similar future projects will help to better define the processes at work on cluster galaxies across their formation history and to understand how these processes behave in the most massive clusters in the universe.

Several specific results have been obtained through this still ongoing project. These results are already in itself very important, as they provide a direct and precise view of the complex processes that take part in the shaping of the galaxy population in clusters, and how differently these processes can affect the cluster as a whole depending on its interactions with the surrounding cosmic structures. They also help understanding to a deeper extent the very high end of the cluster population, as the study specifically targets the most massive and luminous clusters known.

The most outstanding achievement of this thesis, however, goes well beyond the single results. In fact, through this work I have shown how powerful can be the combined analysis of clusters from different and complementary points of view, both as observational strategies (X-ray, optical photometry, optical spectroscopy, UV photometry) and as analysis techniques (X-ray and optical morphology, colour-magnitude diagrams, spectral index analysis, luminosity functions, virial mass analysis). Com-

---

combination of these different sources of data can indeed provide a large wealth of information, through which it is possible to characterise in an unprecedented way the specific phenomena at work in the formation of clusters of galaxies.

## 5 Concluding remarks

---



## Useful techniques

### A.1 Surface density maps

Here I summarize the technique developed to derive galaxy surface density maps presented in Chapters 2 and 3.

Galaxies are counted locally by applying a fixed width mesh to the input catalogue of cluster members. A fixed mesh width is found to better map both high-density peaks and background, while adaptive meshes proved to be too sensitive to small-scale fluctuations, with the risk of a wrong evaluation of background. The galaxies are thus separated and counted in each element of the mesh.

The mesh width is found to partly affect the final density map, mainly by smoothing small-scale density peaks; its best value is found to be between 7 and 10 arcsec, corresponding to a physical scale of 30 to 45 kpc at the typical redshift of  $\sim 0.3$  of the DXL sample. A scale of 10 arcseconds was found by trial-and-error to suitably detect and map substructures in dense regions, while ensuring a good and stable sampling of low-density regions without being heavily affected by small-scale fluctuations.

Background is calculated in each mesh point by counting all objects in a fixed radius around the point. The chosen radius acts as a smoothing filter, ensuring a good sampling of the large-scale shape of background (so to correctly evaluate background mean and RMS). The background mean value and RMS are then calculated by fitting the background values distribution with a gaussian, assuming that the field should represent a population of randomly scattered objects with normal fluctuations. The gaussian is fitted through recursive 3-sigma clipping until convergence, which is always reached with 3 to 10 cycles. The final gaussian parameters are taken as mean

## A Useful techniques

---

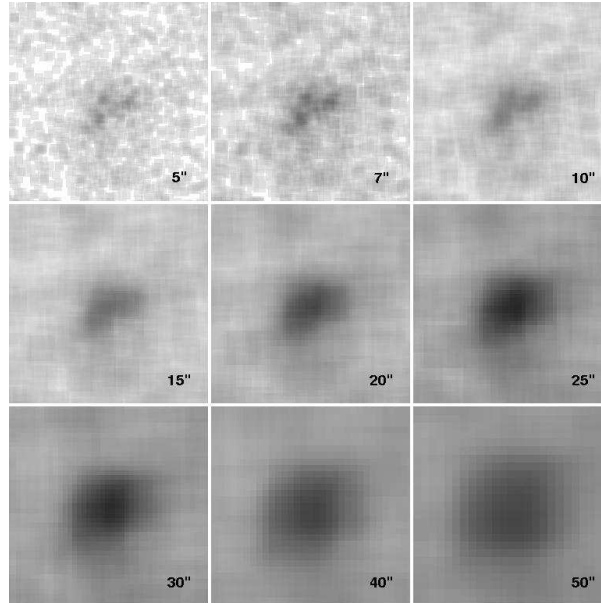


**Figure A.1:** Example of density map for the central part of RXCJ0014.3-3022. From top left to bottom right, density maps for different mesh widths are shown. The mesh width value in arcseconds is also shown for each map.

and RMS of background.

To select the most efficient smoothing radius, several test were run on the sample with different radius values. The background was thus calculated with increasing radii and then fitted with a gaussian, assuming it is dominated by random noise (i.e. randomly scattered field galaxies). The background mean value and RMS are weakly sensitive to the smoothing radius for radius values between 60'' and 120''. Below 60'', small-scale fluctuations make the background dominated by small numbers, while beyond 120'' the mean goes slowly but steadily down, due to undersampling of background counts at the field borders. Between 60'' and 120'' the background value is almost stable, with errors becoming slightly lower with increasing smoothing radius. The behaviour, along with the background RMS, is shown in Fig. A.2. A final smoothing scale of 110'' was chosen; this is equivalent to 500 kpc at the typical cluster redshift of  $\sim 0.3$ .

After evaluating background mean and RMS, the true density maps are generated. Galaxies are counted in each mesh box and their number is divided by the box area and then renormalized to Mpc scale by converting the box area in the physical area sampled at the cluster redshift, calculated assuming a standard  $\Lambda$ CDM cosmology. Galaxy counts are thus expressed in  $\text{Mpc}^{-2}$ . The counts are then smoothed with a gaussian filter to clean numerical spikes (arising at the map border due to wrong sam-



## A.2 Calculation of spectral indices

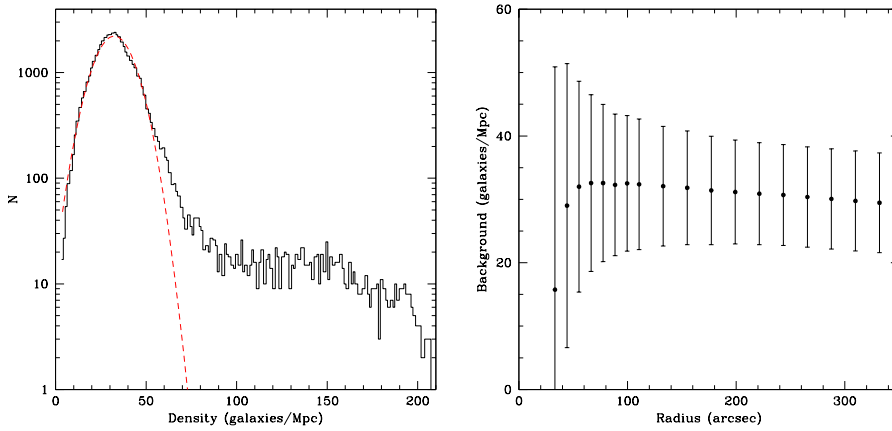


**Figure A.2:** Left panel: background fit for a smoothing radius of  $110''$  in the field of RXCJ0014.3-3023. The histogram is the count distribution in the field, with the high density tail due to overdense structures (i.e. the cluster and its filaments); the dashed line is the gaussian fit to the background. Right panel: background mean and error versus smoothing radius for the full catalogue of cluster members. For very low values (under  $60''$ ) the value rapidly goes down due to oversampling of small fluctuations, while beyond  $120''$  a trend towards lower values is due to undersampling of counts at the field border. Between  $60''$  and  $120''$ , the background value is stable. Error bars are  $1\sigma$  errors.

pling) and for better, continuous connection of counts in neighboring mesh cells. The same smoothing radius as for background calculation gives reliable results, cleaning spikes without deleting substructuring information.

A number of simulated background maps is then generated as randomly distributed values with normal distribution as given by the background best-fit parameters and chosen smoothing scale; the background map is then independently subtracted from the raw density map and the resulting background-subtracted maps are stacked together and renormalized. This ensures a background subtraction as smooth as possible and is unaffected by true overdensities in the cluster field. 100 iterations already give a good mean background subtraction.

The background-subtracted, stacked and renormalized image is in the end taken as the final surface density map of the field.

## A.2 Calculation of spectral indices

Here I summarize the technique used to calculate the equivalent width for observed VIMOS spectra and extensively used in the analysis shown in Chapter 3.

## A Useful techniques

---

Each spectrum is shifted to rest-frame. To calculate the spectrum continuum, wavelength windows are determined which avoid the potential presence of any known spectral feature in the observed range. The continuum emission in these broken spectral regions is then locally smoothed with a boxcar of 5 pixels (corresponding to a width of about 20Å) and interpolated between neighbouring windows in order to estimate the continuum emission underlying the spectral features of interest. Alternatively, the continuum emission across the whole spectrum was determined through a polynomial fit of the continuum emission in all wavelength windows. The ensuing fit provided a too smooth description of the continuum emission underlying the spectral features of interest, so that the ability of detecting low-S/N features like  $H_\delta$  was endangered. Therefore, this second method was discarded.

$W_0([OII])$  and  $W_0(H_\delta)$  are calculated by first fitting the emission or absorption line with a gaussian (representing the feature) plus a linear term in order to establish where the emission/absorption line begins and ends with respect to the continuum. This is done in a region centred on the rest-frame central wavelength of each line: the [3700,3750]Å interval for the [OII] emission line, and the [4080,4125]Å interval for the  $H_\delta$  absorption line. Where the line is found to be present (i.e. the gaussian term is different from zero), the line equivalent width is calculated by summing its excess/decrement flux with respect to the local continuum and then dividing by the total value of the continuum across the region, i.e.:

$$W = \sum_{\lambda_1}^{\lambda_2} \frac{F_l(\lambda) - F_c(\lambda)}{F_c(\lambda)}$$

where  $F_l(\lambda)$  is the total line flux at each wavelength,  $F_c(\lambda)$  is the flux value at each wavelength and  $\lambda_1$  and  $\lambda_2$  are the extremes of the regions. For comparison with other works, the sign of this definition was adapted so that [OII] emission provides a positive value for  $W_0([OII])$ , while  $W_0(H_\delta)$  is positive in absorption (as in Balogh et al. (1999)). The error on the equivalent width is calculated from equation (A8) in Bohlin et al. 1983).

The value of D4000 is determined as the flux ratio of the mean continuum emission in two neighbouring spectral regions of the 4000Å break, one bluewards and the other redwards. The blue and red continua are defined as the spectral region [3800,3890]Å and [4000,4050]Å, respectively. Uncertainties on D4000 are calculated as from the standard error-propagation theory, being this definition simply a ratio.

# B

## **Spectroscopic members catalogue of RXCJ0014.3-3022 (A 2744)**

Hereafter the full catalogue of spectroscopic objects in the field of RXCJ0014.3-3022 is provided. Along with position and redshift, for each object are also provided the values of spectral indices and BVR magnitudes with corresponding errors. Where equivalent widths were not calculated due to the line not being sampled in the instrument's spectral range, the table reads ND, i.e. Not Detected.

## B Spectroscopic members catalogue of RXCJ0014.3-3022 (A 2744)

Table B.1.

ID	R.A.	DEC.	z	$W_0(\text{[OII]})$ [Å]	$D_{4000}$ [Å]	$W_0(\text{H}\delta)$ [Å]	$B_{AB}$ [mag]	$V_{AB}$ [mag]	$R_{AB}$ [mag]
5246	00:14:33.3	-30:32:31.9	0.7781	18.59	ND	ND	22.44	22.16	21.51
5571	00:14:36.9	-30:32:09.15	0.4980	-1.81	1.686	0.111	24.23	23.07	21.63
5593	00:14:45.5	-30:32:06.35	2.5126	ND	ND	ND	22.02	21.84	21.94
5701	00:14:30.1	-30:32:08.70	0.4973	6.609	1.534	0.413	23.31	22.49	21.30
5758	00:14:48.2	-30:31:56.3	0.4996	-2.59	1.841	0.304	24.67	23.61	22.24
5897	00:14:28.7	-30:31:44.1	0.4981	0.935	1.044	-0.95	23.65	23.05	22.56
5973	00:14:42.0	-30:31:46.3	0.5225	10.61	1.119	1.191	21.52	21.11	20.28
6066	00:14:45.7	-30:31:34.3	0.5239	12.49	1.121	3.288	22.92	22.54	21.75
6418	00:14:23.7	-30:31:10.8	0.3028	0.485	1.516	0.664	23.24	22.16	21.12
6691	00:14:41.4	-30:30:53.3	0.7307	2.817	0.073	ND	24.46	23.44	22.47
6714	00:14:25.9	-30:30:53.0	0.3907	8.625	1.574	1.434	23.47	22.79	22.05
6819	00:14:12.2	-30:30:33.9	0.0639	2.690	1.545	0.940	20.11	19.57	18.98
6955	00:14:38.3	-30:30:40.5	0.4102	2.557	1.236	1.089	21.83	21.13	20.28
7063	00:13:46.5	-30:30:36.3	0.3042	3.336	1.193	1.248	21.59	20.86	20.24
7079	00:13:58.4	-30:30:32.0	0.4157	5.254	1.174	0.692	22.12	21.49	20.68
7185	00:13:50.4	-30:30:21.8	0.3594	9.853	1.158	1.892	22.74	21.96	21.32
7194	00:14:25.8	-30:30:20.0	0.5979	0.674	0.962	2.637	23.93	23.10	22.07
7223	00:14:09.66	-30:30:22.7	0.6097	-2.57	1.665	2.014	22.92	22.23	21.03
7227	00:14:34.3	-30:30:23.7	0.4345	8.289	1.143	0.977	21.91	21.33	20.60
7234	00:14:55.3	-30:30:18.6	0.3947	6.681	1.263	1.405	23.01	22.26	21.59
7279	00:14:14.1	-30:30:19.3	0.3025	0.214	1.388	0.965	23.61	22.53	21.64
7285	00:14:44.3	-30:30:17.0	0.3037	17.02	1.047	0.339	22.73	22.19	21.68
7361	00:14:07.90	-30:30:17.4	0.6060	1.418	1.023	0.630	21.31	20.90	19.94
7503	00:14:14.3	-30:30:03.41	0.4994	1.378	1.722	0.222	23.88	22.89	21.43
7800	00:14:25.5	-30:29:42.7	0.4983	1.707	1.207	1.241	22.24	21.71	20.72
7801	00:14:14.3	-30:29:42.4	0.3015	-0.48	1.519	0.485	23.01	22.02	20.95
7867	00:14:59.1	-30:29:39.7	0.1286	4.879	1.215	0.656	21.69	21.17	20.69
7928	00:14:14.7	-30:29:29.8	0.5010	-1.31	1.577	0.017	25.10	23.94	22.39
7932	00:13:40.0	-30:29:30.8	0.6129	-1.58	1.682	1.006	24.23	23.23	21.91
7933	00:14:06.08	-30:29:30.8	0.3032	-1.67	1.663	0.161	20.28	19.37	18.57
7953	00:13:55.9	-30:29:38.2	0.3066	-0.83	1.423	1.294	22.72	21.80	21.04
7954	00:14:26.5	-30:29:31.3	0.4795	11.69	1.271	1.630	23.23	22.73	21.84
7955	00:14:32.5	-30:29:32.5	0.2715	7.191	1.234	1.631	23.22	22.46	21.76
7973	00:14:38.4	-30:29:32.5	0.1075	6.231	1.219	0.841	21.94	21.51	21.07
7987	00:14:48.0	-30:29:29.3	0.4467	6.598	1.193	1.620	22.43	21.88	21.19
8015	00:14:07.44	-30:29:28.5	0.4223	1.234	1.358	0.824	23.02	22.14	20.96
8061	00:14:50.0	-30:29:13.4	0.1890	0.483	1.728	0.352	18.86	18.15	17.53
8098	00:14:47.1	-30:29:26.5	0.2915	1.597	1.213	1.049	21.37	20.56	19.90
8134	00:14:50.7	-30:29:24.2	0.0531	6.525	1.437	0.595	22.21	21.87	21.51
8169	00:14:01.74	-30:28:37.3	0.0538	2.781	1.479	0.774	19.49	19.16	18.76
8214	00:14:34.7	-30:29:17.0	0.6012	3.544	1.556	-0.58	23.22	22.49	21.21
8261	00:14:48.0	-30:29:13.3	0.6269	8.980	1.054	0.729	21.88	21.57	20.73
8309	00:14:25.2	-30:29:13.6	0.5003	3.752	1.288	2.222	23.10	22.45	21.17
8314	00:14:26.6	-30:29:12.2	0.2713	6.636	1.162	1.335	21.35	20.68	20.20
8389	00:14:28.5	-30:29:05.52	0.7793	3.869	ND	ND	22.61	22.04	21.14
8392	00:14:53.8	-30:28:58.2	0.0084	-0.32	1.604	-0.30	24.02	23.45	22.66
8409	00:13:55.1	-30:28:59.0	0.0313	1.944	1.144	-0.25	23.50	23.13	22.46

Table B.1—Continued

ID	R.A.	DEC.	z	$W_0([\text{OII}])$ [Å]	$D4000$ [Å]	$W_0(\text{H}\delta)$ [Å]	$B_{\text{AB}}$ [mag]	$V_{\text{AB}}$ [mag]	$R_{\text{AB}}$ [mag]
8425	00:14:31.7	-30:28:58.3	0.1448	6.448	1.297	0.947	22.34	21.92	21.51
8471	00:14:45.4	-30:28:55.0	0.6505	6.680	1.125	-6.68	23.00	22.59	21.77
8507	00:14:21.3	-30:28:54.3	0.3034	0.815	1.360	1.224	24.09	23.14	22.22
8530	00:14:09.31	-30:28:55.8	0.4098	3.673	1.297	0.950	22.83	21.72	20.62
8542	00:14:39.8	-30:28:52.5	0.6018	2.805	1.303	1.388	22.46	21.97	20.93
8584	00:14:45.8	-30:28:57.2	0.2898	4.898	1.792	-1.17	20.68	19.79	19.03
8630	00:14:47.3	-30:28:42.3	0.6510	3.546	1.306	-2.45	24.62	23.64	22.13
8658	00:13:50.8	-30:28:42.7	1.0163	ND	ND	ND	22.96	22.39	21.75
8719	00:14:59.8	-30:28:41.0	0.2662	-0.53	1.483	1.035	21.70	20.62	19.71
8742	00:14:18.0	-30:28:36.0	0.3032	3.129	1.233	1.081	23.38	22.60	21.94
8809	00:14:01.20	-30:28:38.1	0.0532	21.41	0.274	-2.28	21.41	20.98	20.82
8825	00:13:29.3	-30:28:33.4	0.1250	3.441	1.402	0.545	22.46	22.11	21.60
8837	00:14:25.0	-30:28:29.3	0.3057	1.589	1.650	0.186	24.05	22.94	21.90
8842	00:14:29.2	-30:28:32.3	0.1878	-1.40	1.606	1.227	19.54	18.90	18.36
8843	00:14:32.3	-30:28:27.8	0.5004	0.487	1.627	0.512	24.26	23.07	21.58
8938	00:14:11.7	-30:28:23.6	0.4965	6.243	1.018	0.067	22.97	22.55	21.52
8946	00:14:33.7	-30:28:23.1	0.3809	9.922	1.661	0.765	23.60	22.67	21.77
8973	00:14:48.8	-30:28:25.6	0.4535	9.167	1.063	1.421	22.76	22.20	21.50
9002	00:14:59.3	-30:28:18.1	0.6237	10.81	1.095	-0.06	22.34	22.04	21.25
9031	00:13:56.7	-30:28:20.7	0.6176	6.081	1.064	2.281	23.24	22.82	21.75
9063	00:14:41.9	-30:28:10.7	0.1074	4.234	1.328	0.840	21.75	21.28	20.79
9140	00:13:12.8	-30:28:05.40	0.2746	-3.65	1.510	1.595	20.69	19.95	19.33
9144	00:14:30.0	-30:28:11.3	0.5161	2.960	1.266	1.100	23.44	22.75	21.57
9153	00:13:46.2	-30:28:10.9	0.1097	-1.45	1.043	1.196	22.97	22.60	22.04
9219	00:14:55.7	-30:28:08.66	0.2640	0.713	1.660	-0.50	22.00	20.87	19.96
9223	00:14:26.4	-30:28:07.71	0.4975	6.526	1.110	1.936	22.70	22.25	21.33
9226	00:13:17.2	-30:28:07.97	0.5605	-2.17	1.488	0.239	22.54	21.79	20.59
9227	00:13:39.7	-30:28:06.62	0.6375	-0.91	1.541	0.154	23.95	22.97	21.73
9262	00:13:05.12	-30:28:00.58	0.7720	3.598	ND	ND	23.51	23.09	22.17
9302	00:13:55.8	-30:27:55.3	0.3139	-1.02	1.375	2.006	20.60	19.66	18.71
9327	00:14:27.2	-30:27:57.2	0.3066	-0.66	1.539	0.919	24.08	23.12	22.02
9370	00:14:50.3	-30:27:58.3	0.3631	2.573	1.382	2.480	21.72	20.83	20.06
9381	00:14:07.19	-30:27:24.9	0.5895	-1.39	1.665	4.749	19.52	19.01	18.29
9392	00:13:28.4	-30:27:55.1	0.1078	2.369	1.371	0.669	21.61	21.11	20.57
9394	00:14:17.4	-30:27:55.0	0.5001	-1.91	1.605	0.633	23.82	22.87	21.39
9403	00:14:44.0	-30:27:55.5	0.2687	5.973	1.211	0.899	22.40	21.65	21.07
9452	00:14:05.28	-30:27:56.5	0.6923	1.213	0.483	16.19	22.75	22.22	21.33
9522	00:14:26.2	-30:27:44.2	0.4990	5.632	1.290	1.328	23.34	22.89	21.81
9547	00:13:40.5	-30:27:41.0	0.3143	14.96	1.084	-3.00	25.39	24.26	22.99
9552	00:13:16.2	-30:27:43.3	0.7283	8.408	0.304	ND	23.05	22.64	21.78
9574	00:13:23.7	-30:27:42.8	0.1067	1.779	1.128	0.422	21.97	21.59	21.17
9575	00:14:07.09	-30:27:43.1	0.4960	3.498	1.185	1.476	23.20	22.60	21.57
9593	00:14:19.5	-30:27:42.7	0.3006	10.66	1.170	2.055	22.66	22.10	21.55
9638	00:14:35.0	-30:27:42.9	0.1051	4.377	1.237	0.753	21.73	21.23	20.68
9740	00:13:56.4	-30:27:28.5	0.1443	-0.23	1.385	0.592	23.38	22.67	21.85
9756	00:13:39.0	-30:27:29.2	0.2953	1.157	0.997	0.574	23.33	22.88	22.34
9759	00:14:04.31	-30:27:31.1	0.3074	-1.09	1.365	1.794	23.40	22.41	21.57

## B Spectroscopic members catalogue of RXCJ0014.3-3022 (A 2744)

Table B.1—Continued

ID	R.A.	DEC.	z	$W_0([\text{OII}])$ [Å]	$D4000$ [Å]	$W_0(\text{H}\delta)$ [Å]	$B_{\text{AB}}$ [mag]	$V_{\text{AB}}$ [mag]	$R_{\text{AB}}$ [mag]
9768	00:13:18.1	-30:27:29.3	0.2684	6.439	1.236	0.958	22.36	21.58	21.03
9852	00:13:46.9	-30:27:26.9	0.3128	2.549	1.334	0.998	21.95	21.07	20.32
9882	00:14:55.9	-30:27:20.4	0.1898	3.425	1.236	1.480	22.48	22.03	21.42
9893	00:14:42.8	-30:27:19.6	0.6522	1.556	1.344	-1.63	24.20	23.33	21.88
9895	00:13:19.6	-30:27:16.5	0.1077	6.364	1.288	0.425	22.37	21.94	21.56
9898	00:14:25.0	-30:27:23.5	0.3067	2.467	1.488	1.623	21.66	20.78	19.89
9964	00:14:38.7	-30:27:17.4	0.6092	5.365	1.403	0.051	23.35	22.32	20.96
9966	00:13:40.5	-30:27:17.5	0.1449	-1.62	1.178	-0.87	19.20	18.86	18.45
9976	00:13:47.8	-30:27:17.5	0.4394	11.42	1.069	1.783	21.89	21.31	20.66
9980	00:14:05.90	-30:27:17.9	0.3056	2.548	1.227	1.166	20.33	19.53	18.87
9991	00:13:44.9	-30:26:53.7	0.1607	4.949	1.422	1.234	20.17	19.62	19.12
10012	00:14:31.5	-30:27:14.0	0.3077	-0.34	1.565	1.459	24.07	23.17	22.29
10036	00:14:01.02	-30:27:08.47	0.3145	-0.35	1.394	0.984	23.54	22.56	21.77
10071	00:14:33.3	-30:27:05.45	0.5014	-3.61	1.729	0.542	24.69	23.36	21.98
10115	00:13:29.9	-30:27:10.7	0.1045	2.077	1.458	0.722	20.84	19.74	18.79
10125	00:13:40.4	-30:27:08.76	0.6063	-1.86	1.393	2.090	22.60	21.86	20.82
10145	00:14:22.0	-30:27:08.79	0.0573	11.53	1.340	0.186	19.96	19.62	19.23
10162	00:14:05.08	-30:26:59.8	0.6174	9.576	1.083	1.286	23.34	22.52	21.60
10187	00:14:15.4	-30:26:55.4	0.3118	-1.59	1.410	0.975	24.03	23.00	22.13
10224	00:14:54.6	-30:27:06.68	0.4009	-0.93	1.431	2.076	21.91	21.15	20.25
10260	00:14:38.2	-30:26:56.6	0.2685	5.050	1.193	1.538	21.84	21.11	20.54
10318	00:13:30.6	-30:26:56.2	0.5720	1.385	1.249	-1.33	21.09	20.08	19.09
10346	00:14:31.0	-30:26:46.6	0.4987	8.696	1.207	1.473	22.99	22.59	21.70
10355	00:14:28.4	-30:26:53.3	0.2985	7.109	1.205	0.658	22.09	21.42	20.92
10362	00:14:06.33	-30:26:49.0	0.6392	15.88	1.022	1.444	22.30	22.01	21.19
10381	00:13:28.4	-30:26:51.9	0.3110	1.751	1.240	0.657	21.20	20.37	19.58
10397	00:13:48.3	-30:26:44.0	0.6053	4.351	1.103	1.259	22.84	22.37	21.33
10446	00:14:50.8	-30:26:38.2	0.1623	4.015	0.808	-0.37	22.21	22.00	21.44
10452	00:13:50.7	-30:26:25.8	0.0610	2.719	1.556	0.457	18.91	18.54	18.12
10464	00:14:25.2	-30:26:39.4	0.2603	7.189	1.247	0.643	22.74	22.17	21.71
10469	00:14:44.0	-30:26:38.9	0.7772	5.757	ND	ND	22.33	22.10	21.45
10537	00:14:14.5	-30:26:33.4	0.3100	-0.79	1.670	0.118	23.50	22.37	21.33
10587	00:13:53.3	-30:26:39.1	0.3039	-0.81	1.485	1.755	21.14	20.29	19.54
10602	00:13:18.0	-30:26:26.1	0.5838	4.024	1.207	1.044	23.77	23.17	22.13
10639	00:14:32.1	-30:26:29.5	0.2672	6.710	1.194	0.436	21.84	21.16	20.59
10655	00:14:38.8	-30:26:23.6	0.4504	0.447	1.252	2.067	22.92	22.42	21.25
10690	00:14:01.55	-30:26:31.2	0.3042	-1.08	1.470	0.190	21.94	20.81	19.83
10722	00:13:26.6	-30:26:23.8	0.1080	5.316	1.302	0.131	20.96	20.51	20.07
10731	00:14:12.3	-30:26:10.8	0.4981	3.341	1.736	0.068	22.84	21.94	20.51
10762	00:13:34.0	-30:26:25.5	0.3062	1.756	1.414	0.748	21.16	20.32	19.54
10856	00:14:15.2	-30:26:11.5	0.3085	1.362	1.494	-0.04	22.85	21.85	20.87
10942	00:14:59.7	-30:26:08.01	0.1857	4.023	1.196	0.895	21.10	20.56	20.11
10953	00:14:37.8	-30:26:10.5	0.0693	7.614	1.448	2.066	19.71	19.37	18.93
10990	00:14:05.60	-30:25:59.9	0.4669	-2.06	1.501	0.281	23.59	22.78	21.43
11038	00:13:30.6	-30:25:57.6	0.5717	2.227	0.940	-1.59	22.66	22.10	20.94
11107	00:14:35.5	-30:26:01.60	0.4290	8.119	1.076	-1.61	22.35	21.76	21.15
11120	00:13:33.4	-30:25:56.8	0.3063	2.742	1.231	0.850	21.44	20.61	19.92

Table B.1—Continued

ID	R.A.	DEC.	z	$W_0([\text{OII}])$ [Å]	$D4000$ [Å]	$W_0(\text{H}\delta)$ [Å]	$B_{\text{AB}}$ [mag]	$V_{\text{AB}}$ [mag]	$R_{\text{AB}}$ [mag]
11121	00:13:07.89	-30:25:56.5	0.2894	3.491	1.231	1.017	21.62	20.86	20.24
11144	00:14:05.68	-30:25:49.3	0.3062	-1.13	1.462	1.189	23.56	22.55	21.59
11196	00:13:44.7	-30:25:48.4	0.2654	8.628	1.173	1.055	22.64	22.02	21.50
11263	00:14:35.1	-30:25:37.7	0.6069	8.257	1.167	1.800	22.92	22.64	21.74
11295	00:13:59.0	-30:25:42.3	0.2829	-1.43	0.841	-0.37	23.11	22.80	22.27
11312	00:14:23.9	-30:25:45.8	0.2649	4.978	1.275	1.550	18.89	17.92	16.87
11323	00:14:03.78	-30:25:45.0	0.3122	2.032	1.320	0.357	21.01	20.12	19.39
11348	00:13:05.42	-30:25:37.6	0.3092	11.70	1.333	0.851	23.05	22.28	21.68
11405	00:13:59.3	-30:25:29.3	0.3105	0.161	1.365	1.254	23.69	22.68	21.76
11437	00:14:37.3	-30:25:27.0	0.3078	-0.27	1.452	1.814	23.85	22.95	21.99
11454	00:14:58.6	-30:25:25.4	0.3146	6.708	1.147	0.847	22.91	22.21	21.62
11522	00:14:12.5	-30:25:23.6	0.4984	4.600	1.195	1.066	22.26	21.65	20.63
11652	00:13:38.5	-30:25:15.8	0.3089	-4.53	4.039	-1.79	21.39	20.99	20.54
11684	00:14:13.8	-30:25:15.2	0.3059	0.766	1.346	1.231	21.31	20.50	19.77
11709	00:13:07.60	-30:25:10.9	0.2649	8.228	1.186	0.949	21.30	20.67	20.20
11789	00:14:24.7	-30:25:00.03	0.3178	-0.69	1.297	0.697	24.35	23.43	22.49
11829	00:13:47.2	-30:25:00.94	0.4790	1.927	1.442	0.862	24.91	23.81	22.22
11842	00:13:20.3	-30:24:59.0	0.6058	19.66	1.048	1.351	22.72	22.45	21.56
11850	00:13:33.0	-30:25:04.35	0.6056	4.173	1.123	0.694	22.14	21.71	20.69
11897	00:13:50.9	-30:25:01.76	0.3576	4.495	1.427	2.442	22.24	21.30	20.19
12019	00:14:00.47	-30:25:01.24	0.4995	-1.41	1.295	1.153	22.67	22.11	20.99
12026	00:13:44.3	-30:24:50.3	0.3116	7.655	1.139	0.914	21.94	21.35	20.84
12066	00:14:07.64	-30:24:45.1	0.4585	19.36	1.008	1.511	24.72	23.95	22.76
12083	00:14:32.4	-30:24:42.4	0.4094	10.09	1.259	1.297	23.11	22.49	21.85
12099	00:13:31.6	-30:24:39.8	0.3054	1.993	1.099	-1.62	24.97	23.88	22.75
12102	00:13:18.5	-30:24:47.8	0.1392	1.697	1.429	2.543	22.20	21.51	20.89
12270	00:14:30.2	-30:24:29.9	0.2928	1.381	1.388	0.556	23.71	23.16	22.32
12305	00:14:09.45	-30:24:40.4	0.3180	0.400	1.502	0.400	21.55	20.54	19.52
12364	00:13:57.6	-30:24:34.2	0.3171	1.756	1.160	0.418	20.96	20.16	19.52
12372	00:13:41.2	-30:24:23.8	0.1067	1.410	1.299	0.734	21.73	21.22	20.68
12404	00:14:09.46	-30:24:25.3	0.4996	3.633	1.179	1.192	21.65	21.16	20.21
12416	00:14:53.4	-30:24:13.8	0.0734	4.761	1.516	-0.32	21.36	21.07	20.68
12430	00:14:00.31	-30:24:22.1	0.5006	1.633	1.444	1.299	22.97	22.31	21.11
12518	00:14:31.6	-30:24:19.1	0.3075	0.533	1.445	0.785	22.19	21.19	20.27
12663	00:14:07.15	-30:24:22.3	0.3019	-0.89	1.924	-0.39	20.16	19.09	18.02
12738	00:13:25.9	-30:23:58.3	0.7298	3.092	0.028	ND	24.30	23.38	22.11
12741	00:14:22.0	-30:24:20.2	0.3163	-0.62	2.002	-1.48	20.21	19.11	17.93
12931	00:13:15.2	-30:23:55.8	0.3059	1.039	1.280	1.094	20.46	19.66	19.04
13099	00:15:34.3	-30:23:29.9	0.6564	-1.38	1.335	0.686	25.45	24.55	22.95
13200	00:13:18.9	-30:23:29.0	0.6059	19.10	0.943	0.260	22.68	22.45	21.58
13225	00:15:26.5	-30:23:31.3	0.1903	6.615	1.281	1.358	20.75	20.33	19.91
13239	00:13:28.7	-30:23:26.1	0.1310	1.421	1.249	0.765	21.55	21.35	21.02
13250	00:13:05.18	-30:23:33.3	0.1868	4.272	1.265	0.593	19.94	19.31	18.77
13257	00:14:28.4	-30:23:34.1	0.3019	13.24	1.092	-0.01	20.88	20.34	19.99
13311	00:14:14.3	-30:23:21.4	0.2999	-1.38	1.480	-0.97	23.58	22.63	21.76
13395	00:14:22.7	-30:23:20.4	0.3031	0.315	1.679	-4.02	22.57	21.52	20.39
13418	00:14:38.0	-30:23:18.1	0.0920	10.15	1.337	0.995	21.26	20.85	20.43

## B Spectroscopic members catalogue of RXCJ0014.3-3022 (A 2744)

Table B.1—Continued

ID	R.A.	DEC.	z	$W_0([\text{OII}])$ [Å]	$D4000$ [Å]	$W_0(\text{H}\delta)$ [Å]	$B_{\text{AB}}$ [mag]	$V_{\text{AB}}$ [mag]	$R_{\text{AB}}$ [mag]
13463	00:15:33.9	-30:23:08.69	0.5166	4.207	1.169	1.709	22.67	21.64	20.65
13490	00:13:30.0	-30:23:20.8	0.3605	0.364	1.315	0.712	20.64	19.87	19.15
13505	00:14:22.7	-30:23:29.5	0.2998	1.164	1.633	-0.67	20.67	19.57	18.50
13597	00:13:18.3	-30:23:14.3	0.1384	2.855	1.570	1.183	20.97	20.45	20.02
13638	00:14:15.3	-30:23:03.24	0.3560	4.269	1.093	1.590	22.03	21.24	20.59
13651	00:14:09.15	-30:23:09.37	0.3112	1.087	1.485	0.690	20.62	19.62	18.81
13717	00:13:13.5	-30:22:51.4	0.2125	0.975	1.239	0.672	23.50	22.95	22.20
13768	00:14:33.7	-30:22:49.8	0.6630	4.342	0.998	5.142	23.26	22.87	21.98
13839	00:15:21.2	-30:22:46.1	0.4742	3.319	1.166	0.834	22.29	21.78	20.97
13899	00:13:24.3	-30:22:45.3	0.3161	2.366	1.395	-0.31	21.13	20.56	20.12
13905	00:15:03.67	-30:22:42.0	0.3325	4.885	1.212	1.716	22.69	21.99	21.36
13916	00:14:26.2	-30:22:43.2	0.2389	-1.02	1.983	0.036	21.18	20.72	20.37
13985	00:13:09.89	-30:22:36.7	0.5635	5.628	1.249	0.829	22.98	22.54	21.52
13996	00:14:17.5	-30:22:40.3	0.3184	0.208	1.556	0.139	23.15	22.10	21.03
13998	00:15:08.11	-30:22:31.9	0.7639	4.111	ND	ND	25.25	23.66	22.40
14202	00:15:19.3	-30:22:19.7	0.8260	18.31	ND	ND	23.51	23.27	22.51
14240	00:14:39.1	-30:22:19.8	0.6057	4.397	1.193	1.389	23.83	23.21	22.05
14241	00:15:08.80	-30:22:18.2	0.6768	-1.19	0.900	11.95	24.85	23.79	22.48
14248	00:14:41.7	-30:22:40.8	0.1199	5.867	1.254	1.085	20.91	20.55	20.21
14322	00:15:27.6	-30:22:12.8	0.7707	8.667	ND	ND	23.75	23.30	22.68
14362	00:14:16.1	-30:22:24.5	0.2964	-0.29	1.436	0.658	21.83	20.93	20.04
14748	00:15:15.2	-30:21:46.7	0.6017	4.497	1.061	1.554	23.16	22.84	21.75
14983	00:13:51.1	-30:21:36.9	0.4955	5.317	1.167	2.900	24.17	23.08	21.65
15006	00:14:07.60	-30:21:35.3	0.3146	-0.90	1.368	-0.66	22.01	20.91	19.84
15024	00:14:36.5	-30:21:32.3	0.6882	1.432	1.010	16.47	25.00	23.52	22.10
15041	00:15:17.7	-30:21:32.5	0.3160	7.423	1.211	1.243	22.08	21.39	20.87
15050	00:13:40.5	-30:21:37.7	0.1482	6.177	1.236	1.257	21.48	21.05	20.74
15054	00:14:27.3	-30:21:34.5	0.3035	-0.53	1.597	-0.73	22.41	21.53	20.73
15075	00:15:27.1	-30:21:33.5	0.3025	3.805	1.252	1.461	21.41	20.68	20.17
15123	00:15:10.0	-30:21:24.8	0.0702	10.36	1.127	-1.71	24.37	23.90	22.78
15229	00:14:11.6	-30:21:21.7	0.3193	0.989	1.678	0.597	22.21	21.23	20.17
15323	00:13:52.2	-30:21:19.7	0.4942	0.585	1.439	1.207	22.67	22.02	20.63
15369	00:14:26.2	-30:21:11.3	0.6229	1.800	1.541	-0.71	24.78	23.86	22.57
15431	00:13:48.2	-30:21:06.90	0.4862	0.246	0.673	-6.20	21.99	21.74	21.35
15470	00:15:28.4	-30:21:01.35	0.3936	-3.98	0.895	1.285	25.41	24.54	22.98
15497	00:14:32.4	-30:21:19.9	0.1228	1.830	1.424	1.286	19.98	19.40	18.82
15532	00:14:33.6	-30:21:09.44	0.2968	0.396	1.531	0.825	21.22	20.16	19.36
15599	00:14:05.12	-30:21:03.68	0.2893	5.049	1.201	1.159	21.39	20.74	20.19
15738	00:15:15.6	-30:20:49.1	0.6892	4.405	0.778	17.26	23.23	22.69	21.78
15761	00:15:31.7	-30:20:47.4	0.3061	1.683	1.319	0.781	22.77	22.03	21.32
15837	00:14:30.1	-30:20:58.6	0.2966	-0.62	1.902	-1.29	21.18	20.10	19.07
15863	00:14:57.6	-30:20:59.0	0.3000	1.836	1.451	1.118	19.76	18.90	18.20
15877	00:15:06.08	-30:20:49.3	0.3010	3.241	1.290	1.431	21.86	20.93	20.21
15883	00:14:14.8	-30:20:39.5	0.3074	-0.56	1.528	0.062	24.23	23.20	22.09
15884	00:13:59.9	-30:20:45.3	0.4509	5.694	1.183	1.572	21.93	21.26	20.37
15956	00:13:43.3	-30:20:38.2	0.6104	2.240	0.946	1.756	22.46	21.46	20.37
16030	00:14:37.7	-30:20:32.9	0.3041	-0.65	1.441	1.443	23.64	22.65	21.87



Table B.1—Continued

ID	R.A.	DEC.	z	$W_0([\text{OII}])$ [Å]	$D4000$ [Å]	$W_0(\text{H}\delta)$ [Å]	$B_{\text{AB}}$ [mag]	$V_{\text{AB}}$ [mag]	$R_{\text{AB}}$ [mag]
16037	00:14:21.2	-30:20:40.9	0.1869	6.758	1.167	0.914	21.23	20.70	20.29
16050	00:14:26.0	-30:20:33.9	0.4476	8.010	1.051	1.829	22.75	22.25	21.59
16057	00:15:19.2	-30:20:32.7	0.3099	10.98	1.149	0.386	21.95	21.35	20.91
16092	00:15:28.5	-30:20:26.4	0.1710	8.286	1.422	0.987	22.44	21.97	21.52
16135	00:14:58.9	-30:20:34.3	0.6268	5.063	1.241	0.022	22.75	21.94	20.55
16149	00:14:32.5	-30:20:23.8	0.6034	-0.73	1.539	-0.26	24.72	23.71	22.45
16201	00:14:19.9	-30:20:24.3	0.6043	6.448	1.151	1.606	22.12	21.76	20.71
16272	00:14:10.1	-30:20:18.6	0.2396	7.097	1.247	1.368	22.59	21.98	21.46
16354	00:15:12.5	-30:20:12.9	0.7256	4.833	0.157	ND	22.90	22.32	21.41
16377	00:14:37.2	-30:20:12.4	0.1407	16.89	1.149	-0.47	22.28	21.89	21.57
16418	00:15:03.16	-30:20:06.76	0.8256	16.29	ND	ND	24.02	23.32	22.19
16446	00:14:47.8	-30:20:05.97	0.5364	6.436	1.156	0.531	23.46	23.02	21.99
16455	00:14:45.5	-30:20:11.9	0.7423	5.143	-0.83	ND	24.26	23.45	22.17
16470	00:14:58.6	-30:19:23.5	0.0638	3.573	1.501	0.867	18.44	18.04	17.54
16481	00:14:16.1	-30:20:05.88	0.7457	7.375	-0.14	ND	23.58	23.04	22.25
16538	00:13:58.5	-30:20:08.57	0.6020	0.517	1.514	0.186	24.02	23.02	21.62
16703	00:14:25.1	-30:19:54.1	0.4991	7.543	1.065	0.802	22.85	22.36	21.48
16710	00:14:45.9	-30:19:54.7	0.5078	-6.34	1.091	-0.80	23.32	22.65	21.83
16787	00:14:14.8	-30:19:51.6	0.6436	1.183	1.316	1.610	22.01	21.46	20.37
16819	00:14:37.4	-30:19:50.1	0.6053	3.354	1.160	1.776	22.34	22.02	21.06
16874	00:13:18.4	-30:19:28.3	0.3357	0.417	1.151	1.323	20.49	19.70	19.06
16913	00:14:06.49	-30:19:46.6	0.6922	6.938	0.450	14.61	22.04	21.60	20.67
17030	00:14:50.0	-30:19:31.8	0.7419	21.81	-0.16	ND	22.54	22.32	21.72
17034	00:14:35.5	-30:19:31.7	0.2499	-1.90	3.102	-7.15	23.60	22.86	22.08
17073	00:13:56.5	-30:19:33.9	0.6032	1.370	1.664	0.546	23.10	22.39	21.11
17124	00:15:17.6	-30:19:24.6	0.2372	10.99	1.172	0.821	22.55	21.90	21.33
17176	00:14:48.4	-30:19:22.0	0.5656	8.357	1.170	1.715	23.02	22.60	21.75
17188	00:13:54.8	-30:19:26.9	0.3152	0.464	1.868	-0.81	21.67	20.50	19.29
17228	00:14:39.4	-30:19:17.2	0.6038	8.093	1.077	2.261	23.33	22.88	21.86
17281	00:14:38.5	-30:19:19.8	0.6019	6.644	1.071	1.495	23.13	22.78	21.82
17300	00:15:03.92	-30:19:10.9	0.3195	0.062	1.227	0.446	23.32	22.66	21.95
17302	00:14:29.8	-30:19:15.2	0.3992	8.162	1.140	0.857	22.59	21.96	21.28
17391	00:13:45.9	-30:19:08.43	0.6845	12.19	0.817	7.850	21.94	21.74	21.03
17394	00:14:31.1	-30:19:13.8	0.3059	-0.90	1.847	-1.04	20.48	19.39	18.32
17403	00:13:23.7	-30:19:07.38	0.6493	2.794	1.250	-4.75	23.14	22.64	21.58
17478	00:15:23.7	-30:19:05.36	0.4106	10.17	1.099	0.813	21.83	21.29	20.58
17507	00:15:12.8	-30:18:57.8	0.7163	-2.50	0.173	ND	25.18	23.70	22.22
17536	00:13:10.7	-30:18:57.5	0.3292	9.243	1.152	1.642	22.79	22.08	21.52
17590	00:13:35.9	-30:18:56.6	0.7502	3.816	ND	ND	22.95	22.46	21.60
17629	00:14:23.2	-30:18:50.0	0.3010	0.828	1.476	0.321	23.96	22.84	21.88
17641	00:15:31.2	-30:18:47.1	0.4839	1.094	0.904	-0.98	24.10	23.63	22.78
17703	00:13:02.76	-30:18:44.4	0.3006	0.379	1.191	0.025	24.07	22.99	22.05
17720	00:14:21.0	-30:18:55.5	0.3593	0.779	1.320	1.048	20.86	20.09	19.37
17725	00:14:14.9	-30:18:47.6	0.7790	3.480	ND	ND	23.14	22.70	21.64
17735	00:13:44.3	-30:18:42.7	0.7051	9.787	1.126	2.791	26.10	24.74	22.77
17750	00:14:50.4	-30:18:52.4	0.1082	1.687	1.225	1.063	20.71	20.32	19.94
17755	00:13:34.2	-30:18:53.2	0.1219	3.454	1.269	0.806	20.45	19.87	19.28

## B Spectroscopic members catalogue of RXCJ0014.3-3022 (A 2744)

Table B.1—Continued

ID	R.A.	DEC.	z	$W_0([\text{OII}])$ [Å]	$D4000$ [Å]	$W_0(\text{H}\delta)$ [Å]	$B_{\text{AB}}$ [mag]	$V_{\text{AB}}$ [mag]	$R_{\text{AB}}$ [mag]
17779	00:14:47.6	-30:18:42.1	0.4472	2.040	1.327	-0.19	23.64	22.93	21.85
17796	00:13:56.4	-30:18:45.7	0.3077	6.100	1.219	1.216	21.94	21.23	20.71
17809	00:13:51.5	-30:18:50.0	0.0589	-2.23	1.296	0.497	21.56	21.23	20.85
17810	00:14:32.6	-30:18:42.7	0.7795	16.82	ND	ND	21.69	21.45	20.83
17840	00:14:26.1	-30:18:39.1	0.7340	3.881	0.043	ND	22.60	22.10	21.25
17844	00:15:08.56	-30:18:36.0	0.6789	7.400	0.953	12.57	24.32	23.43	22.28
17905	00:13:12.7	-30:18:34.8	0.4351	-1.64	1.596	0.631	23.32	22.51	21.46
17909	00:13:03.91	-30:18:32.9	0.7488	6.470	ND	ND	22.89	22.43	21.73
17931	00:15:16.8	-30:18:29.4	0.4572	1.724	1.445	1.918	23.91	23.10	21.90
17939	00:15:29.3	-30:18:30.9	0.4831	15.83	1.114	1.174	23.54	22.95	22.03
17944	00:14:14.0	-30:18:30.0	0.3562	1.301	1.227	-2.03	24.17	23.35	22.25
17972	00:14:34.0	-30:18:28.7	0.2987	1.129	1.401	1.322	23.49	22.65	21.86
17982	00:14:00.99	-30:18:31.0	0.3044	0.910	1.334	1.178	22.71	21.84	21.05
17993	00:14:18.6	-30:18:42.1	0.2235	1.207	1.440	0.884	20.66	19.83	19.18
18049	00:14:44.2	-30:18:22.5	0.5930	2.748	1.561	0.247	24.38	23.72	22.21
18124	00:13:01.94	-30:18:25.1	0.3094	1.538	1.314	0.880	20.97	20.18	19.56
18126	00:13:31.9	-30:18:22.1	0.7501	3.517	ND	ND	22.26	21.81	21.07
18127	00:15:12.8	-30:18:17.4	0.1877	6.636	1.214	0.906	23.02	22.53	22.08
18131	00:14:10.0	-30:18:26.9	0.2004	5.631	1.377	1.186	22.56	22.06	21.66
18151	00:13:06.66	-30:18:18.7	0.4049	0.930	0.784	-3.97	22.67	21.89	20.97
18226	00:13:22.6	-30:18:20.3	0.4970	0.578	1.585	0.803	22.44	21.69	20.41
18231	00:14:23.0	-30:18:16.2	0.6016	2.893	1.005	1.345	23.26	22.20	20.83
18241	00:14:52.9	-30:18:13.1	0.4605	2.581	1.375	1.877	23.67	22.98	21.87
18249	00:15:30.1	-30:18:10.3	0.6091	9.333	1.287	-3.00	24.75	23.77	22.58
18331	00:13:35.8	-30:18:07.15	0.3068	0.157	1.457	-0.95	23.85	22.84	22.02
18373	00:14:16.1	-30:18:16.2	0.3544	1.328	1.345	1.155	22.11	21.15	20.20
18419	00:13:22.3	-30:18:05.52	0.2067	2.807	0.658	-4.24	22.78	22.20	21.16
18429	00:15:23.0	-30:18:09.01	0.3607	2.175	1.212	1.289	21.57	20.78	20.08
18435	00:13:03.41	-30:18:00.58	0.6835	-1.52	1.245	7.012	24.61	23.33	22.13
18470	00:13:55.3	-30:18:09.79	0.3086	3.619	1.197	0.415	21.70	20.95	20.34
18499	00:13:12.4	-30:18:00.07	0.2590	2.776	1.104	1.220	22.91	22.45	21.59
18512	00:14:34.7	-30:18:02.49	0.3570	1.317	1.318	1.046	22.92	21.95	20.92
18528	00:14:22.5	-30:17:58.6	0.1220	7.567	1.232	0.454	21.01	20.56	20.06
18532	00:14:13.4	-30:17:54.7	0.6913	-1.00	0.728	15.64	24.12	23.10	22.04
18555	00:13:51.3	-30:17:54.6	0.4376	0.847	1.331	0.990	23.75	22.89	21.72
18564	00:15:35.2	-30:17:51.8	0.2913	-0.91	0.841	-5.46	24.03	23.06	22.18
18578	00:14:01.19	-30:17:57.0	0.3177	8.746	1.149	0.990	21.46	20.86	20.40
18597	00:14:58.5	-30:17:58.5	0.0104	1.667	1.399	-0.14	23.27	22.74	21.66
18599	00:15:02.33	-30:17:52.5	0.3080	1.267	1.396	0.362	22.89	22.07	21.15
18603	00:15:11.1	-30:17:49.5	0.3074	-1.37	1.477	0.577	23.79	22.77	21.88
18630	00:14:42.2	-30:17:49.3	0.3055	14.28	1.096	0.913	22.66	22.08	21.64
18655	00:13:27.3	-30:17:48.1	0.6505	0.704	1.439	-10.3	24.11	23.46	22.03
18695	00:13:05.80	-30:17:47.6	0.3088	11.30	1.146	1.022	21.99	21.36	20.80
18729	00:15:24.1	-30:17:40.3	0.7707	2.570	ND	ND	23.92	23.53	22.47
18799	00:14:26.5	-30:17:35.5	0.7777	4.753	ND	ND	24.54	23.88	22.87
18818	00:13:50.2	-30:17:45.9	0.3086	2.078	1.248	1.114	20.96	20.20	19.58
18841	00:14:51.3	-30:17:38.2	0.5328	8.501	1.098	-0.27	22.61	22.22	21.46

Table B.1—Continued

ID	R.A.	DEC.	z	$W_0([\text{OII}])$ [Å]	$D4000$ [Å]	$W_0(\text{H}\delta)$ [Å]	$B_{\text{AB}}$ [mag]	$V_{\text{AB}}$ [mag]	$R_{\text{AB}}$ [mag]
18867	00:13:51.8	-30:17:30.6	0.1746	1.191	1.101	1.378	23.24	22.80	22.15
18937	00:13:35.0	-30:17:32.8	0.7265	3.790	0.102	ND	24.09	23.09	21.85
18948	00:13:35.8	-30:17:38.1	0.0995	-0.56	1.299	0.399	19.32	18.91	18.50
19002	00:14:57.5	-30:17:26.2	0.6479	6.850	1.016	-6.23	23.15	22.86	21.97
19026	00:13:11.6	-30:17:28.3	0.1886	5.541	1.326	0.899	21.86	21.33	20.65
19043	00:14:26.9	-30:17:21.2	0.2390	9.157	1.246	1.416	22.79	22.24	21.74
19101	00:14:11.4	-30:17:29.1	0.3077	2.179	1.312	0.445	22.72	21.83	21.14
19129	00:14:25.1	-30:17:16.8	0.6213	2.753	1.160	-0.53	23.26	22.78	21.74
19168	00:13:44.1	-30:17:13.5	0.3072	12.87	0.478	2.406	25.17	24.13	22.79
19179	00:13:24.4	-30:17:16.9	0.5214	4.753	1.228	1.279	22.97	22.47	21.45
19182	00:14:04.52	-30:17:18.5	0.1220	5.162	1.398	1.221	21.15	20.65	20.15
19278	00:14:42.3	-30:17:06.60	0.5662	1.573	1.287	2.760	23.72	23.23	22.12
19288	00:14:21.0	-30:17:04.39	0.8301	-5.88	ND	ND	23.25	22.78	22.13
19356	00:14:08.97	-30:17:00.82	0.6507	1.212	1.201	-1.83	23.96	23.20	22.06
19374	00:14:11.6	-30:17:06.82	0.0645	8.722	1.386	0.768	19.87	19.60	19.26
19425	00:13:46.5	-30:16:56.8	0.1438	9.850	1.239	0.660	22.10	21.65	21.37
19440	00:14:07.49	-30:17:01.40	0.6092	5.871	0.891	0.676	22.24	21.88	21.07
19545	00:14:17.3	-30:16:45.9	0.3054	0.380	1.362	0.898	23.52	22.46	21.62
19572	00:13:52.2	-30:16:45.1	0.4975	5.494	1.100	1.489	24.23	23.20	21.96
19576	00:14:53.5	-30:16:50.7	0.3617	2.435	1.219	-0.69	21.16	20.44	19.83
19580	00:13:19.8	-30:16:43.1	0.3081	7.188	1.330	1.743	23.07	22.24	21.43
19603	00:14:50.9	-30:16:43.2	0.3601	1.724	1.107	0.631	22.73	22.15	21.10
19605	00:13:08.28	-30:16:47.2	0.2630	1.429	1.379	0.168	22.63	21.53	20.75
19610	00:14:06.18	-30:16:39.6	0.5415	-0.79	1.587	0.814	24.31	23.41	22.23
19644	00:13:36.2	-30:16:42.5	0.3284	7.037	1.228	2.227	22.43	21.70	21.18
19697	00:13:56.2	-30:16:35.8	0.4363	7.002	1.254	0.985	22.75	22.01	21.16
19760	00:13:27.2	-30:16:44.0	0.4964	-0.96	1.714	1.003	23.03	22.15	20.76
19768	00:14:25.8	-30:16:27.1	0.3091	1.100	1.208	-1.12	24.18	23.27	22.15
19901	00:14:10.4	-30:16:23.9	0.3129	5.590	1.204	1.112	21.58	20.97	20.39
19925	00:13:53.5	-30:16:17.9	0.4522	1.098	1.101	0.158	23.48	22.74	21.44
19977	00:14:18.1	-30:16:17.9	0.1881	19.67	0.752	-2.13	21.73	21.45	20.96
20048	00:13:33.5	-30:16:09.89	0.3069	0.946	1.390	0.058	23.27	22.36	21.63
20066	00:13:20.8	-30:16:10.0	0.4364	3.742	1.203	2.118	22.77	22.20	21.34
20080	00:13:56.3	-30:16:16.8	0.2391	5.161	1.257	1.516	20.70	20.04	19.50
20114	00:14:13.9	-30:16:02.18	0.6352	-0.83	1.432	2.065	25.17	23.99	22.42
20225	00:14:51.4	-30:15:53.6	0.7775	6.485	ND	ND	23.55	23.15	22.26
20233	00:13:55.2	-30:15:59.0	0.3075	10.87	1.083	1.016	21.71	21.03	20.49
20318	00:14:41.3	-30:15:57.6	0.0838	8.080	1.508	1.535	21.79	21.17	20.21
20387	00:14:45.5	-30:15:47.2	0.0608	5.076	1.509	0.295	19.65	19.29	18.86
20405	00:13:55.6	-30:15:42.5	0.6499	15.50	1.500	-6.24	24.54	23.49	22.20
20414	00:14:13.9	-30:15:48.5	0.1058	1.680	1.244	0.340	21.42	21.00	20.59
20520	00:13:48.1	-30:15:44.1	0.6007	11.11	1.080	1.165	22.49	22.28	21.47
20540	00:14:10.2	-30:15:51.7	0.2600	0.750	2.107	0.169	20.15	19.29	18.57
20623	00:13:57.9	-30:15:34.8	0.3113	8.045	1.370	1.507	22.53	21.72	21.03
20744	00:13:47.1	-30:15:28.5	0.3587	3.542	1.119	1.490	21.89	21.13	20.56
20785	00:13:54.0	-30:15:19.6	0.1498	2.163	1.048	-5.64	23.33	22.79	22.05
20786	00:14:07.30	-30:15:23.0	0.3098	1.677	1.298	0.511	21.66	20.83	20.15

## B Spectroscopic members catalogue of RXCJ0014.3-3022 (A 2744)

Table B.1—Continued

ID	R.A.	DEC.	$z$	$W_0([\text{OII}])$ [Å]	$D4000$ [Å]	$W_0(\text{H}\delta)$ [Å]	$B_{\text{AB}}$ [mag]	$V_{\text{AB}}$ [mag]	$R_{\text{AB}}$ [mag]
21005	00:13:51.4	-30:15:10.8	0.4039	1.238	1.317	0.825	22.77	21.86	20.85
21249	00:13:54.5	-30:14:57.7	0.3072	2.198	1.414	0.433	22.71	21.64	20.63
21356	00:13:09.45	-30:14:49.8	0.4525	-1.41	1.409	0.817	21.65	21.01	20.00
21515	00:14:20.1	-30:14:34.5	0.2373	-0.52	0.988	0.443	23.07	22.71	22.26
21525	00:13:17.7	-30:14:34.7	0.6231	-0.94	1.308	-1.85	24.61	23.54	22.24
21547	00:13:25.6	-30:14:33.8	0.4492	11.35	1.002	1.285	22.34	21.86	21.18
21570	00:14:11.2	-30:14:29.6	0.6278	13.86	1.096	0.836	24.03	23.41	22.11
21588	00:13:11.2	-30:14:28.5	0.7772	15.17	ND	ND	22.93	22.51	21.90
21703	00:14:22.1	-30:14:18.6	0.5828	3.451	1.006	0.550	25.44	23.91	22.65
21739	00:14:14.8	-30:14:17.5	0.1584	0.509	1.137	-1.64	23.87	23.33	22.07
21766	00:13:27.0	-30:14:16.0	0.2621	-0.67	1.386	0.131	23.41	22.37	21.48
21881	00:13:03.45	-30:14:13.2	0.2601	6.426	1.082	0.825	22.08	21.44	20.94
22022	00:13:12.6	-30:14:08.20	0.6005	11.07	1.190	2.261	22.73	22.42	21.57
22074	00:13:19.3	-30:13:56.9	0.4733	7.327	1.281	2.020	23.33	22.58	21.50
22310	00:13:29.1	-30:13:39.4	0.6525	4.365	1.105	-3.52	23.43	22.73	21.69
22313	00:14:14.3	-30:13:46.2	0.2644	2.901	1.230	1.266	20.65	19.98	19.44
22392	00:14:00.59	-30:13:44.8	0.1220	5.500	1.334	0.811	20.07	19.68	19.31
22569	00:13:31.5	-30:13:24.8	0.4506	4.535	1.159	2.256	22.11	21.45	20.63
22734	00:13:07.70	-30:13:17.3	0.1394	6.808	1.334	1.094	21.92	21.42	21.07

# C

## **Spectroscopic members catalogue of RXCJ2308.3-0211 (A 2537)**

Hereafter the full catalogue of spectroscopic objects in the field of RXCJ2308.3-0211 is provided. Along with position and redshift, for each object are also provided the values of spectral indices and BVR magnitudes with corresponding errors. Where equivalent widths were not calculated due to the line not being sampled in the instrument's spectral range, the table reads ND, i.e. Not Detected.

## C Spectroscopic members catalogue of RXCJ2308.3-0211 (A 2537)

Table C.1.

ID	R.A.	DEC.	$z$	$W_0(\text{[OII]})$ [Å]	$D_{4000}$ [Å]	$W_0(\text{H}\delta)$ [Å]	$B_{\text{AB}}$ [mag]	$V_{\text{AB}}$ [mag]	$R_{\text{AB}}$ [mag]
3011	23:8:24.6	-2:21:03.06	0.3029	1.919	2.134	0.176	20.00	18.92	17.77
3256	23:9:24.1	-2:21:07.10	0.3134	11.50	1.283	1.184	22.67	21.98	21.38
3298	23:9:03.91	-2:21:12.2	0.6032	16.52	1.108	1.808	21.77	21.48	20.66
3353	23:8:47.3	-2:21:07.05	0.2710	0.488	1.972	0.297	22.96	21.97	20.94
3371	23:9:11.1	-2:21:07.10	0.6611	8.013	1.280	3.479	23.90	23.36	22.10
3386	23:9:12.4	-2:20:58.8	0.5019	6.817	1.277	1.768	21.37	21.02	20.12
3410	23:9:07.32	-2:20:55.4	0.0592	16.36	1.219	-0.98	20.69	20.16	19.78
3414	23:9:19.7	-2:20:52.8	0.1263	2.515	1.368	1.669	19.53	18.99	18.45
3418	23:8:25.3	-2:20:56.2	0.3076	1.994	1.544	0.872	22.87	21.77	20.58
3456	23:9:08.35	-2:20:43.1	0.1821	-1.23	1.865	0.065	20.27	19.24	18.45
3465	23:8:44.0	-2:20:54.7	0.5610	1.365	0.979	-1.39	23.21	22.76	21.56
3499	23:8:35.4	-2:20:45.6	0.3014	1.239	1.733	0.521	22.35	21.26	20.21
3517	23:9:07.69	-2:20:46.4	0.4789	7.337	1.241	1.451	21.90	21.40	20.57
3542	23:8:26.3	-2:20:38.6	0.3013	1.214	2.030	0.086	21.71	20.52	19.33
3574	23:9:18.5	-2:20:36.0	0.2987	1.464	1.125	1.642	22.55	21.54	20.52
3591	23:9:17.6	-2:20:40.3	0.6673	6.895	1.014	8.609	23.19	22.59	21.72
3662	23:9:01.24	-2:20:32.0	0.0839	-2.09	1.673	1.491	22.18	21.58	20.97
3690	23:9:06.83	-2:20:21.4	0.0630	7.464	1.462	0.319	19.66	19.31	18.86
3732	23:9:25.3	-2:20:27.7	0.6641	12.91	0.886	6.207	23.41	23.01	22.14
3747	23:8:38.2	-2:20:21.5	0.4989	2.973	1.240	1.682	21.99	21.39	20.24
3759	23:9:26.9	-2:20:19.7	0.2990	7.141	1.143	1.746	20.92	20.26	19.75
3761	23:8:24.4	-2:20:18.8	0.3003	-0.22	1.882	0.626	22.57	21.46	20.35
3789	23:9:12.2	-2:20:12.4	0.3127	-0.48	1.930	-1.12	21.73	20.65	19.63
3815	23:8:41.0	-2:20:11.8	0.4904	2.108	1.656	-0.16	22.66	21.98	20.76
3824	23:8:36.0	-2:20:08.77	0.3049	7.281	1.155	1.011	20.19	19.51	18.82
3847	23:9:10.3	-2:20:11.6	0.0914	7.590	1.573	1.513	21.79	21.49	21.17
3910	23:9:00.00	-2:20:04.86	0.5797	2.420	1.888	0.415	22.85	21.93	20.81
3958	23:8:27.2	-2:19:59.8	0.4892	4.565	1.229	1.027	21.90	21.44	20.49
3963	23:9:00.13	-2:19:52.6	0.2961	1.488	1.643	0.326	21.64	20.57	19.52
3964	23:8:42.8	-2:19:51.6	0.4879	1.949	1.758	-0.23	22.50	21.62	20.16
4017	23:9:22.1	-2:19:53.7	0.4359	15.18	1.119	0.926	22.02	21.43	20.79
4021	23:8:37.3	-2:19:52.3	0.2905	-0.91	1.647	-0.85	22.77	21.62	20.61
4023	23:9:11.2	-2:19:52.7	0.1278	-1.33	8.514	5.957	22.01	21.41	20.90
4074	23:8:42.2	-2:19:10.7	0.3290	-1.08	0.995	-0.56	17.85	17.37	16.81
4095	23:9:25.3	-2:19:47.6	0.3970	-1.95	1.771	-0.41	22.78	21.87	20.70
4124	23:9:13.6	-2:19:42.2	0.6247	1.643	1.657	0.312	23.82	23.19	21.97
4146	23:9:22.3	-2:19:39.4	0.3982	1.308	1.341	2.343	21.87	20.95	19.88
4156	23:8:22.8	-2:19:38.6	0.4106	4.112	1.362	0.796	22.15	21.31	20.30
4184	23:9:06.94	-2:19:28.2	0.3003	0.382	1.734	0.225	21.05	20.05	18.96
4197	23:8:43.0	-2:19:36.1	0.4904	-1.20	1.577	-0.19	22.79	22.08	20.85
4202	23:8:34.2	-2:19:25.0	0.2991	1.307	1.932	0.090	20.18	19.19	18.24
4230	23:9:06.85	-2:19:34.5	0.3046	0.411	1.613	0.963	22.74	22.17	21.68
4238	23:9:26.7	-2:19:35.7	0.5964	12.78	1.117	1.808	22.87	22.47	21.50
4289	23:8:32.8	-2:19:13.3	0.3029	-0.61	2.029	1.622	21.45	20.36	19.38
4322	23:8:26.9	-2:19:24.3	0.5994	0.375	1.913	-1.13	24.22	22.72	21.09
4326	23:8:59.3	-2:19:16.7	0.2340	5.213	1.285	0.265	21.38	20.70	20.19
4355	23:9:13.0	-2:19:17.5	0.3056	2.291	1.196	1.386	21.36	20.66	20.09

Table C.1—Continued

ID	R.A.	DEC.	z	$W_0([\text{OII}])$ [Å]	$D4000$ [Å]	$W_0(\text{H}\delta)$ [Å]	$B_{\text{AB}}$ [mag]	$V_{\text{AB}}$ [mag]	$R_{\text{AB}}$ [mag]
4358	23:9:19.6	-2:19:21.6	0.6934	2.484	0.710	14.42	24.41	23.27	21.58
4374	23:9:05.21	-2:19:18.8	0.2981	-0.38	1.472	0.757	22.94	21.83	20.85
4376	23:8:47.9	-2:18:28.3	0.1923	8.031	1.131	-0.74	20.41	19.83	19.30
4417	23:8:40.2	-2:18:59.9	0.5028	1.528	1.246	1.172	18.68	17.86	16.84
4431	23:9:14.5	-2:19:01.68	0.2998	0.596	1.654	0.664	20.98	19.99	18.95
4454	23:8:02.19	-2:19:08.07	0.3105	-2.39	1.707	-0.72	22.32	21.20	20.00
4462	23:8:34.5	-2:19:11.7	0.6607	-0.25	1.351	-11.2	23.47	22.83	21.66
4477	23:7:49.3	-2:19:04.44	0.4572	2.546	1.607	0.056	22.54	21.53	19.92
4489	23:8:54.0	-2:19:04.45	0.2231	1.366	1.922	-0.70	21.44	20.40	19.57
4502	23:8:28.8	-2:19:00.70	0.2986	1.008	1.523	1.493	22.50	21.45	20.57
4536	23:9:20.3	-2:19:00.86	0.5580	-2.16	1.476	0.460	22.50	21.49	20.14
4547	23:8:57.4	-2:19:06.11	0.6027	8.890	0.963	-1.38	23.64	23.90	22.35
4579	23:8:42.5	-2:18:57.2	0.5018	5.470	1.252	0.465	23.54	22.91	21.41
4583	23:8:32.2	-2:18:53.9	0.1131	5.578	1.561	0.810	21.51	21.13	20.74
4584	23:8:01.75	-2:18:57.9	0.3115	13.73	1.159	0.912	22.95	22.35	21.84
4634	23:9:10.9	-2:18:50.1	0.2988	-0.97	1.601	1.405	22.54	21.55	20.56
4650	23:7:48.6	-2:18:53.1	0.4552	-0.75	1.444	-0.87	24.35	23.33	21.72
4654	23:8:49.9	-2:18:52.1	0.4891	6.248	1.256	1.854	23.23	22.55	21.55
4677	23:7:56.1	-2:18:40.3	0.2991	2.540	1.159	1.245	21.00	20.35	19.48
4678	23:8:42.0	-2:18:46.5	0.6005	0.914	1.354	0.982	22.20	21.84	20.62
4689	23:9:04.06	-2:18:46.7	0.1812	2.484	1.288	2.372	22.77	22.20	21.57
4718	23:8:26.8	-2:18:36.3	0.2945	-2.56	1.585	0.680	21.88	21.18	20.33
4754	23:8:57.1	-2:18:39.1	0.6033	6.725	1.081	1.535	22.71	22.30	21.26
4770	23:8:32.6	-2:18:36.3	0.5099	4.108	1.527	-0.49	23.58	22.77	21.50
4771	23:8:08.47	-2:18:39.3	0.5085	6.024	1.243	0.990	22.71	22.34	21.32
4785	23:8:47.2	-2:18:39.0	0.6019	7.186	1.035	1.389	23.43	23.45	22.16
4797	23:8:08.11	-2:18:30.1	0.5102	3.242	1.814	0.351	22.59	21.58	20.13
4809	23:8:15.7	-2:18:31.0	0.2365	6.833	1.237	1.488	21.13	20.61	20.17
4823	23:9:25.8	-2:18:28.4	0.5415	-0.87	1.628	0.596	22.19	21.29	19.86
4846	23:9:00.08	-2:18:26.7	0.2952	0.137	1.415	1.206	22.24	21.27	20.44
4861	23:8:01.74	-2:18:29.7	0.6889	3.940	0.708	14.97	24.54	24.15	22.24
4874	23:8:35.1	-2:18:27.8	0.5017	6.836	1.293	2.155	23.59	23.07	21.81
4886	23:8:53.0	-2:18:26.5	0.7261	-0.61	0.073	ND	24.57	23.09	21.77
4888	23:7:58.5	-2:18:21.5	0.6482	11.22	1.041	-11.2	21.61	20.84	19.76
4913	23:9:06.25	-2:18:22.0	0.3355	9.465	1.233	0.997	22.62	21.81	21.23
4921	23:8:11.0	-2:18:20.3	0.4755	6.546	1.150	1.382	22.43	21.99	21.16
4926	23:8:27.3	-2:18:20.1	0.2960	0.535	1.717	-0.66	22.90	21.78	20.76
4932	23:9:24.7	-2:18:19.3	0.2335	8.248	1.263	0.593	21.70	21.18	20.58
4955	23:9:12.0	-2:18:11.9	0.1565	6.415	1.290	1.227	20.56	20.06	19.52
4956	23:9:03.78	-2:18:14.4	0.1825	5.593	1.346	0.914	21.03	20.41	19.91
4964	23:8:04.19	-2:18:16.3	0.1105	2.311	1.205	0.279	22.31	22.06	21.75
4975	23:8:38.7	-2:18:12.2	0.2969	6.127	1.244	1.362	21.99	21.31	20.60
4985	23:9:04.17	-2:18:02.66	0.1816	0.119	1.776	0.225	20.21	19.21	18.45
4998	23:8:53.2	-2:18:06.99	0.2008	7.303	1.264	1.079	21.59	20.97	20.46
5003	23:8:09.24	-2:18:11.5	0.5082	0.332	1.571	1.076	22.79	22.06	20.74
5026	23:8:35.7	-2:18:05.91	0.5024	6.639	1.227	2.821	21.20	20.73	19.96
5051	23:7:49.6	-2:18:07.32	2.0434	ND	ND	ND	21.70	21.41	21.08

## C Spectroscopic members catalogue of RXCJ2308.3-0211 (A 2537)

Table C.1—Continued

ID	R.A.	DEC.	z	$W_0(\text{[OII]})$ [Å]	$D_{4000}$ [Å]	$W_0(\text{H}_\delta)$ [Å]	$B_{\text{AB}}$ [mag]	$V_{\text{AB}}$ [mag]	$R_{\text{AB}}$ [mag]
5055	23:8:05.60	-2:18:06.97	0.6156	0.009	1.705	1.120	23.30	22.73	21.27
5065	23:8:28.8	-2:18:02.61	0.2616	6.842	1.235	0.727	21.23	20.65	20.09
5069	23:8:54.3	-2:17:51.8	0.8041	0.116	ND	ND	20.47	19.34	18.22
5076	23:9:02.59	-2:17:51.5	0.2963	-0.73	1.809	-0.90	21.79	20.52	19.36
5079	23:9:18.5	-2:18:02.58	0.2395	4.863	1.318	1.284	21.60	20.96	20.42
5094	23:9:11.0	-2:17:59.2	0.3028	4.868	0.644	-3.07	21.96	21.26	19.88
5120	23:9:23.8	-2:17:57.6	0.2988	1.196	1.279	1.676	22.99	21.75	20.49
5154	23:9:12.7	-2:17:49.7	0.1597	14.60	1.193	0.313	20.18	19.31	18.32
5161	23:7:51.1	-2:17:56.5	0.5752	1.879	1.211	0.888	23.03	22.65	21.39
5173	23:8:40.4	-2:17:54.3	0.6016	11.34	1.101	2.394	22.48	22.01	21.00
5177	23:7:58.8	-2:17:52.8	0.6059	4.972	1.056	2.293	22.17	21.88	20.86
5180	23:8:41.2	-2:17:47.3	0.3562	6.993	1.173	-0.56	21.21	20.59	20.04
5191	23:8:05.28	-2:17:51.5	0.4762	4.880	1.158	1.913	22.72	22.05	21.09
5194	23:8:12.7	-2:17:51.0	1.0889	ND	ND	ND	21.62	21.47	21.18
5215	23:8:46.3	-2:17:44.4	0.2319	13.81	1.260	0.804	21.47	21.05	20.54
5239	23:9:08.34	-2:17:38.9	0.2982	2.547	1.296	1.348	22.32	21.69	20.72
5250	23:8:59.1	-2:17:30.9	0.0630	7.550	1.442	0.957	19.68	19.36	18.94
5259	23:9:07.60	-2:17:34.4	0.2981	-0.88	1.994	0.204	20.57	19.40	18.28
5260	23:8:53.6	-2:17:44.8	0.6591	4.190	0.972	3.167	22.74	22.30	21.38
5276	23:8:05.55	-2:17:41.9	0.2914	0.190	1.634	0.081	23.13	21.93	20.99
5295	23:7:57.3	-2:17:42.4	0.5261	5.603	10.32	3.011	23.61	22.96	21.82
5345	23:8:25.6	-2:17:35.3	0.5553	0.932	1.635	0.459	23.11	22.18	20.83
5356	23:7:49.1	-2:17:35.5	0.5848	-0.63	1.020	-1.96	21.93	21.80	21.22
5364	23:9:12.9	-2:17:30.7	0.4578	6.442	1.364	2.073	22.18	21.66	20.86
5396	23:8:09.50	-2:17:29.4	0.5100	4.154	1.162	0.931	21.86	21.41	20.54
5400	23:8:54.1	-2:17:31.8	0.3012	-0.58	1.566	0.541	23.09	22.15	21.07
5403	23:8:08.21	-2:17:13.8	0.3105	1.755	1.417	0.736	23.15	22.15	21.11
5435	23:8:34.0	-2:17:29.2	0.2650	-0.47	1.111	1.920	22.56	22.46	21.64
5456	23:9:21.5	-2:17:21.4	0.3273	0.679	1.491	-0.89	22.14	21.21	19.95
5457	23:9:03.39	-2:17:23.1	0.6012	5.111	1.183	2.088	22.06	21.68	20.68
5487	23:8:16.2	-2:17:24.0	0.2990	1.356	1.402	1.306	23.62	22.68	21.75
5490	23:7:58.6	-2:17:23.7	0.8068	4.724	ND	ND	24.08	22.94	21.48
5504	23:8:20.8	-2:17:16.0	0.2066	-1.06	1.683	-0.88	21.20	20.25	19.44
5515	23:7:49.2	-2:17:21.7	0.6851	0.493	0.885	6.931	24.14	23.32	21.72
5550	23:8:01.34	-2:17:14.6	0.6495	0.519	1.421	-5.92	23.09	22.39	21.00
5557	23:9:00.10	-2:16:59.0	0.6037	2.056	1.045	-1.23	21.98	21.51	20.43
5562	23:9:20.7	-2:17:15.2	0.3253	3.031	1.233	1.062	22.92	21.96	20.97
5563	23:9:19.5	-2:17:06.96	0.3263	0.690	1.134	0.472	20.59	19.80	19.05
5566	23:8:20.1	-2:17:17.0	0.3018	0.248	1.631	0.440	23.04	21.93	20.94
5579	23:8:54.1	-2:17:13.4	0.5770	15.67	1.049	0.390	21.79	21.54	20.68
5593	23:8:06.11	-2:17:07.05	0.7059	-1.73	0.236	1.679	22.78	21.73	20.59
5614	23:8:20.7	-2:17:06.66	0.2077	0.724	1.522	0.711	21.65	20.78	20.06
5616	23:8:29.2	-2:17:12.5	0.4787	23.86	1.090	1.935	23.70	23.39	22.43
5642	23:9:02.74	-2:17:07.96	0.2953	-1.32	1.579	0.173	22.88	22.50	21.49
5660	23:8:30.4	-2:16:58.4	0.7351	6.770	-0.68	ND	20.51	19.49	18.36
5680	23:9:24.4	-2:17:04.74	0.6940	-2.88	0.627	20.47	23.79	22.80	21.58
5688	23:8:54.8	-2:16:58.1	0.2236	6.700	1.343	0.820	21.82	21.20	20.60



Table C.1—Continued

ID	R.A.	DEC.	z	$W_0([\text{OII}])$ [Å]	$D4000$ [Å]	$W_0(\text{H}\delta)$ [Å]	$B_{\text{AB}}$ [mag]	$V_{\text{AB}}$ [mag]	$R_{\text{AB}}$ [mag]
5693	23:8:41.7	-2:16:56.6	0.4738	-1.58	1.484	-0.61	20.57	19.72	18.70
5711	23:7:32.3	-2:17:00.61	0.2961	9.552	1.235	1.300	22.96	22.15	21.38
5727	23:8:20.8	-2:16:59.3	0.3000	0.298	1.360	0.612	23.53	22.41	21.43
5729	23:7:17.5	-2:16:57.7	0.3190	1.031	1.152	2.873	22.97	22.26	21.29
5736	23:9:09.54	-2:16:57.1	0.6993	5.071	0.338	8.143	24.56	23.62	22.07
5746	23:8:07.68	-2:16:52.6	0.6038	3.421	1.284	1.371	22.67	22.14	20.97
5785	23:8:36.8	-2:16:47.4	0.6382	5.421	1.169	2.673	22.02	21.56	20.54
5790	23:7:57.4	-2:16:49.7	0.6591	15.92	1.032	4.149	23.51	23.13	22.01
5811	23:8:29.0	-2:16:46.3	0.2974	1.800	1.520	0.358	23.24	22.12	21.19
5815	23:7:17.8	-2:16:44.8	0.1962	2.354	1.501	1.396	20.63	20.01	19.38
5820	23:9:26.1	-2:16:44.4	0.3806	1.771	1.236	0.600	21.78	20.90	19.96
5828	23:7:43.0	-2:16:42.7	0.2540	10.27	1.197	0.979	21.76	21.24	20.77
5832	23:7:33.9	-2:16:44.7	2.1433	ND	ND	ND	22.25	22.00	21.63
5839	23:9:04.13	-2:16:36.7	0.6250	4.542	1.259	0.784	21.97	21.44	20.33
5873	23:8:46.9	-2:16:34.9	0.4372	2.873	1.305	0.246	22.23	21.62	20.56
5883	23:8:08.80	-2:16:36.1	0.4512	-1.70	1.041	-3.55	21.99	21.16	20.33
5898	23:9:08.08	-2:16:35.4	0.5980	-1.20	1.860	1.019	23.75	22.20	20.78
5903	23:9:01.68	-2:16:39.0	0.6343	5.042	1.251	2.663	23.51	23.32	22.12
5919	23:8:21.4	-2:16:27.7	0.3112	2.083	1.669	0.401	22.31	21.46	20.43
5928	23:8:31.2	-2:16:36.2	0.2854	-1.50	1.111	-1.31	23.72	22.83	21.94
5929	23:8:56.3	-2:16:34.9	0.5787	6.673	1.093	3.065	23.41	22.97	21.89
5943	23:8:50.7	-2:16:32.7	0.2935	-0.33	1.330	0.878	22.72	21.81	21.08
5945	23:8:40.3	-2:16:32.5	0.4748	-0.84	1.671	-0.81	23.15	22.27	20.92
5991	23:7:22.7	-2:16:31.1	0.7256	20.58	0.045	ND	22.91	22.85	22.03
6007	23:8:26.9	-2:16:28.3	0.6981	-0.21	0.128	7.283	21.54	21.42	21.12
6011	23:9:02.77	-2:16:27.2	0.6824	2.357	0.827	12.65	22.59	21.86	20.86
6012	23:8:12.7	-2:16:25.7	0.2931	7.658	1.172	0.909	21.67	21.01	20.45
6017	23:8:24.4	-2:16:22.8	0.3017	1.722	1.656	0.754	21.92	20.94	19.87
6023	23:7:33.2	-2:16:25.2	0.4531	7.234	1.200	-0.08	22.51	22.09	21.11
6036	23:7:48.5	-2:16:26.6	0.6152	0.520	1.755	0.536	25.62	23.48	21.99
6045	23:9:23.7	-2:16:23.8	0.5989	3.954	1.288	1.005	22.18	21.94	20.84
6055	23:9:26.1	-2:16:17.8	0.2943	-1.47	1.706	0.162	21.38	20.32	19.25
6061	23:8:20.9	-2:16:15.5	0.6980	6.590	0.295	7.002	24.98	22.76	21.18
6096	23:8:28.1	-2:16:19.1	0.3505	14.09	1.176	0.673	23.07	22.38	20.88
6154	23:9:17.6	-2:16:11.9	0.5985	2.329	1.330	1.641	22.73	22.21	21.11
6157	23:8:32.6	-2:16:10.3	0.5130	1.898	1.243	-0.48	21.23	20.73	19.72
6165	23:7:50.3	-2:16:14.3	0.6006	2.227	1.292	0.433	23.17	22.62	21.53
6168	23:8:33.6	-2:16:09.92	0.2386	-1.85	1.543	0.478	20.95	20.19	19.43
6176	23:9:29.3	-2:16:13.3	0.3873	4.559	1.318	0.842	22.37	21.62	20.76
6190	23:8:14.7	-2:16:12.2	0.4886	5.407	1.271	1.130	23.04	22.28	20.90
6195	23:7:48.9	-2:16:09.19	0.2343	3.860	1.230	-0.25	21.45	20.80	20.30
6199	23:8:36.0	-2:16:09.40	0.2986	1.771	1.625	0.549	23.13	21.88	20.88
6206	23:8:20.6	-2:15:50.3	0.3003	-0.90	1.283	1.436	21.19	20.28	19.46
6217	23:9:03.45	-2:16:07.46	0.6268	1.034	1.405	-2.71	23.58	22.24	20.82
6223	23:8:54.4	-2:15:59.3	0.2958	-0.29	1.727	-0.54	21.29	20.27	19.33
6236	23:7:35.9	-2:16:06.36	0.5017	8.252	1.139	-0.37	22.30	21.95	21.07
6253	23:7:26.8	-2:16:06.44	0.4806	2.691	1.017	1.992	24.12	22.89	21.80

## C Spectroscopic members catalogue of RXCJ2308.3-0211 (A 2537)

Table C.1—Continued

ID	R.A.	DEC.	z	$W_0([\text{OII}])$ [Å]	$D_{4000}$ [Å]	$W_0(\text{H}_\delta)$ [Å]	$B_{\text{AB}}$ [mag]	$V_{\text{AB}}$ [mag]	$R_{\text{AB}}$ [mag]
6266	23:8:07.55	-2:16:04.62	0.4771	10.94	1.163	1.699	22.82	22.43	21.62
6287	23:9:16.9	-2:15:47.9	0.1619	6.349	1.387	1.187	21.38	20.86	20.39
6332	23:9:02.98	-2:15:57.2	0.2596	7.069	1.333	0.296	21.56	20.84	20.19
6336	23:8:56.0	-2:15:41.5	0.1821	-1.14	1.909	-0.28	20.03	19.15	18.39
6337	23:9:01.74	-2:15:50.7	0.6267	7.936	1.472	0.901	24.45	22.64	20.94
6355	23:8:47.0	-2:15:49.6	0.4356	1.072	1.346	1.602	21.77	21.08	20.00
6358	23:7:17.1	-2:15:52.4	0.6432	17.28	1.019	-1.77	21.34	21.18	20.51
6364	23:7:25.0	-2:15:53.3	0.6810	5.464	0.889	8.677	23.51	23.06	22.03
6367	23:7:56.4	-2:15:52.3	0.5102	8.061	1.173	1.673	22.01	21.58	20.67
6368	23:8:47.4	-2:15:53.2	0.4928	4.176	1.240	2.040	23.02	22.50	21.38
6374	23:7:32.3	-2:15:47.5	0.5471	1.200	1.555	1.114	23.27	22.62	21.44
6396	23:8:14.7	-2:15:40.5	0.2941	0.783	1.796	-0.50	21.49	20.40	19.25
6404	23:8:48.8	-2:15:44.4	0.3675	0.304	1.201	0.583	21.14	20.41	19.66
6411	23:8:07.60	-2:15:49.7	0.6095	6.681	1.016	-5.39	25.41	23.89	22.53
6414	23:7:38.1	-2:15:47.7	0.6480	3.041	1.458	-4.20	23.87	23.29	22.10
6422	23:8:36.9	-2:15:43.4	0.2901	-3.23	1.298	-0.98	21.91	20.85	19.85
6428	23:9:02.27	-2:15:42.7	0.2969	0.309	1.635	0.025	22.64	21.61	20.51
6431	23:7:52.0	-2:15:43.1	0.3023	3.463	1.329	1.529	22.05	21.16	20.39
6433	23:8:34.9	-2:15:42.0	0.2980	10.87	1.254	2.047	21.79	21.18	20.73
6444	23:9:16.4	-2:15:47.0	0.3181	4.556	1.263	1.113	19.19	18.69	18.19
6452	23:8:38.7	-2:15:43.3	0.3056	7.170	1.322	0.952	22.58	21.93	21.20
6459	23:8:42.2	-2:15:37.4	0.2890	-0.76	2.126	-1.15	21.75	20.65	19.59
6462	23:8:04.39	-2:15:42.8	0.6540	6.397	1.080	-4.71	22.95	22.65	21.60
6463	23:7:26.2	-2:15:37.1	0.7241	24.13	0.071	ND	22.16	21.92	21.34
6469	23:9:23.4	-2:15:43.7	0.6785	5.305	1.132	13.34	22.87	22.34	21.30
6521	23:8:25.5	-2:15:32.3	0.2340	10.03	1.051	0.632	21.45	21.01	20.52
6529	23:8:37.3	-2:15:30.1	0.4256	-1.35	1.765	0.179	22.60	21.52	20.07
6563	23:7:55.1	-2:15:23.2	0.2348	1.650	1.568	1.679	20.33	19.43	18.81
6565	23:7:52.2	-2:15:29.2	0.2957	11.96	1.074	0.317	22.61	22.01	21.57
6616	23:8:36.7	-2:15:19.2	0.3679	1.028	1.473	1.366	22.17	21.19	20.13
6622	23:7:57.9	-2:14:58.1	0.3009	0.757	1.339	-7.99	20.15	19.09	17.98
6628	23:7:22.4	-2:15:21.7	0.7250	9.094	0.142	ND	22.44	22.30	21.45
6633	23:8:43.0	-2:15:13.8	0.2945	-1.14	1.770	1.212	21.77	20.60	19.49
6651	23:8:20.6	-2:15:21.0	0.6682	12.02	0.867	10.73	22.66	22.47	21.47
6658	23:7:58.7	-2:15:11.1	0.0837	5.572	1.434	1.000	19.13	18.76	18.28
6660	23:8:41.9	-2:15:13.5	0.7482	21.93	ND	ND	21.87	21.53	20.88
6666	23:8:25.6	-2:15:11.7	0.2068	0.497	1.868	1.194	20.30	19.40	18.70
6675	23:8:27.7	-2:15:09.37	0.3023	1.436	1.638	2.267	20.16	19.35	18.36
6679	23:9:02.56	-2:15:18.1	0.2727	9.618	1.310	1.599	22.98	22.41	21.87
6687	23:8:12.3	-2:15:14.0	0.2968	-1.50	1.486	0.566	23.40	22.32	21.28
6697	23:8:03.94	-2:15:13.0	0.2927	4.227	1.357	1.199	22.77	21.97	21.45
6707	23:7:22.4	-2:15:11.9	0.2954	3.865	1.395	-0.54	22.03	21.26	20.50
6721	23:7:30.4	-2:15:08.54	0.3546	2.655	1.316	0.151	22.13	21.37	20.50
6729	23:7:33.1	-2:15:11.4	0.6360	-2.40	1.070	1.800	24.32	22.71	21.96
6733	23:8:36.5	-2:14:50.3	0.2979	-0.86	1.979	0.041	21.05	19.87	18.67
6743	23:9:07.70	-2:15:07.88	0.1432	9.912	1.376	0.214	21.89	21.41	21.01
6763	23:7:57.6	-2:14:47.8	0.2944	3.760	1.184	1.515	20.59	19.94	19.38

Table C.1—Continued

ID	R.A.	DEC.	z	$W_0(\text{[OII]})$ [Å]	$D4000$ [Å]	$W_0(\text{H}\delta)$ [Å]	$B_{\text{AB}}$ [mag]	$V_{\text{AB}}$ [mag]	$R_{\text{AB}}$ [mag]
6773	23:7:58.6	-2:15:04.28	0.4999	8.587	1.143	0.734	22.80	22.27	21.33
6774	23:8:51.5	-2:15:01.53	0.3045	5.033	1.360	1.670	22.45	21.68	20.97
6783	23:9:03.16	-2:15:00.48	0.2997	4.634	1.176	1.556	21.49	20.76	20.17
6789	23:7:40.6	-2:15:04.74	0.6465	1.729	1.259	-2.23	23.20	22.61	21.55
6796	23:8:10.7	-2:15:00.41	0.4757	4.582	1.276	1.358	22.43	21.72	20.47
6799	23:8:21.1	-2:15:00.35	0.2973	-2.35	1.623	0.318	22.68	21.79	20.77
6807	23:7:49.9	-2:15:01.39	0.2638	-0.77	1.470	0.209	23.32	22.33	21.37
6813	23:8:35.5	-2:14:58.5	0.2742	4.551	1.334	1.374	22.22	21.48	20.89
6824	23:8:20.5	-2:14:45.1	0.2913	0.543	2.214	-2.73	21.66	20.46	19.38
6829	23:8:08.49	-2:14:58.4	0.5552	1.986	1.766	0.337	23.99	22.83	21.30
6831	23:7:48.5	-2:14:44.3	0.2644	1.727	1.852	-0.39	20.99	19.84	18.84
6836	23:9:01.44	-2:14:59.7	0.3669	16.64	1.078	1.187	22.81	22.01	21.52
6842	23:7:48.8	-2:14:56.0	0.2656	-1.44	1.493	0.194	22.16	21.01	20.16
6860	23:8:53.5	-2:14:57.4	0.2745	8.230	1.235	1.211	22.91	22.34	21.62
6870	23:8:26.1	-2:14:43.3	0.5098	2.990	1.126	1.188	21.35	20.29	19.26
6871	23:8:02.93	-2:14:49.6	0.2925	-1.23	1.566	0.040	22.74	21.72	20.82
6883	23:8:52.2	-2:14:46.6	0.2740	6.529	1.138	0.310	20.72	20.10	19.49
6885	23:8:06.66	-2:14:45.7	0.2945	1.195	1.695	-1.53	21.73	20.73	19.75
6902	23:7:44.9	-2:14:51.6	0.6153	3.133	1.096	0.623	22.58	22.30	21.33
6912	23:7:33.5	-2:14:50.8	0.6869	-0.94	1.039	11.83	24.12	23.05	21.57
6928	23:9:16.5	-2:14:48.3	0.6114	25.95	0.871	0.641	22.26	22.21	21.73
6934	23:7:23.9	-2:14:50.0	0.6800	4.612	1.108	13.52	23.72	23.10	22.07
6942	23:8:13.8	-2:14:49.6	0.2960	0.889	1.443	0.406	24.18	22.93	21.88
6946	23:8:44.1	-2:14:47.0	0.5396	15.13	1.152	2.351	22.58	22.29	21.23
6962	23:8:16.9	-2:14:46.1	0.7136	15.39	0.165	ND	22.26	22.14	21.48
6967	23:8:40.1	-2:14:42.0	0.2934	-0.92	2.765	0.223	21.67	20.66	19.63
6971	23:8:14.5	-2:14:41.1	0.2954	-0.45	1.405	0.511	23.15	22.03	21.03
6993	23:8:43.6	-2:14:28.7	0.2073	-0.49	1.954	-0.51	20.38	19.34	18.51
7034	23:8:05.58	-2:14:37.7	0.5876	8.446	1.193	1.553	22.79	22.56	21.44
7064	23:7:31.6	-2:14:36.1	0.3051	7.891	1.312	2.041	23.29	22.53	21.76
7087	23:8:07.82	-2:14:28.1	0.4089	1.129	1.068	-0.77	21.51	20.79	20.04
7093	23:8:19.3	-2:14:34.2	0.2902	5.697	1.245	0.925	22.90	22.22	21.45
7106	23:8:51.0	-2:14:29.8	0.3008	-0.40	1.321	1.275	22.69	21.72	20.82
7121	23:8:45.2	-2:14:24.6	0.2868	1.647	1.317	0.937	23.34	22.63	21.80
7142	23:8:22.8	-2:14:24.2	0.3013	-0.88	1.780	0.486	22.06	20.98	19.92
7143	23:7:45.8	-2:14:26.6	0.4925	-1.41	1.559	0.696	23.29	22.61	20.99
7144	23:7:20.2	-2:14:27.7	0.5156	20.29	1.135	0.702	22.48	22.27	21.33
7161	23:8:39.5	-2:14:25.5	0.4351	6.823	1.127	0.743	24.13	22.93	21.68
7171	23:8:27.4	-2:14:23.5	0.6291	7.354	1.259	1.276	22.91	22.17	21.29
7176	23:7:43.4	-2:14:21.4	0.5604	1.196	1.584	1.443	22.66	21.65	20.22
7184	23:8:13.9	-2:14:16.4	0.3044	8.821	1.160	1.495	21.56	20.84	20.28
7218	23:8:01.44	-2:14:12.2	0.2922	1.041	1.603	1.766	21.81	20.80	19.84
7224	23:7:58.8	-2:14:17.5	0.6189	2.368	1.193	-1.15	22.74	22.27	21.20
7237	23:7:45.5	-2:14:15.9	0.4930	2.961	1.490	0.291	23.48	22.46	20.88
7316	23:7:34.7	-2:14:07.84	0.4521	3.590	1.301	1.337	22.59	22.01	21.12
7320	23:8:52.5	-2:14:08.30	0.7127	4.883	0.145	ND	22.40	22.00	21.22
7339	23:7:48.5	-2:14:05.07	0.5600	8.860	1.118	0.659	22.16	21.81	20.90

## C Spectroscopic members catalogue of RXCJ2308.3-0211 (A 2537)

Table C.1—Continued

ID	R.A.	DEC.	z	$W_0(\text{[OII]})$ [Å]	$D_{4000}$ [Å]	$W_0(\text{H}_\delta)$ [Å]	$B_{\text{AB}}$ [mag]	$V_{\text{AB}}$ [mag]	$R_{\text{AB}}$ [mag]
7367	23:8:43.6	-2:14:07.05	0.6383	2.031	1.065	0.976	24.85	23.98	22.54
7370	23:8:29.7	-2:14:00.75	0.2734	1.112	2.289	0.550	22.19	21.15	20.08
7372	23:8:24.9	-2:14:03.77	0.3020	0.180	1.642	0.513	22.71	21.87	20.86
7376	23:7:23.9	-2:14:06.23	0.6440	0.473	1.694	1.078	24.59	23.89	22.09
7384	23:8:33.3	-2:14:03.91	0.2925	0.960	1.213	1.075	23.54	22.56	21.79
7396	23:8:37.1	-2:13:59.9	0.2899	1.469	1.518	0.311	22.20	21.18	20.22
7401	23:8:58.2	-2:14:02.52	0.6019	5.727	1.037	1.469	22.59	22.41	21.62
7421	23:7:25.9	-2:13:57.4	0.5616	0.277	1.738	0.818	23.19	22.14	20.88
7429	23:7:55.8	-2:13:46.9	0.2730	1.287	1.543	1.439	20.73	19.87	19.08
7436	23:8:29.2	-2:13:41.2	0.6374	3.062	1.174	2.341	21.59	20.77	19.49
7452	23:7:33.0	-2:13:56.3	0.2947	3.089	1.165	0.290	22.75	21.76	21.12
7468	23:7:58.1	-2:13:46.5	0.3541	6.381	1.509	-1.50	21.07	20.33	19.47
7478	23:8:14.0	-2:13:52.7	0.0830	3.167	1.404	1.383	21.39	21.24	20.91
7488	23:8:02.41	-2:13:54.2	0.2989	-10.2	1.337	0.661	22.85	22.04	21.09
7489	23:8:48.4	-2:13:53.2	0.2930	5.005	1.142	1.374	22.31	21.70	21.05
7507	23:7:50.0	-2:13:53.2	0.6878	9.458	0.536	14.70	22.70	22.43	21.63
7509	23:8:05.58	-2:13:50.2	0.1340	1.313	1.067	0.530	22.05	21.60	20.65
7510	23:8:13.6	-2:13:45.0	0.2907	-0.32	1.429	0.367	21.40	20.36	19.41
7563	23:8:05.29	-2:13:42.9	0.5099	3.030	1.381	1.907	23.48	22.61	21.26
7590	23:8:34.9	-2:13:42.6	0.3020	-0.70	1.649	1.205	23.16	22.09	21.03
7619	23:8:52.7	-2:13:30.9	0.2926	0.892	1.870	0.123	21.10	19.93	18.84
7620	23:7:34.5	-2:13:40.5	0.6664	0.332	1.489	7.666	24.18	23.16	21.58
7625	23:8:14.3	-2:13:40.7	0.2917	8.687	1.105	1.422	22.84	22.12	21.64
7639	23:7:49.7	-2:13:30.3	0.2342	-0.21	1.184	-3.54	22.32	21.36	20.39
7640	23:8:10.2	-2:13:34.0	0.2896	6.051	1.200	-0.42	21.71	21.07	20.47
7647	23:7:26.8	-2:13:36.3	0.6871	-0.85	0.942	15.25	23.80	23.06	21.79
7651	23:8:26.7	-2:13:38.1	0.8736	-6.19	ND	ND	24.44	23.38	21.74
7669	23:8:15.6	-2:13:27.8	0.0822	3.838	1.335	-0.01	21.49	21.22	20.88
7674	23:8:42.7	-2:13:34.7	0.7146	11.50	0.134	ND	22.88	22.76	21.83
7681	23:8:53.9	-2:13:34.0	0.2925	0.332	1.598	0.123	23.00	22.14	21.15
7688	23:8:33.1	-2:13:27.6	0.2999	-0.98	1.736	-0.03	21.93	20.83	19.74
7733	23:8:22.1	-2:13:27.4	0.2918	-0.66	1.488	0.451	23.31	22.30	21.38
7747	23:8:32.9	-2:13:21.7	0.3006	0.070	1.520	1.507	20.16	19.55	18.75
7752	23:7:32.1	-2:13:27.1	0.6654	8.980	1.207	9.139	23.29	23.05	21.96
7754	23:7:25.2	-2:13:22.6	0.4404	-1.43	1.851	-0.44	22.62	21.80	20.62
7762	23:8:24.9	-2:13:16.0	0.3017	0.975	1.893	0.995	21.26	20.17	19.09
7829	23:8:31.0	-2:13:17.0	0.2950	-0.53	1.203	0.390	22.49	21.75	20.77
7834	23:8:08.16	-2:13:18.2	0.5959	12.37	1.218	1.320	23.51	22.98	21.88
7846	23:8:14.7	-2:13:14.6	0.3020	3.620	1.345	-1.15	22.05	21.32	20.63
7847	23:8:48.9	-2:13:14.7	0.2974	3.041	1.234	1.420	22.06	21.30	20.73
7858	23:8:16.8	-2:13:14.3	0.5863	0.275	1.381	-0.41	22.80	22.27	21.09
7872	23:8:20.3	-2:13:06.64	0.3040	-1.07	1.726	-0.16	20.87	19.94	19.10
7890	23:8:27.4	-2:13:13.5	0.5972	0.165	1.099	-0.46	23.79	22.80	21.22
7893	23:7:27.9	-2:13:14.8	0.7703	2.270	ND	ND	24.86	23.18	22.10
7922	23:8:47.0	-2:12:54.2	0.2021	4.485	1.227	0.785	19.32	18.89	18.47
7927	23:8:08.58	-2:13:04.38	0.2938	0.529	1.589	-0.74	21.55	20.48	19.41
7930	23:8:08.86	-2:12:45.5	0.3016	1.848	1.355	2.159	20.88	19.74	18.68

Table C.1—Continued

ID	R.A.	DEC.	z	$W_0(\text{[OII]})$ [Å]	$D4000$ [Å]	$W_0(\text{H}\delta)$ [Å]	$B_{\text{AB}}$ [mag]	$V_{\text{AB}}$ [mag]	$R_{\text{AB}}$ [mag]
7933	23:8:16.5	-2:13:06.29	0.4776	3.146	1.270	0.823	22.46	21.80	20.64
7938	23:7:57.3	-2:13:03.65	0.2391	4.195	1.397	0.724	22.11	21.42	20.59
7967	23:8:06.37	-2:13:08.32	0.5674	-1.49	1.714	0.522	24.43	23.07	21.92
7974	23:8:33.6	-2:12:59.4	0.2940	8.161	1.167	-0.02	23.54	22.88	21.95
7987	23:7:53.3	-2:13:03.20	0.2970	-0.58	1.718	-0.36	22.54	21.34	20.24
7998	23:8:16.8	-2:12:53.6	0.3008	-3.30	1.547	1.292	21.43	20.39	19.51
8007	23:8:06.18	-2:13:04.05	0.5708	1.308	1.397	-2.49	24.31	23.21	21.79
8033	23:7:25.8	-2:13:01.21	0.5115	-1.72	1.669	-0.80	23.59	22.62	21.36
8039	23:8:49.8	-2:12:58.2	0.7507	4.308	ND	ND	22.39	22.13	21.18
8094	23:8:55.6	-2:12:52.1	0.2938	0.312	1.336	1.109	21.42	20.59	19.78
8105	23:7:57.3	-2:12:48.6	0.2396	4.164	1.278	1.269	22.20	21.63	20.88
8110	23:7:59.6	-2:12:48.7	0.3203	2.515	1.380	-1.66	21.25	20.65	19.82
8112	23:8:05.78	-2:12:54.7	0.6020	3.022	1.090	-0.73	24.68	23.65	21.95
8125	23:8:11.8	-2:12:43.1	0.2997	-0.37	1.914	-0.53	21.63	20.53	19.41
8127	23:7:39.7	-2:12:47.2	0.4517	-1.34	1.457	0.656	22.30	21.68	20.54
8128	23:8:16.9	-2:12:44.7	0.2900	-1.22	1.825	-3.26	21.70	20.54	19.53
8149	23:8:38.9	-2:12:48.9	0.8112	9.203	ND	ND	23.27	22.75	21.51
8166	23:8:25.3	-2:12:41.8	0.3017	4.230	1.336	1.537	21.62	20.65	19.83
8219	23:8:18.1	-2:12:37.0	0.3003	0.750	1.500	1.221	21.81	20.75	19.70
8271	23:8:25.8	-2:12:35.6	0.3030	1.297	1.222	0.980	21.90	21.09	20.58
8274	23:8:24.7	-2:12:13.3	0.3036	-0.81	1.932	-0.93	19.45	18.47	17.36
8307	23:8:10.5	-2:12:32.8	0.3027	1.256	1.149	1.064	22.68	21.89	21.03
8315	23:7:23.3	-2:12:14.3	0.0923	1.595	2.483	-0.06	18.98	18.18	17.45
8364	23:8:30.8	-2:12:18.8	0.0818	11.91	1.248	0.874	19.97	19.67	19.32
8416	23:8:08.20	-2:12:19.8	0.2771	-1.42	2.119	0.814	22.24	21.10	20.02
8419	23:9:14.7	-2:12:15.1	0.2241	2.775	1.293	0.861	20.49	19.84	19.24
8430	23:7:23.7	-2:12:20.2	0.2659	10.57	1.128	1.633	22.02	21.38	20.79
8445	23:8:16.5	-2:12:21.7	0.2945	-1.73	1.533	1.259	23.11	22.09	21.16
8483	23:8:29.4	-2:12:16.5	0.2978	-0.90	1.876	-0.48	22.69	21.64	20.56
8493	23:8:17.9	-2:12:15.8	0.2077	6.547	1.355	0.717	20.92	20.37	19.82
8498	23:8:23.8	-2:12:09.29	0.2907	-2.44	2.068	-0.78	21.19	20.02	18.89
8503	23:8:41.8	-2:12:11.2	0.2358	4.450	1.237	1.387	20.58	20.02	19.54
8509	23:8:25.2	-2:12:11.0	0.3046	-1.02	1.974	-0.88	21.10	20.08	19.10
8549	23:8:19.5	-2:12:07.04	0.4921	4.691	1.238	1.062	21.84	21.22	20.29
8575	23:7:44.0	-2:12:11.0	0.0722	1.693	1.031	-0.08	21.29	20.85	20.45
8621	23:8:03.24	-2:11:59.6	0.4993	1.088	1.494	0.390	23.38	22.44	20.87
8645	23:8:13.8	-2:12:04.57	0.2876	-0.54	1.622	-0.67	23.08	21.91	20.97
8659	23:9:19.5	-2:12:01.24	0.3025	5.760	1.197	0.199	21.40	20.78	20.36
8675	23:9:12.3	-2:11:59.0	0.2981	-0.42	1.633	0.796	22.04	21.01	20.03
8686	23:7:41.9	-2:12:01.78	0.2758	3.877	1.005	1.974	22.92	22.18	21.65
8690	23:8:36.4	-2:11:58.1	0.2993	-1.22	1.947	-1.13	21.99	20.84	19.71
8706	23:7:27.4	-2:12:00.21	0.6852	14.25	0.827	9.109	22.62	22.39	21.74
8725	23:9:27.2	-2:11:53.4	0.4477	-0.65	1.203	1.697	23.17	22.24	21.15
8741	23:8:10.9	-2:11:50.4	0.2915	0.844	1.947	-0.70	22.41	21.65	20.76
8749	23:7:25.5	-2:11:52.6	0.0814	13.23	1.571	0.597	20.53	20.11	19.71
8760	23:7:39.1	-2:11:39.2	0.2733	10.18	1.163	0.736	19.95	19.35	18.85
8768	23:8:35.1	-2:11:52.4	0.2964	0.503	1.533	0.741	23.04	22.32	21.38

## C Spectroscopic members catalogue of RXCJ2308.3-0211 (A 2537)

Table C.1—Continued

ID	R.A.	DEC.	z	$W_0([\text{OII}])$ [Å]	$D_{4000}$ [Å]	$W_0(\text{H}_\delta)$ [Å]	$B_{\text{AB}}$ [mag]	$V_{\text{AB}}$ [mag]	$R_{\text{AB}}$ [mag]
8771	23:8:25.7	-2:11:48.3	0.2907	-1.59	1.750	0.257	21.89	20.80	19.73
8779	23:8:23.8	-2:11:36.1	0.2892	-1.38	1.847	-0.58	20.77	19.58	18.43
8795	23:8:21.4	-2:11:51.8	0.2950	1.071	2.123	0.542	22.48	22.25	21.11
8797	23:8:19.9	-2:11:43.2	0.3053	7.158	1.124	-0.15	20.01	19.47	19.02
8811	23:9:08.31	-2:11:49.8	0.7119	7.788	0.171	0.370	22.07	21.81	20.97
8832	23:8:17.6	-2:11:34.9	0.2983	-2.89	1.952	1.351	21.29	20.25	19.22
8833	23:7:19.4	-2:11:37.4	0.1625	9.064	1.896	1.214	20.39	19.91	19.41
8851	23:9:02.16	-2:11:47.7	0.2977	-2.17	1.564	0.370	23.67	22.54	21.57
8877	23:7:58.6	-2:11:45.7	0.6174	2.674	1.107	2.125	23.35	22.89	21.78
8881	23:8:20.8	-2:11:42.1	0.2937	-1.11	1.751	1.029	23.56	22.30	21.08
8886	23:8:08.29	-2:11:24.1	0.2908	-0.87	1.396	1.516	21.25	20.28	19.57
8920	23:8:31.7	-2:11:41.6	0.2952	-2.36	1.892	0.602	23.45	22.50	21.35
8946	23:8:30.6	-2:11:33.9	0.2925	-0.71	1.744	0.158	22.39	21.21	20.11
8963	23:8:12.4	-2:11:37.5	0.7263	4.868	0.148	ND	23.03	22.84	21.78
8972	23:9:19.2	-2:11:37.0	0.2361	1.576	1.501	0.944	23.15	22.25	21.54
8996	23:9:12.3	-2:11:33.8	0.2987	0.216	1.594	0.311	23.28	22.41	21.47
9004	23:8:47.3	-2:11:26.4	0.2954	-1.44	1.609	0.756	21.90	21.48	20.52
9017	23:9:06.52	-2:11:32.9	0.5113	1.355	1.609	-1.24	23.97	22.97	21.60
9024	23:8:19.4	-2:11:30.7	0.2934	-4.94	1.583	0.727	21.26	20.56	19.93
9035	23:7:28.7	-2:11:26.1	0.2955	5.996	1.213	1.188	21.27	20.53	19.96
9045	23:8:32.0	-2:11:32.5	0.2960	5.260	1.317	-1.30	23.99	23.08	22.01
9052	23:8:17.3	-2:11:21.2	0.3009	4.594	1.184	1.876	20.38	19.57	18.85
9094	23:9:02.86	-2:11:23.1	0.5137	8.429	1.643	-0.99	23.53	22.28	20.47
9103	23:9:23.1	-2:11:22.2	0.3011	3.656	1.214	1.194	20.96	20.25	19.64
9109	23:8:39.8	-2:11:25.2	0.2945	6.471	1.196	1.250	22.88	22.28	21.53
9117	23:8:44.0	-2:11:18.7	0.2932	2.150	1.355	0.208	21.51	20.61	19.67
9125	23:7:34.5	-2:11:18.3	0.6429	2.761	1.125	-2.11	21.17	20.67	19.65
9128	23:7:18.9	-2:11:20.8	0.5123	10.54	1.198	0.696	21.95	21.64	20.49
9130	23:8:30.6	-2:11:21.1	0.2982	0.885	1.698	-0.50	22.50	21.37	20.34
9137	23:9:06.24	-2:11:18.5	0.5116	4.009	1.899	-0.97	22.69	21.63	20.29
9157	23:8:07.84	-2:11:19.3	0.2928	7.390	1.184	1.127	22.82	21.91	21.51
9158	23:8:13.4	-2:11:05.47	0.3029	0.809	2.153	0.863	20.74	19.62	18.50
9159	23:8:27.8	-2:11:16.8	0.2920	1.140	1.589	-0.72	22.20	21.04	19.91
9161	23:9:16.2	-2:11:20.5	0.2092	9.078	1.272	1.131	22.47	21.94	21.36
9164	23:9:24.7	-2:11:17.7	0.3001	1.512	1.460	1.075	22.75	21.94	21.01
9176	23:7:22.8	-2:11:17.0	2.0141	ND	ND	ND	20.30	19.93	19.35
9199	23:8:33.6	-2:11:07.13	0.3003	-0.83	1.711	0.200	21.64	20.53	19.42
9212	23:8:12.7	-2:11:09.83	0.2911	-1.71	1.518	0.913	22.06	21.07	20.08
9213	23:8:25.3	-2:11:17.6	0.6014	-0.57	1.122	0.036	23.67	22.85	21.57
9225	23:8:44.3	-2:11:12.4	0.3684	9.762	1.119	0.604	21.77	21.24	20.65
9230	23:8:22.9	-2:11:10.6	0.2714	-0.92	1.950	0.438	22.14	20.88	19.71
9233	23:8:20.1	-2:11:07.63	0.2976	-2.46	1.925	0.548	22.17	21.07	19.97
9246	23:8:02.04	-2:11:09.26	0.2946	1.817	1.329	0.942	22.48	21.38	20.67
9262	23:8:13.9	-2:10:56.4	0.3005	-0.42	2.252	10.02	21.65	20.42	19.27
9265	23:8:21.5	-2:11:11.4	0.2926	-0.82	1.671	0.526	23.20	22.13	21.09
9285	23:9:20.8	-2:11:09.22	0.2351	6.853	1.205	0.748	22.63	21.81	21.29
9294	23:8:47.6	-2:11:08.67	0.4278	0.673	1.578	1.655	22.87	21.87	20.43

Table C.1—Continued

ID	R.A.	DEC.	z	$W_0(\text{[OII]})$ [Å]	$D_{4000}$ [Å]	$W_0(\text{H}\delta)$ [Å]	$B_{\text{AB}}$ [mag]	$V_{\text{AB}}$ [mag]	$R_{\text{AB}}$ [mag]
9304	23:8:59.7	-2:11:08.52	0.6253	8.849	1.016	0.165	22.69	22.30	21.24
9306	23:9:02.98	-2:11:03.22	0.2960	0.540	1.630	0.202	22.05	21.05	19.97
9307	23:9:00.10	-2:10:51.4	0.2965	-2.09	1.742	1.424	21.02	20.13	19.25
9318	23:8:25.5	-2:11:04.93	0.2915	-1.55	2.006	0.780	22.86	22.02	20.93
9320	23:9:14.4	-2:11:02.27	0.4604	5.751	1.306	0.818	22.67	22.07	21.18
9346	23:8:35.7	-2:11:02.29	0.6504	1.695	1.277	-4.00	23.34	22.61	21.23
9347	23:8:42.0	-2:11:00.65	0.5002	10.00	1.247	1.890	23.33	22.76	21.52
9399	23:8:18.5	-2:10:59.9	0.3012	-0.65	1.415	0.864	23.24	22.27	21.61
9400	23:8:19.7	-2:10:54.2	0.2923	-0.28	1.965	0.478	22.34	21.18	20.17
9403	23:8:24.2	-2:10:58.6	0.2967	-0.79	1.525	0.683	23.10	22.26	21.22
9418	23:8:33.2	-2:10:55.7	0.2894	-1.55	1.953	0.081	22.44	21.51	20.33
9419	23:9:08.00	-2:10:49.2	0.5135	9.610	1.276	1.351	21.67	20.69	19.80
9442	23:9:10.7	-2:10:52.5	0.4564	-1.14	1.200	0.442	21.99	21.28	20.10
9449	23:8:30.7	-2:10:44.5	0.2987	-0.65	1.876	0.440	21.39	20.29	19.21
9476	23:8:37.6	-2:10:39.2	0.2947	-0.63	1.831	0.096	21.15	20.08	19.00
9483	23:7:58.3	-2:10:43.4	0.6227	-1.36	0.971	-2.02	20.68	19.93	19.26
9503	23:8:12.5	-2:10:44.1	0.2897	0.210	1.556	2.350	21.49	20.51	19.61
9506	23:8:26.9	-2:10:48.6	0.5396	-1.38	1.615	0.506	23.25	22.29	21.17
9530	23:9:10.9	-2:10:41.7	0.3018	-0.44	1.790	0.040	21.86	20.77	19.66
9546	23:9:21.3	-2:10:47.6	0.4938	-2.05	1.299	-2.84	25.78	23.67	22.29
9549	23:8:48.0	-2:10:39.9	0.4266	2.293	1.683	-0.81	22.92	21.91	20.42
9550	23:9:17.1	-2:10:40.5	0.2357	0.313	1.965	-0.78	21.21	20.09	19.19
9557	23:8:13.2	-2:10:44.7	0.8031	2.121	ND	ND	22.93	22.44	21.72
9562	23:8:27.1	-2:10:35.9	0.2876	-1.11	1.595	-0.29	21.18	20.19	19.27
9587	23:8:21.4	-2:10:40.7	0.2972	0.127	1.713	-0.82	22.96	21.85	20.84
9625	23:8:29.2	-2:10:28.9	0.2954	-0.80	1.686	0.180	21.97	20.89	19.75
9634	23:9:01.91	-2:10:26.5	0.2988	0.945	1.637	0.274	23.91	22.58	21.50
9642	23:8:23.5	-2:10:30.2	0.2845	-1.80	1.631	-2.49	22.32	21.28	20.26
9671	23:8:43.1	-2:10:30.8	0.3284	0.689	1.549	0.781	22.75	21.75	20.66
9687	23:9:27.9	-2:10:34.8	0.7811	9.612	ND	ND	23.27	23.32	22.28
9700	23:9:27.0	-2:10:29.7	0.3001	1.308	2.012	0.044	22.19	21.12	19.78
9742	23:8:40.0	-2:10:23.9	0.6304	2.839	1.205	-0.50	23.06	22.61	21.22
9757	23:8:36.4	-2:10:20.1	0.3020	-1.71	1.231	-3.08	22.56	21.46	20.40
9769	23:9:20.6	-2:10:25.1	0.2347	5.918	1.136	0.925	22.49	21.95	21.46
9783	23:9:06.21	-2:10:17.8	0.5603	1.531	1.559	1.154	22.19	21.51	20.18
9829	23:9:27.5	-2:10:20.4	0.3185	4.763	1.242	1.551	22.09	21.41	20.76
9852	23:9:04.07	-2:10:07.55	0.3007	-2.08	1.879	-0.52	21.22	20.17	19.08
9854	23:7:55.6	-2:10:20.7	0.6233	1.339	1.328	-2.97	24.66	23.73	22.37
9861	23:8:15.5	-2:10:14.6	0.2873	-1.22	2.123	0.480	21.95	21.02	20.00
9862	23:8:14.8	-2:09:45.7	0.3045	-1.11	2.131	-0.76	20.35	19.24	18.07
9867	23:8:01.65	-2:10:18.8	0.6258	8.036	1.054	-0.24	23.79	23.21	22.09
9869	23:7:51.9	-2:10:15.0	0.6174	1.883	0.936	-2.73	22.58	21.77	20.44
9881	23:8:38.7	-2:10:02.47	0.2966	-0.63	1.626	0.334	21.21	20.15	19.13
9898	23:8:23.1	-2:10:07.87	0.4111	8.172	1.362	0.876	19.19	18.78	18.31
9908	23:9:10.7	-2:09:46.9	0.2643	1.252	1.585	0.469	21.20	20.16	19.24
9910	23:9:08.13	-2:10:15.6	0.7529	22.92	ND	ND	23.10	22.96	22.25
9929	23:8:13.5	-2:10:10.0	0.3057	-0.87	1.684	-0.51	23.67	22.48	21.45

## C Spectroscopic members catalogue of RXCJ2308.3-0211 (A 2537)

Table C.1—Continued

ID	R.A.	DEC.	z	$W_0([\text{OII}])$ [Å]	$D_{4000}$ [Å]	$W_0(\text{H}\delta)$ [Å]	$B_{\text{AB}}$ [mag]	$V_{\text{AB}}$ [mag]	$R_{\text{AB}}$ [mag]
9946	23:8:55.2	-2:09:52.0	0.2986	0.453	2.047	0.402	17.38	16.78	16.02
9976	23:9:00.81	-2:10:07.00	0.6254	1.808	1.098	1.046	22.40	22.02	20.87
9998	23:9:26.0	-2:10:08.48	0.2374	7.569	1.289	0.584	22.83	22.03	21.33
10010	23:8:14.5	-2:10:03.71	0.5780	-1.02	1.525	2.001	22.94	22.07	20.71
10012	23:9:00.15	-2:09:58.6	0.3000	-1.92	1.525	0.749	22.86	21.68	20.58
10014	23:8:29.0	-2:10:04.69	0.2888	0.029	1.708	0.063	23.19	22.24	21.32
10016	23:8:12.6	-2:10:04.87	0.3056	-0.76	1.902	-0.61	23.13	21.95	20.92
10018	23:9:19.2	-2:10:02.53	0.2928	11.18	1.290	1.454	22.38	21.82	21.51
10019	23:7:49.7	-2:10:05.66	0.2941	6.328	1.303	1.324	22.44	21.77	21.15
10023	23:8:36.3	-2:10:06.04	0.2086	7.972	1.389	0.748	23.02	22.48	21.76
10028	23:8:26.8	-2:09:46.5	0.2893	2.651	1.378	1.945	21.95	21.13	20.40
10060	23:8:31.3	-2:09:48.9	0.2960	-1.34	1.279	1.156	21.10	20.45	19.75
10083	23:8:12.2	-2:09:55.2	0.3084	-3.43	1.981	0.250	22.50	21.52	20.39
10121	23:8:21.4	-2:09:55.8	0.6914	5.892	0.450	15.82	22.85	22.50	21.58
10125	23:7:48.4	-2:09:29.7	0.2935	0.371	1.841	0.017	20.43	19.33	18.25
10129	23:8:47.0	-2:09:55.9	0.4271	2.572	1.156	1.384	23.31	22.66	21.73
10133	23:7:59.7	-2:09:55.9	0.2946	0.505	1.349	1.396	23.19	22.32	21.46
10154	23:9:26.0	-2:09:41.0	0.2933	-0.62	1.902	-0.53	20.65	19.63	18.55
10164	23:7:53.3	-2:09:54.3	0.6308	-1.09	1.682	1.318	24.44	23.43	21.75
10215	23:7:49.8	-2:09:33.6	0.1612	9.361	1.341	1.078	20.57	19.44	18.32
10216	23:8:16.2	-2:09:49.8	0.2960	-0.94	1.836	-0.59	23.19	21.94	20.81
10219	23:9:01.85	-2:09:44.5	0.2995	-0.80	1.981	0.289	22.16	21.10	20.05
10220	23:8:30.8	-2:09:47.5	0.2948	-0.14	1.468	0.224	22.63	21.80	20.81
10239	23:9:27.9	-2:09:46.6	0.2930	3.177	1.252	0.928	22.10	21.50	20.65
10269	23:8:37.1	-2:09:31.8	0.1820	2.760	1.897	0.124	20.35	19.51	18.73
10278	23:7:59.4	-2:09:41.2	0.5594	1.656	1.440	-1.92	23.73	22.63	21.29
10283	23:8:48.1	-2:09:06.75	0.2964	1.222	1.306	1.159	21.88	20.98	20.09
10285	23:9:03.85	-2:09:45.2	0.4970	5.214	0.998	-0.67	23.44	23.15	22.53
10291	23:8:01.41	-2:09:39.7	0.2956	0.370	1.739	0.286	22.23	21.21	20.18
10298	23:8:06.32	-2:09:39.8	0.4367	8.308	1.403	2.161	23.59	22.65	21.51
10314	23:8:12.2	-2:09:37.2	0.3005	-0.38	1.593	0.391	22.82	21.94	20.80
10332	23:9:27.6	-2:09:38.0	0.4802	11.13	1.124	0.509	23.90	22.46	21.19
10340	23:9:07.44	-2:09:37.1	0.6881	7.903	0.695	7.889	24.04	23.67	22.18
10345	23:8:22.8	-2:09:34.3	0.2891	-0.70	1.326	1.017	22.13	21.27	20.42
10353	23:8:29.3	-2:09:32.2	0.5607	0.871	1.494	1.322	22.12	21.32	19.88
10360	23:8:14.5	-2:09:23.8	0.2307	3.696	1.265	0.776	20.54	19.88	19.35
10371	23:9:14.7	-2:09:34.3	0.7002	3.477	0.310	11.39	23.87	23.11	21.93
10376	23:7:57.9	-2:09:10.1	0.2919	0.135	1.357	1.339	20.48	19.32	18.19
10408	23:9:22.1	-2:09:25.2	0.2349	2.284	1.314	0.940	22.12	21.36	20.79
10409	23:9:06.75	-2:09:29.1	0.2726	2.331	1.525	0.849	22.41	21.41	20.59
10421	23:7:58.2	-2:09:25.4	0.2967	0.653	1.564	0.646	21.66	20.60	19.54
10428	23:8:36.7	-2:09:25.6	0.1820	2.760	1.897	0.124	22.57	21.67	20.80
10431	23:8:18.7	-2:09:24.9	0.1612	3.534	1.440	-0.41	22.05	21.38	20.98
10471	23:9:08.73	-2:09:21.9	0.2968	-1.19	1.560	-0.75	22.74	21.70	20.68
10473	23:8:04.27	-2:09:14.3	0.2912	3.572	1.160	0.378	21.66	20.63	19.79
10474	23:8:50.2	-2:09:21.6	0.3013	1.855	1.558	1.454	22.14	21.21	20.19
10479	23:8:16.3	-2:09:23.6	0.2961	-0.39	1.591	-0.20	23.51	22.23	21.12



Table C.1—Continued

ID	R.A.	DEC.	z	$W_0(\text{[OII]})$ [Å]	$D4000$ [Å]	$W_0(\text{H}\delta)$ [Å]	$B_{\text{AB}}$ [mag]	$V_{\text{AB}}$ [mag]	$R_{\text{AB}}$ [mag]
10480	23:9:28.9	-2:09:27.1	0.7906	17.90	ND	ND	23.49	23.31	22.60
10491	23:8:19.9	-2:09:21.4	0.2956	-1.71	1.935	0.815	22.37	21.50	20.35
10509	23:8:18.8	-2:09:10.7	0.2968	-2.07	1.863	0.038	21.37	20.23	19.15
10515	23:9:04.72	-2:09:17.9	0.2947	-0.96	1.596	-0.12	22.43	21.39	20.37
10524	23:9:29.0	-2:09:17.5	0.3002	1.574	1.304	0.881	22.28	21.56	20.55
10561	23:8:33.6	-2:08:51.3	0.0834	8.512	1.473	1.275	20.48	20.13	19.69
10568	23:8:39.7	-2:09:12.6	0.5544	11.37	1.149	1.182	21.91	21.64	20.65
10574	23:9:09.97	-2:09:12.6	0.1849	17.19	1.127	-0.20	21.96	21.64	21.36
10592	23:9:16.6	-2:09:09.42	0.3259	5.207	1.321	1.984	21.80	21.09	20.57
10599	23:9:20.3	-2:08:59.1	0.3000	-1.15	1.701	-0.19	21.38	20.37	19.30
10605	23:7:56.4	-2:08:50.2	0.2961	2.875	1.800	0.092	20.77	19.71	18.65
10613	23:8:12.0	-2:09:01.47	0.3026	0.534	1.832	-0.68	21.50	20.45	19.32
10615	23:8:27.7	-2:09:07.75	0.2979	3.126	1.559	-1.39	21.63	21.01	20.46
10623	23:9:24.7	-2:09:09.75	0.1769	5.192	1.333	1.049	21.33	20.84	20.44
10669	23:8:44.0	-2:09:06.68	0.6295	0.790	1.464	0.847	23.95	22.79	21.47
10672	23:8:50.9	-2:08:54.6	0.2076	1.703	1.739	0.549	20.40	19.59	18.85
10677	23:9:24.0	-2:08:59.7	0.2316	1.494	1.419	-2.11	21.08	20.08	19.14
10680	23:9:27.7	-2:08:58.8	0.2999	2.695	1.408	1.084	20.51	19.55	18.74
10719	23:7:56.1	-2:08:58.7	0.2941	1.359	1.460	0.782	22.75	21.62	20.63
10730	23:9:01.35	-2:08:57.7	0.1625	8.625	1.420	1.495	21.41	20.92	20.51
10737	23:8:19.2	-2:08:58.8	0.3016	1.087	1.505	-0.42	23.22	22.31	21.29
10738	23:8:40.3	-2:08:56.3	0.5691	-1.78	1.248	0.367	22.26	21.79	20.72
10742	23:8:49.2	-2:08:58.3	0.7524	6.314	ND	ND	23.66	22.87	21.71
10753	23:8:02.71	-2:08:57.0	0.3965	4.477	1.247	1.789	22.76	21.93	21.19
10786	23:7:49.7	-2:08:49.9	0.1619	4.680	1.373	1.316	20.81	20.18	19.51
10792	23:8:14.0	-2:08:55.6	0.6257	1.749	1.189	0.557	23.31	22.65	21.53
10793	23:8:52.5	-2:08:42.5	0.7130	18.93	0.190	ND	23.67	23.04	21.60
10804	23:8:39.2	-2:08:31.3	0.2317	1.444	1.443	0.635	20.18	19.15	18.25
10806	23:8:11.3	-2:08:47.9	0.6744	1.451	0.786	12.45	21.27	20.87	19.95
10820	23:8:26.7	-2:08:45.3	0.0499	0.101	1.348	-0.47	21.93	21.63	20.95
10824	23:8:09.02	-2:08:45.2	0.3190	4.968	1.196	1.473	21.84	21.32	20.62
10831	23:9:16.2	-2:08:50.0	0.3807	5.947	1.234	1.402	22.68	21.93	21.14
10854	23:9:24.5	-2:08:15.4	0.2361	0.905	2.033	0.125	19.25	18.16	17.23
10856	23:8:23.2	-2:08:46.1	0.3016	0.127	1.763	0.099	22.33	21.26	20.16
10857	23:8:12.1	-2:08:35.7	0.2923	-2.50	1.646	0.032	21.07	19.93	18.88
10870	23:9:09.87	-2:08:30.6	0.3020	1.149	1.912	0.170	20.55	19.52	18.51
10899	23:8:14.8	-2:08:45.8	0.3050	0.041	1.505	-1.44	23.84	22.95	21.66
10901	23:8:45.6	-2:08:32.2	0.3044	4.349	1.257	1.490	21.67	20.99	20.37
10913	23:8:42.6	-2:08:42.9	0.0588	19.55	1.338	-1.15	23.27	22.50	21.64
10921	23:8:06.81	-2:08:35.6	0.7265	3.757	0.104	ND	22.05	21.59	20.79
10927	23:9:26.2	-2:08:41.5	0.2373	2.436	1.384	1.517	22.46	21.91	21.15
10935	23:7:51.6	-2:08:36.7	0.2952	-1.78	1.949	-0.69	22.27	21.15	20.03
10948	23:9:07.64	-2:08:39.5	0.4991	8.474	1.161	2.365	22.71	22.29	21.42
10955	23:7:49.8	-2:08:29.5	0.3020	3.706	1.235	0.648	21.27	20.23	19.32
10962	23:8:15.6	-2:08:36.6	0.2950	0.825	1.411	-0.29	23.75	22.79	21.87
10997	23:9:24.8	-2:08:31.4	0.3010	3.081	1.261	1.109	21.60	20.84	20.10
11010	23:7:51.7	-2:08:13.7	0.2946	1.332	1.850	-0.35	20.97	19.85	18.80

## C Spectroscopic members catalogue of RXCJ2308.3-0211 (A 2537)

Table C.1—Continued

ID	R.A.	DEC.	z	$W_0([\text{OII}])$ [Å]	$D_{4000}$ [Å]	$W_0(\text{H}\delta)$ [Å]	$B_{\text{AB}}$ [mag]	$V_{\text{AB}}$ [mag]	$R_{\text{AB}}$ [mag]
11012	23:8:33.0	-2:08:31.8	0.9332	ND	ND	ND	23.95	22.75	21.44
11032	23:8:32.7	-2:08:20.2	0.2960	2.229	1.497	1.873	20.14	19.58	19.15
11056	23:8:46.3	-2:08:24.2	0.2974	0.756	1.578	0.143	22.89	21.93	20.82
11077	23:7:52.1	-2:08:24.0	0.2958	-0.46	1.741	0.464	22.07	20.92	19.85
11078	23:9:09.41	-2:08:18.6	0.3037	0.479	1.733	0.186	21.55	20.53	19.46
11091	23:8:01.26	-2:08:24.0	0.5622	3.448	1.251	0.906	22.57	22.18	21.08
11127	23:9:11.6	-2:08:21.6	0.3047	2.208	1.547	-0.74	23.41	22.66	21.88
11132	23:9:00.43	-2:08:22.4	0.5817	9.717	1.089	2.654	24.18	23.42	22.34
11144	23:7:17.7	-2:08:17.6	0.2967	4.531	1.256	0.946	21.83	21.14	20.54
11175	23:7:32.1	-2:08:16.5	0.6904	1.618	0.569	25.23	24.45	23.46	21.89
11176	23:8:14.7	-2:08:17.8	0.6942	-0.50	0.505	14.33	24.91	23.61	22.01
11181	23:9:03.88	-2:08:04.17	0.3016	1.454	1.650	0.914	21.24	20.25	19.36
11187	23:8:32.1	-2:08:13.5	0.2963	1.222	1.285	1.206	23.24	22.12	21.10
11200	23:8:47.4	-2:08:09.05	0.2950	3.831	1.473	1.208	22.43	21.55	20.53
11206	23:8:20.4	-2:08:13.3	0.3669	3.313	1.214	0.874	22.32	21.63	20.81
11208	23:8:23.0	-2:08:15.3	0.5775	3.063	1.339	0.954	23.02	22.51	21.14
11217	23:8:50.8	-2:08:08.54	0.3288	14.96	1.131	1.161	21.88	21.33	20.87
11219	23:7:42.6	-2:08:12.3	0.3264	6.845	1.356	1.142	22.46	21.50	20.60
11242	23:8:02.36	-2:07:35.9	0.2994	-1.01	1.813	0.150	21.63	20.50	19.41
11245	23:8:57.7	-2:08:07.96	0.4273	10.02	1.129	-0.45	21.70	21.10	20.36
11252	23:8:44.6	-2:07:56.5	0.3671	-0.49	1.718	-0.65	21.10	20.21	18.99
11256	23:7:54.0	-2:08:02.23	0.2901	2.941	1.288	1.066	21.32	20.75	20.40
11260	23:8:44.8	-2:08:08.65	3.1625	ND	ND	ND	21.55	21.33	21.08
11262	23:8:16.3	-2:08:08.08	0.2954	-1.10	1.904	0.212	23.22	21.80	20.67
11284	23:8:24.0	-2:08:04.39	0.4365	8.648	1.222	1.509	22.43	21.80	21.03
11307	23:7:43.3	-2:08:00.13	0.0810	2.166	1.433	1.687	21.33	20.99	20.51
11308	23:8:35.5	-2:08:02.91	0.2942	4.963	1.232	1.187	22.91	22.27	21.57
11314	23:7:33.3	-2:07:57.8	0.3038	0.599	1.921	0.520	22.04	20.90	19.79
11317	23:7:19.9	-2:08:04.12	0.4419	-4.38	1.210	0.922	23.44	23.01	21.76
11325	23:8:56.4	-2:08:00.82	0.8098	48.28	ND	ND	23.47	22.64	21.27
11332	23:9:08.89	-2:07:48.7	0.3267	0.964	1.339	1.044	20.58	19.83	19.04
11336	23:9:16.6	-2:08:01.16	0.8067	13.87	ND	ND	23.04	22.74	21.93
11356	23:8:42.1	-2:07:54.0	0.2327	8.596	1.232	0.726	21.81	21.19	20.72
11359	23:8:26.1	-2:07:55.4	0.4364	4.852	1.256	0.670	22.06	21.57	20.64
11361	23:8:35.0	-2:07:55.1	0.1229	8.885	1.348	0.725	21.32	20.92	20.54
11380	23:8:17.9	-2:07:54.1	0.2213	9.843	1.258	1.050	21.73	21.25	20.73
11382	23:8:42.2	-2:07:42.3	0.0919	16.30	1.431	0.757	20.00	19.66	19.16
11392	23:8:00.13	-2:07:53.2	0.2949	2.065	1.372	1.827	22.54	21.81	20.97
11401	23:8:14.6	-2:06:56.4	0.2922	-0.60	1.840	0.338	19.32	18.67	17.86
11403	23:9:27.5	-2:07:49.7	0.3019	0.839	1.907	-0.69	21.53	20.44	19.30
11435	23:8:00.63	-2:07:44.5	0.5025	2.007	1.467	0.284	23.04	22.30	20.92
11437	23:8:30.1	-2:07:45.5	0.2149	2.122	0.913	1.827	22.33	21.27	20.39
11440	23:8:26.3	-2:07:46.9	0.6252	-1.11	1.449	-0.78	23.78	22.69	21.24
11449	23:9:28.0	-2:07:48.9	0.3031	4.492	1.294	1.396	22.63	21.82	21.21
11450	23:7:26.9	-2:07:25.7	0.3533	3.027	1.494	-0.91	21.78	20.79	19.60
11454	23:8:26.9	-2:07:45.2	0.4116	22.69	0.982	-0.36	21.54	21.06	20.56
11463	23:9:27.5	-2:07:29.1	0.2739	-0.79	1.897	0.641	20.69	19.54	18.50

Table C.1—Continued

ID	R.A.	DEC.	z	$W_0(\text{[OII]})$ [Å]	$D4000$ [Å]	$W_0(\text{H}\delta)$ [Å]	$B_{\text{AB}}$ [mag]	$V_{\text{AB}}$ [mag]	$R_{\text{AB}}$ [mag]
11491	23:8:50.0	-2:07:41.3	0.6249	1.283	1.604	0.241	23.96	22.48	20.97
11497	23:9:20.4	-2:07:44.1	0.7004	9.816	0.213	38.03	23.22	22.59	21.70
11509	23:8:45.9	-2:07:38.9	0.2934	-0.50	1.635	0.638	22.12	21.05	20.07
11516	23:8:28.0	-2:07:37.8	0.2925	-1.18	1.902	0.719	22.22	21.09	20.04
11530	23:8:44.0	-2:07:38.8	0.6516	2.397	1.256	-1.61	22.82	22.49	21.35
11531	23:7:27.2	-2:07:35.0	0.3002	2.393	1.348	0.686	22.23	21.39	20.62
11534	23:8:32.3	-2:07:39.8	0.5550	0.751	1.615	0.025	24.52	23.27	21.74
11554	23:9:01.68	-2:07:33.3	0.4285	8.900	1.239	0.665	22.51	21.80	21.04
11565	23:7:42.5	-2:07:34.7	0.2960	8.094	1.182	0.628	22.33	21.63	20.83
11567	23:8:31.7	-2:07:28.6	0.5547	6.168	1.143	0.604	22.76	22.38	21.37
11579	23:8:53.4	-2:07:30.7	0.5369	3.298	1.032	0.530	23.11	22.49	21.48
11584	23:8:13.7	-2:07:30.4	0.3004	9.963	1.225	2.015	22.28	21.50	20.89
11599	23:9:17.9	-2:07:33.0	0.8056	8.018	ND	ND	22.55	22.26	21.65
11626	23:8:15.8	-2:07:23.2	0.2970	0.537	1.344	0.428	20.08	19.16	18.08
11633	23:8:41.8	-2:07:28.2	0.4586	10.22	1.097	2.108	22.33	21.85	21.19
11637	23:9:11.1	-2:07:22.6	0.3272	3.055	1.525	0.867	21.40	20.40	19.53
11650	23:8:20.1	-2:07:27.9	0.2973	-6.01	1.550	0.745	22.70	21.85	20.88
11670	23:8:48.3	-2:07:21.9	0.6518	-0.21	1.582	-7.71	23.31	22.28	20.88
11688	23:9:24.3	-2:07:25.5	0.7128	26.40	0.145	ND	22.71	22.65	21.63
11718	23:7:57.9	-2:07:22.3	0.2955	2.943	1.275	1.017	23.06	22.36	21.74
11722	23:8:44.2	-2:07:20.6	0.5865	8.175	1.077	3.148	23.09	22.20	21.18
11738	23:8:54.2	-2:07:19.2	1.3173	ND	ND	ND	24.03	22.88	21.69
11747	23:9:23.3	-2:07:17.4	0.5030	2.304	1.615	2.390	23.59	22.45	21.09
11787	23:8:20.5	-2:06:34.0	0.1115	0.854	1.756	0.341	19.90	19.25	18.62
11796	23:8:31.4	-2:07:08.99	0.3549	1.354	1.600	1.614	22.66	21.59	20.38
11800	23:7:28.1	-2:07:10.4	0.3763	4.547	0.945	-1.76	22.85	21.98	20.84
11808	23:8:03.69	-2:07:10.3	0.3013	7.552	1.279	1.729	21.74	21.21	20.69
11810	23:8:26.4	-2:07:15.6	0.6566	1.237	1.413	-2.99	24.35	23.58	22.22
11822	23:8:02.41	-2:07:09.81	0.2965	0.421	1.756	0.115	22.77	21.63	20.48
11826	23:9:09.90	-2:07:11.9	0.5834	0.210	1.665	0.303	23.79	22.81	21.31
11836	23:8:35.8	-2:07:07.26	0.2902	-0.60	1.507	0.434	22.86	21.77	20.86
11838	23:7:18.5	-2:07:11.9	0.2637	2.181	1.257	0.420	23.13	22.20	21.58
11855	23:7:35.1	-2:07:09.02	0.7234	-0.25	0.144	ND	24.00	22.81	21.57
11857	23:9:28.1	-2:06:58.5	0.2369	2.007	1.844	-1.12	21.02	19.85	18.94
11864	23:8:43.0	-2:07:08.84	0.5152	8.295	1.829	1.029	23.15	22.73	21.76
11874	23:8:53.4	-2:06:59.7	0.7556	3.377	ND	ND	22.28	21.52	20.59
11931	23:8:34.9	-2:06:55.2	0.4999	2.558	1.331	1.503	21.85	21.12	19.96
11935	23:9:10.2	-2:07:00.71	0.4461	6.616	1.124	2.476	22.47	21.81	21.11
11936	23:9:04.17	-2:07:01.91	0.5784	6.143	1.341	3.195	23.21	23.16	22.06
11937	23:8:16.6	-2:07:00.66	0.2737	3.178	1.255	0.916	22.57	21.75	21.08
11949	23:8:54.8	-2:06:46.1	0.2977	1.257	1.948	0.175	20.63	19.57	18.52
11972	23:8:43.6	-2:06:56.5	0.5817	4.397	1.159	1.850	23.78	23.10	22.01
11975	23:8:30.7	-2:06:51.3	0.5568	-0.31	2.035	-0.78	23.28	22.02	20.39
11984	23:9:10.5	-2:06:46.6	0.0928	3.708	1.269	0.464	19.89	19.51	19.01
12000	23:8:38.2	-2:06:41.8	0.2198	-2.73	1.551	0.592	21.69	20.85	19.92
12013	23:9:23.6	-2:06:47.3	0.2365	-1.13	1.425	0.171	22.35	21.34	20.41
12015	23:8:05.67	-2:06:47.8	0.2732	9.421	1.131	0.783	22.51	21.80	21.24

## C Spectroscopic members catalogue of RXCJ2308.3-0211 (A 2537)

Table C.1—Continued

ID	R.A.	DEC.	z	$W_0([\text{OII}])$ [Å]	$D_{4000}$ [Å]	$W_0(\text{H}\delta)$ [Å]	$B_{\text{AB}}$ [mag]	$V_{\text{AB}}$ [mag]	$R_{\text{AB}}$ [mag]
12019	23:7:18.6	-2:06:48.0	0.3047	15.86	1.150	-0.40	22.38	22.00	21.54
12034	23:8:40.4	-2:06:32.7	0.2960	1.582	1.663	0.177	21.10	20.05	19.01
12046	23:9:27.9	-2:06:48.4	0.2373	-1.17	1.513	-0.47	23.03	22.03	21.14
12049	23:8:31.5	-2:06:48.0	0.5544	0.112	1.399	-0.72	23.88	22.89	21.81
12054	23:8:32.8	-2:06:46.0	0.5430	-0.70	1.391	1.223	24.04	23.17	21.93
12056	23:9:17.2	-2:06:43.9	0.2075	8.741	1.365	0.838	21.38	20.86	20.43
12064	23:8:17.6	-2:06:39.1	0.2942	1.706	1.375	1.440	21.89	21.07	20.26
12066	23:7:24.9	-2:06:40.6	0.2727	4.070	1.377	1.070	21.08	20.39	19.87
12082	23:9:03.83	-2:06:46.6	0.7689	3.954	ND	ND	23.53	23.10	22.42
12106	23:8:51.2	-2:06:38.9	0.6272	6.548	1.046	-0.39	22.52	22.22	21.25
12114	23:7:56.4	-2:06:14.4	0.2971	1.528	1.395	0.744	21.33	20.42	19.49
12150	23:8:19.6	-2:06:38.3	0.4414	1.865	1.259	1.176	24.07	22.88	21.78
12155	23:9:14.2	-2:06:31.0	0.6498	8.649	1.067	-1.93	22.25	21.89	20.88
12159	23:8:30.0	-2:06:36.6	0.4589	0.219	1.419	1.367	24.64	23.53	21.92
12168	23:7:48.1	-2:06:36.5	0.3857	7.257	1.079	1.515	22.79	22.42	21.68
12175	23:8:46.2	-2:06:33.8	0.2007	5.525	1.310	0.088	21.35	20.79	20.33
12184	23:9:22.3	-2:06:35.6	0.2358	-0.80	1.537	0.704	23.38	22.46	21.70
12195	23:7:28.6	-2:06:33.6	0.4273	5.671	1.198	1.646	23.65	23.21	22.08
12196	23:9:20.9	-2:06:26.2	0.3033	5.904	1.224	0.918	21.21	20.50	19.87
12223	23:8:32.0	-2:06:28.1	0.4116	2.529	1.412	-0.47	23.27	22.62	21.25
12226	23:8:45.4	-2:05:54.2	0.3557	4.702	1.163	0.394	19.77	19.01	18.28
12228	23:8:44.0	-2:06:27.4	0.3054	6.699	1.276	0.699	22.71	21.89	21.33
12248	23:8:17.9	-2:06:24.7	0.3545	0.768	1.464	0.067	23.88	22.68	21.41
12249	23:8:20.4	-2:06:23.6	0.3670	5.795	1.313	0.153	22.69	21.85	20.81
12251	23:9:28.0	-2:06:26.9	0.2419	6.944	1.283	0.751	22.68	22.11	21.55
12254	23:8:54.7	-2:06:26.4	0.7205	12.44	0.175	ND	22.97	22.59	21.66
12280	23:8:06.81	-2:06:21.7	0.2940	-1.43	1.609	0.550	22.95	21.86	20.86
12284	23:9:26.8	-2:06:20.1	0.2378	1.120	1.827	0.231	21.62	20.49	19.62
12295	23:9:12.1	-2:06:18.6	0.3264	3.657	1.433	1.623	21.80	20.87	20.07
12300	23:8:19.3	-2:06:02.13	0.2687	15.14	1.419	-0.53	18.19	17.71	17.10
12331	23:7:55.4	-2:06:11.4	0.1942	5.425	1.260	0.922	21.48	20.93	20.31
12343	23:8:20.7	-2:06:08.09	0.2945	1.959	1.373	0.412	22.08	21.03	20.12
12347	23:9:04.20	-2:06:15.5	0.3030	-1.39	1.610	-1.06	22.80	21.72	20.74
12360	23:8:55.3	-2:06:06.56	0.2998	0.727	1.352	0.335	21.55	20.61	19.72
12361	23:8:57.8	-2:06:14.1	0.3058	2.593	1.621	-0.78	23.44	22.21	21.23
12367	23:9:18.7	-2:06:15.9	0.6632	9.452	1.081	4.885	22.93	22.73	21.80
12369	23:8:30.5	-2:06:14.7	0.4577	0.091	1.792	0.226	23.60	22.64	21.36
12373	23:8:35.5	-2:06:08.33	0.4357	7.584	1.079	-2.28	21.58	21.02	20.16
12396	23:8:03.04	-2:06:12.4	0.2925	-1.18	1.648	0.405	23.16	22.02	20.98
12452	23:8:12.1	-2:06:06.92	0.7461	6.192	-0.13	ND	22.93	22.61	21.90
12474	23:7:26.3	-2:06:07.15	0.2199	2.206	1.118	-1.40	23.26	22.92	22.52
12481	23:8:57.3	-2:06:01.53	0.6076	1.558	1.344	1.030	23.77	22.55	21.04
12483	23:8:03.90	-2:06:00.99	0.2740	2.831	1.200	0.928	21.62	20.80	20.16
12495	23:8:21.5	-2:06:00.64	0.3025	7.257	1.373	1.593	23.27	22.28	21.62
12528	23:8:38.8	-2:05:57.7	0.5580	11.11	1.210	1.561	22.59	22.26	21.21
12530	23:8:46.6	-2:05:59.6	0.2956	1.965	1.415	1.412	23.80	22.79	21.73
12554	23:7:48.8	-2:05:56.7	0.2992	5.121	1.338	0.401	23.43	22.54	21.82

Table C.1—Continued

ID	R.A.	DEC.	z	$W_0(\text{[OII]})$ [Å]	$D4000$ [Å]	$W_0(\text{H}\delta)$ [Å]	$B_{\text{AB}}$ [mag]	$V_{\text{AB}}$ [mag]	$R_{\text{AB}}$ [mag]
12566	23:7:45.8	-2:05:56.4	0.4768	7.449	1.246	0.835	23.71	23.23	22.15
12574	23:8:36.6	-2:05:43.6	0.0824	9.502	1.280	1.610	20.29	19.94	19.52
12604	23:8:34.6	-2:05:48.5	0.7358	2.595	0.436	ND	22.47	22.28	21.57
12611	23:7:51.2	-2:05:47.2	0.4523	15.45	1.032	0.505	21.17	20.72	20.16
12616	23:8:22.1	-2:05:50.0	0.7363	5.771	-0.07	ND	23.00	22.50	21.61
12632	23:7:22.5	-2:05:34.7	0.8964	ND	ND	ND	18.10	17.56	16.89
12670	23:8:14.8	-2:05:47.4	0.6930	-2.35	0.620	14.07	99.00	24.01	22.56
12693	23:7:57.8	-2:05:42.2	0.5689	0.573	1.688	0.097	24.11	22.89	21.36
12695	23:8:00.05	-2:05:40.1	0.2940	-1.45	1.525	-0.61	22.14	21.09	20.09
12701	23:7:36.2	-2:05:42.2	0.2713	10.58	1.214	1.511	23.39	22.53	21.96
12705	23:8:58.1	-2:05:41.2	0.5781	-1.71	1.739	0.943	23.88	22.66	21.28
12736	23:8:07.93	-2:05:35.8	0.5049	6.481	1.200	1.409	22.25	21.74	20.74
12778	23:7:30.7	-2:05:25.8	0.4991	-1.58	2.092	0.576	22.59	21.55	20.09
12784	23:8:10.1	-2:05:30.9	0.2234	7.642	1.261	0.892	22.03	21.39	20.96
12790	23:8:38.1	-2:05:31.8	0.5028	1.475	1.527	1.147	23.79	22.75	21.27
12791	23:7:58.5	-2:05:30.9	0.5487	0.169	1.986	0.441	23.99	23.01	21.45
12813	23:7:29.6	-2:05:29.9	0.4994	1.955	1.713	-0.61	24.14	23.15	21.57
12819	23:8:18.8	-2:05:26.7	0.2948	6.500	1.237	1.200	22.06	21.26	20.61
12838	23:8:13.9	-2:05:23.4	0.3570	1.255	1.164	0.483	22.70	21.74	20.74
12847	23:7:54.5	-2:05:26.7	0.6240	-1.35	1.669	-2.40	25.80	23.76	22.19
12936	23:7:31.1	-2:05:16.4	0.2384	11.56	1.254	1.022	23.16	22.60	22.11
12937	23:8:46.5	-2:05:12.3	0.3008	2.993	1.514	1.410	23.35	22.35	21.23
12938	23:7:54.7	-2:05:11.0	0.2996	6.394	1.307	1.277	22.54	21.82	21.28
12966	23:7:39.0	-2:05:00.78	0.4846	0.801	1.065	0.601	20.72	19.96	19.27
12975	23:7:51.9	-2:05:05.63	0.1782	0.567	1.130	-2.19	21.88	20.96	20.10
12983	23:8:01.89	-2:04:39.1	0.2962	1.262	1.987	0.011	20.61	19.53	18.42
12993	23:8:40.9	-2:05:01.31	0.5769	2.518	1.287	-0.08	23.23	22.58	21.22
12994	23:8:25.1	-2:05:08.86	0.3027	4.566	1.217	1.386	23.20	22.20	21.51
12996	23:8:57.5	-2:05:00.33	0.2976	-0.34	1.715	0.283	21.49	20.56	19.62
12998	23:7:21.6	-2:05:09.23	0.2063	10.42	1.279	1.199	22.66	22.20	21.70
13001	23:7:22.1	-2:05:01.02	0.2984	8.135	1.281	0.806	21.62	20.95	20.47
13007	23:8:02.08	-2:04:56.9	0.1616	0.617	1.863	-0.45	20.13	19.18	18.38
13013	23:8:52.1	-2:05:06.30	0.6502	1.510	1.095	-2.55	22.47	22.11	21.25
13024	23:8:49.6	-2:04:51.7	0.2021	6.559	1.268	0.323	21.72	21.29	20.73
13052	23:7:49.4	-2:05:00.24	0.2931	2.090	1.273	1.636	22.47	21.55	20.79
13077	23:8:11.2	-2:04:57.3	0.5990	3.300	1.293	1.131	22.97	22.59	21.44
13124	23:8:10.2	-2:04:46.8	0.3559	1.266	1.594	0.023	22.09	21.08	19.92
13126	23:7:27.0	-2:04:48.5	0.3010	3.487	1.276	1.073	21.86	21.16	20.53
13141	23:8:22.1	-2:04:50.0	0.5037	3.179	1.742	-0.44	22.53	22.10	20.86
13194	23:7:22.3	-2:04:40.8	0.5002	1.399	1.366	0.748	23.31	22.40	20.98
13223	23:7:32.5	-2:04:36.3	0.2508	7.948	1.215	0.841	21.94	21.33	20.87
13247	23:8:43.4	-2:04:40.7	0.4256	-1.28	1.763	-0.68	24.38	22.84	21.48
13249	23:7:38.1	-2:04:38.6	0.2051	10.56	1.291	0.825	22.25	21.73	21.25
13253	23:8:49.9	-2:04:34.9	0.3043	4.545	1.210	0.769	21.54	20.82	20.17
13256	23:7:52.5	-2:04:41.2	0.2708	2.089	1.162	1.034	23.88	23.57	22.46
13260	23:8:35.8	-2:04:23.3	0.1623	0.304	1.850	0.029	19.80	18.89	18.15
13281	23:8:01.62	-2:03:59.2	0.2966	-0.97	1.830	0.287	19.93	18.80	17.66

## C Spectroscopic members catalogue of RXCJ2308.3-0211 (A 2537)

Table C.1—Continued

ID	R.A.	DEC.	z	$W_0([\text{OII}])$ [Å]	$D_{4000}$ [Å]	$W_0(\text{H}\delta)$ [Å]	$B_{\text{AB}}$ [mag]	$V_{\text{AB}}$ [mag]	$R_{\text{AB}}$ [mag]
13290	23:8:04.71	-2:04:30.2	0.3560	2.457	1.146	1.292	21.99	21.41	20.53
13332	23:8:02.50	-2:04:23.6	0.2971	1.045	1.306	-0.36	21.50	20.50	19.55
13355	23:7:56.8	-2:04:32.7	0.6008	1.999	1.330	1.242	24.53	23.68	22.45
13369	23:8:00.28	-2:04:27.6	0.2985	2.087	1.359	1.318	22.75	21.90	21.05
13381	23:7:27.3	-2:04:22.5	0.5019	-1.98	1.687	4.275	22.60	21.80	20.52
13395	23:8:47.9	-2:04:28.3	0.1395	1.181	1.286	0.608	22.97	22.71	22.24
13406	23:7:55.6	-2:04:20.7	0.2978	2.989	1.327	1.229	21.72	20.82	19.92
13419	23:7:57.8	-2:04:21.8	0.3077	-0.63	1.242	-0.23	22.96	22.04	21.44
13422	23:8:14.9	-2:04:21.4	0.3555	-1.16	1.541	-0.27	23.69	22.48	21.16
13423	23:8:31.5	-2:04:21.6	0.3572	9.016	1.149	1.104	23.18	22.54	21.68
13445	23:7:37.0	-2:04:18.7	0.1967	6.849	1.340	1.162	22.20	21.79	21.23
13501	23:7:59.7	-2:04:05.18	0.4485	1.260	1.478	1.038	22.61	21.82	20.60
13506	23:7:25.1	-2:04:07.21	0.4952	-3.43	1.663	0.521	21.56	20.99	20.17
13533	23:7:33.2	-2:04:05.08	0.3263	3.088	1.293	1.817	21.95	21.21	20.51
13544	23:8:22.7	-2:04:07.17	0.5544	3.652	1.774	0.526	23.43	22.67	21.09
13573	23:8:09.37	-2:04:04.86	0.3013	-0.87	1.672	0.347	22.88	21.91	20.86
13581	23:7:51.1	-2:03:53.9	0.1925	-6.36	1.334	1.122	20.24	19.70	19.17
13654	23:8:19.7	-2:03:51.5	0.3016	9.597	1.200	-0.18	20.33	19.75	19.23
13663	23:7:33.7	-2:03:52.9	0.2563	0.255	1.626	0.204	22.67	21.46	20.50
13678	23:7:41.7	-2:03:48.8	0.2940	0.915	1.469	1.592	22.37	21.51	20.62
13698	23:8:07.84	-2:03:46.6	0.2692	5.141	1.198	2.000	21.87	21.03	20.48
13732	23:8:22.3	-2:03:34.8	0.7750	5.913	ND	ND	23.53	23.00	21.85
13737	23:7:27.0	-2:03:46.0	0.0068	-2.01	1.225	1.537	22.57	22.45	21.77
13741	23:8:20.9	-2:03:44.7	0.3011	12.66	1.195	0.801	21.59	21.05	20.53
13810	23:7:30.9	-2:03:37.3	0.8728	-6.72	ND	ND	23.35	22.51	21.35
13841	23:8:06.88	-2:03:32.2	0.2965	1.346	1.408	-0.26	23.34	22.44	21.59
13869	23:8:00.01	-2:03:24.3	0.4493	1.201	1.803	0.377	22.15	21.17	19.70
13887	23:7:37.5	-2:03:19.5	0.3549	-2.16	1.680	1.836	21.13	20.41	19.27
13900	23:7:38.5	-2:03:28.7	0.7045	7.570	0.172	23.34	23.24	22.80	21.78
13925	23:7:29.8	-2:03:19.4	0.6222	2.365	1.148	-0.22	22.69	22.22	21.10
13955	23:8:13.6	-2:03:15.7	0.3548	0.396	1.659	0.766	20.02	19.49	18.82
13998	23:8:10.1	-2:03:19.0	0.4861	-1.67	1.602	0.279	24.33	24.06	22.28
14019	23:7:21.8	-2:03:11.4	0.1922	2.890	1.305	0.779	21.84	21.36	20.87
14039	23:8:07.79	-2:03:01.11	0.2988	0.860	1.551	0.423	20.83	19.92	19.12
14085	23:7:42.0	-2:03:07.11	0.2655	7.081	1.308	1.920	22.40	21.74	21.20
14113	23:8:26.1	-2:03:01.28	0.3031	3.071	1.703	0.372	22.10	21.11	20.21
14150	23:7:25.6	-2:02:52.9	0.3468	4.588	1.241	0.458	20.58	19.81	19.04
14156	23:8:05.25	-2:03:01.18	0.3569	3.250	1.277	1.703	23.82	22.89	21.94
14212	23:7:20.5	-2:02:50.6	0.5008	14.01	1.175	0.622	22.45	22.10	21.22
14225	23:8:19.8	-2:02:51.3	0.3060	0.800	1.553	0.995	21.77	20.84	20.04
14256	23:8:11.5	-2:02:46.4	0.3514	-1.24	1.772	0.331	22.46	21.53	20.35
14261	23:7:29.3	-2:02:50.3	0.5620	3.744	1.156	1.378	23.44	22.91	21.83
14292	23:8:09.43	-2:02:44.1	0.3587	1.435	1.679	1.452	22.27	21.27	20.12
14359	23:8:04.73	-2:02:38.1	0.4538	3.355	1.135	1.368	22.55	21.92	20.96
14387	23:8:06.70	-2:02:17.2	0.3828	7.689	1.463	-0.89	21.13	20.21	19.17
14397	23:8:21.1	-2:02:30.9	0.4392	16.33	1.115	-1.14	21.22	20.76	20.15
14426	23:7:20.1	-2:02:35.0	0.5007	-2.24	1.458	0.452	24.58	23.44	22.27

Table C.1—Continued

ID	R.A.	DEC.	$z$	$W_0(\text{[OII]})$ [Å]	$D4000$ [Å]	$W_0(\text{H}\delta)$ [Å]	$B_{\text{AB}}$ [mag]	$V_{\text{AB}}$ [mag]	$R_{\text{AB}}$ [mag]
14435	23:7:28.7	-2:02:14.9	0.2947	4.956	1.281	1.038	20.97	20.12	19.37
14448	23:7:38.7	-2:02:30.0	0.7029	2.663	0.191	5.931	22.96	22.40	21.39
14461	23:8:21.6	-2:02:27.7	0.4380	6.179	1.129	0.837	22.34	21.78	20.89
14468	23:8:09.35	-2:02:30.6	0.3834	8.087	1.343	2.004	23.49	22.66	21.98
14477	23:8:01.77	-2:02:27.9	0.3233	0.725	1.508	1.150	22.69	21.91	20.91
14485	23:7:31.2	-2:02:28.2	0.2726	5.353	1.316	2.031	23.23	22.42	21.80
14556	23:8:09.70	-2:02:19.5	0.2979	-1.68	1.639	-0.48	23.92	23.15	22.13
14561	23:7:40.7	-2:02:18.9	0.5060	8.328	1.255	1.587	23.31	22.91	21.81
14777	23:7:26.3	-2:01:53.3	0.7025	11.05	0.113	32.29	23.63	23.24	22.25
14816	23:7:42.7	-2:01:46.9	0.2951	6.490	1.245	1.136	22.66	21.79	21.18

**C Spectroscopic members catalogue of RXCJ2308.3-0211 (A 2537)**

---



# Curriculum vitae

## Personal data

Birthdate	07/10/1977, Milano, Italy
Citizenship	Italian
Permanent address	Via L.G. Faravelli 7, Milano, 20149 Italy
Current address	Max-Planck-Institut für extraterrestrische Physik, Garching bei München, 85748 Germany
e-mail	fbraglia@mpe.mpg.de ; filiberto.braglia@googlemail.com
Phone number	Office: +49-89-30000-3892

## Languages

Italian	native language
English	fluent
French	good
Spanish	basic
German	learning
Russian	learning

## Education

1/1/2005 - present	Ph.D. student in the International Max-Planck Research School (IMPRS) at Max-Planck-Institut für extraterrestrische Physik (Munich, Germany). Supervisor: Prof. Hans Böhringer
11/02/2004	Master Degree in Physics, Università di Milano-Bicocca (Milano, Italy). Supervisor: Dr. Luigi Guzzo
Oct. 2001 - Feb. 2004	Student at Università di Milano-Bicocca (Milano, Italy)
Oct. 1996 - Sep. 2001	Student at Università degli Studi di Milano (Milano, Italy)
10/07/1996	High school Diploma (Maturità classica), Liceo-Ginnasio C. Beccaria (Milano, Italy)

## Curriculum vitae

---

### Conferences, workshops and schools

- March 31-April 3 2008    **“From exoplanets to galaxy clusters: science with Astro-WISE”**, Leiden, Netherlands  
Invited speaker, *“Galaxy ethology in a massive  $z\sim 0.3$  cluster”*
- June 25-29 2007        **“Tracing Cosmic Evolution with Galaxy Clusters: Six Years Later”**, Sesto (Italy)  
Poster contribution, *“Flaming giant galaxies along filaments in A2744”*
- May 14-16 2007        **REXCESS Workshop**, Frauenwoerth am Chiemsee (Germany)  
Contributed talk, *“Giant star-forming galaxies along filaments in-falling on a massive cluster”*
- August 6-11 2006      **“Heating vs. Cooling in Galaxies and Clusters of Galaxies”**, Garching (Germany)  
LOC member: webmaster, conference room technics manager and general IT manager
- September 5-17 2005    **“Summer School Novicosmo 2005: The Dark and Luminous Sides of The Formation of Structures”**, Novigrad-Cittanova (Croatia)

### IT skills

OS	GNU/Linux, Unix, Windows
Programming	IDL, Bash, SM
Publishing	L <sup>A</sup> T <sub>E</sub> X, HTML, Perl
Data reduction	IRAF, VIPGI, IRDR, SExtractor, HyperZ
Proposals	p2pp, VMMPs, GuideCam

### Publication list

**Braglia, F.**; Pierini, D.; Böhringer, H. 2007, *“Flaming, bright galaxies along the filaments of A 2744”*, A&A 470, 425

Böhringer, H.; **Braglia, F.**; Pierini, D.; Biviano, A.; Schuecker, P.; Zhang, Y.Y.; Finoguenov, A.; Pratt, G.W.; et al. 2006, *“Unveiling the Structure of Galaxy Clusters with Combined ESO-VLT WFI, and XMM-Newton Observations”*, Msngr. 123, 49

Moretti, A.; Guzzo, L.; Campana, S.; Lazzati, D.; Panzera, M. R.; Tagliaferri, G.; Arena, S.; **Braglia, F.**; et al. 2004, *“The Brera Multi-scale Wavelet HRI Cluster Survey. I. Selection of the sample and number counts”*, A&A 428, 21